INAUGURAL - DISSERTATION
zur
Erlangung der Doktorwürde

der
Naturwissenschaftlich-Mathematischen
Gesamtfakultät

der
Ruprecht-Karls-Universität
Heidelberg

vorgelegt von
Diaa Gad El-Mawla
aus Kairo/Ägypten

Tag der mündlichen Prüfung: 14. 02. 2001

Generation and Propagation of Longitudinal Tube Waves in Late-Type Stellar Atmospheres and the Rotation - Emission Activity Relation

Gutachter: Prof. Dr. Peter Ulmschneider

Dr. Hans Martin Schmid

Dissertation
submitted to the
Combined Faculties for the Natural Sciences and for Mathematics
of the Rupertus Carola University of
Heidelberg, Germany
for the degree of
Doctor of Natural Sciences

Presented by
Diaa Gad El-Mawla
born in: Cairo/Egypt

Heidelberg, 14. 02. 2001

Referees: Prof. Dr. Peter Ulmschneider

Dr. Hans Martin Schmid

Generation and Propagation of Longitudinal Tube Waves in Late-Type Stellar Atmospheres and the Rotation - Emission Activity Relation

Generated longitudinal tube wave (LTW) energy fluxes as a result of the interaction of magnetic flux tubes with the turbulent medium of the convection zones of late-type stars were computed.

Solar magnetic flux tubes of different filling factors were heated with adiabatic and radiatively damped LTW. It was found that the tube geometry plays an important role for heating the outer layers.

The response of the chromospheres of the Sun and two late-type stars (of spectral types F5V & M0V) to the excitation by different wave modes was studied. It was found that the magnetic atmosphere shows resonance oscillations with longer periods in comparison with the non-magnetic plane parallel atmosphere.

Magnetic chromosphere models were constructed for late-type stars based on our computed LTW fluxes. The mean temperatures of all spectral types for a given magnetic filling factor show a monotonic outward (classical) temperature rise.

A new picture of the heating of stellar chromospheres is presented. The chromospheric emission can be explained by an ordered sequence of different heating processes which systematically vary as a function of height in the star and with its rotation rate.

The *low chromosphere* is heated by acoustic shock waves. The *middle and upper chromosphere* by longitudinal and transverse MHD waves via shock dissipation. For the *highest chromosphere*, wave heating is insufficient and additional non-wave heating (e.g. magnetic reconnection) is necessary. With increasing rotation, the magnetic heating mechanisms become more important (rotation - emission activity relation). Based on our computed Mg II fluxes we estimate the rotational periods of G- and K- type-stars.

Erzeugung und Ausbreitung longitudinaler Röhrenwellen in Atmosphären Später Sterne und die Rotations-Emissionsaktivitäts-Relation

Die Energieflüße erzeugter longitudinaler Röhrenwellen (LTW) als Ergebnis der Wechselwirkung von magnetischen Flußröhren mit der Turbulenz in den Konvektionszonen später Sterne wurde berechnet.

Solare magnetische Flußröhren mit unterschiedlichem Füllungsfaktor wurden mittels adiabatischer und strahlungsgedämpfter LTW's geheizt. Die Geometrie spielt eine wichtige Rolle bei der Heizung der äußeren Atmosphärenschichten.

Die Reaktion der Chromosphäre der Sonne und von zwei späten Sternen (vom Spektraltyp F5V & M0V) auf die Anregung durch verschiedene Wellenmoden wurde untersucht. Für die magnetische Atmosphäre wurden Resonanzoszillationen mit längeren Perioden gefunden als bei nicht-magnetischen Atmosphären.

Basierend auf den berechneten LTW Flüssen wurden magnetische Chromosphären-modelle berechnet. Die mittleren Temperaturen zeigen bei allen Spektraltypen und für gegebenen Füllungsfaktor einen monotonen nach außen ansteigenden (Klassischen) Verlauf.

Ein neues Bild der Heizung von stellaren Chromosphären wird vorgestellt. Die Chromosphärische Emission kann durch eine geordnete Sequenz verschiedener Heizungsprozesse erklärt werden, die als Funktion der Höhe im Stern und seiner Rotationsrate systematisch variieren.

Die *untere Chromosphäre* wird durch akustische Stoßwellen geheizt. Die *mittlere und obere Chromosphäre* durch longitudinale und transversale MHD-Wellen via Stoßwellendissipation. Für die *höchste Chromosphäre* ist Wellenheizung nicht ausreichend und ein weiterer nicht-Wellen-Heizungsmechanismus (e.g. magnetische Rekonnektion) ist nötig. Mit zunehmender Rotation wird die magnetische Heizung wichtiger (Rotation-Emissionsaktivitäts-Beziehung). Basierend auf unseren berechneten Mg II Flüssen wurden Rotationsperioden von G- und K- Sternen abgeschätzt.

Contents

Chapter 1

Introduction

1.1 Stellar Outer Layers

Observations of spectral lines formed in the outer layers of the Sun show different temperature regimes, the chromosphere, the first layer after the temperature minimum (of temperature $\approx$ 4000 K) in which the temperature reaches 10 000 K. Following this layer is the transition region with temperatures $\approx 10^5$ K. The corona is the hottest outer layer with temperatures $\geq 10^6$ K. The Mg II h and k resonance lines at 2803 Å and 2796 Å and the Ca II H and K lines at 3968 Å and 3934 Å are sensitive indicators of the temperature structure of the chromosphere. The C IV λ1550 emission line is usually used to probe the transition region plasma, while soft X-rays (0.1-4 kev) come from the $10^6 - 10^7$ K corona.

Observations of the Sun show that strong Ca II emission is associated with plages and the supergranulation network, since both regions have strong magnetic fields, this suggests that Ca II emission originates from magnetic structures. Since late-type stars (with surface convection zones) have similar structure to the Sun, they show similar temperature structure in their outer layers. Mg II emission lines have been detected in all late-type stars later than F2 (Böhm-Vitense and Dettman 1980). The full understanding of how these outer layers are heated has not yet been achieved, the mechanisms responsible for heating these layers are thought to be of non-radiative origin (see, Narain & Ulmschneider 1996). The existence and the energy balance of the outer hot layers require a continuous source of energy to overcome the radiative cooling, which should be continuously supplied from stellar convective motions.

1.2 Heating Mechanisms

Turbulence due to convective motions near stellar surfaces generate pressure fluctuations and magnetic fields. Pressure fluctuations produce traveling acoustic waves which steepen while propagating outward due to the strongly decreasing density forming shocks and dissipating energy. The generated magnetic field traps plasma and works as a connecting channels for transferring the sub-photospheric mechanical energy to upper layers. Stellar convection zones are the main engines of generating mechanical energy of different forms.

Part of the energy might be in form of waves which travel upward and heat the outer layers.

Heating by dissipating shock waves was first suggested by Biermann (1946) and Schwarzschild (1948). Two fundamental mechanisms (acoustic and magnetic heating) should exist in addition to other mechanisms, these two mechanisms are the dominant heating mechanisms for late-type stars (see, Narain & Ulmschneider 1996). It is now widely believed that non-magnetic chromospheric regions are heated by shock dissipation of acoustic waves, also this mechanism is dominant for slowly rotating stars. On the other hand, magnetic chromospheric regions and the chromospheres of rapidly rotating stars are believed to be heated by dissipation of magnetic waves. For very active stars, very rapidly rotating stars (periods of the order of few days), or compact binary stars, other mechanisms like magnetic reconnections may play an important role to account for the observed high chromospheric and coronal activity.

Magnetic heating is the dominant mechanism for rapidly rotating late-type stars (except F-stars) and acoustic heating is the dominant mechanism for slowly rotating stars. For F-stars, the acoustic heating is more dominant than the magnetic heating because of the very large convective velocities found for these stars (Narain & Ulmschneider 1996). Observations by Simon and Landsman (1991) show no correlation between the chromospheric emission and rotation for stars earlier than F5, which means that the chromospheres of these stars are heated mainly by shock dissipation of acoustic waves.

The observed large nonthermal velocities (Nesis et al. 1990) in the regions where the magnetic flux tubes are concentrated and the overlaying large chromospheric emission supports the magnetic heating mechanism in addition to the acoustic heating mechanism.

1.3 Solar and Stellar Magnetic Fields

The magnetic field on the Sun was first identified in sunspots by Hale (1908). Later Howard and Stenflo (1972) and Frazier and Stenflo (1972) showed that at least 90 percent of the magnetic field in the solar photosphere outside active regions is concentrated in narrow filaments of high field strength. The term magnetic flux tubes is used to model the magnetic field in the solar photosphere and lower chromosphere. The magnetic flux tubes are bundles of magnetic field lines controlled by horizontal pressure balance with the surrounding gas; the sum of the internal gas pressure and the magnetic pressure should be balanced by the external field-free gas pressure. As a result of the pressure balance, the flux tubes spread out with increasing height forming a canopy over the non-magnetic regions. Recent observations by SOHO spacecraft show that flux tubes are concentrated in the downflow lanes between supergranulation cells (see, Fig. 1.1). These magnetic flux tubes can carry energy to the outer stellar layers . The line widths of magnetically sensitive absorption lines serve as a diagnostic tool to probe the magnetic fields, extra broadening was found in the intergranular regions. The magnetic field of late-type stars are thought to be generated by the dynamo mechanism. Measuring the surface magnetic fields of stars is a complicated task because of the lack of high spectral resolution.

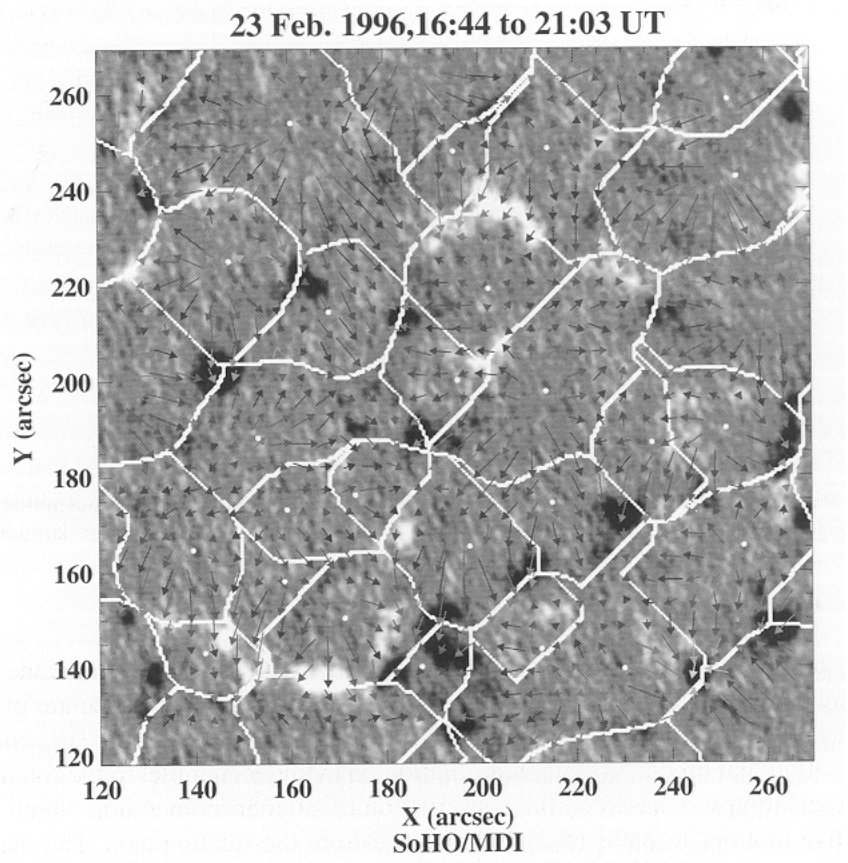

Fig. 1.1 Supergranular flow determined by tracking granulation, superimposed on a magnetogram, both observed by SOHO/MDI in the high resolution mode with a 1.2- arcsec (or 870-km) angular resolution. The vectors represent averages of the flow over a 3-h interval. The magnetic field (shown in black and white for opposite polarities) clusters predominantly within the downflow lanes, from: Schijver & Zwaan (2000).

1.4 Solar Magnetic Activity

The structure of solar atmosphere is determined by various forces, magnetic forces, turbulent motions, and by different heating processes. The solar activity is a manifestation of the interaction between these forces. The magnetic field plays the prominent role in forming the solar and stellar activities. Because of the high spatial and temporal resolution, detailed structures of the magnetic fields, different magnetic features with different sizes and strengths are seen on the Sun.

The most important observed characteristics of the solar magnetic field are: (1) The magnetic field emerges in bipolar regions (active regions) with different sizes, the time development of these features depends on the size of the feature. (2) The process of emerging magnetic flux to the surface is complete within a few days even for large bipolar regions, then decay starts at once with much slower rates (Harvey and Zwaan 1993). (3) The area of the bipolar regions is proportional to their flux content with an average flux density ($< fB >$; with f is the magnetic filling factor and B is the magnetic field strength) of 100 Gauss to 150 Gauss (Schrijver and Harvey 1994). (4) The life time of the active regions ranges from less than a day up to a few months, depending on their

size. Around 11% have life times comparable to the time of one solar rotation, and about 3% live as long as two rotations (Harvey 1993). Larger regions live longer than smaller regions.

(5) The emergence latitude of the bipolar regions follow a cyclic behavior, it starts near a latitude of 60^0 on both hemispheres (the beginning of the cycle) then they appear closer and closer to the equator at the end of the cycle. (6) Dark spots (sunspots) with strong magnetic field strengths inhibit the convective energy from penetrating the surface, allowing only radiative energy transport. The number and appearance latitude of these spots changes in a cyclic way of an average period of 11 yr. Sunspots usually appear in pairs of opposite magnetic polarities. The magnetic field lines near the center of the spot are nearly vertical.

(6) The magnetic field strengths range from hundred gausses to several kilo gausses, e.g., plages have a magnetic field strength in the range of 100 - 500 Gauss, while magnetic flux tubes show field strengths of 1 - 2 K Gauss, and Sunspots have field strengths range from 2 to 3 K Gauss. (7) Most of the magnetic field is concentrated in the regions where strong downflows take place, along the boundaries of the supergranulation cells (see, Spruit et al. 1990). (8) Bright emission points form a network (e.g., upper photospheric network and chromospheric network), which occurs along the boundaries of the supergranulation cells, this network gets coarser with height indicating that cross sections of the structures diverge with height (Stenflo 1994).

(9) The cross sections of the magnetic elements expand with height as a result of the exponentially decreasing external gas pressure with height. (10) It has been found that the chromospheric and coronal radiative losses are closely connected to the detailed structure of the underlying photospheric magnetic flux density. The processes lead to the generation and intensification of the solar magnetic field are not well understood, while the dynamo mechanism is thought to be the mechanism for generating magnetic field, the convective collapse is taken to be the mechanism for the amplification of weak magnetic fields near stellar surfaces.

a. Dynamo Mechanism

The presence of magnetic fields in the Sun and stars and the resulted activities raises the question of their origin, are these fields primordial or regenerated by renewable mechanisms ?. Priest (1984) stated that, the eddy magnetic diffusivity in the convection zone is around $10^9\ m^2 s^{-1}$ which would destroy the magnetic flux there after about 10 yr, also the magnetic buoyancy would tend to expel magnetic flux at some fraction of the Alfvén speed. He also concluded that even if a primordial field exists in the core it should be decoupled from the solar cycle, this means that the generation of magnetic field is done by a renewable mechanism.

Recent theories support the idea that the magnetic field of the sun is generated by a dynamo mechanism. The dynamo mechanism can be defined as a process in which some of the kinetic energy of an electrically conducting fluid is converted into magnetic energy, the motion of the plasma across a magnetic field leads to an induced electric field, which generates electric currents which in turn generates a magnetic field. The cyclic

solar magnetic activity is one of the important phenomenae which should be explained within the dynamo theory.

There are different types of dynamo, the dynamo which works for the sun is not the same as that of the Earth (where the field is steady), different mechanisms exist for rapidly and slowly rotating stars. The efficiency of a dynamo is proportional to the rotation rate, also the existence and the depth of the convection zone is of great importance for the dynamo mechanism. Here, we restrict attention to the solar dynamo.

The magnetic field may be described by two components, toroidal and poloidal, the toroidal is the azimuthal component, and the poloidal component represents the sum of the polar and radial components in cylindrical coordinates. The highly turbulent motions in the solar convection zone generate differential rotation through transport of angular momentum, because of the high electrical conductivity of the plasma in this region, the magnetic field lines are frozen into the plasma and can be moved easily, under the effect of differential rotation, from a purely poloidal field to a toroidal flux system. When this toroidal field becomes strong enough, lines of force are shaped like Ω - loops, which emerge to the surface because of buoyancy forces. The emerging Ω - loops through the surface of the Sun have field strengths of 500 G (Parker 1994). All activities seen in the solar photosphere and outer layers are attributed to the emergence of the Ω - shaped loops (Zwaan 1996).

Hale et al. (1919) stated two rules of the observed polarities of sunspots, (1) during a sunspot cycle, the leading polarities on the northern hemisphere have the same sign, which is opposite to that of the southern hemisphere, and (2) during the next cycle all polarities are reversed. Zwaan (1978, 1996) argued that the first polarity rule indicates that bipolar active regions emerge from toroidal flux bundles below the solar surface, and this toroidal flux system is located below and close to the bottom of the convection zone, in the overshoot region between the radiation dominated interior and the outer convection zone.

Moreno-Insertis (1992) showed that the magnetic field strength of the stored toroidal field is of the order of 10^5 G. Numerical simulations by D'Silva & Choudhuri (1993) and Fan et al. (1993) show that the latitude and the tilt (relative to the east-west direction) of bipolar magnetic regions at the surface can be reproduced if rising Ω - loops are formed from toroidal field with strengths of $0.5 - 1 \cdot 10^5$ G. These flux concentrations are always modeled as magnetic flux tubes in mechanical equilibrium. When a critical value of the magnetic field strength is reached, the flux tubes become unstable, leading to the formation of flux loops which rise to the surface forming bipolar active regions (Schüssler et al. 1994). It is widely accepted that the toroidal magnetic field of the Sun is produced by the shearing of the poloidal field (Parker 1994).

The regeneration of the toroidal and poloidal fields is combined in what is called an $\alpha\omega$-type dynamo. Toroidal magnetic field can be generated from poloidal field by differential rotation (ω-effect), and the poloidal field can be formed around an initially toroidal field through the Coriolis force (α-effect). The concept of an α-effect originated from the idea that the interaction between the cyclonic fluid motion with velocity u and the magnetic field B would result in an average electromotive force, $< u \times B >$, which has a component $\alpha < B >$ in the direction of the mean magnetic field, $< B >$ (see, Parker

1955 a,b), the coefficient α represents the α-effect (Moffatt 1978; Krause & Rädler 1980). Recent MHD simulations (Brandenburg & Schmitt 1998) confirmed that in a rotating medium, the magnetic buoyancy instability leads to an α-effect.

b. Convective Collapse

The processes which lead to the intensification of solar magnetic flux tubes are not well understood, while the currently accepted theory is based on the thermal convective instability driven by buoyancy forces acting on a weak magnetic field leading to its concentration in a process called convective collapse (Parker 1978; Webb and Roberts 1978; Spruit 1979; Spruit and Zweibel 1979; Hasan 1985; Steiner 1996), while no observational evidence supporting this theory exists.

Parker (1963) showed that magnetic flux tubes or sheets are formed in the intergranular downflow lanes as a result of the convective motions which sweep the magnetic flux toward downflow regions. The initial field strength is around 500 Gauss, reaching around 1500 Gauss after amplification by the convective instability. In a scenario described by Spruit (1979), when the rising plasma with the magnetic field reaches the photosphere it cools by radiation, then it becomes more denser than surroundings flowing down again along the field lines. The magnetic flux tube tries to reach pressure equilibrium with the surroundings by contraction which increases the field strength. The downflow stops when the magnetic and the internal gas pressures balance the gas pressure outside the tube.

The study of the convective collapse started in the frame work of thin flux tube approximation with linear stability without taking radiation into account (Webb & Roberts 1978; Spruit & Zweibel 1979; Unno & Ando 1979). The effect of radiative heat transfer between the tube and the surroundings has been studied by Hasan (1986) within the linear regime, this study showed that the convective stability depends on the tube radius and plasma β (the ratio of the gas pressure to the magnetic pressure inside the tube), also a critical value of β is found; above which the tube is convectively unstable. Later 2- dimensional MHD numerical simulations of the convective collapse showed an upwardly propagating shock wave as a result of the interaction between the downflow rising materials (Steiner 1996; Grossman-Doerth et al. 1998).

1.5 Lower and Upper Limits of the Emitted Fluxes

Stars on the right hand side (cool side) of the Herzsprung-Russell diagram show different levels of the chromospheric activities as seen through the Ca II and Mg II emission fluxes. A clear lower limit of the emitted Ca II H+K and Mg II h+k core fluxes (basal fluxes) is seen in the flux-color diagrams of Rutten (1991) (see, Fig. 1.2). This lower limit is mainly determined by old slowly rotating stars, in which the magnetic field is very weak or died away completely. For these stars, the chromospheric and coronal activities depend primarily on the effective temperature and with little sensitivity on surface gravity or the elemental abundances (see, Schrijver 1995). The lower limit show a clear dependence on the luminosity class, the reason for that is not clear (Schrijver et al. 1989).

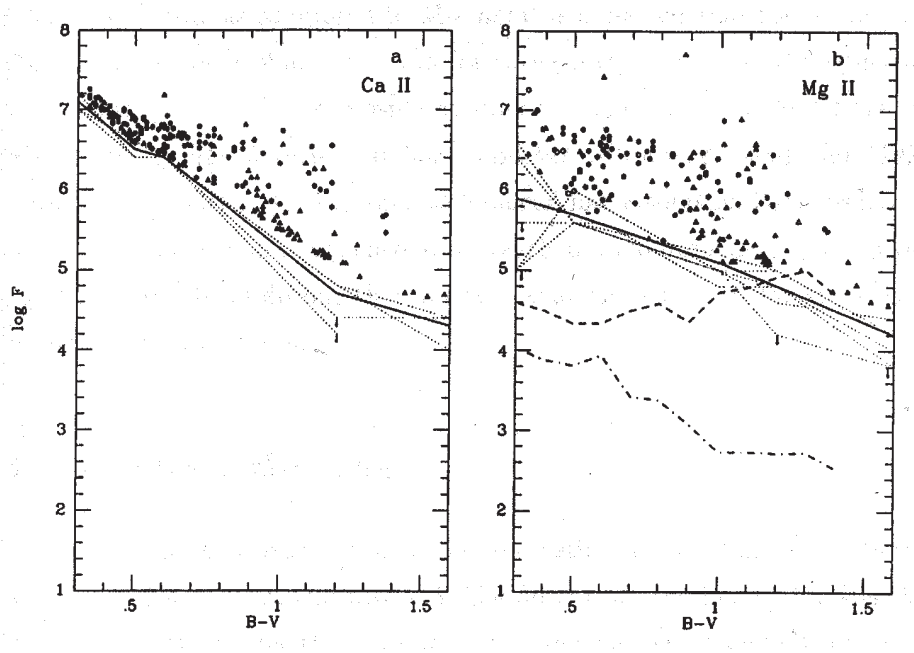

Fig. 1.2 The observed radiative fluxes in the Ca II H+K and Mg II h+k lines vs. color $B-V$. Circles mark dwarfs and giants are marked by triangles. Solid line is the basal flux line, the dashed and dot-dashed lines in (b) are the detection limits of the IUE for dwarfs and giants respectively, from: Rutten et al. (1991).

On the Sun, the basal flux is observed over the interiors of the supergranulation cells in the quiet Sun, which appear devoid of magnetic fields. Schrijver (1987) showed that the observed chromospheric line fluxes may consist of two components, one component is independent on stellar rotation (basal) and an additional one to account for the excess flux which depends on the stellar rotation (magnetic). Since the magnetic field does not play any role in the heating of the atmospheres of slowly rotating stars, it is widely accepted that the main heating mechanism is caused by the shock dissipation of purely acoustic waves (Schrijver 1987; Schrijver et al. 1989).

Ulmschneider (1989) and Buchholz et al. (1998) calculated time-dependent models of purely acoustically heated chromospheres for late-type stars and found a good agreement with the observed basal fluxes. As shown in the flux-color diagrams of Rutten (1991), the chromospheric emission (Mg II & Ca II) shows a wide spread (from basal fluxes) for large $B-V$ and a continuously decreasing spread with decreasing $B-V$ toward early F type stars. This is explained by Buchholz et al. (1998) on the basis of two-component (acoustic and magnetic) heating models where the acoustic heating component increases strongly toward decreasing $B-V$. This is because the efficiency of the acoustic wave generation strongly increases with decreasing $B-V$, and as a result the acoustic component become more dominant over the magnetic component leading to less variation for hot stars. This suggests that acoustic heating is a dominant heating mechanism for inactive and slowly rotating stars (basal flux stars), while for rapid rotators of active stars, the magnetic component should be added to the basal background fluxes. On the high emission side,

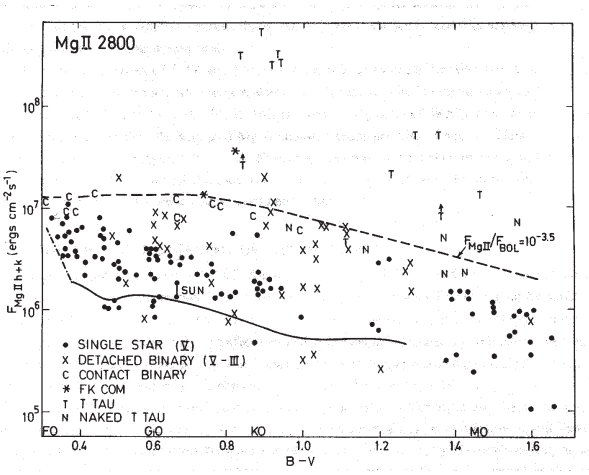

Fig. 1.3 The observed surface flux of the chromospheric Mg II emission lines, from: Vilhu et al. (1987).

an upper limit (saturation limit) of the observed emission fluxes of Mg II and C IV is found by Vilhu (1987). This upper limit is occupied by active stars, young and fast rotators, and short period close binaries. As shown in Fig 1.3, the upper limit is determined by contact binary stars, while T Tauri stars lie above the saturated limit, suggesting that these stars due to infalling material from the accretion disk have extra sources of heating compared to the other stars. Saturated stars have very high magnetic filling factors close to unity with large magnetic field strengths close to the equipartition field. The reason for this saturation limit is not clear, is it a saturation in the dynamo mechanism or because the stellar surface has the maximum allowed magnetic filling in order to still permit convection. For very active stars, heating by magnetic reconnection may be an important additional mechanism.

1.6 Rotation - Emission Activity Relation

Observations of stars with the same effective temperature and gravity show great difference in their chromospheric and coronal emissions (Basri and Linsky 1979; Ayres et al. 1981; Vaiana et al. 1981; Rutten et al. 1991), this implies that stellar activities are related to rotation. More rapidly rotating stars show higher levels of chromospheric activity than do slowly rotating stars. The idea that rotation plays an important role in the generation of magnetic activity is supported by observations (Wilson 1968; Kraft 1967; Skumanich 1972) which show that tracers of magnetic activity (e.g. Ca II H+K emission lines) are enhanced in more rapidly rotating main sequence stars. On the Sun the chromospheric and coronal emissions are concentrated in the magnetic elements above the supergranulation boundaries. The magnetic activity is closely related to stellar rotation and convection zone, rapidly rotating stars, young stars, show high levels of magnetic activities and consequently high level of chromospheric and coronal activities, and vice versa for slowly rotating stars. Figure 1.2 shows the observed radiative fluxes in the Ca II H+K and Mg II h+k lines (a,b respectively) with basal fluxes shown as solid lines and stars which show excess fluxes than the basal limit.

Rutten (1986) found a color dependent linear relation between the observed Ca II H

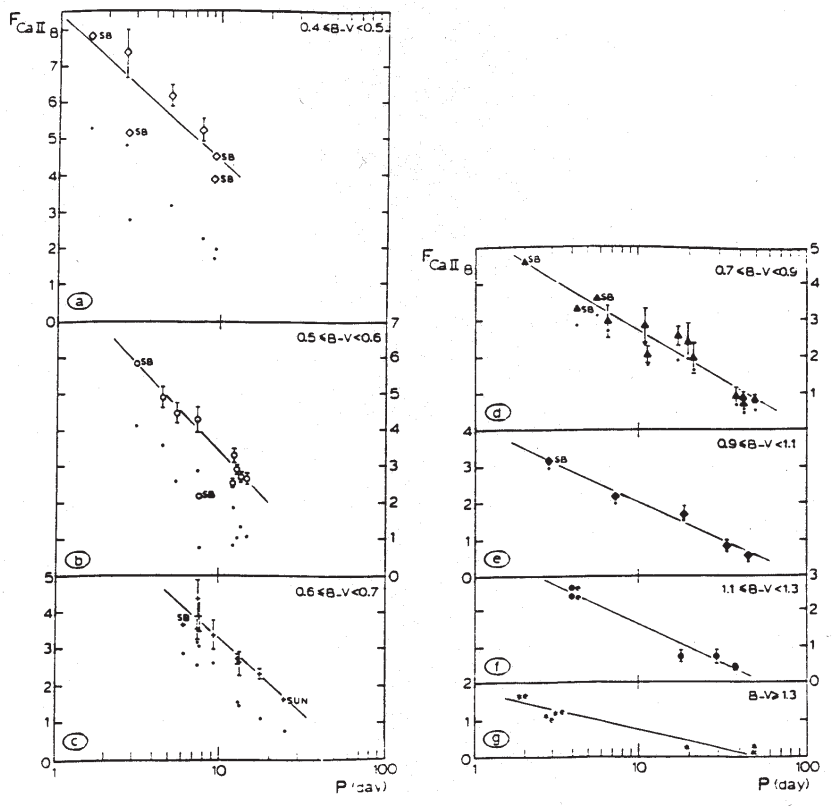

Fig. 1.4 Line core flux density F_{CaII} versus rotation period P for various $B-V$ intervals. The lines are fits to the observed data, the small dots indicate flux densities after subtraction of the line-wing contribution. Synchronized binaries are indicated by "sb" and emission-line stars by "e", from: Rutten (1986).

and K line core fluxes and the rotation rate for main sequence stars as shown in Fig. 1.4 for various $B-V$ intervals. Figure 1.4 a through g show that components of synchronized spectroscopic binaries (marked by "sb") follow the same relation between the emitted core flux and the rotation rate. He also concluded that the observed high activity levels of synchronized binaries are due to the rapid rotation which results from the tidal coupling between both stars. The same relation is also valid for emission-line stars (marked by "e" in Fig. 1.4f and g).

Montesinos et al. (1987) found for late-type stars a connection between the dynamo effect and the observed chromospheric activities as, for a fixed color index, the magnetic field increases when the rotation period decreases, and for a fixed period, the magnetic field is larger for stars with deeper convection zones. This means that the efficiency of the generation of magnetic fields increases with the stellar rotation rate and the depth of the convection zone.

1.7 The Present Work

The close relation between the observed chromospheric line losses and the interior-generated processes can be followed from the following sequence:

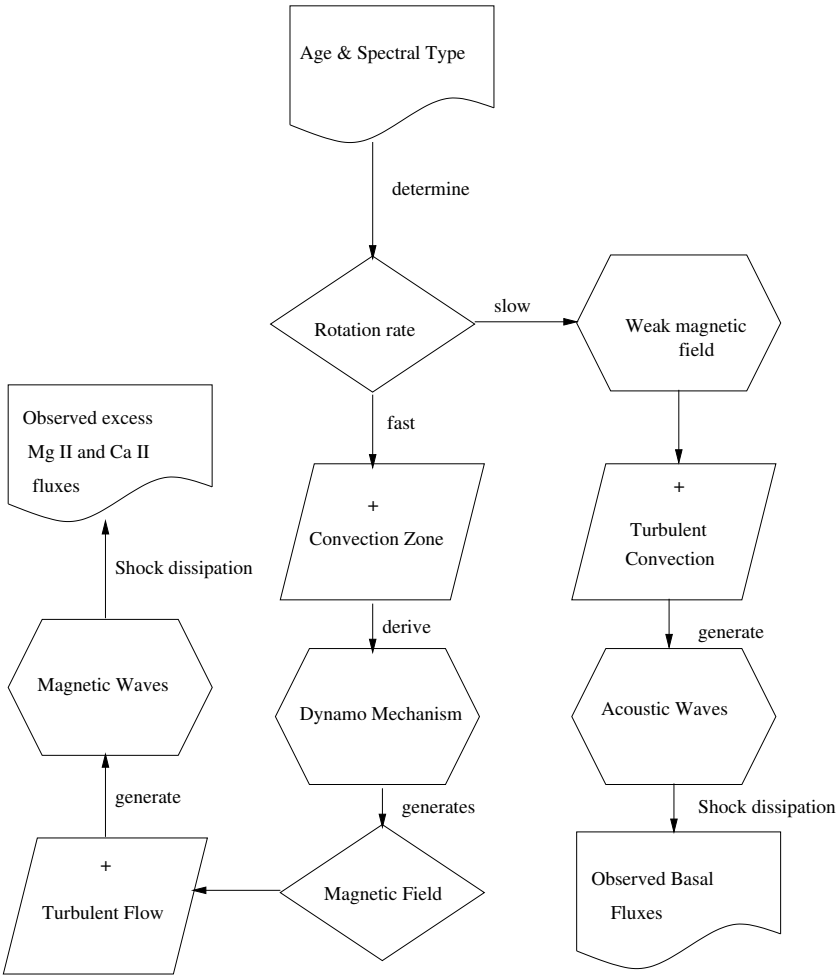

Fig. 1.5 The development of the interior-generated processes to the observed chromospheric line losses for single stars.

On the Sun, activity is related to magnetic fields, this leads to the suggestion that activity is traceable to a magnetic dynamo which results from the interaction of rotation and differential rotation with convection. The precise nature of these relations are not well understood.

The main stellar parameters which determine the chromospheric activity are the stellar age, and spectral type (T_{eff} & G) together with the rotation rate. The dynamo mechanism generates magnetic field at the base of the convection zone, then this field rises to the stellar surface and interacts with the turbulent flow due to convective motion, this interaction generates waves which propagate upward in the chromosphere, by forming shocks, the energy is released and the chromosphere is heated and the result is the production of emission lines.

The current study starts from the stage at which the generated magnetic field lines interact with the turbulent flow. In Chapter 2, the generated energy fluxes are computed and the time-averaged fluxes of the total (propagating and non-propagating) and only propagating waves are presented.

In Chapter 3, we simulate the propagation of the longitudinal tube waves along solar magnetic flux tubes of different filling factors (both adiabatic and radiatively damped

waves) by performing theoretical self consistent and time-dependent computations.

The response of the atmospheres of the Sun and two late-types stars to the excitation by different wave modes is studied and presented in Chapter 4.

In Chapter 5, we present theoretically time-dependent model chromospheres for late-type stars, by using the previously computed wave energy fluxes.

Then, in Chapter 6 we simulate the rotation - emission activity relation for late-type main sequence stars of different magnetic activities. We also study the dependence of stellar activity on the basic stellar parameters, surface gravity, effective temperature, and the rotation period. Finally, Chapter 7 contains our conclusions and discussions.

Chapter 2

The Generation of Longitudinal Tube Waves

Summary. In the present chapter we compute the generated nonlinear wave energy fluxes of longitudinal tube waves as a result of the interaction between a vertically directed thin magnetic flux tube and the outside turbulent medium in the stellar convection zone of late-type stars. The computations are based on work by Ulmschneider & Musielak (1998). The current computations are for stars of gravities $log\ g = 3, 4, 5$ and temperature range from $T_{eff} = 3500$ K to $T_{eff} = 7000$ K (see, Fawzy et al. 1999).

2.1 Introduction

The solar magnetic field is concentrated in strong flux bundles of field strength ranging from 1 to 2 kG. The field is in equilibrium with the photospheric gas pressure surrounding it (e.g., Zwaan 1987). These flux concentrations are called "magnetic flux tubes", in which the horizontal pressure balance between the internal magnetic and gas pressures and the external gas pressure confines the magnetic field. Because of the lack of the spatial resolution, we assume that the stellar magnetic fields are concentrated in magnetic flux tubes similar to the Sun.

The magnetic flux tubes are embedded in a very turbulent medium, in which the pressure fluctuations generated by the unsteady turbulence interact with the tubes in different forms, e.g. twisting, squeezing and bending. This interaction has been suggested as a source of the generation of different types of magnetohydrodynamic waves; e.g. torsional, longitudinal and transverse tube waves, respectively. These waves can propagate through the flux tubes up to the chromosphere and can dissipate energies in form of shocks which lead to local heating.

The generation of the magnetohydrodynamic waves by turbulent fluid motions has been studied by many authors (Kulsrud 1955; Lighthill 1952; Osterbrock 1961), most of these treatments are based on the classical Lighthill theory for wave generation. Recently the generation of longitudinal and transverse tube waves have been studied analytically (Musielak et al. 1989, 1995, 2000) and numerically (Huang et al. 1995; Ulmschneider & Musielak 1998). In the current computations we use the approach developed by

Ulmschneider & Musielak (1998), to calculate numerically the longitudinal wave energy fluxes for late-type stars as a result of squeezing a vertical magnetic flux tube by external pressure fluctuations produced by turbulent motions.

The generated acoustic wave energy fluxes for late-type stars by turbulent convection has been computed and reported by Ulmschneider et al. (1996) for solar metal abundances and Ulmschneider et al. (1999) for non-solar metalicities. These computations are based on the modified Lighthill-Stein theory (Stein 1967) of the wave generation by Musielak et al. (1994).

2.2 Formulation

The computations start by constructing an initial non-gray radiative equilibrium model atmosphere, in which a thin magnetic flux tube is embedded in pressure equilibrium with the surroundings for which we specify the radius and the magnetic field strength at the bottom of the tube. The tube is then allowed to interact with the external turbulent medium. The spatial and temporal behavior of the turbulence are specified by the turbulent energy spectrum which is described by an extended Kolmogorov spectrum with a modified Gaussian frequency factor (Musielak et al. 1994). The horizontal pressure balance translates the external pressure fluctuations into internal pressure and magnetic field fluctuations. The internal pressure fluctuations can be described by internal velocity fluctuations which serves as piston boundary condition.

a. Stellar Magnetic Flux Tubes

The basic parameters to describe a magnetic flux tube are the size, the effective temperature, T_{eff}, the surface gravity, g, and the surface magnetic field strength, B, at the base of the tube. The geometry of the tube is determined by the filling factor of the region in which the tube exists. On the Sun, the magnetic flux tube has a bottom radius which is roughly half the local pressure scale height, $R_0 \simeq \Re T_{eff}/2\mu g$, where μ is the molecular weight, and $\Re$ is the gas constant. In the current computations we extend the solar case assuming that the stellar flux tubes have bottom radii equal to half the local pressure scale height at the stellar surface.

Theoretical models assume that the magnetic field is intensified by a convective instability acting on the initially weak magnetic field, the convective downflow within a weak field evacuates the magnetic field, the gas pressure within the field lines gets lower, the flowing gas carries the magnetic field lines with it leading to an enhancement of the field (Solanki 1996). Observations of stellar magnetic field strengths (Saar 1996; Rüedi et al. 1997) and 2- dimensional simulations of the convective collapse carried out by Steiner (1995) support the existence of magnetic field strengths close to the maximum field strength at $z = 0\ km$, the equipartition field strength, which is given by $B_{eq} = \sqrt{8\pi p_e}$, where p_e is the gas pressure outside the tube. Saar (1996) shows that $B \leq B_{eq}$ is generally valid for most GK stars and some active M dwarfs, while in sunspots and also in a heavily spotted K dwarf LQ Hya one finds $B > B_{eq}$, this is because more contributions come from starspots on the most active stars. He also showed that, the moderately active G

and early K type main sequence stars have magnetic field strength B ranging from 1.0 to 1.9 kG, and filling factors f ranging from $\approx 1.5\%$ - 35%, while the very active Ke and Me stars have B upto 4.2 kG and f upto 70%.

For the Sun, taking $p_e = 1.17 \cdot 10^5\ dyn\ cm^{-2}$ from model C of Vernazza et al. (1981) at height $z = 0$ km results in an equipartition field strength of $B_{eq} = 1715\ G$, while the observed field strength is $B = 1500\ G$. One therefore gets the ratio $B/B_{eq} = 0.875$. As the observed magnetic field strength on the Sun vary from position to another on its surface, we choose three ratios, $B/B_{eq} = 0.75,\ 0.85,\ 0.95$ for stellar magnetic flux tubes. The different values of the magnetic field strengths enable us to study the effect of the magnetic field on the generated wave energies.

With the specification of the above basic parameters we construct a thin vertically oriented magnetic flux tube which is embedded in a magnetic field-free atmospheres at height $z = 0$ km, in which the external optical depth is $\tau_{5000} = 1$. Using the temperature and flux correction procedure of Cuntz et al. (1994), the magnetic tube model has a non-grey radiative and hydrostatic equilibrium atmosphere. For the current computations the effective temperatures, T_{eff}, have values ranging from $T_{eff} = 3500$ K to $T_{eff} = 7000$ K and surface gravities in the range $log\ g = 3, 4, 5$. The constructed tube models have exponentially increasing radii with height, the magnetic filling factor at the top of the tube is not important for the wave generation, as we consider only a small portion of the tube.

b. Stellar Convection Zones

Stars with masses $M < 1.3 M_{\odot}$ show convective zones, their depths increase with decreasing effective temperature. Early spectral types (e.g., F0V) have shallow convection zones which extends only few pressure scale heights, while for the coolest M type stars, the whole star is completely convective.

The kinetic energy of flows in the upper convective zone can be converted into other modes of energy as a result of the interactions with the magnetic flux tubes. Horizontal motions are more important for generating longitudinal and transverse MHD waves than vertical motions. Convective motions are responsible for different phenomena occurring on stars. Rotation together with the convective motions are believed to drive a dynamo, which generates magnetic fields. The convective motions are the main source of generating magnetohydrodynamic waves that supply energy to stellar chromospheres. In addition, the foot-points of coronal magnetic flux tubes are subjected to the movements caused by the convection zone, which may lead to magnetic reconnections, which also may contribute to the heating of the chromospheres and coronae.

Upflowing materials are hot, with low density and high entropy, as they reach layers of lower density they loose part of their energy by radiation, they become denser and flow down again by gravity. These downflows and upflows create turbulence which my be described by a turbulent spectrum. The upflows appear laminar and the downflows appear turbulent (Nordlund et al. 1997). The magnetic flux tubes are situated in the intergranular regions where downflow materials generate turbulence, this interaction between turbulence and the magnetic flux tubes is an efficient source of generating waves.

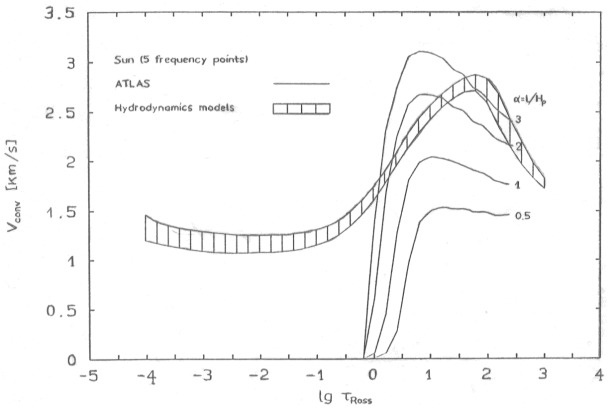

Fig. 2.1 Convective velocity vs. logarithm of the optical depth τ_{Ross}. Velocities in the hatched stripe are temporal-spatial averages of vertically directed gas velocities of 2- dimensional numerical simulations of solar convection zone by Steffen (1992). The lines are the velocities obtained by ATLAS6 mixing length computations, from: Steffen (1992; Fig. 3, p. 31).

The current understanding of the stellar convection zones are based mainly on the mixing length theory. For our computations we construct a convection zone model based on the mixing length theory, as described by Theurer (1993). The mixing length theory simplifies the complicated picture of the convection zone by an average picture with the following assumptions: (1) All convective elements have the same physical properties at a given radial distance, r, from the stellar center. (2) Each convective element is assumed to travel through a distance, Λ, the mixing length before mixing with the surrounding matter. (3) All convective elements are assumed to have the same characteristic dimension in all spatial directions. This characteristic dimension is assumed to be equal to Λ. (4) The convective elements at a certain distance from the stellar center are assumed to have the same speed, v, this speed is the average speed for all convective elements at this radial distance. (5) The mean life time of the convective element is given by $t = \Lambda/v$.

The choice of the mixing length parameter, α, which is the ratio of the mixing length, Λ, to the local pressure scale height is based on a comparison of velocities of 2- dimensional numerical simulations and the mixing length (Steffen 1992). Figure 2.1 (taken from the Habilitation thesis by Steffen (1992), Fig. 3, p. 31) shows this comparison. The mixing length convective velocities are shown (drawn) with indicated values of $\alpha = 3, 2, 1, 0.5$, and the hatched stripe is the temporal-spatial average of the gas velocities of the 2- dimensional numerical simulations of the solar convection zone. By comparing the maximum of the gas velocities of the 2- dimensional numerical simulations and the different mixing length models, an agreement is found for values of $\alpha \simeq 2$.
Recent 3- dimensional simulation by Trampedach et al. (1996) of the convection zones of six different stars are matched with the results of the mixing length theory, to look for the behavior of the mixing length parameter. The resulting values of α also vary around a value of 2. Hünsch & Schröder (1997) and Schröder & Eggleton (1996) found by fitting the evolutionary tracks of the Sun with its present luminosity, effective temperature and age that a value of $\alpha = 2$ results in better agreement. Based on these simulations we choose for our computations of the stellar convective zones the mixing length parameter $\alpha = 2$ and we use the solar metal abundance.

c. Spatial and temporal components of the turbulence

Turbulence is usually specified by a turbulent energy spectrum, the spatial component is used to describe the distribution of the sizes of the eddies, and the dissociation rates

of larger eddies to smaller ones. The temporal component describes the life time of the eddies. Musielak et al. (1994) have combined theoretical and some numerical simulation with observations, and concluded that the spatial component of turbulence can be described by an extended Kolmogorov and the temporal component by a modified Gaussian frequency factor.

To summarize the procedure followed by Ulmschneider & Musielak (1998), the external pressure fluctuations responsible for the squeezing of a thin and vertically oriented magnetic flux tube are represented by a superposition of $N = 500$ (found to be sufficient to cover the whole range of the spectrum) number of partial waves which result in a horizontal velocity given by

$$v_x(t) = \sum_{n=1}^{N} u_n \sin(\omega_n t + \varphi_n) \quad , \tag{2.1}$$

where u_n is the velocity amplitude of the partial waves, ω_n is the wave frequency, and $\varphi_n = 2\pi r_n$ is an arbitrary but constant phase angle with r_n being a random number in the interval [0, 1]. The velocity amplitudes u_n are related to v_x and the rms turbulent velocity fluctuations, u_t, by

$$\overline{v_x^2} = u_t^2 = \frac{1}{2}\sum_{n=1}^{N} u_n^2 \quad , \tag{2.2}$$

and the velocity amplitudes u_n are computed from

$$u_n = \sqrt{\frac{4}{3}E'(\omega_n)\Delta\omega} \tag{2.3}$$

where

$$E'(\omega_n) = \int_0^\infty E(k) G\left(\frac{\omega_n}{k u_k}\right) dk \tag{2.4}$$

and where $E(k)$ and $G(\frac{\omega}{k u_k})$ represent an extended Kolmogorov spatial turbulent energy spectrum and a modified Gaussian frequency factor, respectively. If $z = z_0$ is the height where the spatial component of the turbulence is computed, following Musielak et al. (1995), $E(k)$ is defined as

$$E(k) = \begin{cases} 0 & 0 < k < ak(z_0) \\ b\frac{u^2(z_0)}{k(z_0)}\left(\frac{k}{k(z_0)}\right) & ak(z_0) \le k < k(z_0) \\ b\frac{u^2(z_0)}{k(z_0)}\left(\frac{k}{k(z_0)}\right)^{-5/3} & k(z_0) \le k \le k_{max} \end{cases} \tag{2.5}$$

where $k(z_0) = 2\pi/H(z_0)$, $H(z_0) = \Re T(z_0)/(\mu g)$, with $\Re$ being the gas constant and a molecular weight $\mu = 1.3$, is the local pressure scale height at $z = z_0$, $a = H(z_0)/H(z_d)$ is the ratio between the local pressure scale height at $z = z_0$ and the local pressure scale height corresponds to the largest possible eddies at depth $z = z_d$, $u(z_0)$ is the convective velocity at depth $z = z_0$, k_{max} is the wave number at which the turbulent cascade ends which can be estimated from $k_{max} = 2\pi/l_d$ with $l_d \approx 4\ cm$ (e.g., Theurer et al. 1997) and b is a normalization factor given by $b = \frac{1.5}{(2-a^2/2)}$. In the present work, the extended

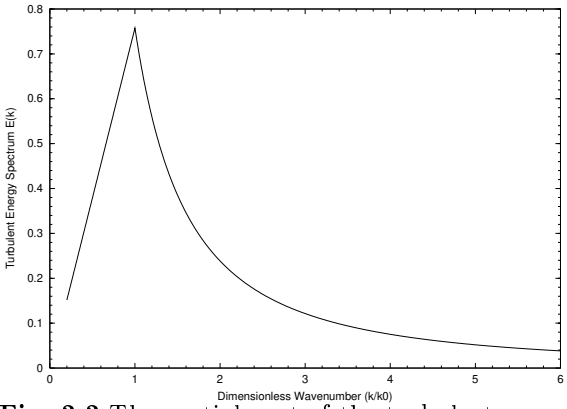

Fig. 2.2 The spatial part of the turbulent energy spectrum as a function of k/k_0

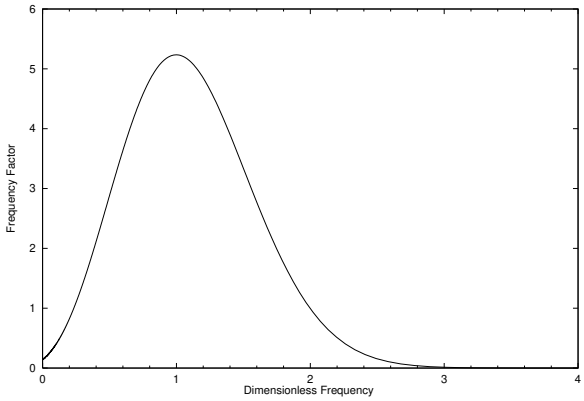

Fig. 2.3 Normalized turbulent frequency factor $G(\omega/ku_k)$ as a function of ω/ku_k, defined by Eq. (2.6)

Kolmogorov spectrum has a linear rise from $a = 0.2$ to 1, this means that the largest bubbles have the vertical size of $5H(z_0)$. The modified Gaussian frequency factor is given by

$$G\left(\frac{\omega}{ku_k}\right) = \frac{4}{\sqrt{\pi}}\frac{\omega^2}{|ku_k|^3}e^{-(\frac{\omega}{ku_k})^2} \quad , \tag{2.6}$$

where u_k is computed from

$$u_k = \left[\int_k^{2k} E(k')dk'\right]^{1/2} \quad . \tag{2.7}$$

The calculated velocity $v_x(t)$ may now be used to define the turbulent pressure fluctuations p'_{turb} that are responsible for the squeezing of the flux tube. As shown by Ulmschneider & Musielak (1998), these fluctuations consist of a time averaged term $\overline{p_{turb}} = 3\rho_e u_t^2$, which augments the external gas pressure p_e, and a fluctuating term $p_{turb} = 3\rho_e v_x^2(t)$, which gives rise to longitudinal tube waves; note that ρ_e is the gas density in the external medium. Combining these two terms, we get

$$p'_{turb} = 3\rho_e(v_x^2 - u_t^2(z_0)) \tag{2.8}$$

These turbulent pressure fluctuations lead to the gas pressure perturbations p' inside the tube

$$p' = \frac{\beta}{2/\gamma + \beta}p'_{turb} \tag{2.9}$$

where $\beta = 8\pi p_0/B_0^2$ is the plasma β. Finally, the gas pressure fluctuations inside the tube can be translated into internal longitudinal velocity fluctuations

$$v_\parallel = \frac{c_S^2}{c_T}\frac{p'}{\gamma p_0} \tag{2.10}$$

where c_S is the sound speed, $c_T = (1/c_S^2 + 1/c_A^2)^{-1/2}$ the tube speed, c_A is the Alfvén velocity, γ is the ratio of specific heats, and p_0 is the gas pressure inside the tube. The

velocity $v_\parallel$ can also be expressed in terms of $v_x(t)$ by using Eqs. (2.7) through (2.9) and writing

$$v_\parallel = \frac{\beta}{2/\gamma + \beta} \frac{3\rho_e(v_x^2 - u_t^2(z_0))}{\rho_0 c_T} \tag{2.11}$$

The derived $v_\parallel$ is specified at the squeezing height and serves as a bottom boundary condition in the MHD-wave code. As the computations of the generated longitudinal flux by Ulmschneider & Musielak (1998) show a little dependence on the location of the squeezing, in the current computations, the tube is squeezed at height $z = 0$ km which corresponds to the optical depth $\tau_{5000} = 1$. With the specification of $v_\parallel(z = 0, t)$, the instantaneous values of the internal pressure perturbation $p'(z = 0, t)$ can be computed by the use of the modified time-dependent, magnetohydrodynamic Lagrangian code (Herbold et al. 1985). Using these two quantities, we then calculate the instantaneous wave energy flux, $F(z, t) = v_\parallel(z, t)p'(z, t)$, and the time-averaged wave energy flux, $\overline{F(z, t)}$ at the squeezing height. The final expression of the longitudinal wave energy flux normalized to the stellar surface is then given by

$$F_L \equiv \overline{F(z = 0, t)} = \overline{v_{\parallel(z,t)} p'(z, t)} \tag{2.12}$$

The wave energy spectra are computed by performing Fourier transform of the obtained instantaneous wave energy fluxes and the computed velocities. Figure 2.2 shows the spatial part of the turbulent energy spectrum as a function of k/k_0, while Fig. 2.3 shows the normalized turbulent frequency factor given by Eq. (2.6) as a function of ω/ku_k.

d. Spatial limits of the turbulence spectrum

The mixing length theory assumes that the energy carrying eddies have vertical sizes comparable to the local pressure scale heights which are the dominant local length scale in the convection zone, with a corresponding wavenumber $k(z_0) = 2\pi/H(z_0)$. The Kolmogorov spectrum (classical) represents well the spatial component of the turbulence in the range of wavenumbers $k(z) > k(z_0)$, while for lower wavenumbers (bubbles with larger sizes), the extension of the Kolmogorov spectrum is not well known. The starting point of the Kolmogorov spectrum is determined by the largest eddies in the system which come from deeper layers.

Musielak et al. (1994) suggested three different spectra to extend the classical (cK) Kolmogorov spectrum to the region of large bubbles ($k(z) < k(z_0)$), the extended (eK), broadened (bK) and raised (rK) Kolmogorov spectra as shown in Fig. 2.4. The extended type has a linear extension toward lower wavenumbers, this extension is limited by the largest eddies in the system which are assumed to have a wavenumber $k_l \approx 2\pi/(5H(z_0))$ in the case of the solar turbulent convection zone. For the broadened Kolmogorov spectrum, the maximum of the turbulent energy spectrum is broad near $k = k(z_0)$. The third type (rK) is deduced from observations by Muller (1989) which shows an increasing in the velocity power spectrum with decreasing wavenumber, but with smaller slope (less than the Kolmogorov value -5/3).

Since larger bubbles come from deeper layers, they loose energy while penetrating the surface, this means for bubbles with sizes larger than the local scale height, the turbulent

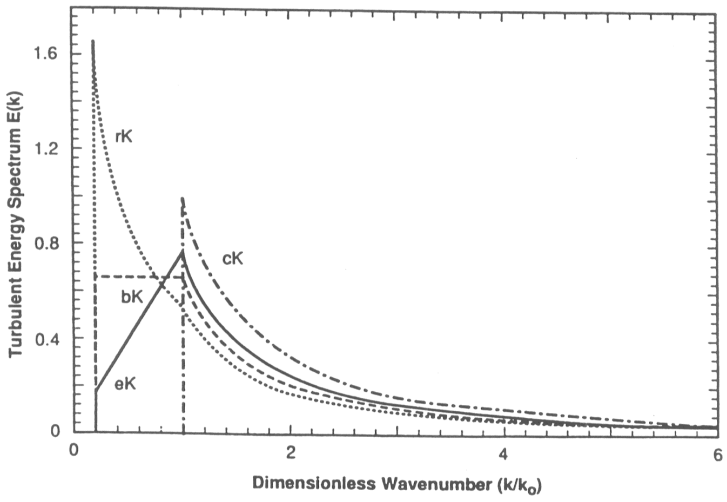

Fig. 2.4 Spatial part of the turbulent energy spectrum $E(k)$ in units of u_0^2/k_0 as function of k/k_0. Four forms of the spectrum are shown: the classical Kolmogorov (cK), the extended Kolmogorov (eK), the broadened Kolmogorov (bK) and the raised Kolmogorov (rK) forms, from: Musielak et al. (1994; Fig. 1).

spectrum should decrease. In both the broadened and raised Kolmogorov spectra, the energy content of the largest bubbles is artificially increased.

So, for the current computations we take the extended Kolmogorov spectrum to describe the spatial component of the turbulence at any depth $z = z_0$, given by Eq. (A.24). The largest eddies come from deeper layers, $z = z_d$, at depths where eddies have sizes of $H(z_d) = 5H(z_0)$, this results in a value of $a = 0.2$. The size of the largest eddies is also critical for determining the starting point of the frequency and the frequency range for the wave generation. Also, the large spikes seen in the instantaneous wave energy fluxes resulted from the largest eddies. From Eq. (2.7), the velocities of the eddies are given by: (using a dimensionless quantity $x = k/k(z_0)$):

$$u_k(x) = u(z_0)u_k^*(x) \quad . \tag{2.13}$$

where: u_k^* is given by:

$$u_k^*(x) = \left[\int_{k/k(z_0)}^{2k/k(z_0)} E^*(x)dx \right]^{1/2} \tag{2.14}$$

and $E^*(x)$ is given by:

$$E^*(x) = \begin{cases} 0 & 0 < x < a \\ bx & a \leq x < 1 \\ bx^{-5/3} & 1 \leq x \leq 1000 \end{cases} \tag{2.15}$$

After integrating Eq. (2.14), the values of $u_k^*(x)$ for different ranges of x are given by:

$$u_k^{*2}(x) = \begin{cases} 0 & x < a/2 \\ \frac{b}{2}(4x^2 - a^2) & \frac{a}{2} \leq x < a \\ 1.5bx^2 & a \leq x < 0.5 \\ \frac{b}{2}(4 - x^2 - 1.8899x^{-2/3}) & 0.5 \leq x < 1 \\ 0.555bx^{-2/3} & x \geq 1 \end{cases} \tag{2.16}$$

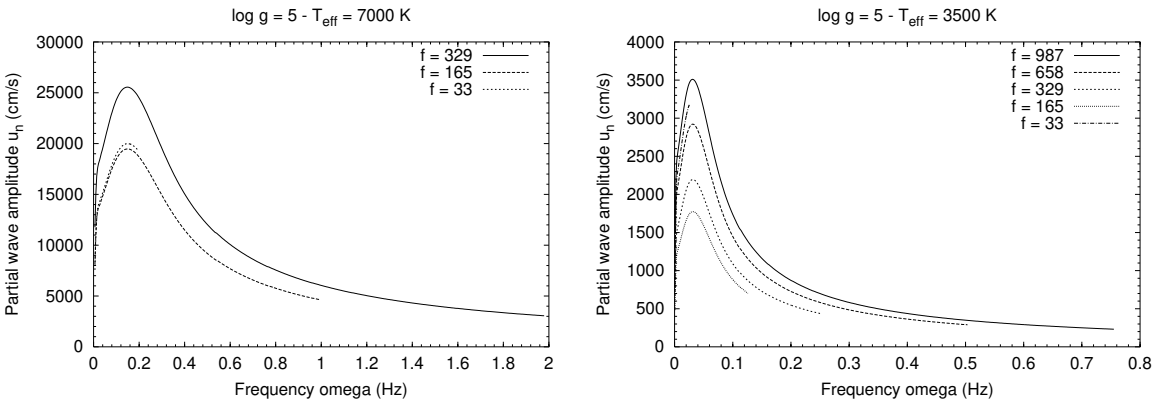

Fig. 2.5 The partial wave amplitudes as function of frequency for different values of $f = \omega_2/\omega_1$ for stars of surface gravity $log\ g = 5$ and effective temperatures $T_{eff} = 7000$ K (left) and 3500 K (right).

e. Temporal limits of the turbulence spectrum

For the computation of the extended Kolmogorov spectrum at the stellar surfaces, the lower and upper limits of the frequency should be specified. The size of the largest bubbles in the system; which come from depth z_d; determines the lower limit as follows:

$$\omega_1 = k(z_d)u_d \tag{2.17}$$

where, $u_d = u_k^*(a)u(z_d)$ is the velocity of the largest eddies, $k(z_d) = 2\pi/H(z_d)$ and $H(z_d) = H_{surf}/a = 5H_{surf}$ is the pressure scale height at the depth $z = z_d$ where the largest eddies exist, and $u(z_d) = v_{conv}(z_d)$ is the convective velocity at that depth calculated from the mixing length model at depth z_d. Since the wavenumber at z_d for these bubbles is $k/k_t(z_d) = 1$, we use Eq. (2.16). The velocity of the largest bubbles at depth z_d is then given by $u_{kl}^* = \sqrt{3b(1-2^{-2/3})/2}\ v_{conv}(z_d) = 0.649\ v_{conv}(z_d)$. As shown above, a is the ratio between the local pressure scale height at the surface and the local pressure scale height of the depth containing the largest eddies. With $a = 0.2$, one has $b = 0.758$ and $u_k^*(a) = 0.2132$.

For the choice of the upper limit of the frequency, ω_2, we compute the velocity amplitudes of the partial waves u_n as a function of frequency for different factors, f, such that $\omega_2 = f\omega_1$, Fig. 2.5 shows the results for two stars. The left figure is for a star of surface gravity $g = 10^5$ and $T_{eff} = 7000$ K, while the right figure is for the same gravity and effective temperature $T_{eff} = 3500$ K. The velocity amplitudes increase as a result of adding high frequency components by increasing the upper limit of ω_2, in a way that Eq. (2.2) should be satisfied. The choice of $f = 329$ is sufficient to cover the studied cases. Testing other surface gravities and effective temperatures, it has been found that the choice of $\omega_2 = 329\ \omega_1$ is sufficient for all cases we are interested in.

f. The root mean square (rms) of the turbulent velocity

Based on hydrodynamic simulations (Steffen 1992) of the convection zone of the Sun (see, Fig. 2.1), it has been found that the velocities of the eddies in the overshooting regions have values roughly half the value of the maximum convective velocity. Since the

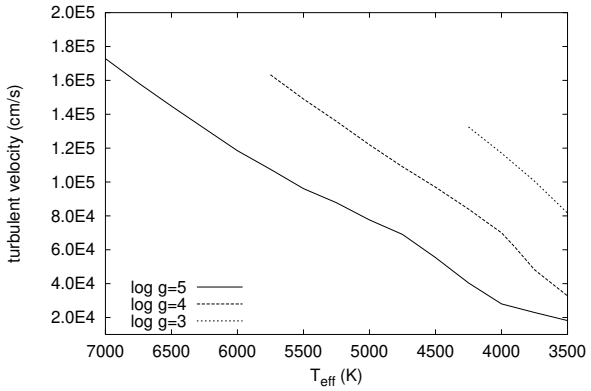

Fig. 2.6 The rms velocities v_{rms} for stars of different surface gravities and for a range of effective temperatures from $T_{eff} = 3500 - 7000$ K.

magnetic flux tubes sit at the stellar surfaces, in regions which show overshooting from the interior, we expect the rms value of the turbulent velocity to be in the range of those of the overshooting region.

A value of $v_{rms} = 0.5\ u_{mcv}$, where u_{mcv} is the maximum convective velocity, is a good choice for the value of the rms of the turbulent velocity at $z_0 = 0$ km (see, Fig. 2.1). Figure 2.6 shows the rms velocities, v_{rms}, for stars of different surface gravities $log\ g = 3, 4, 5$ and effective temperatures $T_{eff} = 3500 - 7000$ K. Stars with low surface gravities have much more extended convection zones compared to the stars of higher surface gravities, and the maximum convective velocities are higher for stars of low surface gravities. For stars of the same surface gravity, hotter stars have higher convective velocities than cool stars. The cases which are considered here are all subsonic cases, supersonic cases are excluded from the computations.

2.3 Computations

In the computation of the wave generation, the phases between different physical variables must be taken into account, so a time-dependent magnetohydrodynamic code has to be used. A Lagrangian code previously used to study the propagation of the longitudinal waves along magnetic flux tubes (Herbold et al. 1985), uses the interior velocity $v_{\|}$ in the flux tube as boundary condition. For the wave generation, it is sufficient to use small sections of the tubes as the computational domain. As shown by Ulmschneider & Musielak (1998), the generated fluxes do not depend critically on the choice of the squeezing height. The squeezing height for the current computations is taken at $z_0 = 0\ km$. The squeezing of the flux tube is symmetric with respect to the tube axis. The computations are done adiabatically and without considering shocks.

Because of the very stochastic nature and the spikyness of the generated waves, the time average of the wave energy flux should be long enough to have a stable value. It has been found that about $T = 35 P_D$, where $P_D = 1/\nu_D$ is the Defouw cut-off period and ν_D is the Defouw cut-off frequency; with c_T, c_s and c_A being the gas velocity inside the flux tube, the sound speed, and the Alfvén speed, respectively, the Defouw cut-off frequency can be defined as (Defouw 1976)

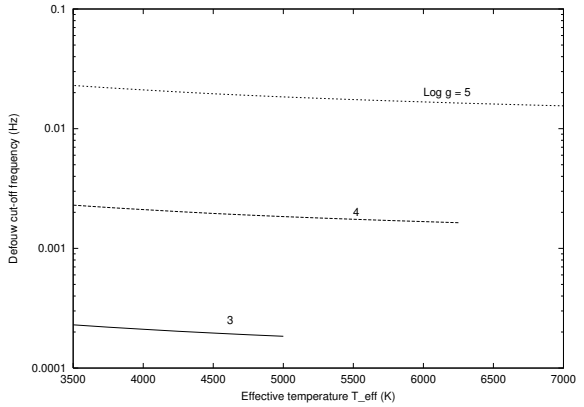

Fig. 2.7 The Defouw cut-off frequency for stars of different surface gravity $log\ g = 3,\ 4,\ 5$ and effective temperatures in the range $T_{eff} = 3500$ K to $T_{eff} = 7000$ K.

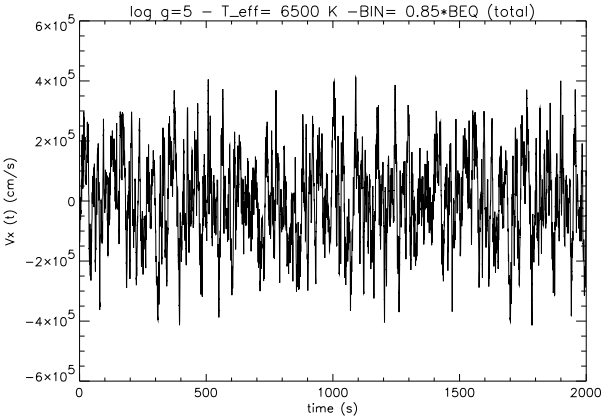

Fig. 2.8 The horizontal turbulent velocity fluctuations, v_x, in the x-direction computed from Eq. (2.1) is shown for the case of surface gravity $g = 10^5\ cm/s^2$, effective temperature $T_{eff} = 6500$ K, and a magnetic field strength $B = 0.85 B_{eq}$.

$$\nu_D = \frac{c_T}{2\pi H}\sqrt{\frac{9}{16} - \frac{1}{2\gamma} + \frac{c_s^2(\gamma-1)}{c_A^2\gamma^2}} \quad . \tag{2.18}$$

is sufficient for hot stars, while for cool stars the computational time should be longer to get a stable average. The longer the computation time the more we avoid the disturbances due to the switch-on effects. The Defouw cut-off frequencies for stars of $T_{eff} = 3500$ to 7000 K, $log\ g = 3$ to 5 and $B/B_{eq} = 0.85$ are shown in Fig. 2.7, which shows little dependence on the magnetic field strength.

Figure 2.8 shows the horizontal turbulent velocity fluctuations, v_x, in the x-direction computed from Eq. (2.1) for a star of surface gravity $g = 10^5\ cm/s^2$, effective temperature $T_{eff} = 6500$ K, and a magnetic field strength $B = 0.85 B_{eq}$, where we have used $u_t = 1.45 \cdot 10^5\ cm/s$, $\omega_1 = 13.2$ mHz, $\omega_N = 4.35$ Hz.

Figures 2.9 and 2.10 show the instantaneous velocity, $v_\parallel$, and the instantaneous longitudinal tube wave fluxes, $F_L(t)$, for the same star as computed from Eqs. (2.11), (2.12). For cool stars ($T_{eff} = 4000,\ 3500$ K), the generated waves fluxes show large spikes compared to the much smaller spikes we got for hotter stars. For these cool stars, the run time of the computations should be longer to get a stable average flux. These spikes resulted from the fact that the largest eddies found on these stars move very fast according to the Kolmogorov law, $u_k \sim l_k^{1/3}$ and by chance superposition of $N = 500$ partial waves.

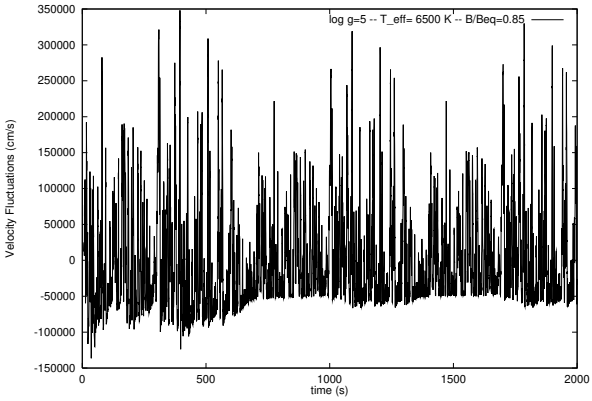

Fig. 2.9 The instantaneous velocity perturbations inside the tube for a star of surface gravity $g = 10^5\ cm/s^2$, with effective temperature $T_{eff} = 6500$ K, and a magnetic field strength $B = 0.85 B_{eq}$, computed from Eq. (2.11).

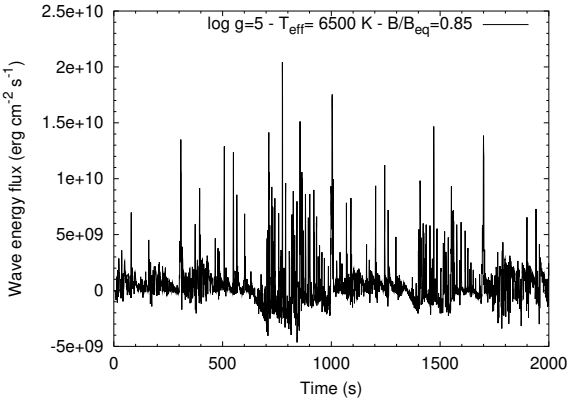

Fig. 2.10 The instantaneous wave energy flux inside the tube for a star of surface gravity $g = 10^5\ cm/s^2$, with effective temperature $T_{eff} = 6500$ K, and a magnetic field strength $B = 0.85 B_{eq}$ computed from Eq. (2.12).

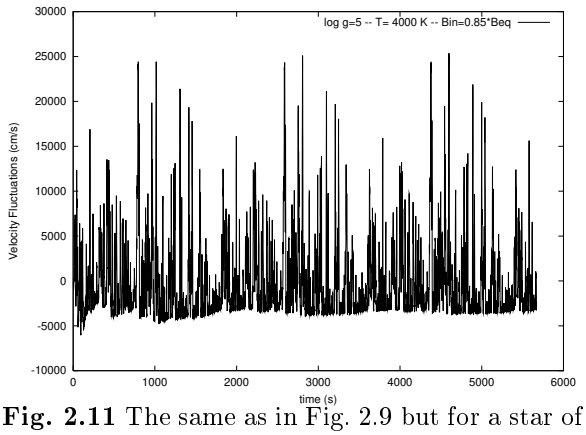

Fig. 2.11 The same as in Fig. 2.9 but for a star of effective temperature $T_{eff} = 4000$ K.

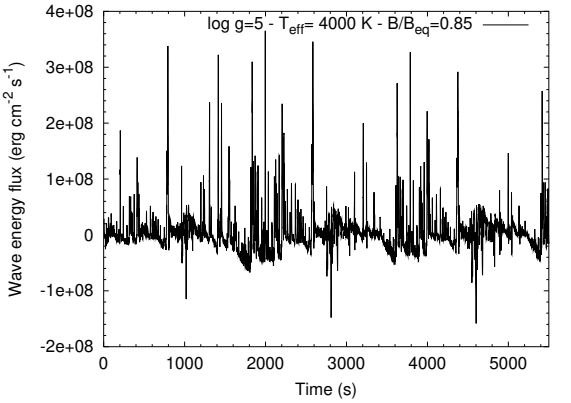

Fig. 2.12 The same as in Fig. 2.10 but for a star of effective temperature $T_{eff} = 4000$ K.

Figures 2.11 and 2.12 are the same as Figs. 2.9 and 2.10 but for a cool star of effective temperature $T_{eff} = 4000$ K. Using the notation $E^*(x) = E(k)k_t/u_t^2$ and $u_k^*(x) = u_k(k)/u_t$, with $x = k/k_t$, Eq. (A.23) can be written as

$$E'(\omega_n) = \frac{4\omega_n^2}{\sqrt{\pi} k_i^3 u(z_0)} \int_0^\infty \frac{E^*(x) e^{\frac{-(\omega_n/u(z_0))^2}{k(z_0)^2 x^2 u_k^*(x)^2}}}{x^3 u_k^*(x)^3} dx \tag{2.19}$$

For each value of ω_n, the x-integration given by Eq. (2.19) should be computed. For a given value of ω_n, as shown in Fig. 2.13, the integrand has a pronounced peak at some value of x_{max} which is caused be the frequency factor G, then after this peak the integrand drops to zero, due to the exponential behavior of G. The function drops to zero for values of $x > 10\ x_{max}$. We first look for the value of x_{max} for each value of ω_n, then we integrate from 0.2 to 10 x_{max} using 2000 points. The computation of the extended Kolmogorov spectrum at the stellar surface requires the value of $u(z_0)$, which is taken to be half the value of the maximum convective velocity.

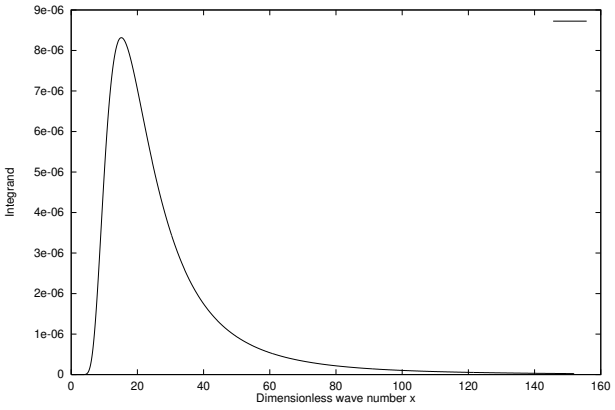

Fig. 2.13 The behavior of the integrand of Eq. (2.19), for different values of ω_n. The case shown here is for $n = 10$, with the wave number x in the range from $zero$ to $10x_{max}$.

The generated waves represent a mixture of propagating and non-propagating longitudinal tube waves, the reason for this is that both the turbulent energy spectrum and the frequency factor of the fluid motions are independent from the cut-off frequency of waves. So, the generated waves have a range of frequencies below and above the cut-off frequency. Since we are only interested in the propagating component, we use some spectral analysis techniques to separate both components. The following section describes shortly some of the used techniques.

2.4 Spectral Analysis

The spectral analysis looks at the frequency content of signals by displaying the signal amplitude as a function of frequency, which is called the spectrum. Most of the spectral analysis techniques are based on linear transforms like Fourier and Laplace transforms. These techniques can be applied to solve many physical problems. One of these problems is to study the nature and the dynamics of waves in stellar atmospheres.

Observations provide us with 3- dimension information about the amplitude, phase, energy, etc. of brightness fluctuations and Doppler shift due to wave motions, as function of frequency and wavenumber (Deubner 1998). The variation of the velocity power spectrum with frequency and height is of great importance for studying the dynamics of the outer layers of the stellar atmospheres. Some techniques like the phase difference spectra between different spectral lines can be used to characterize the waves, either they are propagating waves or standing waves, beside the direction of propagation. The coherence expresses the degree of inhomogeneity of the stellar atmosphere which is responsible for the spatial variation of the temporal behavior of the brightness and velocity fluctuations (Deubner et al. 1996).

The analysis of the 2- dimensional time series of the velocity & intensity perturbations seen through spectral lines show the distribution of the power in the $k_h - \nu$ diagram, k_h is the wavenumber and ν is the frequency. For theoretical simulations these techniques can be applied to the time series of the velocity, pressure, and temperature fluctuations at different heights in form of pairs (e.g. velocity-velocity, or velocity-pressure, etc.).

Suppose that the function $f(t)$ has N values at discrete time steps, the discrete forward Fourier transform is computed according to the following equation:

$$F(\nu_k) = N^{-1} \sum_{j=1}^{N} f(t_j) e^{-i2\pi t_j \nu_k} \tag{2.20}$$

where $t_j = (j-1)\Delta t$ for j = 1,2, ... N and $\nu_k = (k-1)/N\Delta t$ for k=1,2, ..., N, and Δt is the sampling interval in time domain.
The inverse transform is defined as:

$$F(t_j) = \sum_{k=1}^{N} F(\nu_k) e^{+i2\pi t_j \nu_k} \tag{2.21}$$

The Fast Fourier Transform (FFT) algorithm is used to evaluate the discrete Fourier transform given by Eq. (2.20). Based on work done by Cooly and Tukey (1965), the algorithm reduces the computational time by reducing the number of multiplications from N^2 to $2Nlog_2N$, where N is the number of data points. The algorithm works faster if the number of the data points is even (integral power of 2). The discrete Fourier transform approximates the continuous Fourier transform, the validity of this approximation depends on the function of the waveform being analyzed, good approximations can be achieved by reducing the sample interval and increasing the number of data points, N.
Corruption of the transform by aliasing (undersampling in the measurement domain) and sharp ends can affect the results of the data manipulation via the Fourier transform. Some procedures like applying appropriate sampling and smoothing the sharp ends can be used to minimize these effects.
The power spectrum of any function $F(\nu)$ is computed from

$$P(\nu) = F_{real}(\nu)^2 + F_{imag}(\nu)^2 \tag{2.22}$$

where: $F_{real}(\nu)$ and $F_{imag}(\nu)$ are the real and imaginary amplitudes of the function $F(\nu)$. Having information about the phase differences between different wave oscillations is of great importance to differentiate the wave types; e.g. propagating or standing waves. The phase difference is computed from the cross power spectrum of any two functions, e.g., the velocity fluctuations at two different heights. For any two functions $F_1(\nu)$, $F_2(\nu)$, the cross power spectrum is defined as :

$$CP(\nu) = F_1(\nu) * F_2(\nu)^* \tag{2.23}$$

where $F_2(\nu)^*$ is the conjugate function of $F_2(\nu)$. It is important to look for the stability of the phase differences in different data sets between different heights of the atmosphere, do the data sets share common phase patterns or not . The coherence has values range from zero to one as a function of frequency, depends on the degree of coherence. Highly coherent phases mean values approaching to one, while less coherent phases mean values approaching to zero. The coherence expresses the degree of inhomogeneity of the atmosphere as defined by Deubner et al. (1996) and can be computed from

$$C_{AB} = \frac{|\overline{CP_{AB}(\nu)}|}{\overline{|CP_{AB}(\nu)|}} \tag{2.24}$$

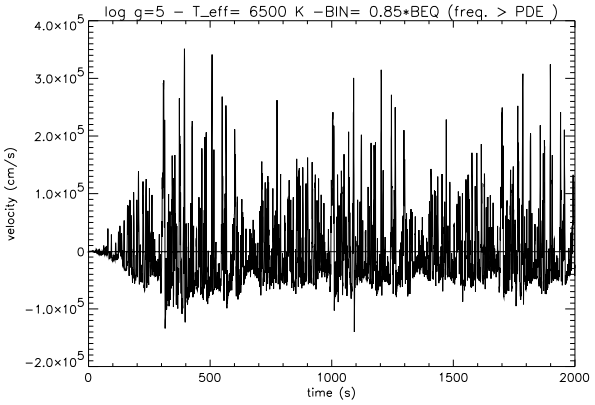

Fig. 2.14 The longitudinal velocity fluctuations for waves of frequencies above the Defouw cut-off frequency, which is 16 mHz for the star of surface gravity $logg = 5$, effective temperature $T_{eff} =$ 6500 K, and magnetic field strength $B = 0.85B_{eq}$.

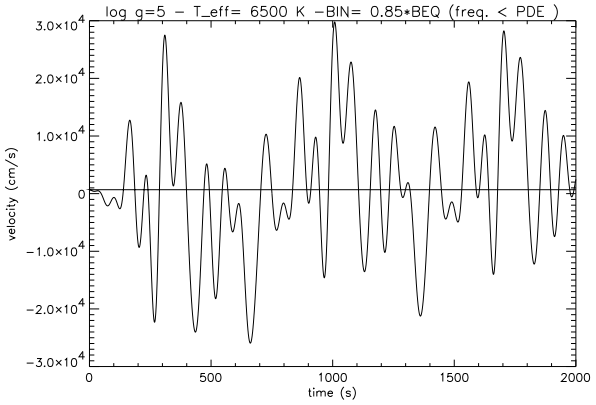

Fig. 2.15 The same as in Fig. 2.14 but for waves of frequencies below the Defouw cut-off frequency

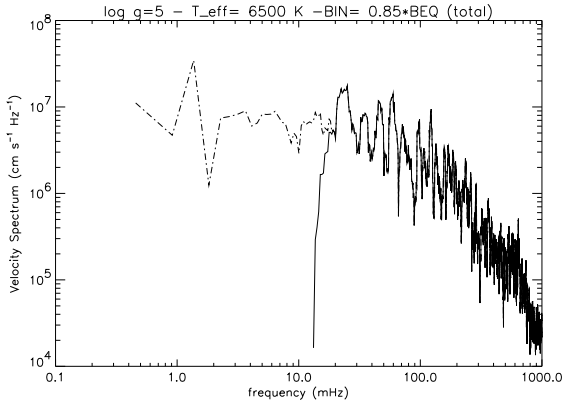

Fig. 2.16 The velocity power spectrum for a star of surface gravity $G = 10^5$, with effective temperature $T_{eff} = 6500$ K, and a magnetic field strength $B = 0.85B_{eq}$, for both propagating (solid) and non-propagating (dashed) waves.

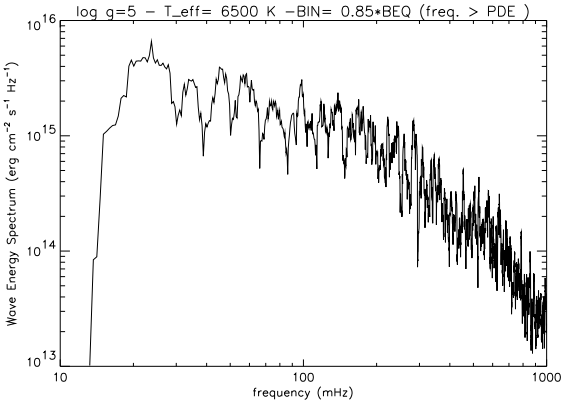

Fig. 2.17 The wave flux power spectrum for a star of surface gravity $G = 10^5$, with effective temperature $T_{eff} = 6500$ K, and a magnetic field strength $B = 0.85B_{eq}$

where: A & B are any two time strings, and $CP_{AB} = \tilde{A} * \tilde{B}^*$ is the cross power, e.g. the mean values here might be over a spatial coordinate, or wavenumber
Another formula can be used to compute the coherence for one data set by smoothing over certain range of frequencies as:

$$C_{AB} = \frac{|\sum_{\nu-a}^{\nu+a} CP_{AB}(\nu)|}{\sum_{\nu-a}^{\nu+a} |CP_{AB}(\nu)|} \tag{2.25}$$

a. Separating the propagating and non-propagating waves

The generated longitudinal tube wave energy spectra are distributed over a wide range

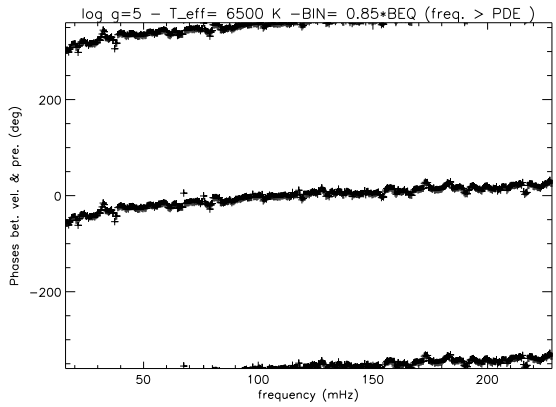

Fig. 2.18 The phase difference (in degrees) between the velocity and pressure fluctuations for the propagating waves vs. frequency (in mHz), for a star of surface gravity $log\ g = 5$, $T_{eff} = 6500$ K, and $B/B_{eq} = 0.85$.

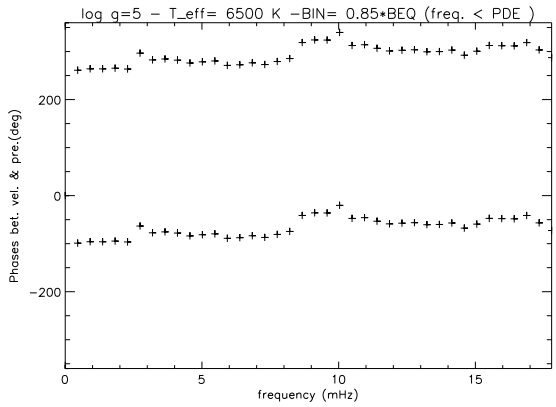

Fig. 2.19 The same as in Fig. 2.18 but for the non-propagating part of the wave spectra.

of frequencies; with frequencies lower (non-propagating) and higher (propagating) than the characteristic Defouw cut-off frequency. Figures 2.14, 2.15 show the instantaneous velocity perturbations, $v_{\|}$, for the propagating and non-propagating waves respectively, the corresponding power spectra are shown in Fig. 2.16, the solid line for the propagating waves while the dashed line for the non-propagating waves. As we are interested only in the propagating part of spectra, we apply some spectral analysis techniques to separate both contributions. The propagating nature of the waves are clearly shown in the phase difference spectra as clear trends as well as the direction of the wave propagation can be also shown. The amount of energy carried by these waves can be computed and used later as an input mechanical energy flux for constructing theoretical model chromospheres. On the other hand the finite and constant phase spectra show the non-propagating nature of the other part of waves.

The procedure followed can be summarized as follows: (1) The nonzero mean of the time sequence of the velocity and pressure inside the tube should be removed, then a suitable apodising function should be applied to the beginning and the end of the time string to avoid having sharp edges which results in adding high frequency noise. (2) By means of the fast Fourier transform, an equidistant time sequence of the velocity and pressure perturbations can be represented in the frequency domain. (3) A smoothed (to avoid adding high frequency noise) high pass filter in the form of Heaviside step function, which is zero below and one above the Defouw cut-off frequency, centered at the Defouw cut-off frequency is applied to both the velocity and pressure perturbations. This filter passes out all frequencies above the Defouw cut-off frequency and cut out those of frequencies below the Defouw cut-off frequency. (4) The distribution of the velocity and pressure power spectra can be computed in the frequency domain, also the phase difference spectra. By means of the inverse fast Fourier transform, the separated (propagating) frequency sequence of the velocity and pressure perturbations can be transformed back to the time domain. Then, the velocity and pressure can be multiplied and the time average wave energy flux carried by the propagating waves can be computed as shown in Tab. 2.4.

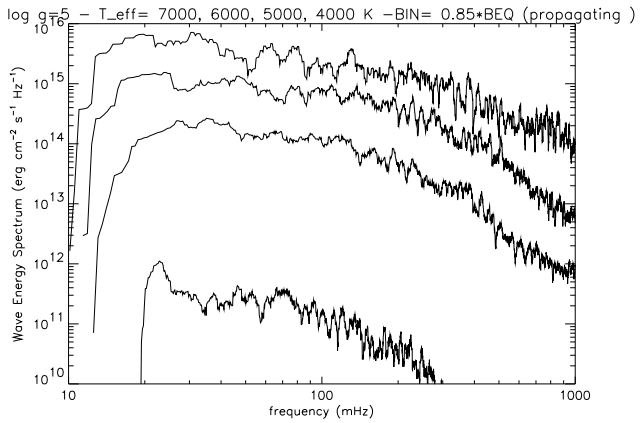

Fig. 2.20 The wave flux powers (for propagating waves) are shown for stars of the same surface gravity $G = 10^5$ and different effective temperatures (T_{eff} = 7000, 6000, 5000, 4000 K, the magnetic field strength is $B = 0.85 B_{eq}$.

To show the application of the procedure mentioned above, we consider here the same case we studied before ($g = 10^5\ cm/s^2$, $T_{eff} = 6500$ K, and Defouw cut-off frequency of $\omega_D = 16$ mHz). Figure 2.14 shows the instantaneous velocity inside the tube of the propagating wave component, the time average of these velocity fluctuations is always zero. The large spikes shown are caused by large rapidly moving eddies. The velocity inside the tube of the non-propagating wave component is shown in Fig. 2.15. As shown in Fig. 2.16 the distribution of the power spectra of the propagating component reaches its maximum at around $\omega = 2\omega_D$ and then decreases towards higher frequency, the distribution of the flux power spectrum is shown in Fig. 2.17. To ensure the propagating and non-propagating nature of the two components, the phase difference spectra have been computed and shown in Figs. 2.18 and 2.19. The computed wave power spectra for stars with $T_{eff} = 4000,\ 5000,\ 6000,\ 7000$ K, log $g = 5$ and $B = 0.85 B_{eq}$ are shown in Fig. 2.20, which also show changes of the Defouw cut-off frequency ω_D with T_{eff}. These spectra reach their maximum at roughly $\omega = 2\omega_D$, then they decrease slowly toward high frequencies.

2.5 Results

a. Time-averaged Wave Energy Fluxes

The distribution of the time averaged total (propagating & non-propagating) longitudinal wave energy fluxes for stars of different surface gravities and effective temperatures as well as different values of the magnetic field strengths ($B = 0.75, 0.85,$ and $0.95 B_{eq}$) is shown in Fig. 2.21. The values are normalized to the stellar surface. Figure 2.22 shows the same distribution but for the energy carried by the propagating wave component. Table 2.4 gives the values of the total and propagating longitudinal tube waves for different magnetic field strengths. The generated energy fluxes are higher for hot stars because of the higher turbulent velocities in comparison with cool stars, the decreasing in the wave fluxes is due to the lower turbulent velocities and the sharp increasing in the magnetic field strengths, which results in increasing the stiffness of the magnetic tube. The sharp increasing of the magnetic field strengths for stars of higher surface gravity and lower effective temperatures

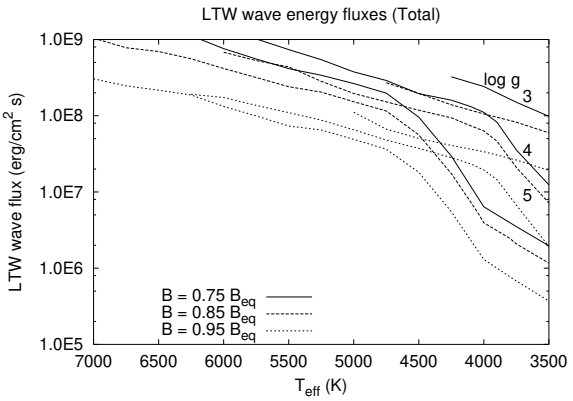

Fig. 2.21 The longitudinal tube wave fluxes vs. effective temperatures for different values of surface gravities ($log\ g = 3,\ 4,\ 5$) and magnetic field strengths $B/B_{eq} = 0.75,\ 0.85,$ and 0.95.

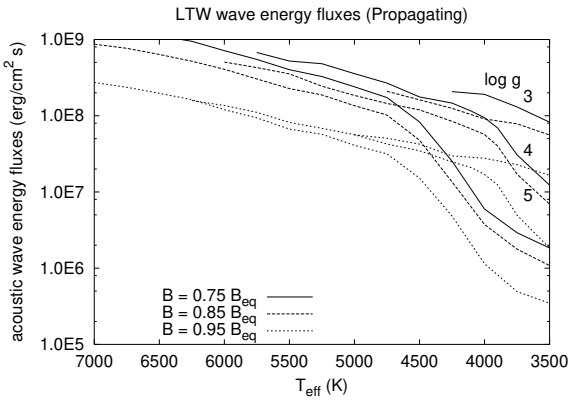

Fig. 2.22 The same as in Fig. 2.21 but for the propagating waves.

is due to increasing the density. The extreme spikyness of the generated waves is in good agreement with observations by Muller (1989) and Muller et al. (1994), and with models by Choudhuri et al. (1993 a,b). This peculiar nature of the wave fluctuations shows that it is essential to include nonlinear effects in the longitudinal wave generation.

b. Dependence on Turbulent Velocity

Stars with low surface gravity have larger fluxes than stars with higher gravity, this is because stars with low gravity have larger maximum convective velocities comparing to stars of larger gravities, as a results the *rms* of the turbulent velocities are larger for lower gravities. Table 2.1 shows three cases for $log\ g = 3,\ 4,\ 5$ and the corresponding turbulent velocities, the computed fluxes show a great dependence on gravity as shown in the third column. The reason for this behavior can be explained as follows, for a given T_{eff} the convective flux is equal to the total flux, $\rho v_{conv}^3 \approx \sigma T_{eff}^4$. Hence the lowering of gravity in giants leads to a decrease of the atmospheric density ρ and thus to an increase of v_{conv}.

log g	u_t	F_L
3	$1.49 \cdot 10^5$	$1.96 \cdot 10^8$
4	$9.70 \cdot 10^4$	$1.18 \cdot 10^8$
5	$5.54 \cdot 10^4$	$5.59 \cdot 10^7$

Table 2.1 The dependence of the generated longitudinal tube waves on the *rms* of the turbulent velocity (cm/s) for a stars of surface gravities in the range $log\ g = 3,\ 4,\ 5$ and of effective temperature $T_{eff} = 4500$ K, the magnetic field strength is $B = 0.85 B_{eq}$.

c. Dependence on Magnetic Field

Increasing the magnetic field strength results in a more stiff flux tube. The stiffness of the tube decreases the generated fluxes, this is because when the tube is stiff, the density inside the tube decreases and as a result it is hard to be squeezed. Table 2.1 shows different

log g	B/B_{eq} =	0.75	0.85	0.95
3		$3.24 \cdot 10^8$	$1.39 \cdot 10^8$	$4.07 \cdot 10^7$
4		$1.95 \cdot 10^8$	$9.39 \cdot 10^7$	$2.82 \cdot 10^7$
5		$2.96 \cdot 10^7$	$1.75 \cdot 10^7$	$5.52 \cdot 10^6$

Table 2.2 The generated longitudinal tube wave energies for stars of the same effective temperature T_{eff} = 4250 K, and different surface gravities $log\ g$ = 3, 4, 5, with the magnetic field strengths B = 0.75, 0.85, $0.95B_{eq}$.

values of the generated wave energy fluxes for different values of magnetic field strengths and different stars of the same effective temperature and different surface gravities. As shown in Tab. 2.2, the average wave energy fluxes increases with decreasing the magnetic field strength inside the tube.

d. Results for Late-Type Stars

On the basis of these wave energy fluxes, it is possible to construct chromospheric models and to simulate the Mg II and Ca II line emissions to be compared with observations. A sample of stars representing late-type stars ranges from F5V to M0V is chosen for the current study. Table 2.3 shows the parameters and the computed wave energy fluxes for both propagating and non-propagating waves for $B = 0.85B_{eq}$ as well as the monochromatic wave periods corresponding to the maximum contribution of the velocity power spectrum of the generated waves. Figure 2.23 shows the velocity power spectrum of the propagating component of the generated waves.

Star	T_{eff}	log g	B-V	F_{tot}	F_{prop}	P
F5 V	6 440	4.34	0.44	$7.6 \cdot 10^8$	$5.7 \cdot 10^8$	85
G0 V	6 030	4.39	0.58	$4.9 \cdot 10^8$	$4.4 \cdot 10^8$	75
G5 V	5 780	4.44	0.68	$3.6 \cdot 10^8$	$2.8 \cdot 10^8$	63
K0 V	5 770	4.49	0.68	$2.0 \cdot 10^8$	$1.9 \cdot 10^8$	58
K5 V	5 250	4.49	0.81	$6.3 \cdot 10^7$	$5.5 \cdot 10^7$	54
M0 V	3 850	4.59	1.40	$5.1 \cdot 10^4$	$5.0 \cdot 10^6$	50

Table 2.3 The total (propagating & non-propagating) generated longitudinal tube wave fluxes F_{tot} (in $erg\ /cm^2 s$) for the late- type stars are given in the fifth- column, while only the propagating fluxes F_{prop} are given in the sixth column. The first four columns show the basic parameters of these stars, the spectral type, the effective temperature T_{eff} (in K), surface gravity (in cm/s^2) and the color index $B - V$, respectively. The last column shows the monochromatic wave periods P (in sec) corresponding to the maximum velocity power spectrum.

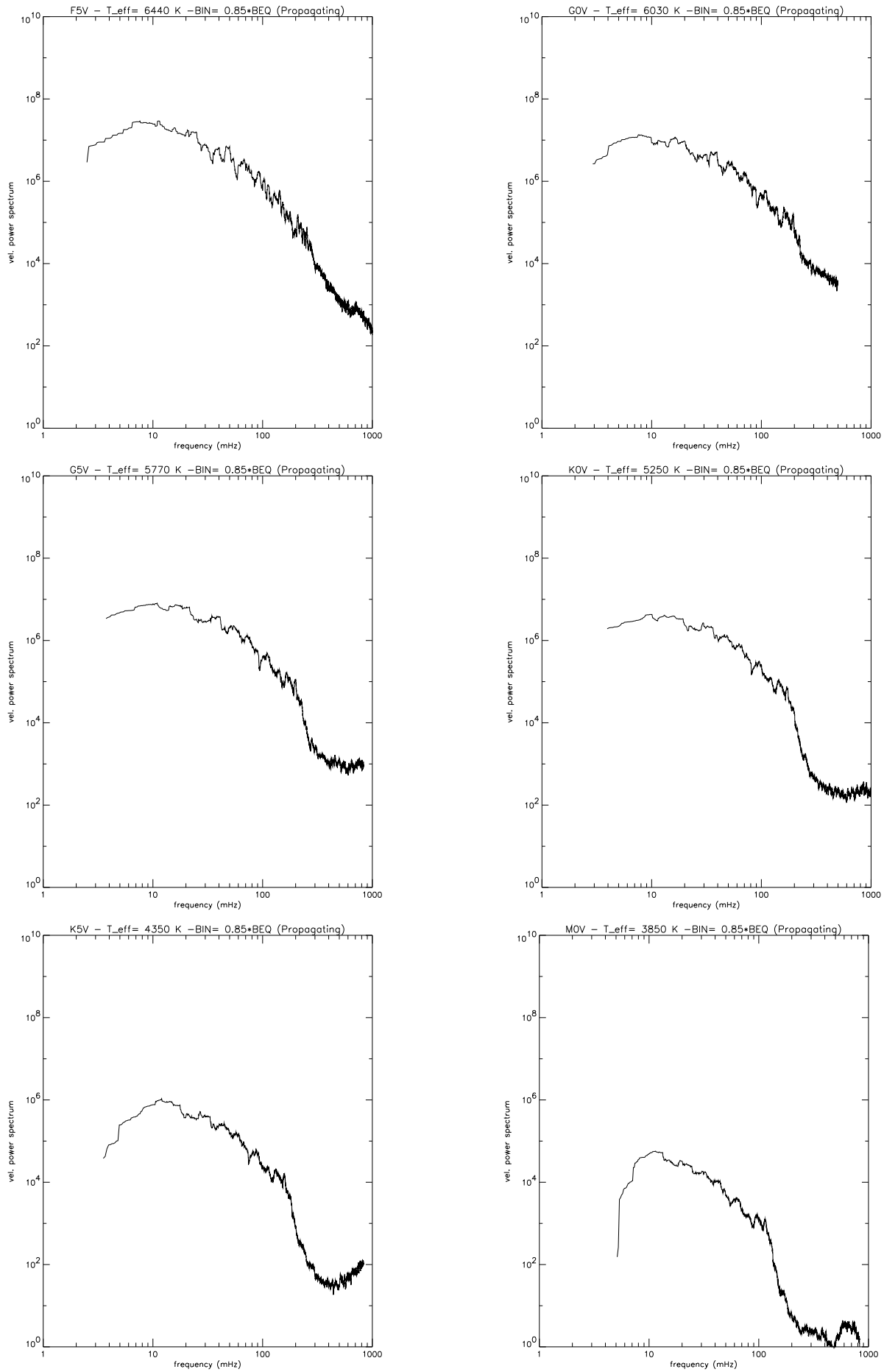

Fig. 2.23 The velocity power spectra of the propagating waves for late-type stars of spectral types F5V (*top, left*), G0V (*top, right*), G5V (*middle, left*), K0V (*middle, right*), K5V (*bottom, left*), and M0V (*bottom, right*), respectively.

T_{eff}	$\log g =$ 3	4	5	3	4	5
3500	$9.83 \cdot 10^7$	$1.24 \cdot 10^7$	$1.96 \cdot 10^6$	$8.24 \cdot 10^7$	$1.23 \cdot 10^7$	$1.84 \cdot 10^6$
3750	$1.50 \cdot 10^8$	$3.55 \cdot 10^7$	$3.51 \cdot 10^6$	$1.30 \cdot 10^8$	$3.07 \cdot 10^7$	$2.92 \cdot 10^6$
4000	$2.42 \cdot 10^8$	$1.11 \cdot 10^7$	$6.39 \cdot 10^6$	$1.91 \cdot 10^8$	$9.42 \cdot 10^7$	$5.99 \cdot 10^6$
4250	$3.24 \cdot 10^8$	$1.60 \cdot 10^8$	$2.96 \cdot 10^7$	$2.07 \cdot 10^8$	$1.47 \cdot 10^8$	$2.54 \cdot 10^7$
4500		$1.95 \cdot 10^8$	$9.56 \cdot 10^7$		$1.76 \cdot 10^8$	$8.29 \cdot 10^7$
4750		$2.90 \cdot 10^8$	$1.98 \cdot 10^8$		$2.68 \cdot 10^8$	$1.73 \cdot 10^8$
5000		$3.77 \cdot 10^8$	$2.65 \cdot 10^8$		$3.57 \cdot 10^8$	$2.40 \cdot 10^8$
5250		$5.44 \cdot 10^8$	$3.40 \cdot 10^8$		$4.81 \cdot 10^8$	$3.26 \cdot 10^8$
5500		$7.37 \cdot 10^8$	$4.15 \cdot 10^8$		$5.22 \cdot 10^8$	$4.02 \cdot 10^8$
5750		$1.02 \cdot 10^9$	$5.56 \cdot 10^8$		$6.75 \cdot 10^8$	$5.48 \cdot 10^8$
6000			$7.59 \cdot 10^8$			$7.15 \cdot 10^8$
6250			$1.12 \cdot 10^9$			$9.48 \cdot 10^8$
6500			$1.48 \cdot 10^9$			$1.12 \cdot 10^9$
6750			$1.74 \cdot 10^9$			$1.38 \cdot 10^9$
7000			$2.20 \cdot 10^9$			$1.66 \cdot 10^9$
3500	$5.97 \cdot 10^7$	$7.19 \cdot 10^6$	$1.16 \cdot 10^6$	$5.58 \cdot 10^7$	$6.92 \cdot 10^6$	$1.08 \cdot 10^6$
3750	$8.22 \cdot 10^7$	$2.09 \cdot 10^7$	$2.08 \cdot 10^6$	$7.84 \cdot 10^7$	$1.71 \cdot 10^7$	$1.78 \cdot 10^6$
4000	$1.06 \cdot 10^8$	$6.32 \cdot 10^7$	$3.94 \cdot 10^6$	$9.08 \cdot 10^7$	$5.66 \cdot 10^7$	$3.74 \cdot 10^6$
4250	$1.39 \cdot 10^8$	$9.39 \cdot 10^7$	$1.75 \cdot 10^7$	$1.25 \cdot 10^8$	$8.45 \cdot 10^7$	$1.36 \cdot 10^7$
4500	$1.96 \cdot 10^8$	$1.18 \cdot 10^8$	$5.59 \cdot 10^7$	$1.62 \cdot 10^8$	$1.19 \cdot 10^8$	$4.77 \cdot 10^7$
4750	$2.71 \cdot 10^8$	$1.52 \cdot 10^8$	$1.15 \cdot 10^8$	$2.09 \cdot 10^8$	$1.45 \cdot 10^8$	$1.02 \cdot 10^8$
5000		$1.96 \cdot 10^8$	$1.53 \cdot 10^8$		$1.85 \cdot 10^8$	$1.36 \cdot 10^8$
5250		$2.83 \cdot 10^8$	$2.04 \cdot 10^8$		$2.44 \cdot 10^8$	$1.88 \cdot 10^8$
5500		$4.38 \cdot 10^8$	$2.40 \cdot 10^8$		$3.54 \cdot 10^8$	$2.27 \cdot 10^8$
5750		$5.30 \cdot 10^8$	$3.18 \cdot 10^8$		$4.28 \cdot 10^8$	$3.04 \cdot 10^8$
6000		$6.80 \cdot 10^8$	$4.17 \cdot 10^8$		$5.06 \cdot 10^8$	$4.07 \cdot 10^8$
6250			$5.58 \cdot 10^8$			$5.19 \cdot 10^8$
6500			$6.96 \cdot 10^8$			$6.37 \cdot 10^8$
6750			$7.81 \cdot 10^8$			$7.66 \cdot 10^8$
7000			$1.04 \cdot 10^9$			$8.69 \cdot 10^8$
3500	$1.92 \cdot 10^7$	$1.93 \cdot 10^6$	$3.71 \cdot 10^5$	$1.65 \cdot 10^7$	$1.84 \cdot 10^6$	$3.48 \cdot 10^5$
3750	$2.63 \cdot 10^7$	$6.70 \cdot 10^6$	$6.79 \cdot 10^5$	$2.28 \cdot 10^7$	$4.95 \cdot 10^6$	$4.92 \cdot 10^5$
4000	$3.37 \cdot 10^7$	$1.94 \cdot 10^7$	$1.30 \cdot 10^6$	$2.77 \cdot 10^7$	$1.70 \cdot 10^7$	$1.14 \cdot 10^6$
4250	$4.07 \cdot 10^7$	$2.82 \cdot 10^7$	$5.52 \cdot 10^6$	$2.97 \cdot 10^7$	$2.48 \cdot 10^7$	$4.84 \cdot 10^6$
4500	$5.04 \cdot 10^7$	$3.73 \cdot 10^7$	$1.80 \cdot 10^7$	$4.24 \cdot 10^7$	$3.47 \cdot 10^7$	$1.52 \cdot 10^7$
4750	$6.65 \cdot 10^7$	$4.79 \cdot 10^7$	$3.63 \cdot 10^7$	$5.07 \cdot 10^7$	$4.25 \cdot 10^7$	$3.16 \cdot 10^7$
5000	$1.11 \cdot 10^8$	$6.55 \cdot 10^7$	$4.89 \cdot 10^7$	$5.62 \cdot 10^7$	$5.64 \cdot 10^7$	$4.09 \cdot 10^7$
5250		$8.74 \cdot 10^7$	$6.50 \cdot 10^7$		$6.83 \cdot 10^7$	$5.71 \cdot 10^7$
5500		$1.10 \cdot 10^8$	$7.32 \cdot 10^7$		$8.16 \cdot 10^7$	$6.67 \cdot 10^7$
5750		$1.37 \cdot 10^8$	$9.95 \cdot 10^7$		$1.11 \cdot 10^8$	$9.35 \cdot 10^7$
6000		$1.73 \cdot 10^8$	$1.32 \cdot 10^8$		$1.36 \cdot 10^8$	$1.20 \cdot 10^8$
6250		$1.91 \cdot 10^8$	$1.87 \cdot 10^8$		$1.58 \cdot 10^8$	$1.63 \cdot 10^8$
6500			$2.16 \cdot 10^8$			$1.97 \cdot 10^8$
6750			$2.47 \cdot 10^8$			$2.37 \cdot 10^8$
7000			$3.06 \cdot 10^8$			$2.73 \cdot 10^8$

Table 2.4 The total (propagating & non-propagating) longitudinal tube wave fluxes F_L ($erg\ cm^{-2}\ s^{-1}$) (left panels) and the propagating longitudinal tube wave fluxes (right panels), the values at the top are for the magnetic field strength $B = 0.75Beq$, those in the middle for $B = 0.85Beq$, while those at the bottom for $B = 0.95Beq$.

Chapter 3

The Heating of Magnetic Flux Tubes

Summary. The propagation of longitudinal tube waves both adiabatic and radiatively damped along magnetic flux tubes in the solar atmosphere is studied. It has been found that the tube geometry plays an important role in the heating of outer layers. Flux tubes which spread least with height (large filling factors) show an increase in the continuum (H^-) and line (Mg II + Ca II + Fe II) emissions. Exponentially spreading flux tubes do not show any remarkable heating.

3.1 Introduction

Observations of the Solar photosphere show strong vertical magnetic fields ($\approx$ 1500 G) in the form of flux tubes emerging from the boundaries of the supergranular cells, with diameters of about 100 km (see, Stenflo 1994), while less concentrations are found in the cell interiors. These magnetic flux tubes work as the connecting channels linking the stellar convection zones in which energy are generated to the higher atmospheric layers in which energy are dissipated. Different modes of waves are generated in the convection zones as a result of the interaction between the flux tubes with the turbulent media (see, Chapter 2), e.g., longitudinal, transverse, and torsional waves (see, Spruit 1982; Edwin & Roberts 1983). The longitudinal and transverse waves are propagating when their frequencies are lower than the corresponding cut-off frequency, while the torsional waves can propagate with any frequency.

The longitudinal tube waves are suggested to be the prime candidate for the heating of magnetic chromospheres for the following reasons, (1) The longitudinal tube waves closely related to the acoustic waves, which Buchholz & Ulmschneider (1994) and Buchholz et al. (1998) have identified as the main heating mechanism for non-magnetic regions of the chromospheres of the Sun and late-type stars. (2) Other types of wave modes, e.g., the transverse waves, are found to suffer from energy leakage from the tubes, this result is found in 3- dimensional wave computations of Ziegler & Ulmschneider (1997 a,b). (3) Longitudinal tube waves can be dissipated easier by forming shocks than other modes like Alfvén waves. (4) Longitudinal tube waves can also be produced by the non-linear mode coupling from other wave types, which allows the transverse tube waves to be dissipated (see, Narian and Ulmschneider 1996).

3.2 Propagation of Longitudinal Tube Waves

The basic Magnetohydrodynamic equations governing the propagation of the longitudinal tube waves along a magnetic flux tube within the thin flux tube approximation, are the mass conservation equation, the equation of motion, the the energy conservation equation, as well as Maxwell equations and the equation of state.

3.2.1 Magnetohydrodynamic Equations

The assumption of a thin flux tube assumes that the variation of the physical variables across the tube is negligible compared to the variation along the tube axis (Defouw 1976; Roberts and Webb 1979), therefore the state of each mass element is described by the physical variables at the tube axis.

Following Herbold et al. (1985), for a vertical flux tube with axial symmetry embedded in a non-magnetic atmosphere, the system of MHD equations governing the propagation of the longitudinal tube waves along magnetic flux tubes can be written as

$$\frac{\partial}{\partial t}\left(\frac{\rho}{B}\right)+\frac{\partial}{\partial z}\left(\frac{\rho u}{B}\right)=0\ , \tag{3.1}$$

$$\frac{\partial u}{\partial t}+u\frac{\partial u}{\partial z}+\frac{1}{\rho}\frac{\partial p}{\partial z}+g=0\ , \tag{3.2}$$

$$p+\frac{B^2}{8\pi}=p_e\left(z\right)\ , \tag{3.3}$$

$$\frac{\partial S}{\partial t}+u\frac{\partial S}{\partial z}=\left.\frac{dS}{dt}\right|_{Rad}\ . \tag{3.4}$$

where ρ is the density, p the gas pressure, S the entropy, u the gas velocity, and B the magnetic field strength, these variables are functions of height z and time t. While the external gas pressure $p_e(z)$ is only a height dependent function. In addition to the above equations we have the equation of state of an ideal gas

$$p=\rho\frac{\Re T}{\mu} \tag{3.5}$$

The sound speed is given by (Ulmschneider et al. 1977)

$$c_S^2=\gamma\frac{\Re T}{\mu}=\gamma\frac{p}{\rho} \tag{3.6}$$

where γ is the ratio of specific heats, μ the molecular weight, and $\Re$ the gas constant. In addition, we have the following thermodynamical relations after combining the first and second laws.

$$\frac{d\rho}{\rho}=\frac{2}{\gamma-1}\frac{dc_S}{c_S}-\frac{\mu}{\Re}dS\ , \tag{3.7}$$

$$\frac{dp}{p} = \frac{2\gamma}{\gamma - 1}\frac{dc_S}{c_S} - \frac{\mu}{\Re}dS \ . \tag{3.8}$$

Solving the above system of equations together with the thermodynamic equations, we get a system of three partial differential equations for the unknowns c_S, S and u (see, Appendix A for details). Then, to apply the method of characteristics we transform this system of three partial differential equations into a system of six ordinary differential equations defined along the characteristic lines. The ordinary differential equations along the three characteristics after some algebra (see, Appendix A) can be rewritten as

$$du \pm \frac{2}{\gamma - 1}\frac{c_S}{c_T}dc_S \mp \frac{\mu c_S}{\gamma\Re}\frac{c_S}{c_T}dS \mp \frac{\mu c_T(\gamma - 1)}{\gamma\Re}\left.\frac{dS}{dt}\right|_{Rad} dt \mp \frac{uc_T}{\rho c_A^2}\frac{dp_e}{dz}dt + gdt = 0 \tag{3.9}$$

along the C^+ and C^- characteristics given by

$$\frac{dz}{dt} = u \pm c_T \tag{3.10}$$

where the upper (lower) sign corresponds to the C^+ (C^-) characteristic. The tube speed c_T is given by

$$\frac{1}{c_T^2} = \frac{1}{c_S^2} + \frac{1}{c_A^2} \tag{3.11}$$

Eqs. (3.10) and (3.11) are four ordinary differential equations. The two remaining ordinary differential equations are obtained from (4) written in characteristic form

$$dS = \left.\frac{dS}{dt}\right|_{Rad} dt \tag{3.12}$$

along the (fluid path) C^0 characteristic

$$\frac{dz}{dt} = u \tag{3.13}$$

3.2.2 Model Assumptions

The following assumptions were included in our treatment to make the problem tractable. (1) We assume that the longitudinal tube waves propagate in one direction (vertical direction). (2) The mean molecular weight μ and the ratio γ of specific heats are taken to be constant, the values we use are, $\mu = 1.3$ g/mol and $\gamma = 5/3$. The ionization of the atoms (for the Mg II, Ca II, and H^- radiation) is computed by solving the statistical equilibrium equations. (3) Shocks are treated as discontinuities with optical thickness zero. (4) Viscous and thermal conduction effects are neglected in non shock regions. (5) No mutual interactions between waves inside the flux tube and the waves outside the tube. (6) For diagnostic purposes, we approximate the generated wave spectra by monochromatic waves. As found in a work by Theurer (1998), the heating of stellar chromospheres by

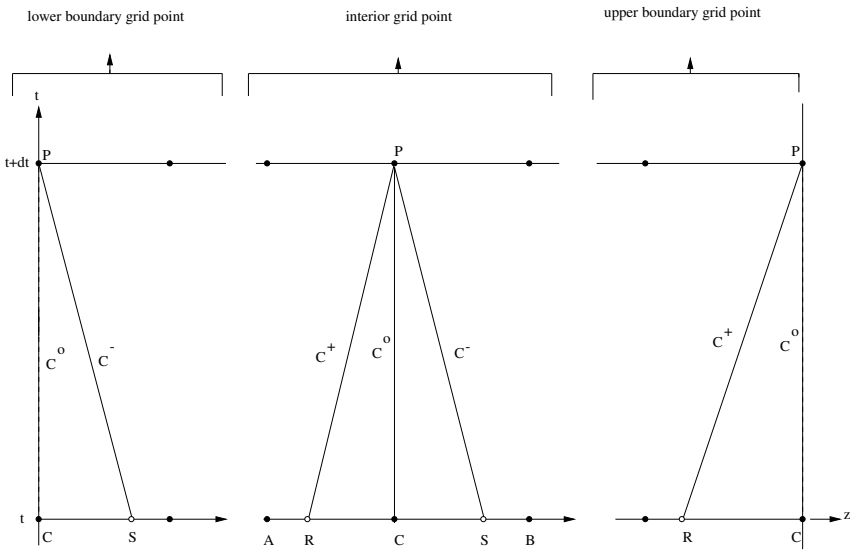

Fig. 3.1 The development of the characteristics with time for the lower, interior, and the top grid points. Gridpoints are shown with filled circles, while open circles are the footpoints of the characteristics.

wave spectra results in a very few and strong shocks which need in their treatments to take into account the time-dependent ionization of the hydrogen atoms, which is at the moment still in preparation by Rammacher and Ulmschneider (2001).

3.2.3 Boundary Conditions

At the lower spatial boundary, waves are introduced to the atmosphere by means of a piston with velocities given by

$$u(t) = u_0 \sin\left(\frac{2\pi}{P}t\right) \tag{3.14}$$

where P is the wave period and the velocity amplitude u_0 is given by (Herbold et al. 1985)

$$u_0 = \sqrt{\frac{2F_M}{\rho_0 c_{T0}}} \tag{3.15}$$

where F_M is the initial flux introduced at the lower boundary, with ρ_0 and c_{T0} being the values at the bottom of the flux tube ($z = 0$ km).

As our models are limited to a certain range of the atmosphere (up to the chromosphere) and do not account for other layers (transition layer or corona), and to avoid the unphysical situations, a transmitting boundary condition $u_{\rm P} = u_{\rm R}$ is applied at the upper boundary to allow for the upward traveling disturbances to leave the computational domain (Buchholz 1995) and also to ensure a non-reflection of the waves back to the computational domain. As discussed by Buchholz, this upper boundary condition is not exactly valid for gravitationally stratified atmospheres with shocks as it leads in some cases (e.g. strong shocks) to unphysically depression of the temperature at the top grid point. Buchholz suggested the following correction to reduce this effect

$$u_{\rm P} = u_{\rm R} \cdot \begin{cases} f^+ & u_{\rm R} \geq 0 \\ f^- & u_{\rm R} < 0 \end{cases} \tag{3.16}$$

with $f^+ < 1$ and $f^- > 1$. He also found that the values of f^+ and f^- which give reasonable results differ slightly from unity as $f^+ = 0.999$ and $f^- = 1.001$.

This corrected boundary condition is applied only in case of subsonic outflow, where the temperature drops below a certain limit which sometimes happens after the passage of the first shock through the atmosphere. It has been found that after the passage of few shocks this corrected boundary condition could be switched off and the old boundary condition could be applied.

3.2.4 Method of Characteristics

The method of characteristics is used for solving a system of quasi-linear partial differential equations of the hyperbolic type, for n-equations there are n-characteristic directions. This method solves the exact equations of magnetohydrodynamics in one-dimension, also the spatial range of the atmospheres can be covered with small number of mesh points and shocks can be represented by only two additional grid points, which decreases the run time. This makes the method of characteristics very convenient for large computations. On the other side, the method is not vectorizeable which means that it is difficult to be generalized to 2- or 3- dimensions (see, Lister 1960).

The method of characteristics represents an initial value problem, in which an initial atmosphere model in hydrostatic and radiative equilibrium should be first specified to provide the initial values of the physical variables as function of height at time $t = 0$. The atmosphere is divided into N- grid points with height interval Δa chosen as (Ulmschneider et al. 1977)

$$\Delta a = Min\left(\frac{\lambda}{10}, \frac{H}{10}\right) \tag{3.17}$$

with H being the scale height, this choice ensures that the sinusoidal wave is represented by at least ten points per wavelength and there should be at least ten points per scale height, also this gives enough resolution for resolving shocks. The time step Δt is chosen as (Hartree 1952)

$$\Delta t = 0.9\frac{\Delta a}{c_0} \tag{3.18}$$

with c_0 being the initial sound speed.

The computational sequence starts with an initial atmosphere in hydrostatic and radiative equilibrium which has $D = dS/dt|_{rad} = 0$ and $u = 0$ for all grid points. For interior grid point **P** (see, Fig. 3.1) far away from shocks or boundaries, the values of the entropy S at new time step $t + \Delta t$ for all grid points are first calculated by integrating Eq. (3.12) along the C^+ characteristic given by Eq. (3.13) using the trapezoidal rule. In order to compute the other two unknowns u and c at **P**, the values at the intersection points of the characteristics with the old time level **R**, **C**, and **S** are found by interpolation from the

known values of the neighboring grid points **A**, **C**, and **B**. Then by integrating Eqs. (3.9), respectively along the C^+ and C^- characteristics given by Eqs. (3.10) the values of u and c at **P** can be computed and enhanced iteratively until convergence is achieved. The new damping function D at the new time step is then calculated and the newly computed values at time $t + \Delta t$ serve as a known state for the next time step.

At the bottom boundary, the C^+ characteristic is missing, therefore one unknown should be specified by a boundary condition. A piston with a prescribed velocity $u(t)$ given by Eq. (3.14) which introduces monochromatic waves to the atmosphere serves as a lower boundary condition.

At the top boundary, only two characteristics (C^+ and C^0) are inside the computational domain, while the third characteristic C^- is missing which is specified as shown above by a transmitting boundary condition $u_{\rm P} = u_{\rm R}$. The positions of shocks are found by monitoring the intersection points of adjacent C^+ characteristics.

3.2.5 Treatment of Shocks

The nonlinear nature of the MHD equations together with the decreasing density gradient of the outer layers are responsible for the development of the sinusoidal waves into a sawtooth-type shock waves. The method of characteristics treats shocks as discontinuities, with two different regions, in front of the shock (variables have index 1) and behind the shock (with index 2). The Rankine-Hugoniot relations relate the physical variables across the shock. Let the variables ρ_1, p_1, c_{S1}, S_1, u_1, A_1, and $H_1 = \gamma p_1/((\gamma - 1)\rho_1)$ are the density, gas pressure, sound speed, entropy, gas velocity, the tube cross section and the enthalpy in front of the shock. The conservation of mass, momentum and energy across the shock can be written as:

$$\rho_1 v_1 A_1 = \rho_2 v_2 A_2 \ , \tag{3.19}$$

$$A_1 \left(\rho_1 v_1^2 - 2p_e + 2p_1\right) = A_2 \left(\rho_2 v_2^2 - 2p_e + 2p_2\right) \ , \tag{3.20}$$

$$\frac{1}{2} v_1^2 + H_1 = \frac{1}{2} v_2^2 + H_2 \ , \tag{3.21}$$

where v_1, v_2 are the gas velocities in the shock frame. The transformation of the gas velocity from the laboratory (Euler) frame into the shock frame is accomplished by

$$v_1 = u_1 - U_{SH} \quad , \quad v_2 = u_2 - U_{SH} \ , \tag{3.22}$$

where U_{SH} is the shock velocity in the laboratory frame. The Rankine-Hugoniot relations are solved by assuming that the front shock state is known and by specifying a post-shock velocity u_2. The front shock state is updated through the iteration process for the respective hydrodynamic time-step. With $\Delta u = u_2 - u_1$ and known quantities in front of the shock the cubic equation

$$E_0 + E_1 A_2 + E_2 A_2^2 + E_3 A_2^3 = 0 \ , \tag{3.23}$$

with

$$E_0 = \frac{\gamma - 2}{\gamma - 1} A_1^2 \ , \tag{3.24}$$

$$E_1 = A_1 \left[\frac{4 - 3\gamma}{\gamma - 1} - \frac{4\pi}{\Phi^2} \Delta u^2 \rho_1 \frac{A_1^2}{\gamma - 1} - \frac{8\pi}{\Phi^2} H_1 \rho_1 A_1^2 \right] \ , \tag{3.25}$$

$$E_2 = 2 - \frac{4\pi}{\Phi^2} \Delta u^2 \rho_1 A_1^2 + \frac{\gamma}{\gamma - 1} \frac{8\pi}{\Phi^2} p_e A_1^2 + \frac{8\pi}{\Phi^2} H_1 \rho_1 A_1^2, \tag{3.26}$$

$$E_3 = \frac{\gamma}{\gamma - 1} \frac{8\pi}{\Phi^2} p_e A_1 \left[\frac{4\pi}{\Phi^2} \Delta u^2 \rho_1 A_1^2 - 1 \right] \ , \tag{3.27}$$

is solved for A_2 by using a Newton-Raphson iteration scheme. Here $\Phi = A_1 B_1$ is the magnetic flux. The other post-shock quantities are then computed using

$$\rho_2 = \frac{\rho_1 \frac{A_1}{A_2} (A_1 - A_2)}{\frac{4\pi}{\Phi^2} \Delta u^2 \rho_1 A_1^2 A_2 + A_1 - A_2} \ , \tag{3.28}$$

$$v_2 = \frac{\rho_1 A_1 \Delta u}{\rho_2 A_2 - \rho_1 A_1} \ , \tag{3.29}$$

$$U_{SH} = u_2 - v_2 \ , \tag{3.30}$$

$$p_2 = p_e - \frac{\Phi^2}{8\pi A_2^2} \ , \tag{3.31}$$

$$c_{S2} = \sqrt{\gamma \frac{p_2}{\rho_2}} \ , \tag{3.32}$$

and

$$S_2 = S_1 + \Delta S = S_1 + \frac{\Re}{\mu} \log \left(\frac{v_2 A_2}{v_1 A_1} \left(\frac{c_{S2}}{c_{S1}} \right)^{2/(\gamma - 1)} \right) . \tag{3.33}$$

3.3 Radiation Treatment

Radiative energy losses and gains are computed by solving the radiative transfer equations for H^-, and with the assumption that the Mg II k, Ca II K and Fe II are representatives for the chromospheric energy losses. As a result of decreasing density of the stellar outer layers, the NLTE line emission should be taken into account for the computation of the H^- treatment.

The determination of the chromospheric line emission for Mg II k and Ca II K lines are computed for each time step of the time-dependent wave calculations done assuming the pseudo-PRD treatment, as will be discussed in section 3.3.2.

3.3.1 Continuum Radiation Treatment

The main source of continuous radiation in the atmospheres of the sun and late-type stars is the negative hydrogen ion H^-. Ionized metals can provide neutral hydrogen atoms by electrons to form H^-. The number density can be determined by taking into account several processes, the most important are the destruction of the ion by photo dissociation,

$$H^- + \nu \leftrightarrow H + e \tag{3.34}$$

The ion may also be destroyed by collisions with electrons, and collisional detachment by hydrogen atoms,

$$H^- + e \leftrightarrow H + 2e \tag{3.35}$$

$$H^- + H \leftrightarrow H_2 + e \tag{3.36}$$

For the radiation by the H$^-$-continuum, it is clear that because the solar surface is defined to be at optical depth unity and since the density in the tube is roughly one sixth of the outside medium, that the tube can be considered as optically thin for continuum radiation in the photosphere and chromosphere. In our computation we treat the flux tube as bathed in the height-dependent mean intensity $J_\nu(z)$ of the external surroundings. The total radiative damping function (in $erg\ g^{-1}K^{-1}s^{-1}$), is given by

$$\left.\frac{dS}{dt}\right|_{Rad} = \left.\frac{dS}{dt}\right|_{H^-} + \left.\frac{dS}{dt}\right|_{MgIIk} + \left.\frac{dS}{dt}\right|_{CaIIK} + \left.\frac{dS}{dt}\right|_{FeII} \tag{3.37}$$

where the H$^-$- continuum contribution is evaluated following Schmitz et al. (1985) and is given by

$$\left.\frac{dS}{dt}\right|_{H^-} = \frac{\Phi_{H^-}}{\rho T}$$

$$= \frac{4\pi}{T}\int_0^\infty \left[\kappa_\nu^{bf}\left(J_\nu - S_\nu^{bf}\right) + \kappa_\nu^{ff}\left(J_\nu - B_\nu\right)\right] d\nu \quad , \tag{3.38}$$

where Φ_{H^-} is the net radiative heating rate, ρ the density, T the temperature and ν the frequency. The bound-free source function is given by

$$S_\nu^{bf} = \frac{2h\nu^3}{c^2}\frac{1}{b_{H^-}e^{h\nu/kT} - 1} \quad , \tag{3.39}$$

and due to LTE, the free-free source function is equal to the Planck function B_ν. The bound-free absorption coefficient is given by

$$\kappa_\nu^{bf} = \frac{n_{H^-}}{\rho}\alpha_\nu^{bf}\left(1 - \frac{e^{-h\nu/kT}}{b_{H^-}}\right) \quad , \tag{3.40}$$

where for the number density of H$^-$ ions one has

$$n_{H^-} = b_{H^-} \frac{n_H n_e}{4} \left(\frac{h^2}{2\pi m_e kT} \right)^{3/2} e^{0.754eV/kT} \quad , \tag{3.41}$$

with n_H being the hydrogen number density and n_e the electron number density. m_e is the mass of the electron, h Planck's constant and k the Boltzmann constant. The free-free opacity is given by

$$\kappa_\nu^{ff} = \frac{n_H}{\rho} n_e \alpha_\nu^{ff} \quad , \tag{3.42}$$

where the cross-sections α_ν^{bf} and α_ν^{ff} are given by polynomials fitted by Kurucz (1970; see also, Schmitz et al. 1985). From the statistical rate equation the departure from LTE coefficient of H^- can be written

$$b_{H^-} = \frac{R_{k1}^\dagger + C_{1k}}{R_{1k} + C_{1k}} \quad , \tag{3.43}$$

where

$$R_{1k} = \int_{\nu 1}^{\infty} \alpha_\nu^{bf} \frac{4\pi}{h\nu} J_\nu d\nu \quad , \tag{3.44}$$

is the radiative absorption rate,

$$R_{k1}^\dagger = \int_{\nu 1}^{\infty} \alpha_\nu^{bf} \frac{4\pi}{h\nu} \left(\frac{2h\nu^3}{c^2} + J_\nu \right) e^{-\frac{h\nu}{kT}} d\nu \quad , \tag{3.45}$$

the radiative recombination rate and

$$C_{1k} = 2 \cdot 10^{-9} \left(\frac{n_H}{1+\delta} + \theta^{-3/2} n_e \right) \quad , \tag{3.46}$$

the collisional ionization rate between the one bound level 1 and the continuum level k, with $\theta = 5040/T$ and

$$\delta = 58\sqrt{\theta} e^{1.736\theta} n_e / n_H \quad . \tag{3.47}$$

In our present work we first evaluate the departure coefficient b_{H^-} by using the specified mean intensity $J_\nu(z)$ at the given Eulerian height z together with the local values of T, n_H and n_e in the tube. The opacities and the source functions are then computed and the damping function $dS/dt|_{H^-}$ is found from Eq. 3.38.

3.3.2 CRD versus PRD

The scattering of photons in spectral lines form an important problem while modeling dynamic stellar atmospheres. Two assumptions are usually assumed, coherence or complete redistribution (CRD). In stellar atmospheres, the redistribution of photons in angle and frequency should be considered. This process with coherent scattering is known as partial redistribution (PRD). In the frame of PRD, the absorption and emission profiles

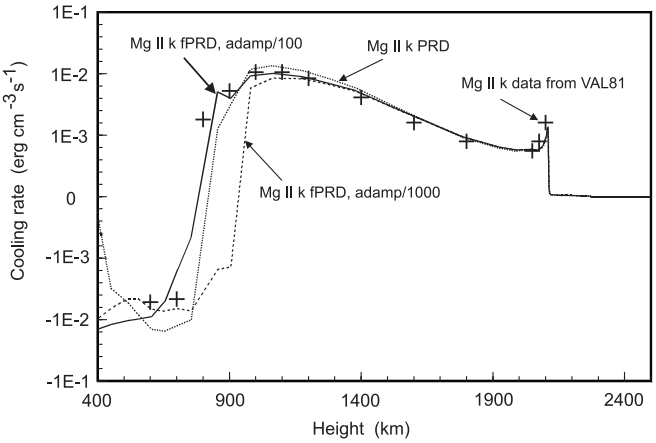

Fig. 3.2 The Mg II k-line cooling rate is computed with two-level approach and two-beam method in PRD is compared with the model C of Vernazza et al. (1981) and those computed with the pseudo-PRD procedure by reducing the damping parameter by factors of 100 and 1000.

need not to be identical. The assumption of PRD is very important in the higher layers of stellar atmosphere, where the collisional rates are too low because of the very low gas density. The resonance lines of Mg II and Ca II which are formed high in the atmospheres have wings which are dominated by coherent scattering, the assumption of PRD should be taken into account while modeling the formation of these lines. The assumption of complete redistribution (CRD) overestimates the radiative loss rates of spectral lines by more than an order of magnitude (see, Hünerth and Ulmschneider 1995). The computed radiative energy loss is very sensitive to the amount of coherent scattering that is assumed (see, Uitenbroek 1989).

The inclusion of the assumption of PRD in the time-dependent computations when shocks are included is time consuming. In such computations the transfer equation has to be solved many times in each time step. A fast method is needed for this type of computations. Different methods were developed (see, Uitenbroek 1989), but they do not allow for treating shocks as discontinuities; grid spacing of zero optical depth. A fast treatment which also includes treating shocks as discontinuities was developed by Ulmschneider (1994). Hünerth and Ulmschneider (1995) also developed an approximate method for simulating the PRD effects in time-dependent computations. This method is based on decreasing the damping parameter given by Eq. (3.52) in normal CRD computations. A close agreement with the PRD results is obtained and a much reduced computational time is obtained.

This pseudo-PRD procedure is implemented in our time-dependent computations and a comparison is done between our computations by decreasing the damping parameter by factors of 100 and 1000 with the model C of Vernazza et al. (1981) and with real PRD computations. Figure 3.2 shows the results for Mg II k-line, a good agreement is obtained for the case which has a reduced damping parameter by factor of 100. This method is quite fast to be implemented in our time-dependent computations.

3.3.3 Line Radiation Treatment using CRD

The computations of the line losses in atmospheres with shocks assuming complete redistribution (CRD) overestimates the radiation losses. On the other hand the assumption of

partial redistribution (PRD) is a time consuming procedure to be implemented in a time-dependent computations. Hünerth and Ulmschneider (1995) suggested a faster procedure to simulate the PRD computations by using normal CRD computations and artificially cutting out the damping wings of the line. They found that in the lower and middle chromosphere the CRD cooling rate deviate greatly from the PRD rate, while at greater height they become approximately 1, which means at great heights the assumption of CRD is correct and gives the same results as the PRD assumption. In the simulation by Hünerth and Ulmschneider (1995), the damping parameter a in Eq. (3.52) is multiplied by 1/10, 1/100, 1/1000 and 0. The results show that the decrease of a brings the CRD rate to be closer to the PRD rate. The suggestion of pseudo-PRD has been implemented to the current time-dependent computations.

Clearly it is inappropriate to carry out this large amount of numerical work for a one-dimensional tube structure where the magnetohydrodynamics is modeled on basis of the thin tube approximation. It thus is necessary to look for an efficient treatment of the chromospheric line losses which is on a comparable level of sophistication used in our thin tube models, but still displays the essential physics which occurs in chromospheric line radiation. For this reason we keep the NLTE treatment of the line losses since the overpopulation of the ground states is a typical property of chromospheres. More than an order of magnitude reduction of numerical work is possible by following Hünerth & Ulmschneider (1995) where the PRD treatment is replaced by the use of CRD with removed damping wings (taking $a = 0$ in Eq. (3.52) below). However, even a multiple line CRD treatment would still be too elaborate for our type of model.

A fast treatment of radiation in the chromosphere is done by replacing all chromospheric lines by only one or two single lines which are scaled such that they approximately represent the total chromospheric line losses. Since Ca II with its two resonance lines (H, K) and three IRT lines would need an elaborate 6 level atom treatment, while Mg II has only two resonance lines (h, k). The Mg II k-line and the Lyα line have been selected as representative lines which to a first approximation can be treated by a two-level atom model. Moreover, since in the present flux tube computations do not extend to great height it is even possible to neglect the H-line losses. In a one line computation, the Mg II k-line losses need to be scaled to represent the total losses. As shown by Hünerth & Ulmschneider (1995), the use of CRD in the Mg II k-line leads to about a factor of ten more line cooling than when using PRD. Since the total chromospheric line losses are about a factor of ten larger than the Mg II k-line losses, treating Mg II k using CRD thus very crudely incorporates the bulk of the chromospheric line emitters. This procedure has been tested (Ulmschneider et al. 1987) for the Sun by a comparison with the total cooling rate of chromosphere model C of Vernazza et al. (1981). Thus by computing the single Mg II k-line in a two-level atom approximation in CRD we would have a reasonable and simple estimate of the total chromospheric radiation losses.

It remains to find a simpler treatment for the 2- dimensional radiative transfer as well. Here, following Ulmschneider et al. (1987), we note that the horizontal optical depth across the flux tube is much larger than the optical depth to the top of the chromosphere. This allows to treat the tube in the Mg II k-line as a plane-parallel atmosphere where the radiative exchange is primarily in vertical direction which amounts practically to a one-dimensional treatment where the radiative transfer is solved using an operator splitting

method by Buchholz et al. (1994), which is fast and thus well suited for time-dependent applications.

Within the CRD approximation, for a spectral line with background continuum the transfer equation can be written as

$$\mu \frac{\partial I_{\nu\mu}(\tau)}{\partial \tau} = \left[\varphi_{\nu\mu}(\tau) + r(\tau)\right]\left[I_{\nu\mu}(\tau) - S_{\nu\mu}(\tau)\right] \quad , \tag{3.48}$$

where

$$\tau(z) = \int_z^\infty \chi_L(z')dz' \quad , \tag{3.49}$$

is the reference (line center) optical depth and

$$r(z) = \frac{\chi_C(z)}{\chi_L(z)} \quad , \tag{3.50}$$

is the ratio of background to line center opacities. $I_{\nu\mu}$ is the specific monochromatic intensity of a beam of radiation inclined by an angle ϑ with respect to the outwardly directed z-axis. $\mu = \cos\vartheta$ and ν is the frequency. χ_L and χ_C are frequency-independent line and continuum opacities. For the absorption profile $\varphi_{\nu\mu}$ we take a Voigt profile, given by

$$\varphi_{\nu\mu} = \frac{H(a,v)}{\sqrt{\pi}\Delta\nu_D} \quad , \tag{3.51}$$

where the damping parameter a and the normalized frequency separation v are given by

$$a = \frac{\Gamma}{4\pi\Delta\nu_D} \quad , \tag{3.52}$$

$$v = \frac{\nu - \nu_{12}\left(1 - \mu\ u(z)/c_L\right)}{\Delta\nu_D} \quad . \tag{3.53}$$

Γ is the damping constant, $\Delta\nu_D = (\nu_{12}/c_L)\sqrt{2kT/m_{Mg}}$ the thermal Doppler width, m_{Mg} the mass of the Mg atom, ν_{12} the line-center frequency, u the gas velocity and c_L the light velocity. The absorption profile satisfies the normalization condition

$$\int_{-\infty}^{\infty} \varphi_{\nu\mu} d\nu = 1 \quad . \tag{3.54}$$

The total source function is given by

$$S_{\nu\mu}(\tau) = \frac{\varphi_{\nu\mu}(\tau)S_{12}(\tau) + r(\tau)B_{\nu 12}(\tau)}{\varphi_{\nu\mu}(\tau) + r(\tau)} \quad . \tag{3.55}$$

Here $B_{\nu 12}$ is the Planck function and S_{12} the line source function for a two-level atom in CRD

$$S_{12}(\tau) = \frac{\int_{-\infty}^{\infty} \varphi_{\nu\mu} J_\nu(\tau) d\nu + \epsilon(\tau) B_{\nu 12}(\tau)}{1 + \epsilon(\tau)} \quad , \tag{3.56}$$

where the photon destruction probability is given by

$$\epsilon(\tau) = \frac{n_e \Omega_{21}}{A_{21}} \left(1 - \mathrm{e}^{-h\nu_{12}/kT}\right) \quad . \tag{3.57}$$

Ω_{21} the collisional de-excitation rate and A_{21} is the Einstein coefficient for spontaneous emission. The radiative damping function and the net radiative heating rate for the Mg II k-line can then be written (Kalkofen & Ulmschneider 1984) as

$$\left.\frac{dS}{dt}\right|_{MgIIk} = \frac{\phi_{MgIIk}}{\rho T} = \frac{4\pi\chi_L}{\rho T}\epsilon(S_{12} - B_{\nu 12}) \quad , \tag{3.58}$$

where

$$\chi_L = n_1 B_{12} \frac{h\nu_{12}}{4\pi} \frac{1}{1 + c_L^2 S_{12}/(2h\nu_{12}^3)} \quad . \tag{3.59}$$

Here n_1 is the number density of the Mg II ground state and B_{12} the Einstein coefficient for absorption. The atomic data for the Mg II k-line, that is, the values for Ω_{21}, Γ and the element abundance A_{Mg}, are given in Tab. 1 of Kalkofen et al. (1984). A similar procedure is followed to compute the damping function

$$\left.\frac{dS}{dt}\right|_{CaIIK} = \frac{\phi_{CaIIK}}{\rho T} = \frac{4\pi\chi_L}{\rho T}\epsilon(S_{12} - B_{\nu 12}) \tag{3.60}$$

and the net radiative heating rate ϕ_{CaIIK} for Ca II.

For the evaluation of n_1 the ionization ratio of Mg II to Mg I is computed in LTE while for the Mg III to Mg II ratio an NLTE ionization following Rammacher & Cuntz (1991) is used. The background opacity χ_C is evaluated from tables generated with the ATLAS program of Kurucz (1970). The radiative transfer Eq. (3.48) together with the source function given by Eqs. (3.55), (3.56) are solved for the line intensity $I_{\nu\mu}$ using the operating splitting method of Buchholz et al. (1994), after which the mean intensity J_ν, the line source function and with Eq. (3.59) the radiative damping function for the line is computed. As a further simplification we employ the two-beam approximation which reduces the angle integration to ingoing and outgoing contributions along a single ray with $\mu = 1/\sqrt{3}$. Note incidentally that the two-beam approximation is also employed for the evaluation of the continuum intensity $J_\nu(z)$ outside the flux tube.

3.3.4 The Representation of the Chromospheric Line Losses

In a previous work, the single Mg II k-line was computed assuming CRD and scaled up to represent the whole chromospheric line emission. As mentioned by Hünerth and Ulmschneider (1995), the computed Mg II k-line losses assuming CRD leads to a factor of ten times more emission than assuming PRD, which is roughly of the order of chromospheric

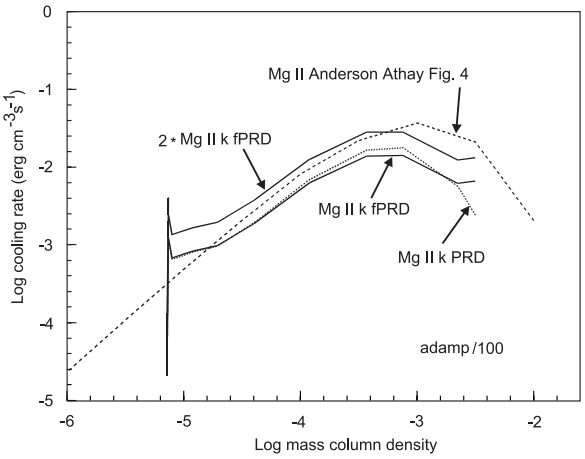

Fig. 3.3 The computed cooling rate of the Mg II k-line assuming PRD and pseudo-PRD (marked by fPRD) is compared with the values of Anderson & Athay (1989). The pseudo-PRD is based on CRD computations with a reduced damping parameter by a factor of 100. Doubling the cooling rate of the Mg II k-line accounts well for the total Mg II losses.

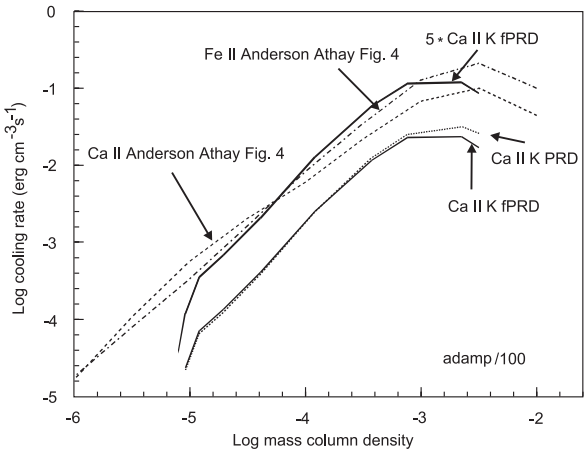

Fig. 3.4 The same as in Fig. 3.3, however for the Ca II K-line, the total Ca II and Fe II cooling rates. Multiplying the Ca II K-line pseudo-PRD (marked by fPRD) with a factor of 10 accounts well for the total Ca II and Fe II cooling rates.

line losses. In the current treatment, we use the procedure of pseudo-PRD with a damping parameter multiplied by 1/100 and line cooling rates of the dominant chromospheric emitters are computed using CRD. From the empirical models of Vernazza et al. (1981) as well as Anderson & Athay (1989) it is known that in addition to the H^- losses, the radiative losses in the middle and upper chromosphere are primarily due to the lines of Ca II H + K, Ca II IRT, Mg II h + k and numerous Fe II lines. In the highest chromosphere, these losses are augmented by those of the H Lyα line. For a rigorous treatment, all these line contributions would have to be computed individually and summed up to provide the total chromospheric radiation losses.

A comparison is done between our PRD and pseudo-PRD with the total cooling rates of Fig. 4 of Anderson & Athay (1989), which is based on model of Maltby et al. (1986). As seen in Fig. 3.3 similar results are obtained for both PRD and pseudo-PRD for Mg II k-line and taking - $2 * \phi_{MgIIk}$ agrees well with the total Mg II losses. This means that doubling the radiative line loss of Mg II k-line can represent also the h-line. A similar comparison for Ca II is shown in Fig. 3.4, similar results for the Ca II K-line are obtained for both PRD and pseudo-PRD. The Ca II K-line cooling is multiplied by a factor of 5 to account for the 5 lines of Ca II (H, K, and IRT). As shown in Fig. 3.4, it has been found that - $5 * \phi_{CaIIK}$ accounts well for the total Fe II losses. This supports the claim by Anderson & Athay (1989) that the Fe II losses are very important compared to the Mg II and Ca II losses. So, the Ca II and Fe II cooling rates can be represented well by - $10 * \phi_{CaIIK}$.

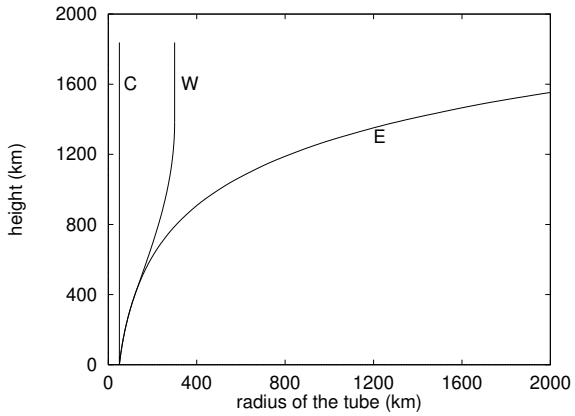

Fig. 3.5 The radii of the exponential (E), constant (C), and wine-glass (W) magnetic flux tubes are shown as function of height.

3.4 Results of Adiabatic Longitudinal Tube Waves

The propagation of adiabatic ($dS/dt|_{Rad} = 0$) longitudinal tube waves along magnetic flux tubes embedded in the solar atmosphere of different magnetic filling factors are simulated in a work by Fawzy et al. (1998). It has been found that the heating of the magnetic flux tube is strongly correlated with the tube geometry, the tube shape plays an important role in the formation and development of the shocks. Three different tube geometries were taken into account to simulate different regions of the solar atmosphere, a very crowded network region is simulated by a tube of constant cross section (C), while for the cell interior an exponentially spreading flux tube (E) was taken. For intermediate regions (e.g. with filling factor $\approx 2.8\%$) representing the outer parts of the network regions, we assumed a tube model named wine-glass tube (W). This tube at first spreads exponentially and then approaches a constant cross-section dictated by the available spreading space. Fig. 3.5 shows the tube geometries, the radii of the tubes are shown as function of height. All tubes have radii of 50 km and a magnetic field strength at height $z = 0$ km is $B_0 = 1500$ G.

Various monochromatic waves of periods between 20 s and 160 s and wave energy fluxes ranging from $1 \cdot 10^7$ to $1 \cdot 10^9$ erg cm^{-2}s^{-1} are introduced into the three flux tubes. Upon the propagation of these waves, shocks quickly form and dissipate their energy for heating the chromosphere. The main results can be drawn as follows:

a. Effect of the Tube Geometry and Wave Period

Figure 3.6 shows the height dependence of the mean temperatures averaged over 400 s for waves with the same wave energy flux $F_M = 1 \cdot 10^7\ erg\ cm^{-2}s^{-1}$ and different wave periods $P = 20$, 40, 80, and 160 s. The averaged temperatures are shown every 400 s (marked as 1, 2, ...), also the initial atmosphere is shown (marked by 0) together with a snapshot of the instantaneous temperature at $t = 800$ s (marked by dashed lines).

The mean temperatures in the case of the *constant cross section tube* (left column of Fig. 3.6) show perpetual increase with time because of the adiabatic treatment. The shock strengths grow and heating becomes stronger with increasing the wave period, this is due to the fact that the shock strength grows approximately linear with the wave period and

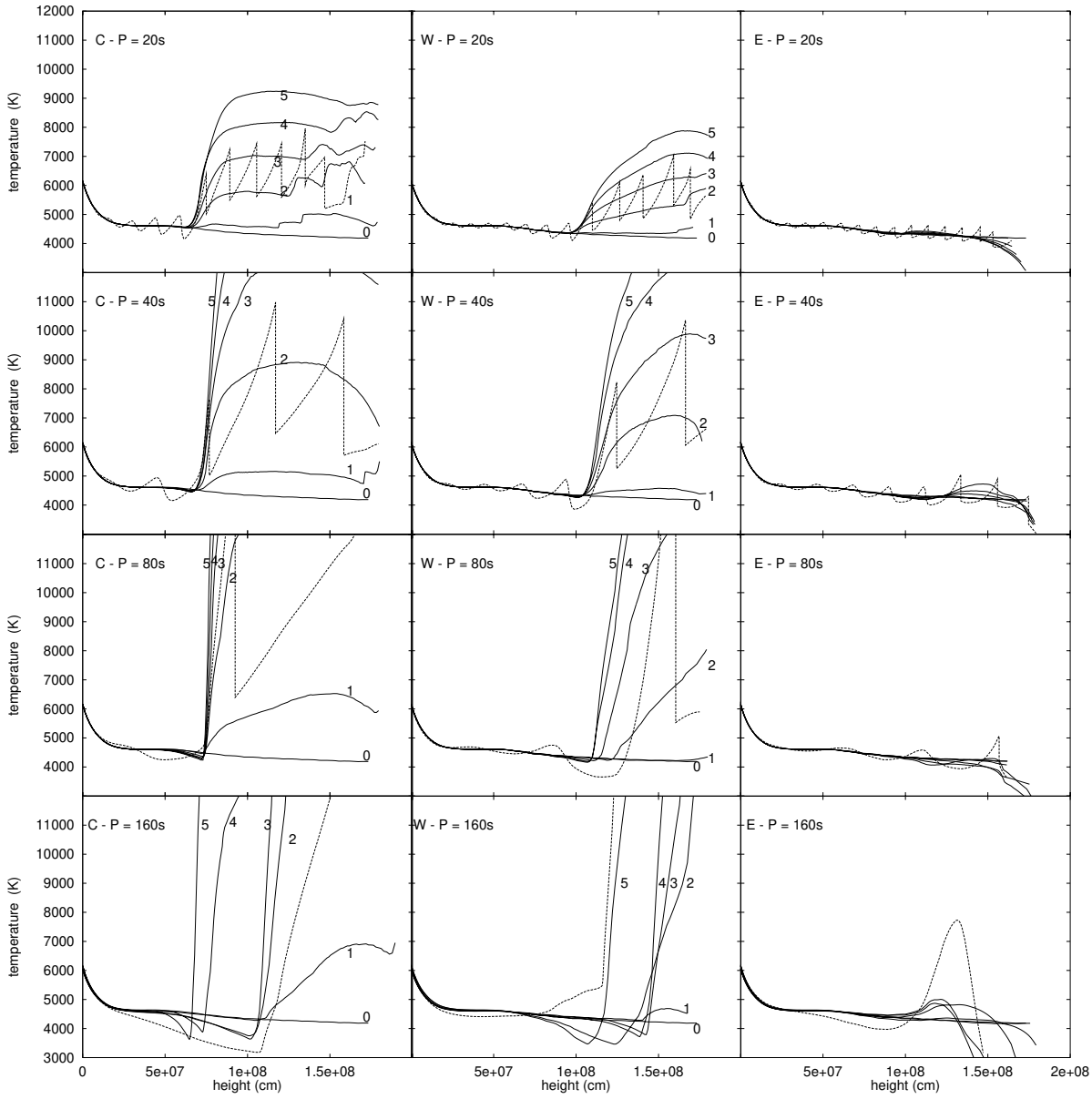

Fig. 3.6 Height dependence of the mean temperature (solid) for waves with the same energy flux $F_M = 1 \cdot 10^7$ erg cm^{-2}s^{-1} and periods $P = 20,\ 40,\ 80,\ 160$ s (from top to bottom) for the three tube models. The left column shows the constant cross-section tube (C), the middle column shows the wine-glass tube (W), and the right column shows the exponential tube (E). The mean temperatures are shown in 400 s intervals (marked by 1, 2, 3, 4, 5, respectively) starting from $t = 400$ s up to the time $t = 2000$ s. Also shown are the initial temperature distribution (marked 0) and the instantaneous temperature at $t = 800$ s (dashed).

the increase of the entropy depend on the third power of the shock strength. Increasing the wave period results in an increasingly steeper chromospheric temperature rise. The shock formation heights are approximately the same for the different value of P, this is because the reason that once the first shock forms, it imparts momentum to the gas which leads to an expansion of the atmosphere and as a result the gas density decreases. As a result of decreasing the gas density, conservation of wave energy produces a larger wave amplitude for the next shock which forms earlier (from 1150 km for the first shock to 500 km for the next one, for $P = 20$ s). After the passage of the first shock, the shock

formation height stays the same for the rest of the time. This effect of lowering the shock formation height is most noticeable for the case of $P = 160$ s, where the momentum deposition is greatest, leading to a shock formation height which is similar to that of $P = 20$ s.

The *exponential tube* did not show any signs of shock formation and no case where appreciable heating occurs. This is due to the rapid expansion with height, and the fact that the energy is distributed over an increasing cross-section. The amplitude increase due to the density stratification is encountered by the rapid growth of the cross-section, which keeps the increase of the wave amplitude very low. For this reason, shocks are very weak and cannot produce any heating (see the right column of Fig. 3.6).

The behavior of the mean temperatures in the case of the *wine-glass tube* (middle column of Fig. 3.6) is intermediate to the other two cases. Considerable heating occurs at heights where the tube show its least expansion, in the constant cross section part where the tube has reaches its maximum diameter. Because of the exponential spreading of the tube below the height $z = 400$ km, shock formation is delayed and occur above the height of $z = 1000$ km. Above 1000 km height, the same temperature jumps as in the case of the constant-cross section tube is seen, this is due to the limiting shock strength behavior of the longitudinal tube waves (see, Ulmschneider 1970).

b. Effect of the Wave Energy

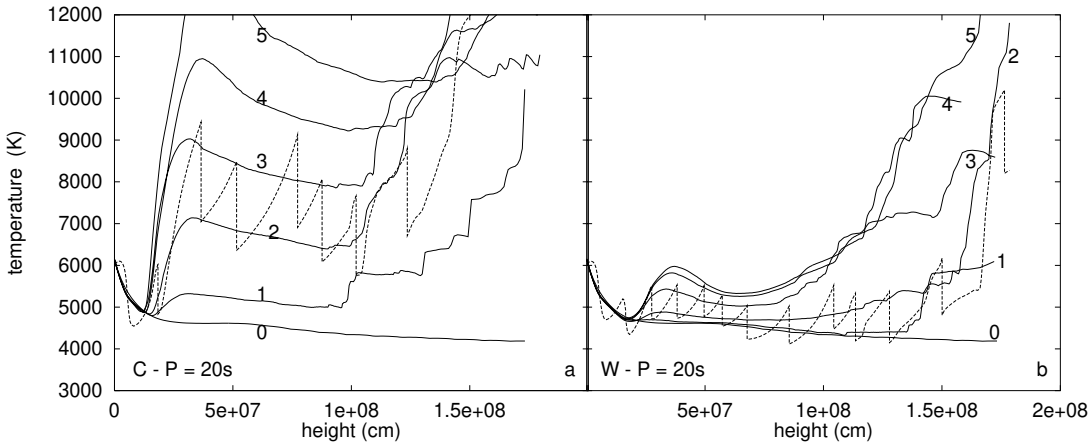

Fig. 3.7 The same as in Fig. 3.6 but for $F_M = 1 \cdot 10^9\ ergcm^{-2}s^{-1}$ and $P = 20$ s, panel (a) shows the constant-cross section tube and panel (b) shows the wine-glass tube.

The same computations were repeated with increased wave energy fluxes, using wave energy fluxes of $F_M = 1 \cdot 10^8$ and $1 \cdot 10^8\ erg\ cm^{-2}s^{-1}$. The computations of the exponential tube failed after times of about 500 to 800 s for these higher fluxes, the reason for this is the amplification of the oscillatory flows at greater heights for large wave energies leading to unrealistic situations. Figure 3.7 shows the mean temperatures for the constant-cross section tube (a) and the wine-glass tube (b) for $P = 20$ s. The increase of the wave energy leads to shock formation at lower heights, to $z = 83$ km and 250 km for constant-cross section and wine-glass tubes, respectively (compared to the shock formation height of

500 km shown in Fig. 3.6. Also, the number of shock merging events increase. As seen in Fig. 3.7 b, shock heating is reduced (small increase of the mean temperature) in the region between 400 and 1000 km, where the tube cross-section increases rapidly, above the height $z = 1000$ km, the tube has a constant cross-section and heating is stronger leading to an increase of the mean temperature similar to that of the constant cross-section tube.

c. Effect of the Magnetic Field Strength

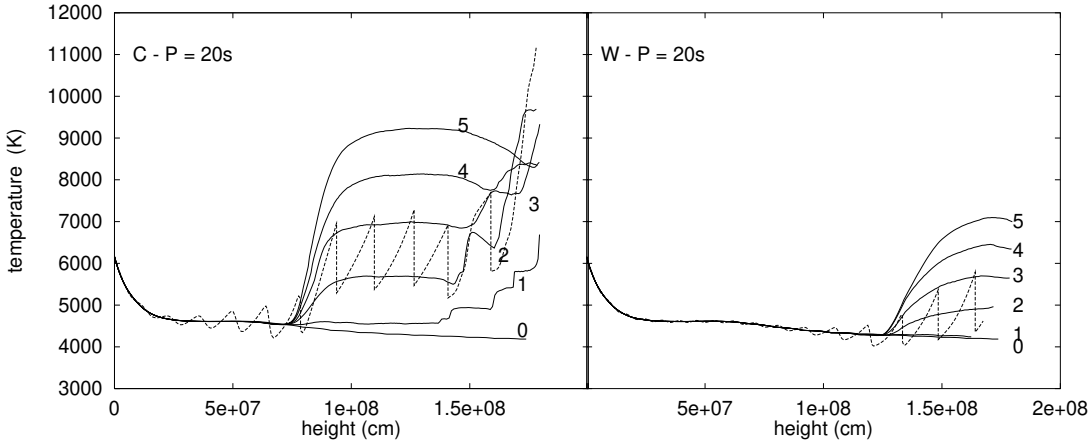

Fig. 3.8 The same as in Fig. 3.6 but for a magnetic field strength of $B = 1000$ G and waves with $P = 20$ s and $F_M = 1 \cdot 10^7\ ergcm^{-2}s^{-1}$ for the constant cross-section (C) and wine-glass tube (W).

Keeping all parameters of Fig. 3.6 the same and changing only the magnetic field strength from $B_0 = 1500$ G to $B_0 = 1000$ G results in a delay of the shock formation height as shown in Fig. 3.8. For the constant cross-section tube the shock formation height is increased by about 200 km (left panel of Fig. 3.8), the same effect is also found for the wine-glass tube (right panel of Fig. 3.8) in which the shock formation height is increased by about 500 km. The reason for that is lowering the field strength results in increasing the gas density inside the tube, which in turn leads to lower wave amplitudes and then to a delay in the shock formation height. As soon as the shocks become fully developed, they reach limiting strength and therefore generate the same heating found in the $B_0 = 1500$ G tube. Also, for the wine-glass tube, lower magnetic field strengths lead to weakening of the shock heating. The exponential tube shows negligible shock heating.

3.5 Results of the Radiatively Damped Longitudinal Tube Waves

Different magnetic flux tube models were constructed using observed magnetic filling factors (fraction of the surface covered by magnetic fields) for the different regions of the solar photosphere. The data collected by Solanki (1997; private communication) shows the following values of f:
For a *normal network*, in which each element is composed of a number of flux tubes, the

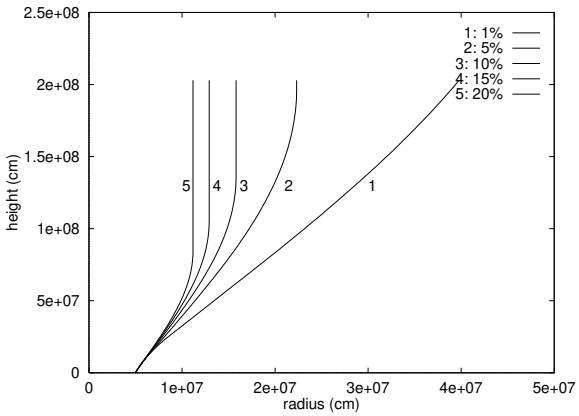

Fig. 3.9 The height dependence of the solar magnetic flux tubes of filling factors: $f = 1\%,\ 5\%,\ 10\%,\ 15\%$ and 20%.

outer edge has a value of $f = 1\%$. The intermediate part of the network f has a value of 5%, while in the central parts it reaches a value of 15%. The average value over the whole network element is 5%.
The central parts of the *enhanced network* have $f = 30\%$ (this value also varies from 1% at its outermost edge to 30% in its core). The average value over the whole enhanced network element is $f = 10\%$. The *strongest plage* shows values of f which reach about 60%. Figure 3.9 shows the geometries of solar magnetic flux tube of different filling factors $f = 1\%,\ 5\%,\ 10\%,\ 15\%$ and 20%. The bottom radius of all tubes is $r_B = 50$ km, and the top radii r_T are determined from the value of f as $r_T = \frac{1}{2} r_B \sqrt{\pi / f}$. The flux tubes first expand exponentially till the merging height and then the reach a constant cross-section above this height. The larger the filling factor, the deeper the neighboring flux tubes merge, the merging height of the thin flux tubes is given by Spruit (1983) as $h_m = 2H\ ln(1/f)$, where H is the local scale height.

In the current computations, the radiatively damped longitudinal tube waves were propagating along two flux tubes of magnetic filling factors $f = 1\%$ and 20%. The procedure start by constructing a non-gray radiative and hydrostatic equilibrium solar atmosphere model with an effective temperature $T_{eff} = 5770\ K$ and gravity $g = 2.736 \cdot 10^4\ cm\ s^{-2}$ using the temperature and flux correction procedure described by Cuntz, Rammacher & Ulmschneider (1994). In this model, NLTE H^- continuum, Mg II k and Ca II K cooling lines have been assumed. The atmosphere thus has a temperature which continuously decreases in outward direction and does not include chromospheric heating. Magnetic flux tubes are subsequently embedded in the external atmosphere at height $z = 0$ km, where the optical depth is $\tau_{5000} = 1$, they have a specified radius $r_B = 50\ km$ and a magnetic field strength $B_0 = 1500$ G. These tubes are allowed to spread with height in pressure balance with the surrounding gas pressure (cf. Eq. (3.3)) up to a height z_H. The spreading from height z_H to a maximum height $z_T = 2000\ km$ is different for the different tube models. The initial models of the two flux tubes are shown in Fig. 3.10 (for the case of $f = 1\%$) and Fig. 3.11 (for the case of $f = 20\%$) with the temperature, density, and magnetic field.

The input mechanical energy fluxes used in our models are taken from the recent computations of generation of longitudinal tube waves in the solar atmosphere by Ulmschneider & Musielak (1998). They found that the wave energy fluxes carried by the longitudinal

tube waves are of the order of $2 \cdot 10^8\ erg/cm^2 s$. Thus the value of $F_M = 2 \cdot 10^8\ erg/cm^2 s$ is implemented in our models. The maximum energy carried by longitudinal tube waves is found to have periods close to 60 s, therefore we take $P = 60$ s in our models.

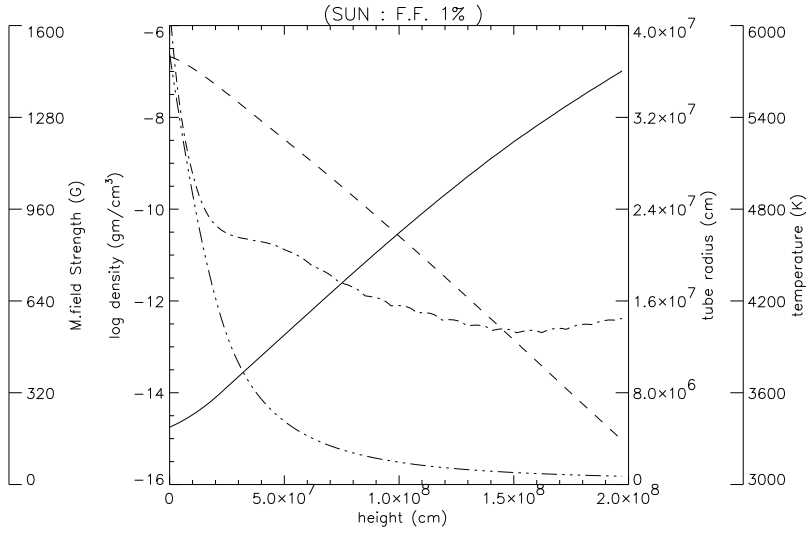

Fig. 3.10 The initial flux tube model of 1% filling factor, shown are the tube radius (solid) (in cm), the temperature (in Kelvin) (dash - dot), the density (in gm/cm^3) (dashed), and the magnetic field strength (in G) (dash - three dots).

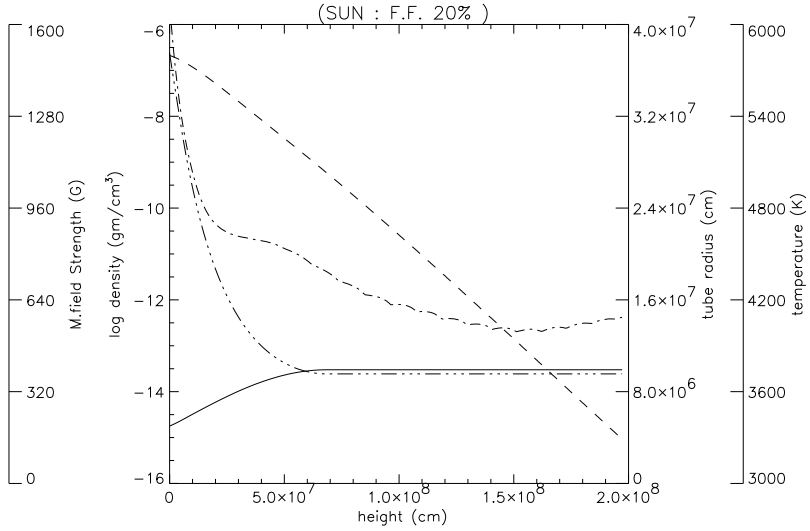

Fig. 3.11 The same as in Fig. 3.10 but for $f = 20\%$.

In this study, it is interesting to know the effect of f on the amount of heating in both models. The continuum cooling function due to H^- and the total line cooling function (Mg II k + Ca II K + Fe II) change greatly from $f = 1\%$ to $f = 20\%$. Shocks form earlier in the case of $f = 20\%$, with larger strengths than the case of 1% filling factor, this can be seen from the jumps of the instantaneous temperature in Fig. 3.12 a,b. The continuum cooling function increases approximately by a factor of 5 from $f = 1\%$ to $f = 20\%$ (see, Fig. 3.12 c,d), while the line cooling function increases by a factor of 7.4 for the same cases (see, Fig. 3.12 e,f).

In summary, the geometry of the flux tubes (or the magnetic filling factors) play an important role in the heating of the atmospheric outer layers. More heating is found in tubes with larger filling factors, which show least spread with height, and as a result more Mg II and Ca II emission fluxes. On the other hand, flux tubes with small filling factors do not contribute too much to the chromospheric heating. Shock formation heights are determined by the input mechanical wave energy, they form at lower heights for large input wave energy, and at greater heights for smaller amounts of wave energy.

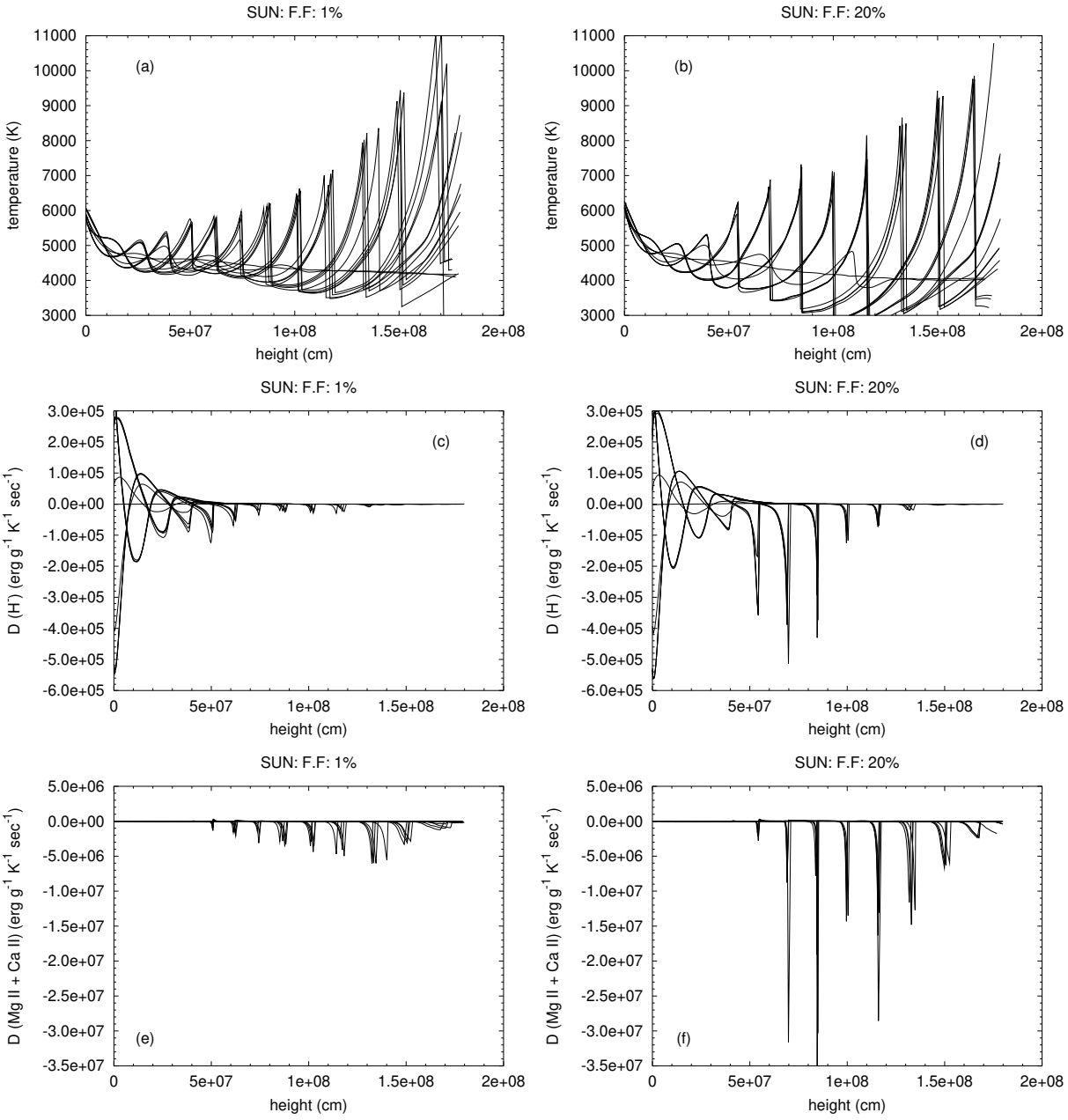

Fig. 3.12 A comparison between the two magnetic flux tube models with 1% and 20% magnetic filling factors.
3.12 a (*top, left*) The instantaneous temperature (K) vs. height (cm) inside the flux tube of 1% magnetic filling factor. The snapshots are taken every 400 s.
3.12 b (*top, right*) The same as in Fig. 3.12 a, but for the tube of 20% filling factor.
3.12 c (*middle, left*) The radiative damping function $\mathbf{D} = dS/dt|_{H^-}$ for the H^- ($erg\ g^{-1}K^{-1}sec^{-1}$) vs. height (cm) for case of 1% filling factor, with snapshots taken every 400 s.
3.12 d (*middle, right*) The same as in Fig. 3.12 c, but for the tube of 20% filling factor.
3.12 e (*bottom, left*) The radiative damping function $\mathbf{D} = dS/dt|_{lines}$ for the Mg II + Ca II + Fe II lines ($erg\ g^{-1}K^{-1}sec^{-1}$) vs. height (cm) for case of 1% filling factor, the snapshots are taken every 400 s.
3.12 f (*bottom, right*) The same as in Fig. 3.12 e, but for the tube of 20% filling factor.

Chapter 4

Chromospheric Resonance Oscillations

Summary. In this chapter, we study the response of the magnetic and non-magnetic chromosphere models of the Sun and late-type stars to the excitation by various types of waves. We consider small amplitude and large amplitude waves, monochromatic and acoustic wave spectra in the form of pure acoustic and longitudinal magnetohydrodynamic waves. The considered atmospheres are isothermal and stratified non-magnetic plane parallel and magnetic flux tube atmospheres. The computations are carried out for the Sun and two other late-type stars, a hot star (F5V) and a cool star (M0V).

4.1 Introduction

Observations of the Sun show that the solar atmosphere has dominant modes of oscillations. The solar photosphere has a dominant 5-min oscillation period, which was discovered by Leighton et al. (1962). This oscillation has been interpreted as trapped subphotospheric acoustic waves. The solar chromosphere also has its own oscillation around 3-min, these oscillations were observed in the emission features of the H and K lines of the Ca II. These emission features arise from two regions of the outer solar atmosphere, the first region is the interior of the supergranulation cells, while the second region is the magnetic network of the cell boundaries. It has been found that the emission features which originate from the interior of the supergranulation cells oscillate around 3-min, this oscillation is interpreted as a resonance at the basic cut-off period of the chromosphere. Observations of the oscillations in emission features from solar magnetic elements have been reported by Beckers & Schulz (1972), Giovanelli et al. (1978), and Moore & Rabin (1985).

Recent analysis of the time-series data of the solar atmosphere using the MDI and SUMER instruments onboard SOHO spacecraft (Judge et al. 2000) shows that the middle chromosphere possess oscillations with predominant power in the range of 5-7 mHz.

4.2 Analytical Treatment

The analytical formula describes the response of an isothermal atmosphere to a continuous *purely acoustic* excitation by velocity oscillations introduced by a piston at the lower boundary, as discussed by Kalkofen et al. (1994) and Sutmann & Ulmschneider (1995 a), has two contributions, the exciting wave with frequency ω and a resonance oscillation around the cut-off frequency ω_A, where $\omega_A = 2\pi/P_A$ with $P_A \approx 3$ min. These waves either propagate or are evanescent, depending on the value of ω, if ω is greater than ω_A the waves propagate, and they are evanescent if ω is less than ω_A. Sutmann et al. (1998, paper III) studied analytically the response of the isothermal solar atmosphere to adiabatic excitations by small amplitude acoustic spectra in form of continuous and pulse excitations. They concluded that in the case of the excitation by wave trains of random pulses, the atmosphere responds with oscillations which decay with time as $t^{-3/2}$, and if these random pulses were continuously generated, the atmospheric oscillations would be present despite their $t^{-3/2}$ decaying time. Also, they concluded that these wave trains may be responsible for the observed 3-min chromospheric oscillations.

Recently, Hasan & Kalkofen (1999) studied analytically the linear response of a *thin vertical magnetic flux tube* to the buffeting action of a granule in form of impulse excitation. They found that after the passage of the primary impulse, the atmosphere oscillates as a whole with a single frequency which is the cut-off frequency associated with the longitudinal waves. Exciting the atmosphere with evanescent waves results in a decaying excitation with height, the resonance contribution decays with time as $t^{-3/2}$, while the decay rate depends on the temperature gradient of the atmosphere.

4.3 Numerical Treatment: Method

For a comparison with the analytical solution, we constructed two solar atmospheric models, both are isothermal ($T_{eff} = 5000$ K), the first one is a plane parallel atmosphere and the second is a magnetic atmosphere. We excite both atmospheres with low amplitude waves, monochromatic waves and wave spectra. The exciting waves have Mach numbers in the range of $2.5 \cdot 10^{-4}$ to $6.5 \cdot 10^{-4}$. The time sequence of the velocity fluctuations at different heights of the atmosphere are followed, and the corresponding power spectrum is computed by means of the Fast Fourier Transforms, this enables us to study the pronounced resonances in the atmosphere.

The present work is a continuation of work by Sutmann & Ulmschneider (1995 a,b - paper I & II). In paper I they studied the linear response of a plane parallel solar atmosphere to adiabatic small amplitude wave excitation, using monochromatic waves and acoustic spectra of different shape. The nonlinear response of the solar atmosphere to large amplitude adiabatic wave excitations has been studied by Sutmann & Ulmschneider (1995, paper II), the solar atmosphere has been excited by both monochromatic waves and acoustic wave spectra, they found upon exciting the atmosphere with monochromatic waves, that a critical frequency ν_{cr} controls the behavior of the resonance decaying rate, if the atmosphere is excited with frequencies $\nu < \nu_{cr}$, the resonance decays rapidly, on the other hand if the atmosphere is excited with frequencies larger than ν_{cr}, a persistent

resonance occurs. Exciting the atmosphere with wave spectrum resulted in a behavior in which $\nu > \nu_{cr}$. They used different shapes of the acoustic wave spectra and found that the resonant frequencies do not depend on the wave shape and the generated resonance frequencies are $\nu = 6 - 7$ mHz at the top of the chromosphere.

In addition to the non-magnetic plane parallel atmosphere, which may represent the interior parts of the supergranulation cells, we constructed in the present work a magnetic flux tube model to represent the cell boundaries. The linear and nonlinear responses to different types of waves were studied for both atmospheres. We extended these computations to other late-type stars to look for the responses of their chromospheres to the different types of excitations.

4.3.1 Initial Model Atmospheres

The computations start by constructing a gray radiative equilibrium plane parallel atmosphere for a given effective temperature T_{eff} and gravity g, using a temperature correction method by Cuntz et al. (1994). A non-gray radiative equilibrium model atmosphere which includes NLTE H^- and the Mg II k line has been constructed. The resulting atmosphere has a temperature gradient which decreases outwardly. For the construction of the initial magnetic flux tube models, the magnetohydrodynamic equations in the thin flux tube approximation were solved together with the equation of state (Herbold et al. 1985). The magnetic model represents a vertically oriented thin magnetic flux tube embedded in an external field free atmosphere. The bottom of the model is taken at height $z = 0$ km, where the external optical depth is $\tau_{5000} = 1$.

The bottom radius of the flux tube is assumed to be 50 km for the Sun, while for other types of late-type stars, the tube radii have been taken to be half the local pressure scale height similar to the Sun. In our models, the magnetic field strength should be specified at height $z = 0$ km, for the Sun it has been observed to be around 1500 G. Because of the inaccurately observed non-solar magnetic field strengths, we assume that the magnetic field strength inside the stellar flux tubes has 85% of the equipartition field similar to the Sun. The magnetic flux tubes expand with height in pressure balance with the external medium; the sum of the internal gas and magnetic pressures is equal to the external gas pressure. The spreading factor is controlled by the magnetic filling factor of the region which contains the tube.

4.3.2 Boundary Conditions and Wave Computations

The bottom boundary condition is a piston which by specifying the velocity introduces waves into the atmosphere. In our Lagrangian code, only this one boundary condition is sufficient. Two types of waves are considered, continuous sinusoidal waves with frequency below and above the cut-off frequency (e.g., 1.0 mHz & 16.7 mHz for the Sun) and wave spectra in which a number of sinusoidal waves are superposed and their amplitudes are distributed in a Gaussian form which is cut at low frequencies. The shape of the Gaussian spectrum does not change much the resulting power spectrum. The wave spectrum extends over a broad range of frequencies in such a way as to include both the propagating and the non-propagating domains.

The top boundary condition is a transmitting boundary. Upon the propagation of the waves in an outer atmosphere with a decreasing density, shocks can form with different strengths which depend on the input mechanical wave energy and wave period. Shocks are treated as discontinuities. Radiation is neglected in the present calculations. The input mechanical energy fluxes were taken by free choice, for the linear regime they have been selected to keep the Mach number as small as possible to avoid shock formation at greater heights. The input mechanical energy flux also affects the shock formation heights, it has been found that when increasing the input mechanical energy flux one has stronger shocks which form at lower heights of the atmospheres (see, Fawzy et al. 1998).

In our code we use a Lagrangian representation, in which the grid points move with the gas (mass) elements. For the Fourier analysis of the velocity fluctuations at different heights of the atmosphere we should have Eulerian grid points (at fixed heights) in both space and time, so we interpolate the velocities both in space and time by the method of weighted parabolas (Ulmschneider 1977), while in the case of shocks, the regions near the shocks are interpolated linearly. For the calculation of the Fast Fourier Transform, the number of samples N has been fixed to 2048 points, and the sampling time interval (τ) is chosen in such a way to get a frequency resolution of $\Delta\nu = 0.0005$ Hz according to $\Delta\nu = 1/(\tau N)$.

4.4 Results: Adiabatic Small Amplitude Waves

a. Non-magnetic Solar Plane Parallel Atmosphere

An isothermal non-magnetic plane parallel solar atmosphere of effective temperature T_{eff} = 5000 K has been excited by monochromatic acoustic waves of frequency ν = 1.0 mHz, and a mechanical energy flux of 10^4 erg $cm^{-2}s^{-1}$, which corresponds to a Mach number of $2.9 \cdot 10^{-4}$. The atmosphere extends up to 2000 km height. Figure 4.1 shows the velocity fluctuations at heights $z = 0$, 980, and 1580 km on the left panel and the corresponding power spectrum on the right panel. These snapshots are taken starting after 2000 seconds to be sure that the waves covered the whole layers of the atmosphere and to avoid the initial disturbances of the atmosphere due to the switch-on effects. The power spectrum is computed for the last 2048 points.

The time sequence of the velocity fluctuations of the input exciting wave (at $z = 0$ km) is shown in Fig. 4.1 a, and the corresponding power spectrum is shown in Fig. 4.1 b. At the middle of the atmosphere ($z = 980$ km), a superposition of two waves is clearly seen in Figs. 4.1 c,d, the exciting wave and an additional component results from the atmospheric reaction (resonance component), while the exciting component is still the dominant one, and the resonance component has a peak around the acoustic cut-off frequency (ν_A = 5.0 mHz), as found from the analytical solution . At the upper atmosphere (z = 1580 km), as shown in Figs. 4.1 e,f, the resonance component becomes more dominant and the exciting one becomes weaker. This means that, over a short period of time, the exciting component becomes weaker with height while the resonance component becomes stronger with height.

After long time (depends on the temperature gradient of the atmosphere) the reso-

nance oscillation decays out with time as $t^{-3/2}$ for the solar case, and only the exciting component is seen in the velocity power spectrum. For the isothermal non-magnetic solar atmosphere, the resonance component takes around 20 000 seconds to decay out completely as shown in Figs. 4.2 c,d at the middle atmosphere ($z = 980$ km), while very small resonance oscillations still exist at the upper layers of the atmosphere (see, Figs. 4.2 e,f) in comparison with the large amplitude resonance seen in Figs. 4.1 e,f after short period of time.

It is interesting to look for the peak period which will be selected by the atmosphere from a wide spectrum, for this purpose we introduced an acoustic wave spectrum instead of the monochromatic waves. Figure 4.3 b shows the Gaussian shape of the spectrum which is cut at low frequencies region. The spectrum covers about 20 mHz and extends from the evanescent to the propagating region. We also kept the Mach number as small as possible to avoid shocks and to stay in the linear regime. The time sequence of the velocity fluctuations and the corresponding power spectrum at the middle atmosphere ($z = 980$ km) are shown in Figs. 4.3 c,d. A clear oscillation is seen around $\nu = 7.5$ mHz in the propagating region, the spectrum shown in Fig. 4.3 d has very little extension in the non-propagating region, which disappears at greater heights (see, Fig. 4.3 f). At $z = 1580$ km height, Fig. 4.3 f shows two oscillations with a dominant one around $\nu = 6.0$ mHz.

b. Solar Magnetic Atmosphere

The isothermal magnetic model atmosphere has been first excited by monochromatic waves of frequency $\nu = 1.0$ mHz and a mechanical energy flux of 10^4 erg $cm^{-2}s^{-1}$, which corresponds to a Mach number of $6.5 \cdot 10^{-4}$. Following the time sequence of the velocity fluctuations at different heights ($z = 0,\ 980,$ and 1580 km) and calculating the corresponding power spectrum results in the same behavior as the plane parallel atmosphere (see, Fig. 4.4). Two components appear due to the reaction of the atmosphere and the exciting component. The exciting component decreases with height while the resonance component becomes stronger with height. The resonance component is shown in Figs. 4.4 d,f. The atmosphere resonates around the Defouw cut-off frequency (which is very close to the acoustic cut-off frequency). The isothermal magnetic atmosphere shows stronger resonance oscillations at $z = 980$ km height than the oscillation seen in the non-magnetic isothermal atmosphere at the same height (see, Figs. 4.1 d & 4.4 d). Over a short period of time, the exciting waves decay faster with height in the magnetic atmosphere in comparison with the non-magnetic atmosphere.

To study the atmospheric response to different types of wave input, we also excite the magnetic solar atmosphere with a wave spectrum composed of partial waves, with amplitudes distributed nearly in a Gaussian form, cut at low frequencies, covering about 20.0 mHz of frequency range (see, Fig. 4.5 b). A pronounced oscillation is observed around $\nu = 6.0$ mHz at height $z = 980$ km in the propagating part of the spectrum, while at greater height ($z = 1580$ km), an oscillation of frequency $\nu = 5.5$ mHz is seen in the velocity power spectrum at this height (see, Figs. 4.5 d,f).

c. The F5V and M0V Stars

Since the late-type stars have a similar structure as the Sun, we expect to find the similar types of atmospheric resonance oscillations around a basic cut-off frequency of their chromospheres. We choose an F5V star with effective temperature $T_{eff} = 6440$ K to represent a hotter late-type star, while for a cooler one, an M0V star with effective temperature $T_{eff} = 3850$ K has been chosen. Initial atmospheric models were constructed (both plane parallel and magnetic - isothermal and stratified), the initial atmosphere of the F5V star extends up to 3500 km height, while for the M0V star up to 1000 km height. We first introduced adiabatic small amplitude monochromatic waves of frequency 1.0 mHz (Mach number of $4.5 \cdot 10^{-4}$) through the isothermal non-magnetic plane parallel atmospheres of these stars, we found the same behavior like the solar case, the exciting component decreases with height and the resonance component is around the acoustic cut-off frequency ($\nu_A = 3.46$ mHz for F5V stars and $\nu_A = 8.23$ mHz for M0V stars). For short periods of time, the power spectra of both stars look very similar as Fig. 4.4 and thus are not shown here. The resonance components peak at 3.5 mHz and 8.2 mHz for the F5V and M0V stars, respectively. The resonances decay after long time, as seen from the disappearance of the high frequency velocity fluctuations (see, Fig. 4.6 e - early fluctuations) and the corresponding power spectrum (Fig. 4.6 f) after about 40 000 seconds. As seen in Figs. 4.6 d,f at the middle and upper atmosphere of the F5V star ($z = 1580,\ 2380$ km), only the exciting wave component exists and the resonance component is completely decayed out.

The M0V star has the same behavior as the F5V star, while the decay time of the resonance oscillations is less ($\approx$ 20 000 seconds). The left and right panels of Fig. 4.7 show the velocity fluctuations and the corresponding power spectrum and heights $z = 0,\ 780,\ 980$ km, the early stages of the velocity fluctuations (Fig. 4.7 c,e) show high frequency component due to resonance oscillations while the late stages show only the exciting component.

These isothermal atmospheres have also been excited with a *wave spectrum* which has a Gaussian distribution (cut at low frequencies) of the velocity amplitudes of its partial waves, and covers about 17.0 mHz for the F5V star, and 35.0 mHz for the M0V star. The left panels of Figs. 4.8 & 4.9 show the velocity fluctuations at heights $z = 0,\ 980,$ and 1580 km for the F5V star and $z = 0,\ 780,$ and 1180 km for the M0V star, during the time span from 2000 seconds up to 5000 seconds and the right panels show the corresponding power spectra. For the F5V star, resonance oscillations of frequencies $\nu = 4.5$ mHz and $\nu = 5.5$ mHz are clearly seen at heights $z = 980$ km and $z = 1580$ km, respectively (see, Figs. 4.8 d,f), while for the M0V star, oscillation exists around $\nu = 8.5$ at height $z = 780$ km and a less pronounced oscillation around $\nu = 10$ mHz as shown in Figs. 4.9 d,f. Table 4.1 summarizes our results. Hot stars show resonance oscillations with longer periods, which decrease with decreasing the effective temperature. The solar magnetic atmosphere show resonance oscillations with longer period than the non-magnetic atmosphere.

	ν (mHz) - F5V	ν (mHz) - Sun	ν (mHz) - M0V
Non-Magnetic Atmos.			
ν_A	3.46	5.0	8.23
ν_{peak} (mono)	3.5	5.0	8.2
ν_{peak} (spectra)	$4.5 - 5.5$	7.5	$8.5 - 10.0$
Magnetic Atmos.			
ν_{Defouw}	3.50	5.0	8.35
ν_{peak} (mono)		5.0	
ν_{peak} (spectra)		$5.5 - 6.0$	

Table 4.1 Summary of the results of the excitation by small amplitude waves, ν_A and ν_{Defouw} are the analytical acoustic and Defouw cut-off frequencies. ν_{peak} (mono) are the numerically found resonance frequencies and ν_{peak} (spectra) are the peak frequencies found in our wave spectrum calculations.

4.5 Results: Adiabatic Large Amplitude Waves

a. Non-magnetic Solar Plane Parallel Atmosphere

The use of large amplitude waves of higher Mach numbers (e.g., $Mach = 0.0205 - 0.0293$) generates shocks, which may merge together forming long period waves out of the short period waves, around which the atmosphere resonates, the number of shock mergings increases and merging occurs lower in the atmosphere when the input mechanical energy fluxes increase.

We first introduced acoustic wave spectra and then monochromatic waves into the non-magnetic plane parallel solar atmosphere. Figure 4.10 shows the time sequence of the velocity fluctuations at different heights ($z = 0,\ 980,\ 1580$ km) of the atmosphere and the corresponding power spectrum for a non-magnetic plane parallel atmosphere excited by large amplitude waves distributed in a Gaussian form, which is cut at low frequencies (covers about 17.0 mHz). The input mechanical energy flux is $1 \cdot 10^8\ erg\ cm^{-2}s^{-1}$ which corresponds to a Mach number of 0.0293. The velocity fluctuations show steepening with height as a result of the decreasing density gradient (see, Figs. 4.10 a,c,e). The additional growth of the velocity between Fig. 4.10 c and Fig. 4.10 e is minor because the shocks have reached limiting strength. The middle and upper layers of the atmosphere ($z = 980,\ 1580$ km) show oscillations with a frequency of $\nu = 6.5$ in the propagating region of the spectra as shown in Figs. 4.10 d,f, indicating that the whole atmosphere oscillates with the same frequency.

Figure 4.11 shows the results of propagating monochromatic waves of period 60 sec through the same atmosphere, the waves have a Mach number of 0.0293 with an input mechanical energy flux of $1 \cdot 10^8\ erg\ cm^{-2}s^{-1}$. The velocity power spectrum at different heights show only the original exciting wave together with the overtone components (the Fourier components of the sawtooth wave) after the rapid decay of the resonance. The rapid decay of the resonance is explained by Sutmann & Ulmschneider (1995; paper II) on the basis of finding a critical frequency, ν_{cr}, which determines the behavior of the resonance, the excitation by waves with frequencies $\nu < \nu_{cr}$ results in an atmospheric

resonance which decays rapidly with time, while a persistent resonance is found when exciting the atmosphere by waves with $\nu > \nu_{cr}$.

b. Solar Magnetic Atmosphere

A Solar magnetic atmosphere has been excited by a large amplitude wave spectrum of the same characteristics, like the one used with the non-magnetic plane parallel atmosphere. These waves have a Mach number of 0.065, with an input mechanical energy flux of $1 \cdot 10^8$ $erg\ cm^{-2}s^{-1}$. The atmosphere shows oscillation around $\nu = 6.0$ mHz at height $z = 980$ as shown in Fig. 4.12 d, while the velocity power spectrum at height $z = 1580$ (Fig. 4.12 f) shows double peaks with a dominant one around the same frequency. Similar to the non-magnetic atmosphere, the magnetic atmosphere as a whole oscillates with the same period, which is longer than that of the non-magnetic atmosphere.

The excitation of the magnetic atmosphere with monochromatic waves results in the same behavior as the non-magnetic atmosphere, Fig. 4.13 shows the results of propagating monochromatic waves of period 60 sec through the magnetic atmosphere, the waves have Mach number of 0.065, with an input mechanical flux $1 \cdot 10^8$. The resonance component decayed out quickly while the exciting component persists with its overtones (Fig. 4.13 d,f.

c. The F5V and M0V Stars

A non-magnetic plane parallel atmosphere of an F5V star has been excited with a wave spectrum of partial waves follow a Gaussian distribution which is cut at low frequencies, with an input mechanical energy flux of $1 \cdot 10^7$ $erg\ cm^{-2}s^{-1}$ (Mach number of 0.036). Figure 4.14 shows the velocity fluctuations and the corresponding power spectrum at heights $z = 0$ km (Figs. 4.14 a,b), $z = 1580$ km (Figs. 4.14 c,d), and $z = 2580$ km (Figs. 4.14 e,f). The middle and upper layers of the atmosphere show resonance oscillations with frequency $\nu = 5.0$ mHz (see, Figs. 4.14 d,f). The excitation of the non-magnetic plane parallel atmosphere of an M0V star with a wave spectrum of the same configurations, with an input wave energy flux of $1 \cdot 10^8$ $erg\ cm^{-2}s^{-1}$ (Mach number of 0.018) results in resonances around $\nu = 11.0$ mHz as shown in Figs. 4.15 d,f.

On the other hand, the excitation of the magnetic atmosphere of an F5V star with a large amplitude wave spectrum of the same configurations as the non-magnetic case results in resonance oscillations around $\nu = 4.5$ mHz at heights $z = 1580,\ 2080$ km (see, Figs. 4.16 d,f). The positions of the Defouw cut-off frequencies ($\nu_D = 3.50$ mHz for the F5V star, and $\nu_D = 8.35$ mHz for the M0V star) for both stars are shown in the figures as dashed lines. Repeating the same computations for an M0V star, with an input energy flux of $1 \cdot 10^7$ $erg\ cm^{-2}s^{-1}$ (Mach number of 0.013) in form of wave spectra, results in resonances around $\nu = 10.0$ & 11.5 mHz at heights $z = 580,\ 880$ km, respectively, for the magnetic atmosphere. This is shown in Figs. 4.17 d,f. Except the last case of the magnetic atmosphere of the M0V star, the different layers of the non-magnetic and magnetic atmospheres of the Sun, F5V and M0V stars show oscillations with the same frequency upon the excitation with large amplitude wave spectra.

Both magnetic and non-magnetic atmospheres of the three spectral types, show de-

	ν (mHz) - F5V	ν (mHz) - Sun	ν (mHz) - M0V
Non-Magnetic Atmos.			
ν_{peak}(spectra)	5.0	6.5	11.0
Magnetic Atmos.			
ν_{peak}(spectra)	4.5	6.0	10.0

Table 4.2 The same as in Tab. 4.1 but for large amplitude waves.

creasing in the oscillation periods with decreasing the effective temperatures. Magnetic atmospheres always show oscillations with longer periods as shown in Tab. 4.2 (compare with Tab. 4.1).

In summary, the excitation by a small amplitude acoustic wave spectrum shows the following resonances: for the Sun, one has atmospheric resonances around $\nu = 5.0 - 7.5$ mHz for the isothermal non-magnetic plane parallel atmosphere depending on the input wave type (monochromatic or spectra), and around $\nu = 5.5 - 6.0$ mHz for an isothermal magnetic atmosphere. For F5V stars, resonances occurred around $\nu = 4.5 - 5.5$ mHz for the isothermal plane parallel non-magnetic atmosphere, and around $\nu = 8.5 - 10.0$ mHz for M0V stars. The excitation by a large amplitude wave spectrum results in the following resonances: In case of the Sun we found an atmospheric resonances around $\nu = 6.5$ mHz for the plane parallel non-magnetic atmosphere and around $\nu = 6.0$ mHz for the magnetic atmosphere. For F5V stars, resonances were found around $\nu = 5.0$ mHz for the plane parallel non-magnetic atmosphere and $\nu = 4.5$ mHz for the magnetic atmosphere, while for M0V stars resonances were observed around $\nu = 11.0$ mHz for the plane parallel non-magnetic atmosphere and $\nu = 10.0 - 11.5$ mHz for the magnetic atmosphere. The magnetic atmospheres of the Sun and the two late-type stars show resonance oscillations with longer periods in comparison with the plane parallel atmospheres.

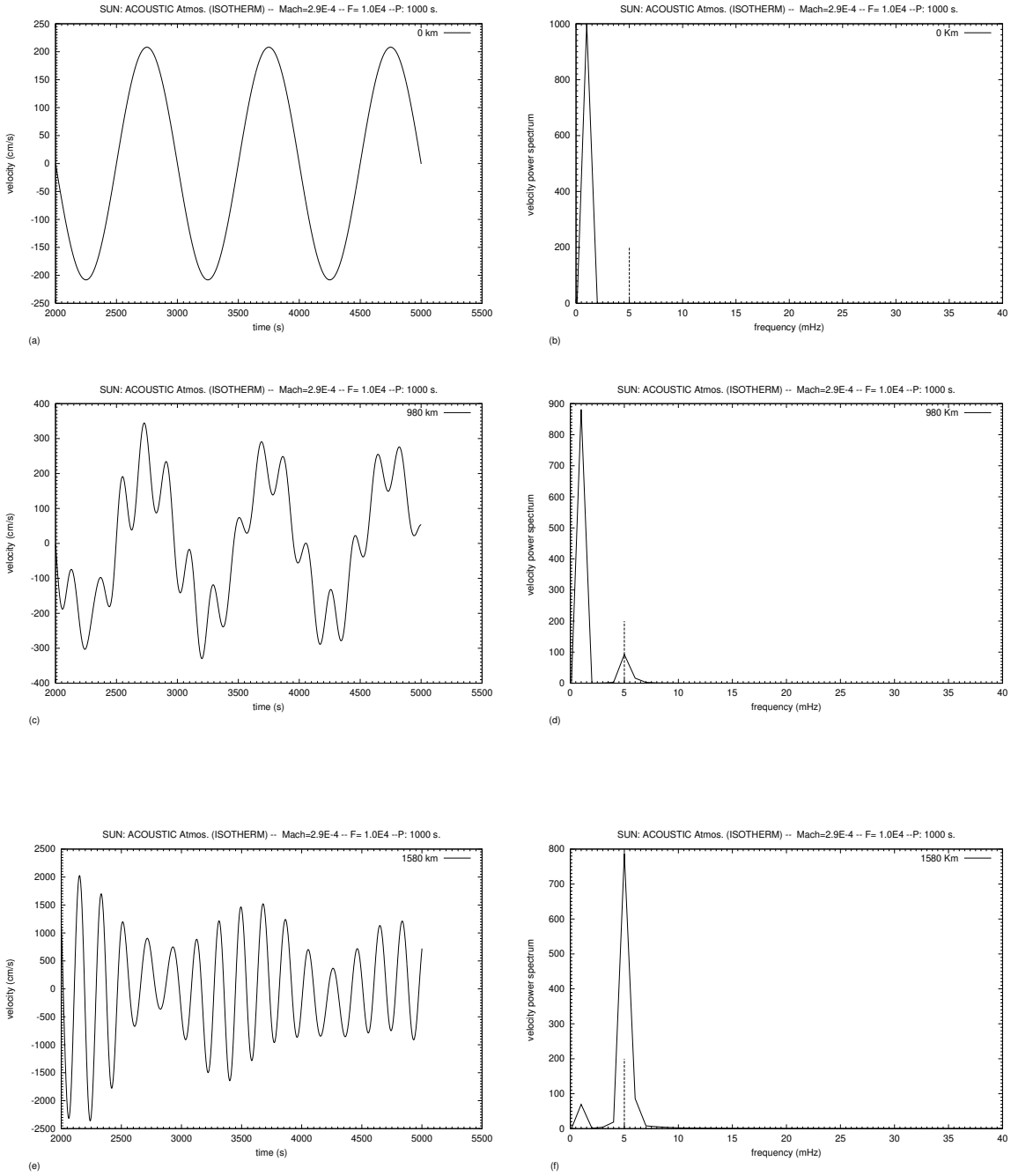

Fig. 4.1 The time sequence of the velocity fluctuations and the corresponding power spectra after the passage of short period of time after exciting an isothermal non-magnetic plane parallel solar atmosphere with monochromatic waves of frequency $\nu = 1.0$ mHz. The dashed line marks the acoustic cut-off frequency.
4.1 a (*top, left*) The time sequence of the velocity fluctuations at height $z = 0$ km.
4.1 b (*top, right*) The corresponding power spectrum at height $z = 0$ km.
4.1 c (*middle, left*) The same as in Fig. 4.1 a, but at height $z = 980$ km.
4.1 d (*middle, right*) The corresponding velocity power spectrum at height $z = 980$ km.
4.1 e (*bottom, left*) The same as in Fig. 4.1 a, but at height $z = 1580$ km.
4.1 f (*bottom, right*) The corresponding velocity power spectrum at height $z = 1580$ km.

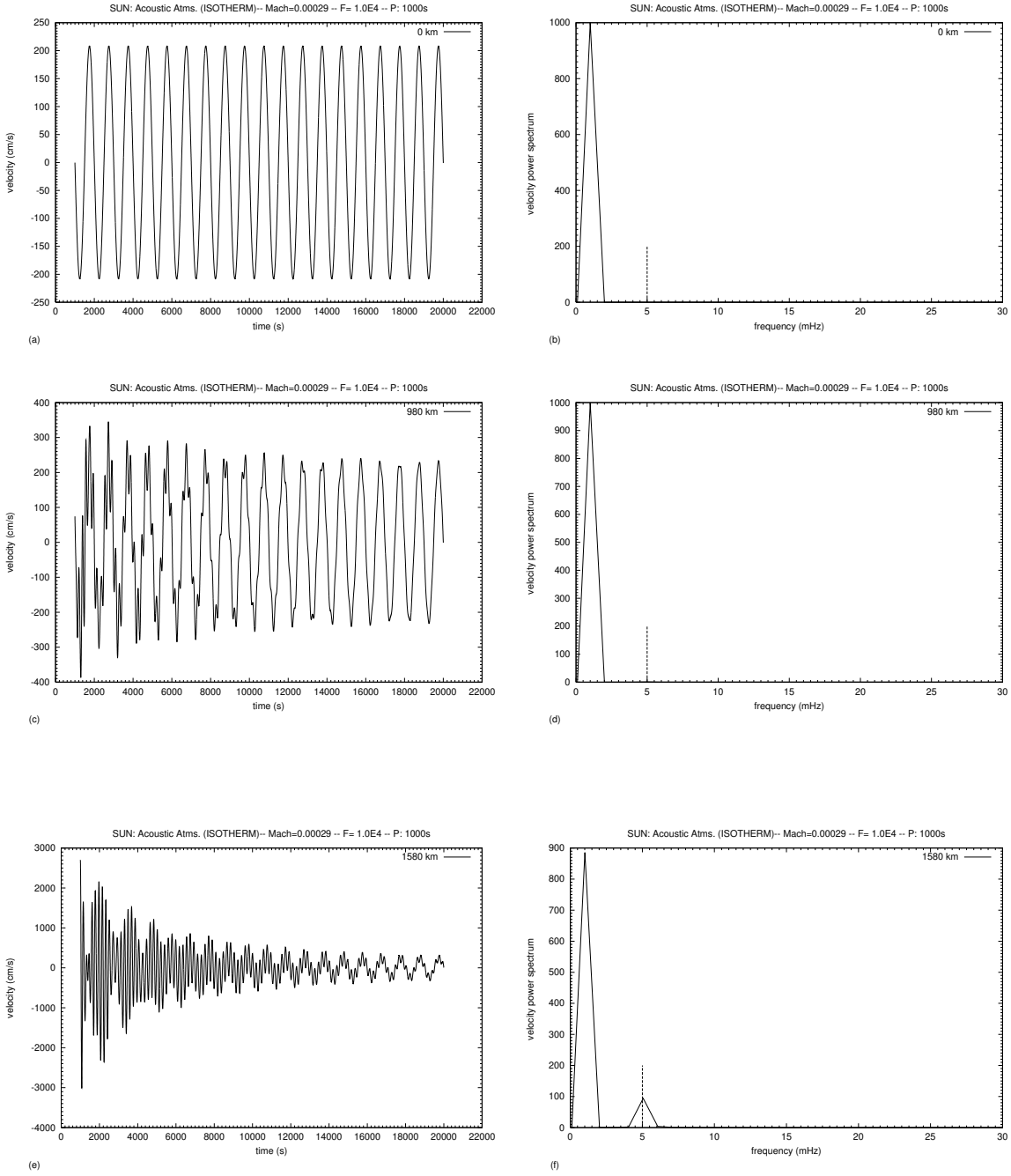

Fig. 4.2 The same computation as in Fig. 4.1, but calculated for a longer time, the velocity fluctuations and the corresponding power spectra at the same heights are monitored to show the decay of the resonance oscillations with time, again the dashed line marks the acoustic cut-off frequency.
4.2 a (*top, left*) The time sequence of the velocity fluctuations at height $z = 0$ km.
4.2 b (*top, right*) The corresponding power spectrum at height $z = 0$ km.
4.2 c (*middle, left*) The same as in Fig. 4.2 a, but at height $z = 980$ km.
4.2 d (*middle, right*) The corresponding velocity power spectrum at height $z = 980$ km.
4.2 e (*bottom, left*) The same as in Fig. 4.2 a, but at height $z = 1580$ km.
4.2 f (*bottom, right*) The corresponding velocity power spectrum at height $z = 1580$ km.

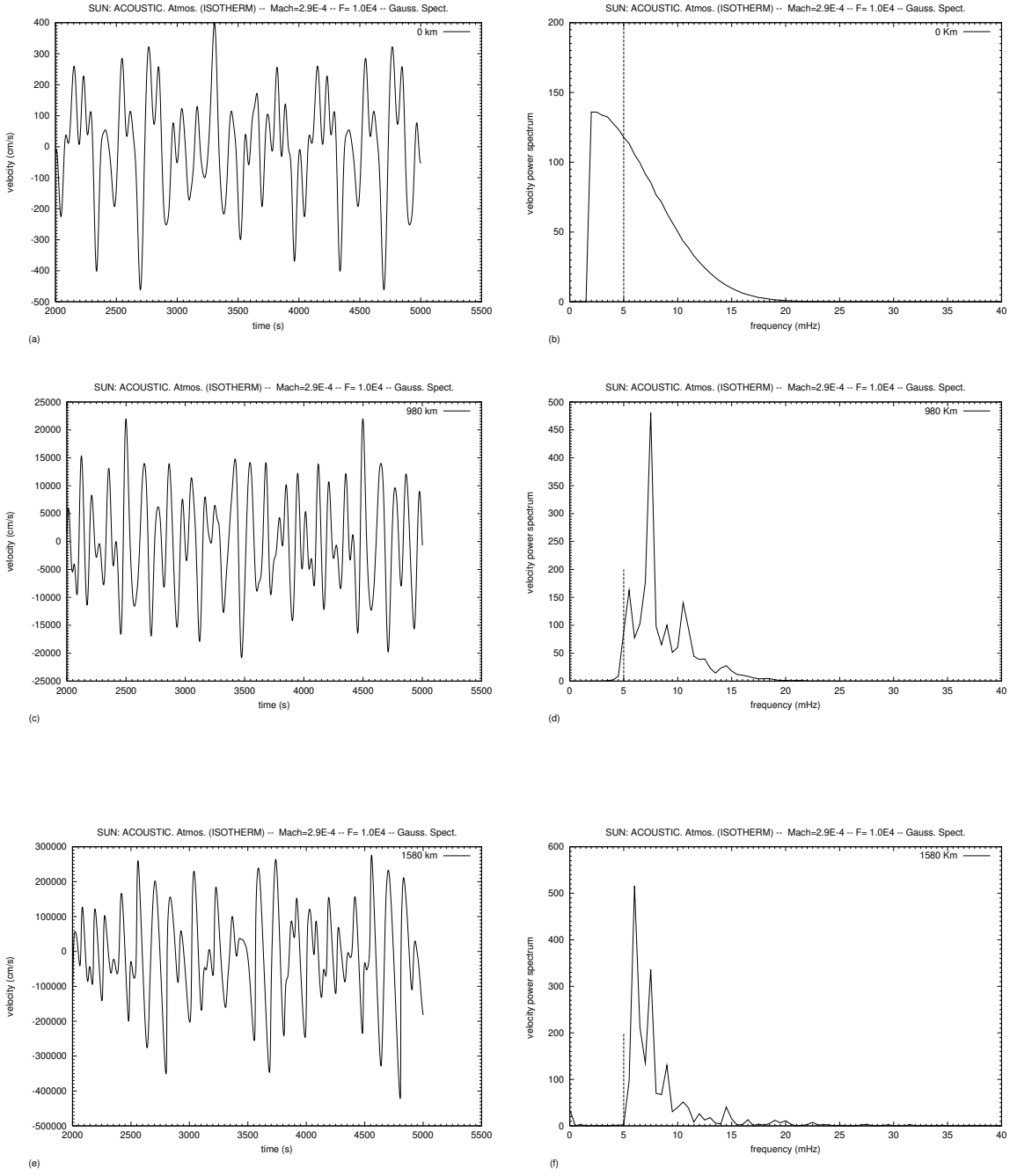

Fig. 4.3 Wave spectra of partial wave amplitudes following a Gaussian distribution which is cut at low frequencies, have been introduced at $z = 0$ km to an isothermal non-magnetic plane parallel solar atmosphere. The dashed line marks the acoustic cut-off frequency.
4.3 a (*top, left*) The time sequence of the velocity fluctuations at height $z = 0$ km.
4.3 b (*top, right*) The corresponding power spectrum at height $z = 0$ km.
4.3 c (*middle, left*) The same as in Fig. 4.3 a, but at height $z = 980$ km.
4.3 d (*middle, right*) The corresponding velocity power spectrum at height $z = 980$ km.
4.3 e (*bottom, left*) The same as in Fig. 4.3 a, but at height $z = 1580$ km.
4.3 f (*bottom, right*) The corresponding velocity power spectrum at height $z = 1580$ km.

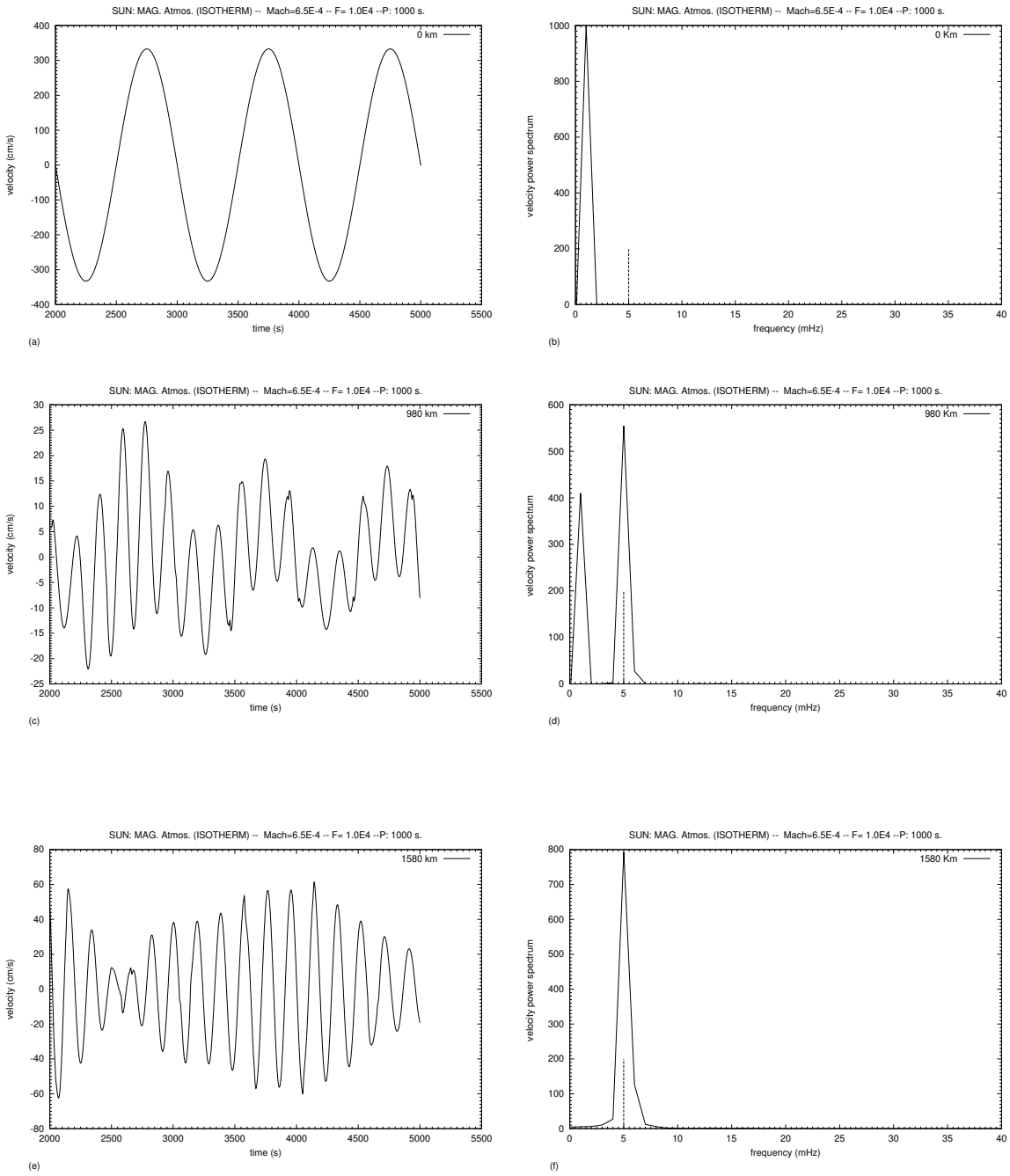

Fig. 4.4 The excitation of an isothermal magnetic solar atmosphere shows the same behavior as the isothermal non-magnetic plane parallel atmosphere. A superposition of two waves, the exciting and the resonance waves are shown. The resonance is around the Defouw cut-off frequency, which is marked by a dashed line.
4.4 a (*top, left*) The time sequence of the velocity fluctuations at height $z = 0$ km.
4.4 b (*top, right*) The corresponding power spectrum at height $z = 0$ km.
4.4 c (*middle, left*) The same as in Fig. 4.4 a, but at height $z = 980$ km.
4.4 d (*middle, right*) The corresponding velocity power spectrum at height $z = 980$ km.
4.4 e (*bottom, left*) The same as in Fig. 4.4 a, but at height $z = 1580$ km.
4.4 f (*bottom, right*) The corresponding velocity power spectrum at height $z = 1580$ km.

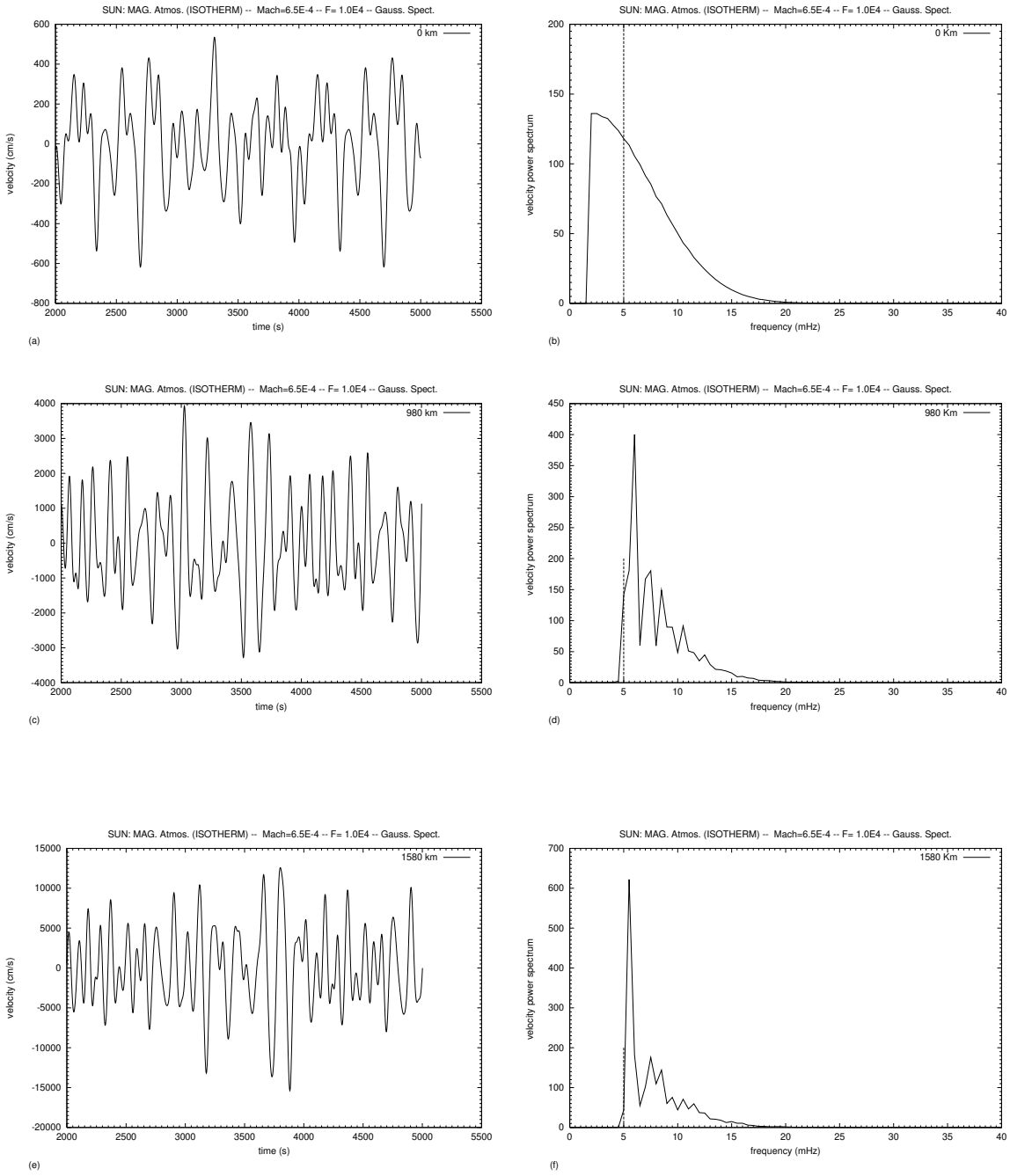

Fig. 4.5 The excitation of an isothermal magnetic solar atmosphere with wave spectra follow a Gaussian distribution which is cut at low frequencies. The dashed line marks the Defouw cut-off frequency.
4.5 a (*top, left*) The time sequence of the velocity fluctuations at height $z = 0$ km.
4.5 b (*top, right*) The corresponding power spectrum at height $z = 0$ km.
4.5 c (*middle, left*) The same as in Fig. 4.5 a, but at height $z = 980$ km.
4.5 d (*middle, right*) The corresponding velocity power spectrum at height $z = 980$ km.
4.5 e (*bottom, left*) The same as in Fig. 4.5 a, but at height $z = 1580$ km.
4.5 f (*bottom, right*) The corresponding velocity power spectrum at height $z = 1580$ km.

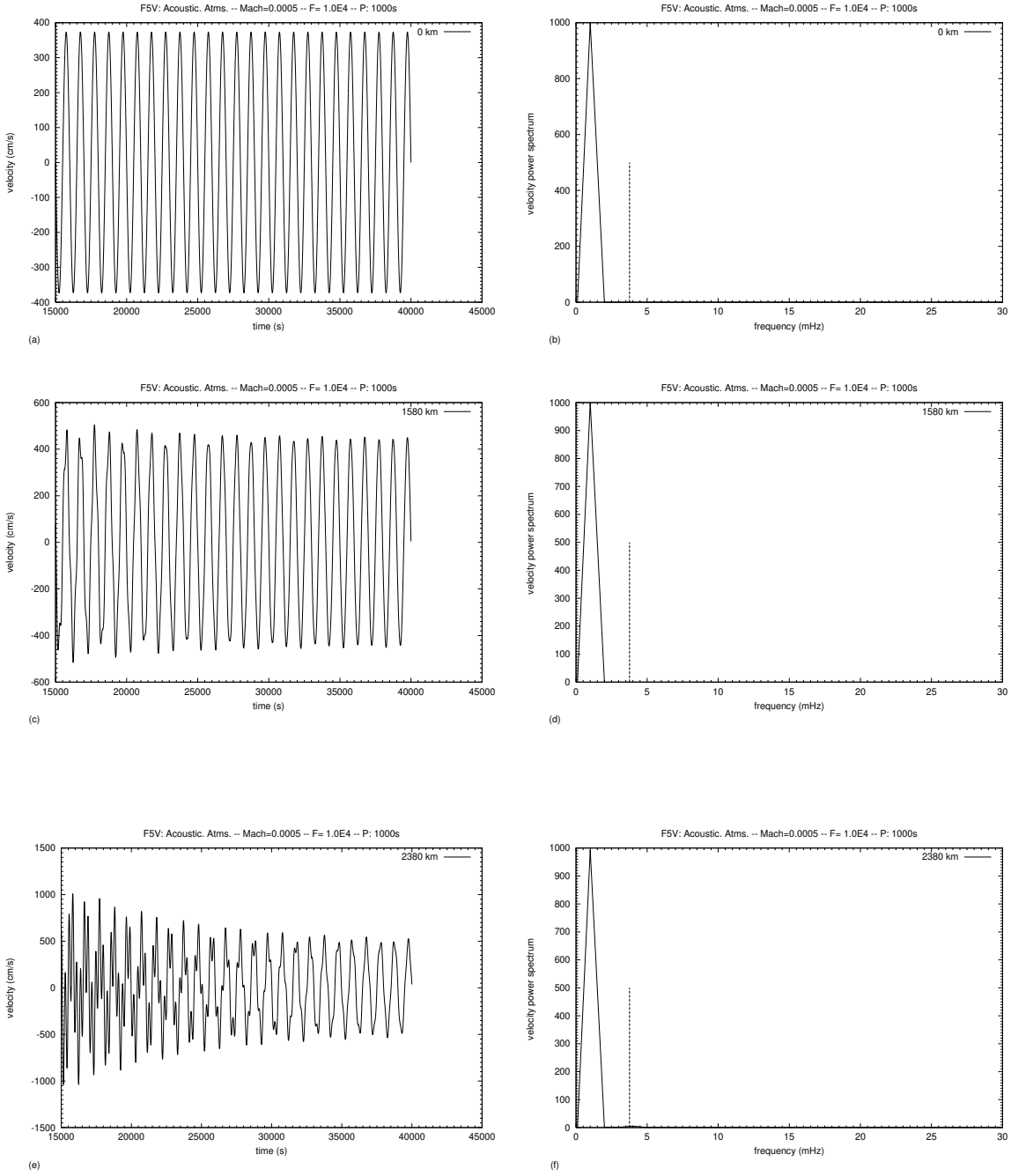

Fig. 4.6 The decay of the resonance component after long time ($\approx 40000\ sec$) for an F5V star, upon the excitation of its isothermal non-magnetic plane parallel atmosphere with monochromatic waves of frequency 1.0 mHz. The dashed line marks the acoustic cut-off frequency.
4.6 a (*top, left*) The time sequence of the velocity fluctuations at height $z = 0$ km.
4.6 b (*top, right*) The corresponding power spectrum at height $z = 0$ km.
4.6 c (*middle, left*) The same as in Fig. 4.6 a, but at height $z = 1580$ km.
4.6 d (*middle, right*) The corresponding velocity power spectrum at height $z = 1580$ km.
4.6 e (*bottom, left*) The same as in Fig. 4.6 a, but at height $z = 2380$ km.
4.6 f (*bottom, right*) The corresponding velocity power spectrum at height $z = 2380$ km.

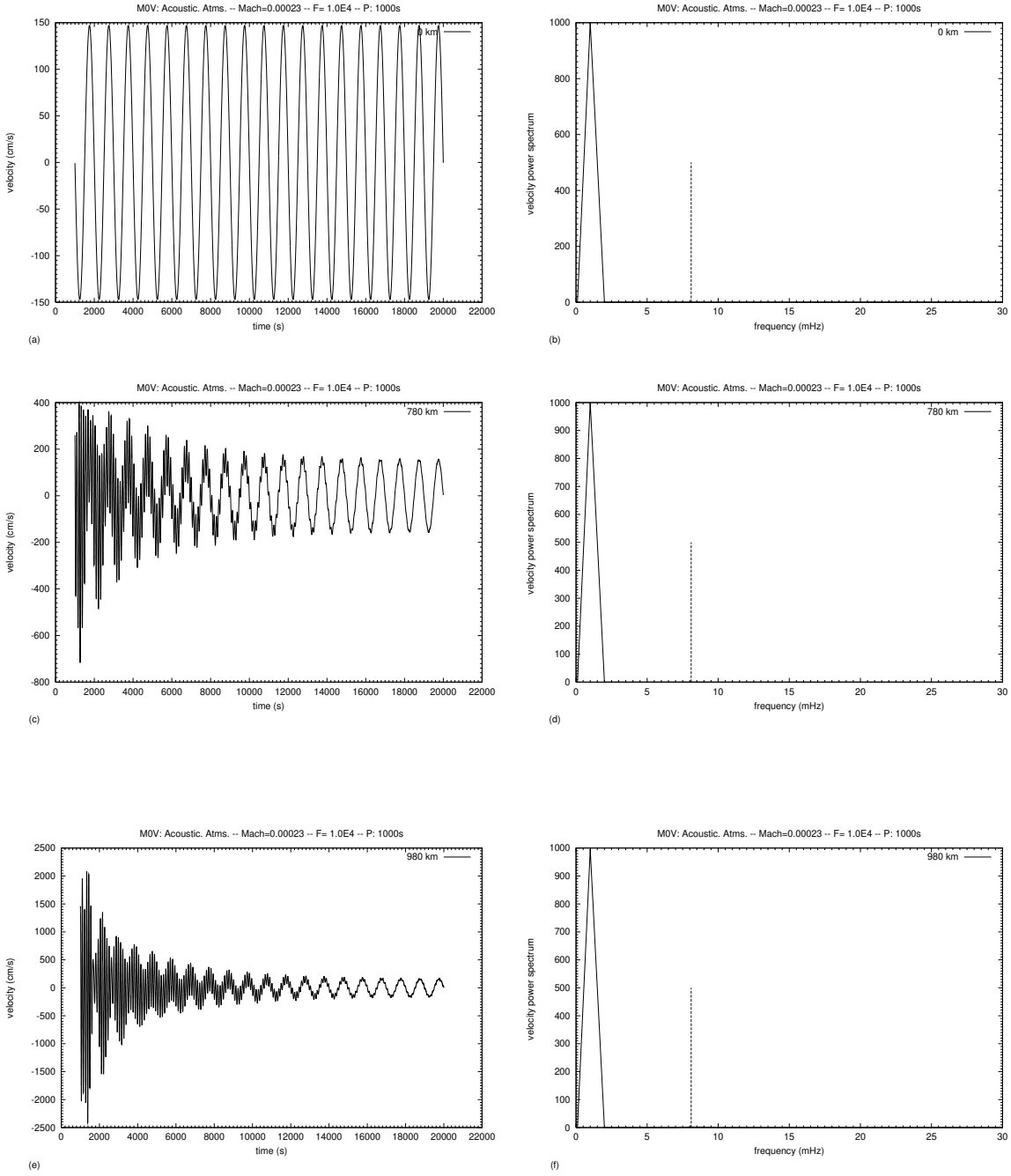

Fig. 4.7 The same as in Fig. 4.6 but for an isothermal non-magnetic plane parallel atmosphere of an M0V star, the atmosphere is excited with a monochromatic waves of frequency 1.0 mHz. The resonance component decays after $\approx 20000 sec$. The dashed line marks the acoustic cut-off frequency.
4.7 a (*top, left*) The time sequence of the velocity fluctuations at height $z = 0$ km.
4.7 b (*top, right*) The corresponding power spectrum at height $z = 0$ km.
4.7 c (*middle, left*) The same as in Fig. 4.7 a, but at height $z = 780$ km.
4.7 d (*middle, right*) The corresponding velocity power spectrum at height $z = 780$ km.
4.7 e (*bottom, left*) The same as in Fig. 4.7 a, but at height $z = 980$ km.
4.7 f (*bottom, right*) The corresponding velocity power spectrum at height $z = 980$ km.

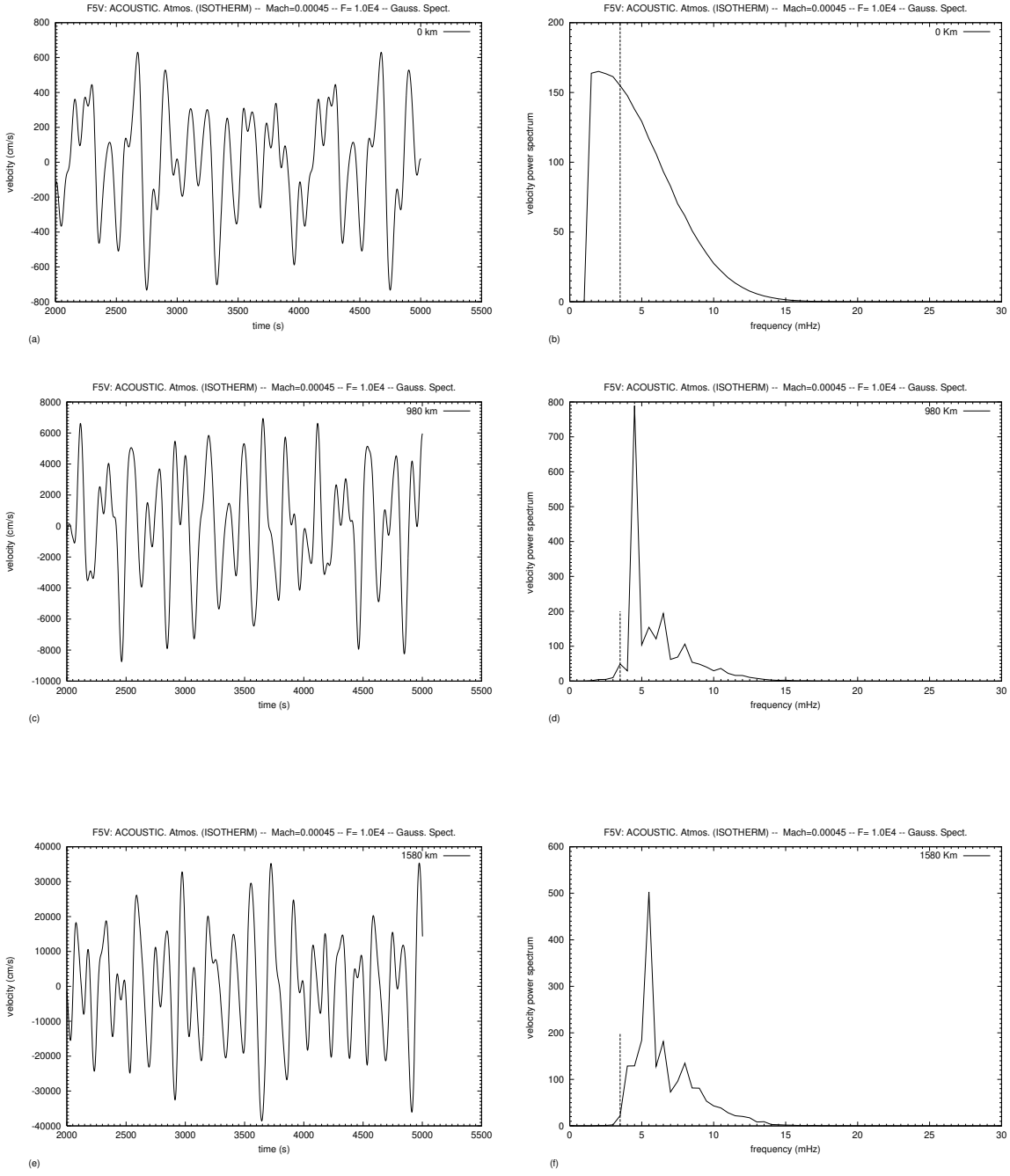

Fig. 4.8 Upon exciting an isothermal non-magnetic plane parallel atmosphere of an F5V star with a Gaussian wave spectra which is cut at low frequencies, the dashed line marks the acoustic cut-off frequency.
4.8 a (*top, left*) The time sequence of the velocity fluctuations at height $z = 0$ km.
4.8 b (*top, right*) The corresponding power spectrum at height $z = 0$ km.
4.8 c (*middle, left*) The same as in Fig. 4.8 a, but at height $z = 980$ km.
4.8 d (*middle, right*) The corresponding velocity power spectrum at height $z = 980$ km.
4.8 e (*bottom, left*) The same as in Fig. 4.8 a, but at height $z = 1580$ km.
4.8 f (*bottom, right*) The corresponding velocity power spectrum at height $z = 1580$ km.

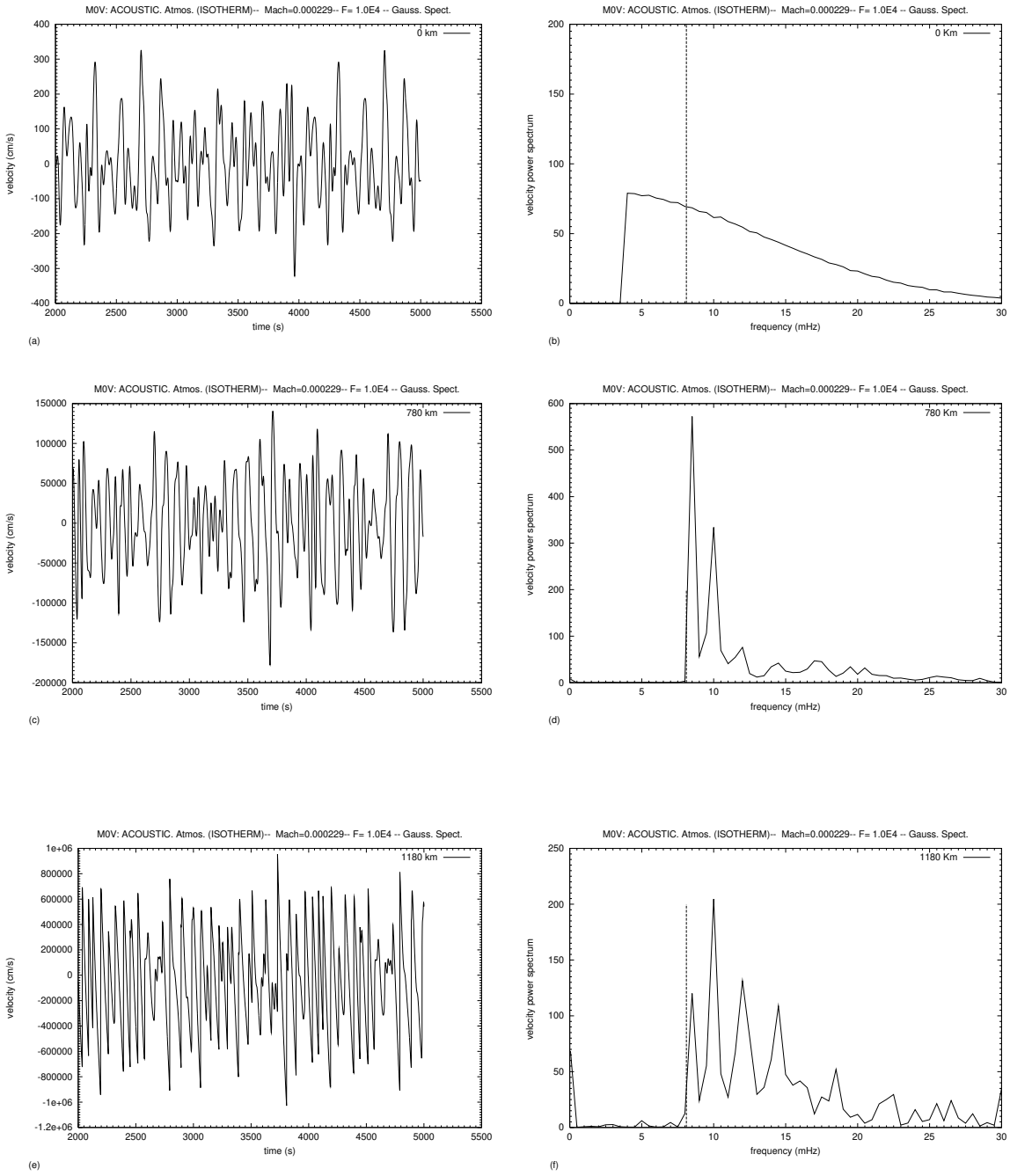

Fig. 4.9 The same as in Fig. 4.8 but for an M0V star, again the dashed line marks the acoustic cut-off frequency.
4.9 a (*top, left*) The time sequence of the velocity fluctuations at height $z = 0$ km.
4.9 b (*top, right*) The corresponding power spectrum at height $z = 0$ km.
4.9 c (*middle, left*) The same as in Fig. 4.9 a, but at height $z = 780$ km.
4.9 d (*middle, right*) The corresponding velocity power spectrum at height $z = 780$ km.
4.9 e (*bottom, left*) The same as in Fig. 4.9 a, but at height $z = 1180$ km.
4.9 f (*bottom, right*) The corresponding velocity power spectrum at height $z = 1180$ km.

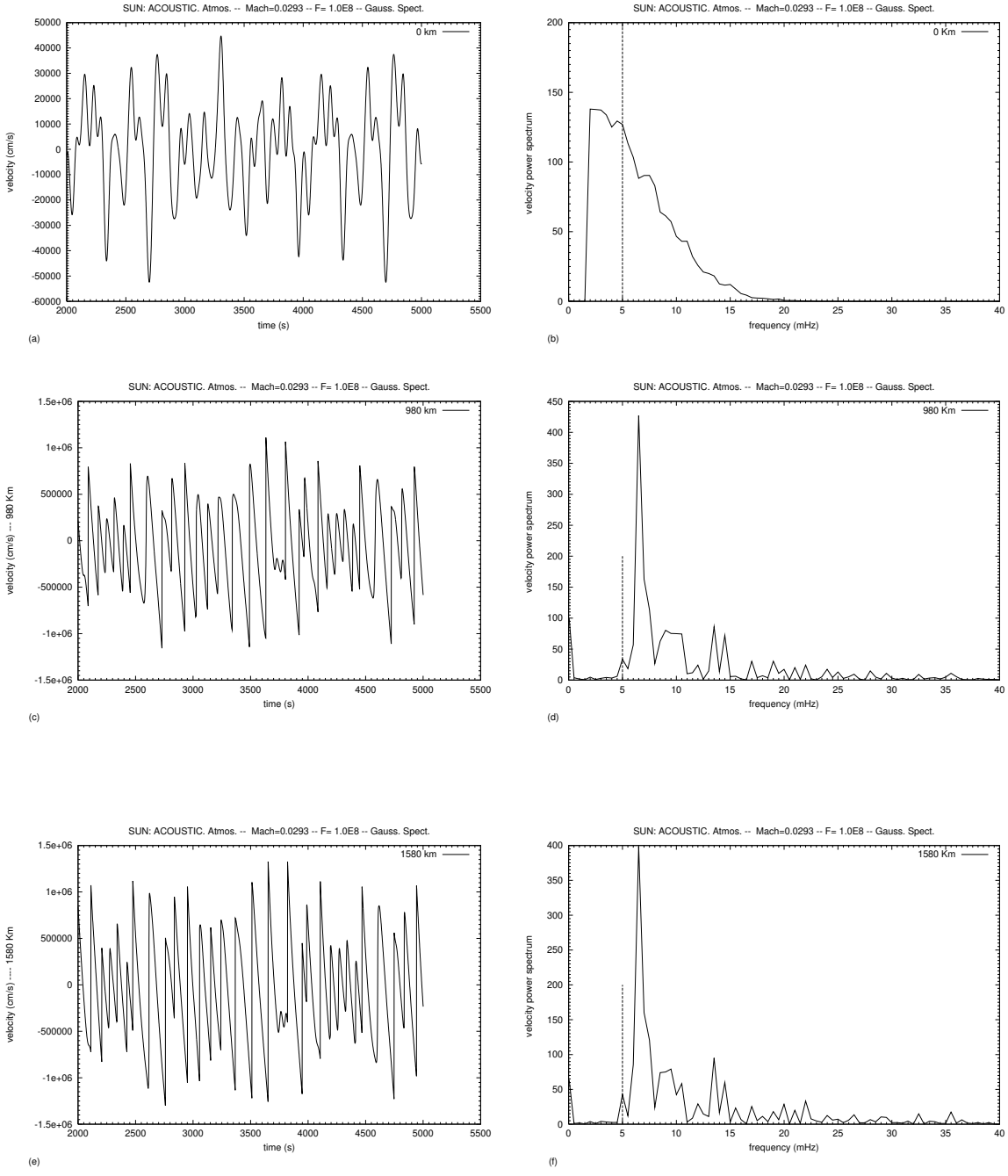

Fig. 4.10 The excitation of a stratified plane parallel non-magnetic solar atmosphere with large amplitude wave spectra follow a Gaussian distribution which is cut at low frequencies. The dashed line marks the acoustic cut-off frequency.
4.10 a (*top, left*) The time sequence of the velocity fluctuations at height $z = 0$ km.
4.10 b (*top, right*) The corresponding power spectrum at height $z = 0$ km.
4.10 c (*middle, left*) The same as in Fig. 4.10 a, but at height $z = 980$ km.
4.10 d (*middle, right*) The corresponding velocity power spectrum at height $z = 980$ km.
4.10 e (*bottom, left*) The same as in Fig. 4.10 a, but at height $z = 1580$ km.
4.10 f (*bottom, right*) The corresponding velocity power spectrum at height $z = 1580$ km.

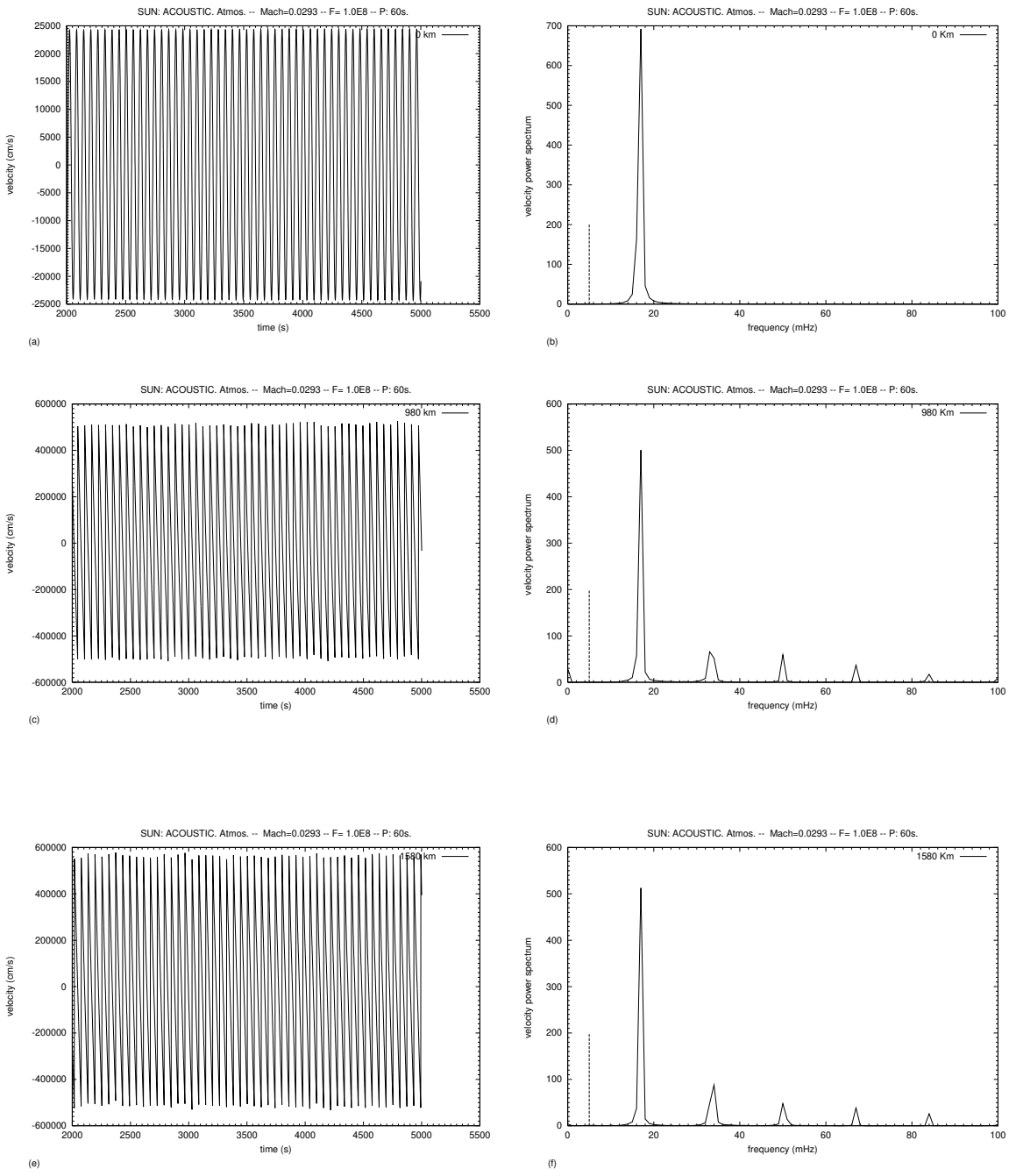

Fig. 4.11 The excitation of a stratified plane parallel non-magnetic solar atmosphere with monochromatic waves of period 60 sec ($\nu = 16.7$ mHz). The dashed line marks the acoustic cut-off frequency.
4.11 a (*top, left*) The time sequence of the velocity fluctuations at height $z = 0$ km.
4.11 b (*top, right*) The corresponding power spectrum at height $z = 0$ km.
4.11 c (*middle, left*) The same as in Fig. 4.11 a, but at height $z = 980$ km.
4.11 d (*middle, right*) The corresponding velocity power spectrum at height $z = 980$ km.
4.11 e (*bottom, left*) The same as in Fig. 4.11 a, but at height $z = 1580$ km.
4.11 f (*bottom, right*) The corresponding velocity power spectrum at height $z = 1580$ km.

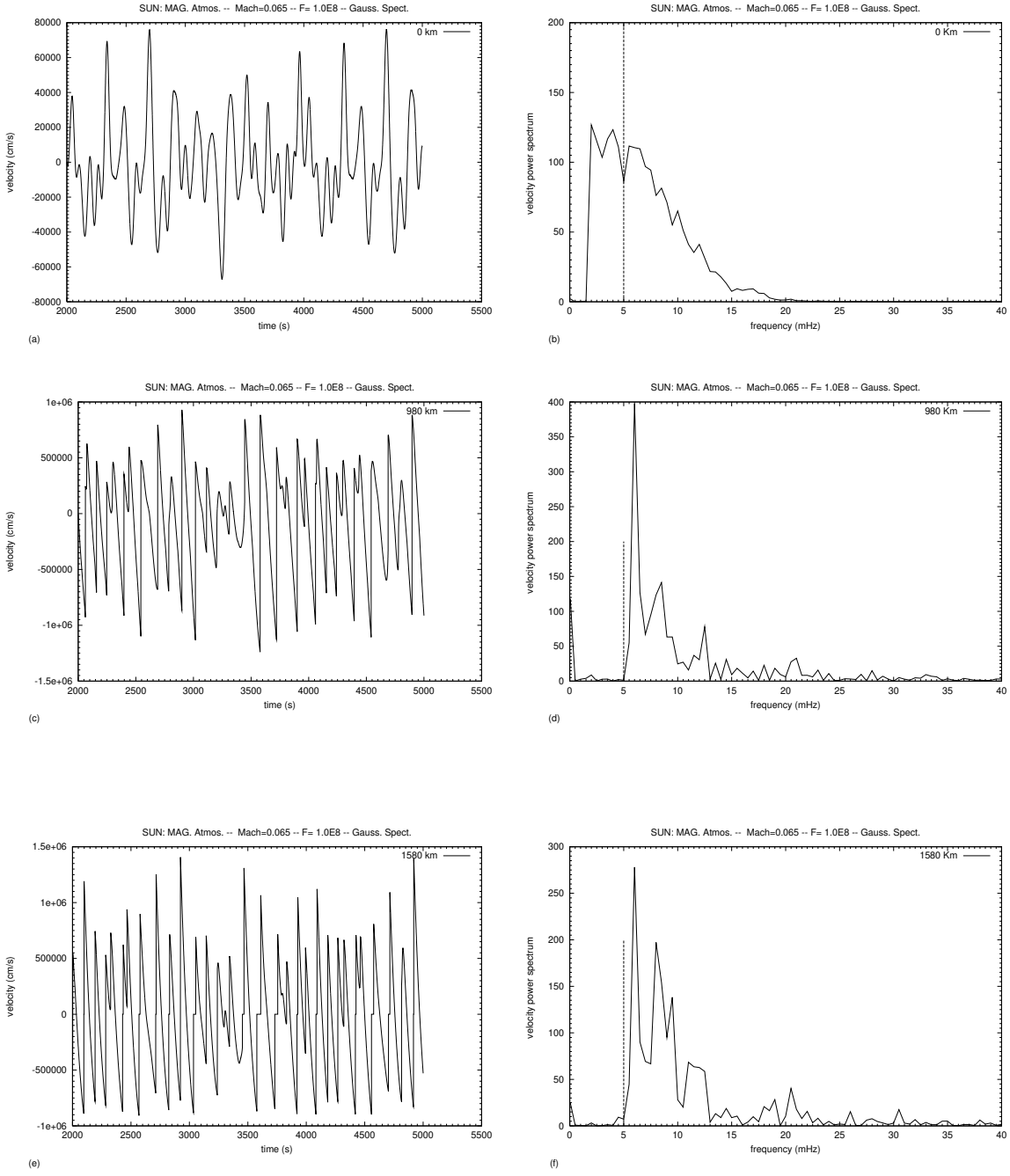

Fig. 4.12 The velocity fluctuations and their power spectrum at different heights due to the excitation of a stratified magnetic solar atmosphere using a Gaussian wave spectra which is cut at low frequencies. The dashed line marks the Defouw cut-off frequency.
4.12 a (*top, left*) The time sequence of the velocity fluctuations at height $z = 0$ km.
4.12 b (*top, right*) The corresponding power spectrum at height $z = 0$ km.
4.12 c (*middle, left*) The same as in Fig. 4.12 a, but at height $z = 980$ km.
4.12 d (*middle, right*) The corresponding velocity power spectrum at height $z = 980$ km.
4.12 e (*bottom, left*) The same as in Fig. 4.12 a, but at height $z = 1580$ km.
4.12 f (*bottom, right*) The corresponding velocity power spectrum at height $z = 1580$ km.

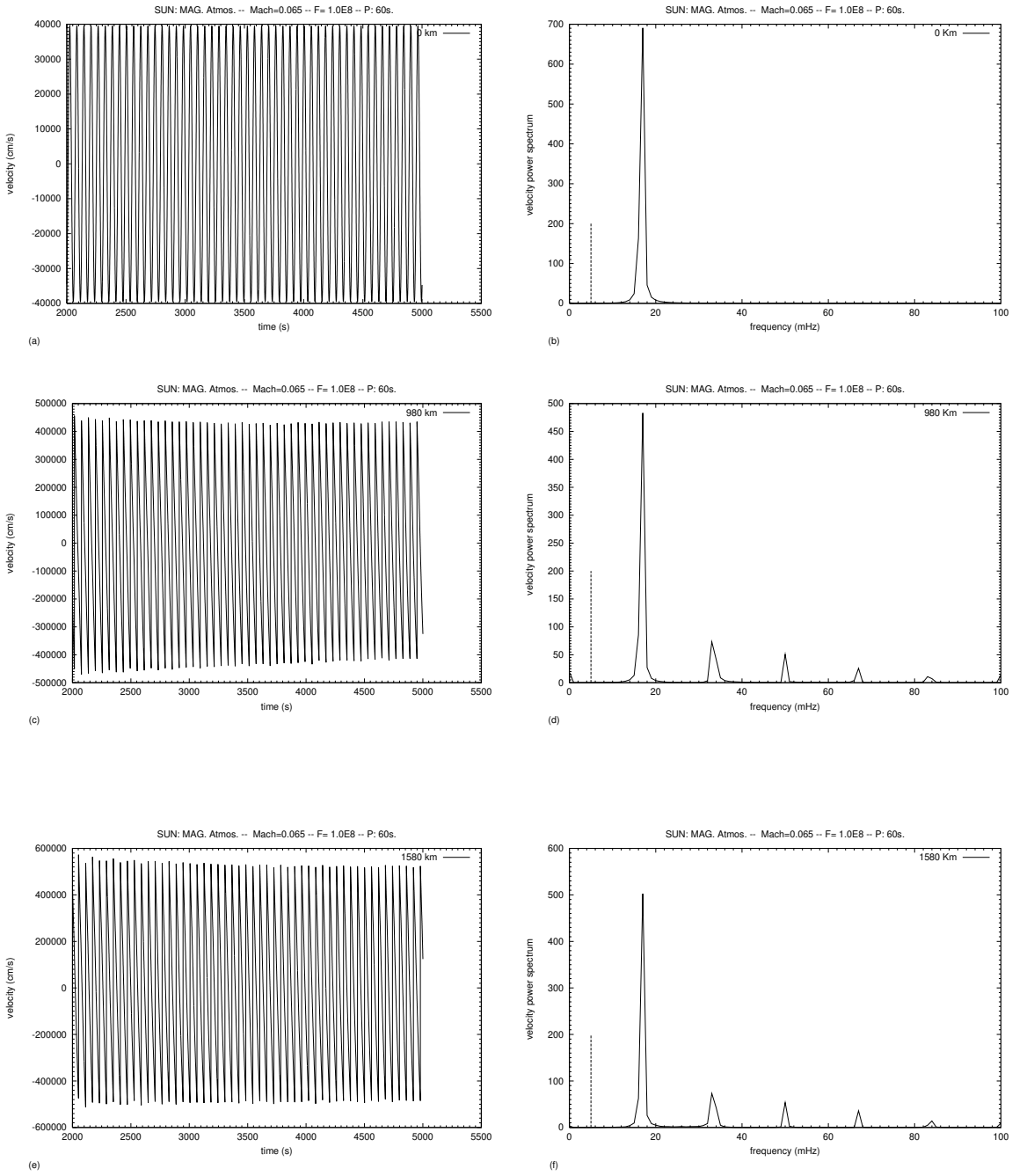

Fig. 4.13 The same as in Fig. 4.11, but for a stratified magnetic solar atmosphere, the dashed line marks the Defouw cut-off frequency.
4.13 a (*top, left*) The time sequence of the velocity fluctuations at height $z = 0$ km.
4.13 b (*top, right*) The corresponding power spectrum at height $z = 0$ km.
4.13 c (*middle, left*) The same as in Fig. 4.13 a, but at height $z = 980$ km.
4.13 d (*middle, right*) The corresponding velocity power spectrum at height $z = 980$ km.
4.13 e (*bottom, left*) The same as in Fig. 4.13 a, but at height $z = 1580$ km.
4.13 f (*bottom, right*) The corresponding velocity power spectrum at height $z = 1580$ km.

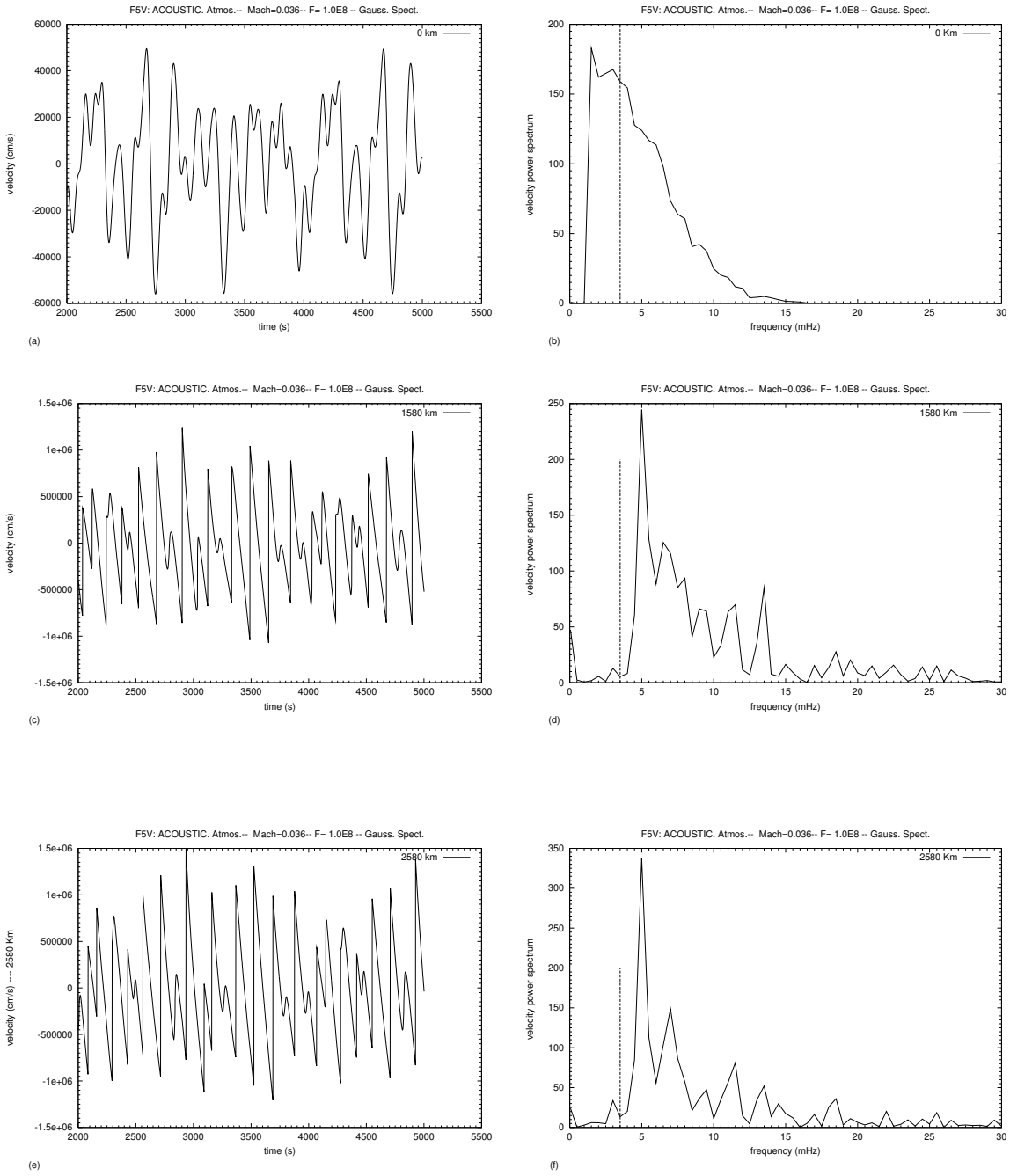

Fig. 4.14 The same as in Fig 4.10 but for an F5V star, again the dashed line marks the acoustic cut-off frequency.
4.14 a (*top, left*) The time sequence of the velocity fluctuations at height $z = 0$ km.
4.14 b (*top, right*) The corresponding power spectrum at height $z = 0$ km.
4.14 c (*middle, left*) The same as in Fig. 4.14 a, but at height $z = 1580$ km.
4.14 d (*middle, right*) The corresponding velocity power spectrum at height $z = 1580$ km.
4.14 e (*bottom, left*) The same as in Fig. 4.14 a, but at height $z = 2580$ km.
4.14 f (*bottom, right*) The corresponding velocity power spectrum at height $z = 2580$ km.

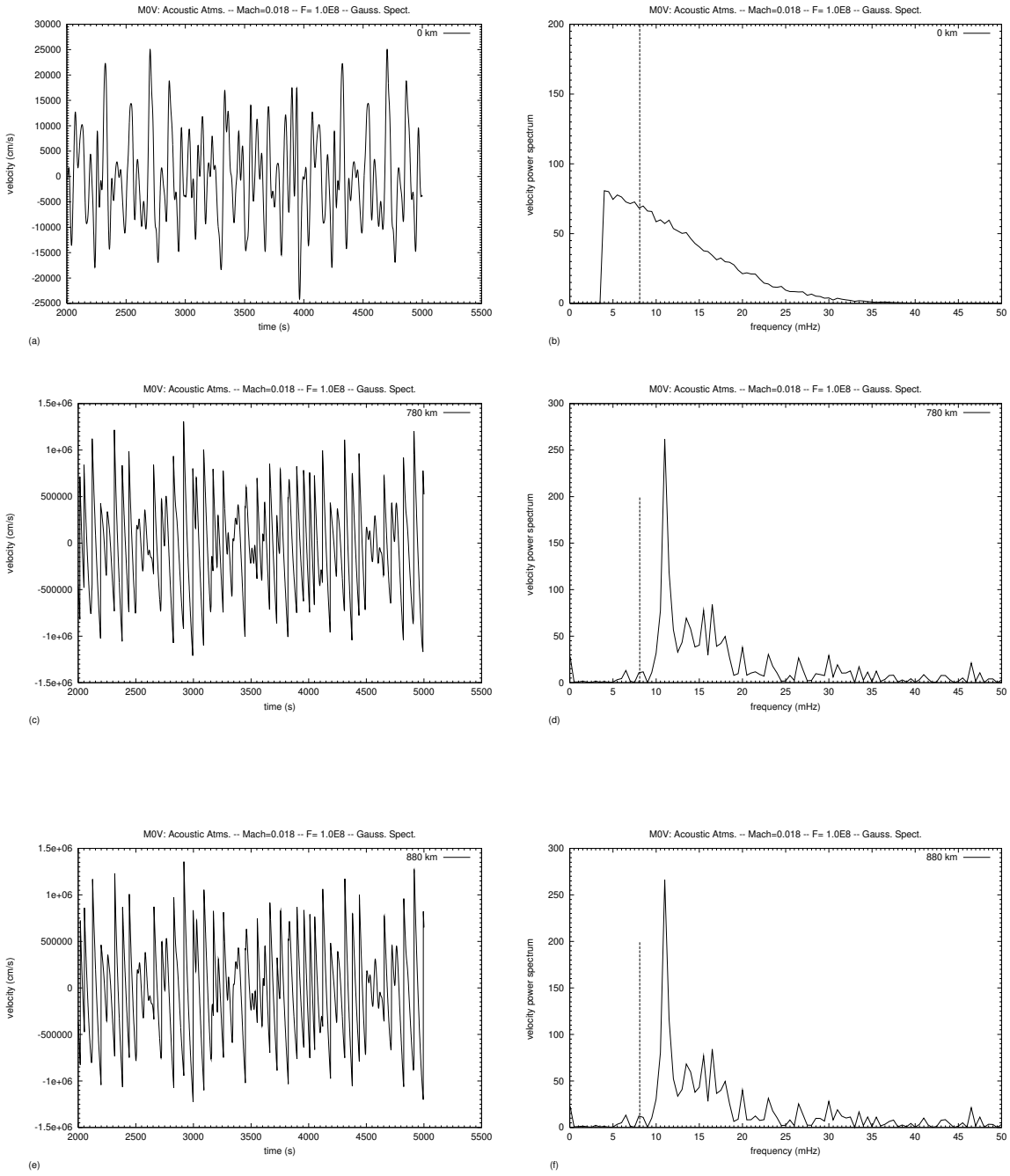

Fig. 4.15 The same as in Fig 4.14 but for an M0V star, and the dashed line marks the acoustic cut-off frequency.
4.15 a (*top, left*) The time sequence of the velocity fluctuations at height $z = 0$ km.
4.15 b (*top, right*) The corresponding power spectrum at height $z = 0$ km.
4.15 c (*middle, left*) The same as in Fig. 4.15 a, but at height $z = 780$ km.
4.15 d (*middle, right*) The corresponding velocity power spectrum at height $z = 780$ km.
4.15 e (*bottom, left*) The same as in Fig. 4.15 a, but at height $z = 880$ km.
4.15 f (*bottom, right*) The corresponding velocity power spectrum at height $z = 880$ km.

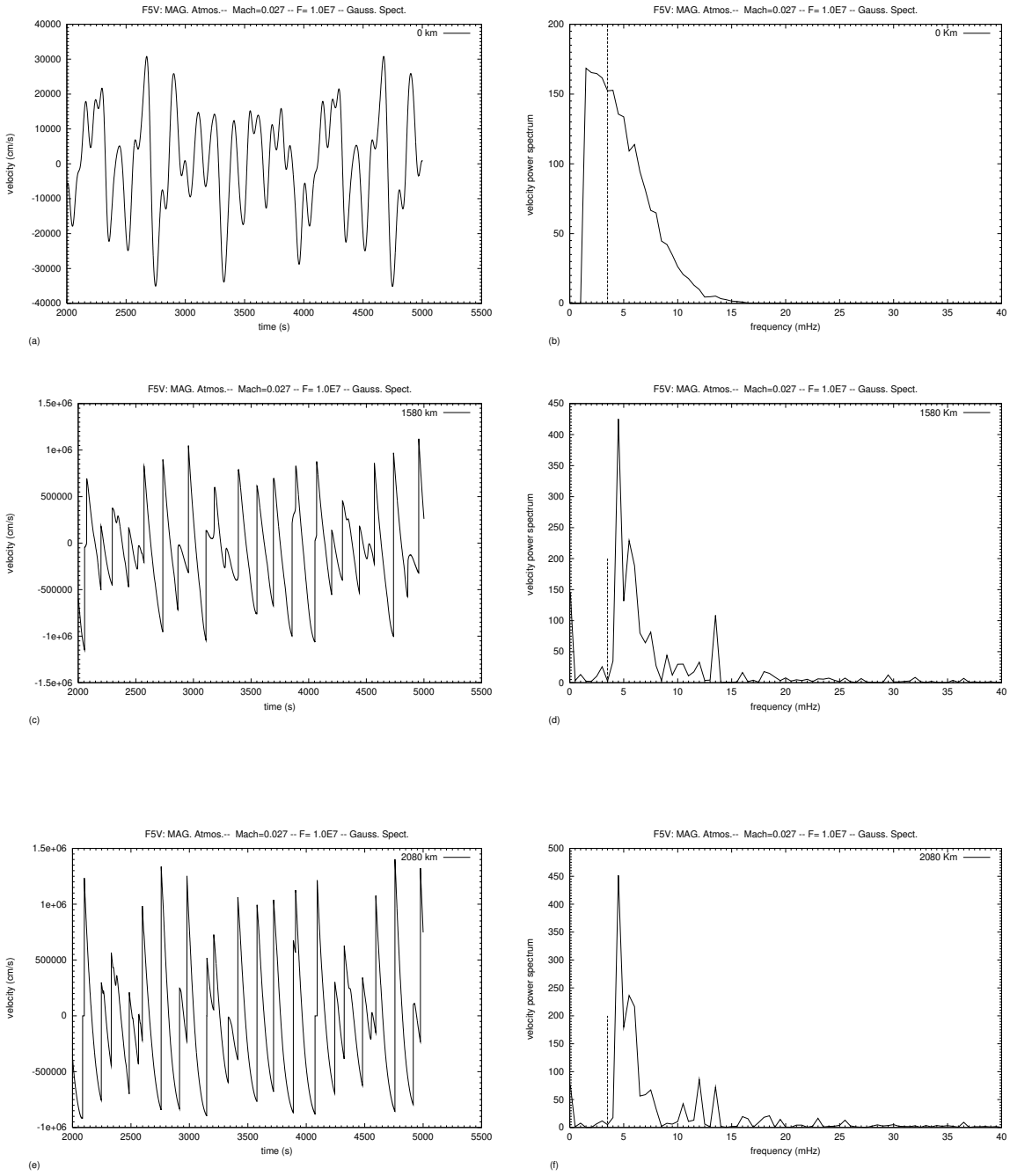

Fig. 4.16 The same as in Fig. 4.14 but for a magnetic atmosphere. The dashed line marks the Defouw cut-off frequency.
4.16 a (*top, left*) The time sequence of the velocity fluctuations at height $z = 0$ km.
4.16 b (*top, right*) The corresponding power spectrum at height $z = 0$ km.
4.16 c (*middle, left*) The same as in Fig. 4.16 a, but at height $z = 1580$ km.
4.16 d (*middle, right*) The corresponding velocity power spectrum at height $z = 1580$ km.
4.16 e (*bottom, left*) The same as in Fig. 4.16 a, but at height $z = 2080$ km.
4.16 f (*bottom, right*) The corresponding velocity power spectrum at height $z = 2080$ km.

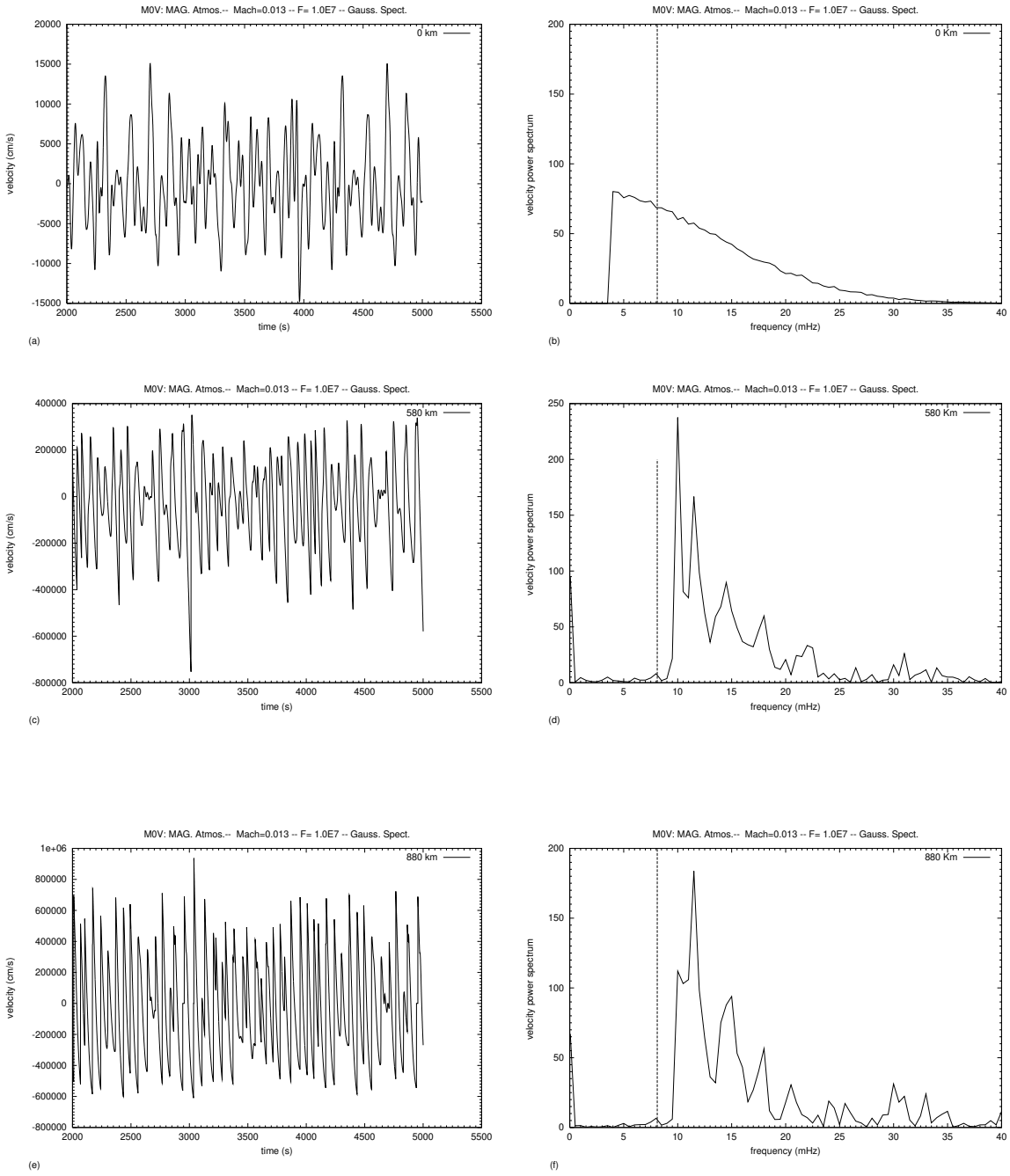

Fig. 4.17 The same as in Fig. 4.16 but for an M0V star. The dashed line marks the Defouw cut-off frequency.
4.17 a (*top, left*) The time sequence of the velocity fluctuations at height $z = 0$ km.
4.17 b (*top, right*) The corresponding power spectrum at height $z = 0$ km.
4.17 c (*middle, left*) The same as in Fig. 4.17 a, but at height $z = 580$ km.
4.17 d (*middle, right*) The corresponding velocity power spectrum at height $z = 580$ km.
4.17 e (*bottom, left*) The same as in Fig. 4.17 a, but at height $z = 880$ km.
4.17 f (*bottom, right*) The corresponding velocity power spectrum at height $z = 880$ km.

Chapter 5

Stellar Chromospheric Models

Summary. In this chapter, we calculate time-dependent models of magnetically heated chromospheres for late-type stars of spectral types between F5V and M0V. The main source of heating is the dissipation of monochromatic longitudinal tube waves by forming shocks. We present here models for stars with surface magnetic filling factor $f_0 = 10\%$, while models with different values of f_0 is studied and presented in Chapter 6.

5.1 Introduction

The question whether the Sun has a classical chromosphere with a monotonic outward temperature rise has been addressed by Kalkofen, Ulmschneider and Avrett (1999) as a response to the results of Carlsson and Stein (1995). Carlsson and Stein found in their simulation a decreasing time-averaged temperature with height, which disputes the existence of a full-time outward temperature rise and therefore implies the formation of absorption lines. Kalkofen et al. found that this simulation ignores most of the input mechanical energy, and that Carlsson and Stein used only 1% of the energy generated in the convection zone in form of acoustic waves of short periods ($P < 100s$). Kalkofen et al. also concluded that the observed UV emission from the solar chromosphere requires an outward temperature rise, in addition, Kalkofen et al. identified the dissipation of short period acoustic waves as the mechanism by which the non-magnetic chromosphere is heated. Recent observations taken by SUMMER instrument on board SOHO satellite in the UV region do not show any indication for the presence of absorption lines, which contradicts the results of Carlsson and Stein.

The chromospheres of late-type stars are believed to be composed of magnetic and non-magnetic components. It is widely accepted that, the non-magnetic regions are heated by the dissipation of acoustic waves, while the magnetic regions are heated by the dissipation of magnetic tube wave. Time-dependent models of acoustically heated chromospheres for main-sequence stars were calculated by Buchholz et al. (1998). Their calculations are based on monochromatic acoustic waves, and employing scaled Mg II k and H $Ly\alpha$ losses as total chromospheric line losses.

We study here the properties of time-dependent models for the magnetic component of the chromosphere, without considering the non-magnetic component. In Chapter 6, more

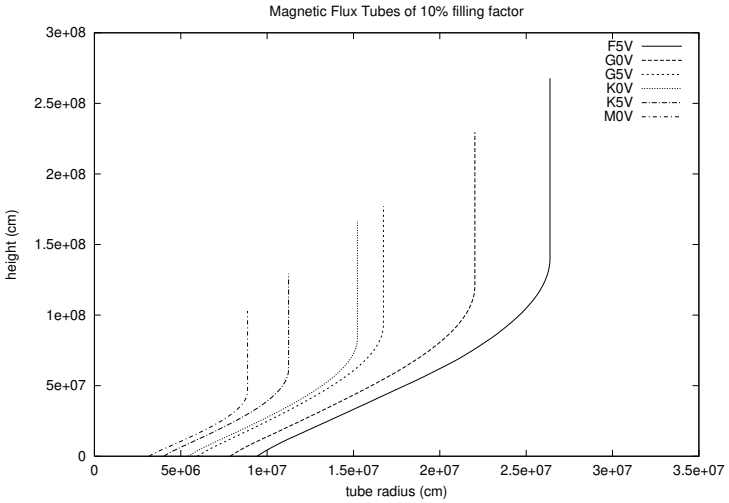

Fig. 5.1 Magnetic flux tube models for stars of different spectral types, and for the case of a magnetic filling factor $f_0 = 10\%$.

realistic two-component models consisting of both magnetic and non-magnetic regions are constructed and their properties are studied. We also discuss here, chromospheric models for an arbitrary magnetic filling factor $f_0 = 10\%$, while the effect of varying f_0 on the emitted flux is discussed in a later chapter.

5.2 Initial Models

The basic parameters required for constructing a flux tube model atmosphere of certain surface magnetic filling factor f_0 are, the effective temperature T_{eff}, the surface gravity g, the magnetic field strength B_0 at the base of the tube, and the bottom radius of the tube r_0. As discussed in Chapter 2, the value of B_0 is computed assuming an equipartition between the thermal and magnetic energy densities, therefore $B_0 = 0.85\%\ B_{eq}$ (see Chapter 2) is considered in the current computations. The bottom radius is assumed to be half the local pressure scale height, $r_0 = 1/2H_p$, with $H_p = \Re T_{eff}/\mu g$ being the local pressure scale height at $z = 0$ km height.

In the current computations, we follow the same procedure described in Chapter 2 for constructing initially non-heated model atmospheres which are in hydrostatic and radiative equilibrium, with the specification of the above parameters and for different arbitrary values of the filling factor f_0 ($f_0 = 1\%,\ 5\%,\ 10\%, ...,\ 50\%$).

The magnetic filling factor together with the geometrical distribution of the tubes determine the tube geometry and the top radius of the tube. Under the assumption of uniformally distributed flux tubes on the stellar surfaces, the top radius r_{max} of the flux tube can be computed from $r_{max} = 0.5\ r_0 \sqrt{\pi/f_0}$, where r_0 is the tube radius at the photospheric level ($z = 0$ km). Figure 5.1 shows the height dependence of the constructed flux tube models of late-type stars for the case of $f_0 = 10\%$. The initial temperatures vs. height are shown in Fig. 5.2 which show a continuous decrease in outward direction.

The input mechanical energy fluxes (in form of longitudinal tube waves) are taken

from the previous computations in Chapter 2 (Tab. 2.3). The monochromatic wave period of the maximum of the velocity power spectrum of the generated waves is used in our models (see, section 2.5-d). The computation uses the piston velocity given by Eq. (3.14). Table. 5.1 lists the stellar parameters and the initial values used in our models, the first column displays the spectral type, the second shows the effective temperature T_{eff} (K), followed by the logarithm of the surface gravity g ($cm\ s^{-2}$), the intrinsic color index $(B-V)$, the magnetic field strength B_0 (G), the bottom radius of the tube r_0 (km), the longitudinal tube wave energy flux F_{LTW} ($erg\ cm^{-2}\ s^{-1}$), and the monochromatic wave period P_M (sec). The constructed models extend up to about 21 pressure scale heights H_p with a total number of $N = 240$ gridpoints.

Star	T_{eff}	$\log g$	B-V	B_0	r_0	F_{LTW}	P_M
F5 V	6 440	4.34	0.44	1407	94	$5.7 \cdot 10^8$	85
G0 V	6 030	4.39	0.58	1574	79	$4.4 \cdot 10^8$	75
G5 V	5 780	4.44	0.68	1741	60	$2.8 \cdot 10^8$	63
K0 V	5 770	4.49	0.68	1846	54	$1.9 \cdot 10^8$	58
K5 V	5 250	4.49	0.81	2370	40	$5.5 \cdot 10^7$	54
M0 V	3 850	4.59	1.40	3258	32	$5.0 \cdot 10^6$	50

Table 5.1 The initial parameters used for constructing magnetic model atmospheres for late-type stars, F_{LTW} is the input mechanical energy flux in form of longitudinal tube wave energy (in $erg\ cm^{-2}\ sec^{-1}$), P_M is the monochromatic wave period (in sec) corresponds to the maximum velocity power spectrum of the generated waves. B_0 (in Gauss) and r_0 (in km) are the magnetic field strength at the base of the tube and the bottom radius of the tube, respectively.

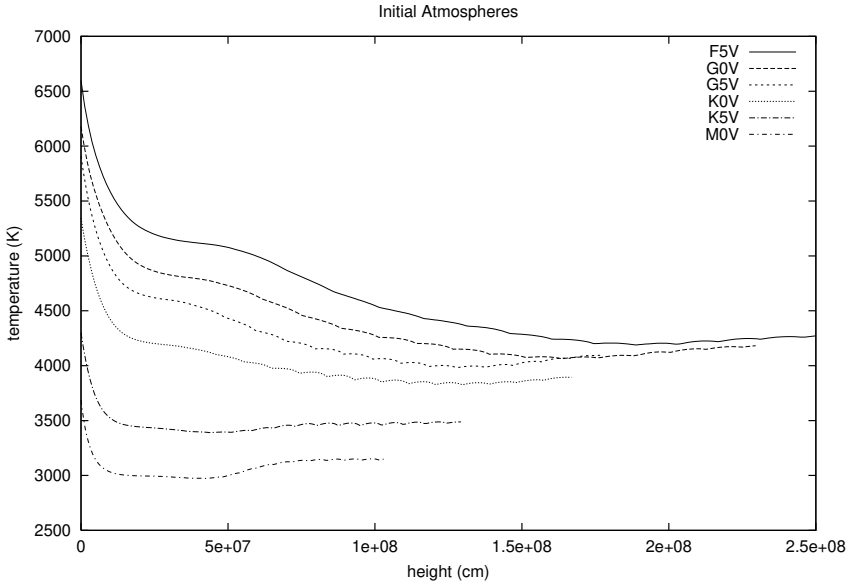

Fig. 5.2 Initial values of the temperature vs. height of the main sequence stars with surface magnetic filling factor $f_0 = 10\%$.

The magnetic field strength B_0 increases with increasing $B-V$, the reason for that is the increase of the density with decreasing effective temperature. The temperature

variation with height for the constructed flux tube models of stars of different spectral types assuming a magnetic filling factor of 10% is shown in Fig. 5.2.

5.3 Time Dependent Models

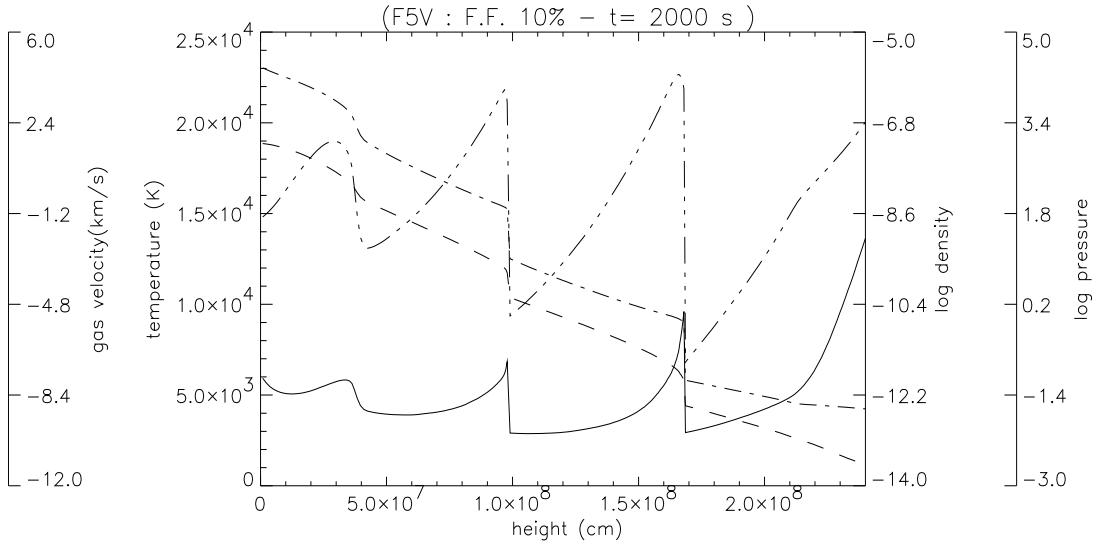

Fig. 5.3 A snapshot of the temperature (in K) (solid line), logarithm of the gas pressure (in dyn/cm^2) (long-short dashes), logarithm of the gas density (in g/cm^3) (long dashes), and the gas velocity (in km/s) (long-short-short dashes) for the F5V star with magnetic filling factor $f = 10\%$ at time t=2000 sec.

The computations start by introducing monochromatic waves to the stellar atmosphere by means of a piston according to Eq. (3.14). The wave amplitude is artificially increased from zero to its full value over a time span of 3 wave periods to avoid the disturbances of the switch-on effects. We consider the radiative continuum losses of H^- together with the line losses of Mg II, Ca II, and Fe II as described in Chapter 3 (section 3.3). The waves propagate upward through a decreasing density atmosphere, forming shocks and dissipating their energy to heat these layers. Shocks form deeper in the atmosphere (lower heights) when T_{eff} increases. in the case of $f_0 = 20\%$, the time average of the shock formation height is about $z = 363$ km for F5V stars (the chromosphere extends up to 2400 km height) and about $z = 467$ km for M0V stars (with a total extension of the chromosphere of about 1000 km). The lower shock formation height despite of the greater extent (see, Fig. 5.2) of the atmosphere for the F- star is due to the increase of the input mechanical energy with increasing T_{eff} (see, Table. 5.1).

Figure 5.4 shows a snapshot of the values of temperature, pressure, density and gas velocity for the F5V star at time $t = 2000$ sec, and after about 23 wave crests entered the atmosphere. In this period about 23 shocks have formed and dissipated their energy in the atmosphere. The gas density and pressure shows large jumps at the shock positions. In this model the gas density decreases 7 orders of magnitude from $z = 0$ km height to the

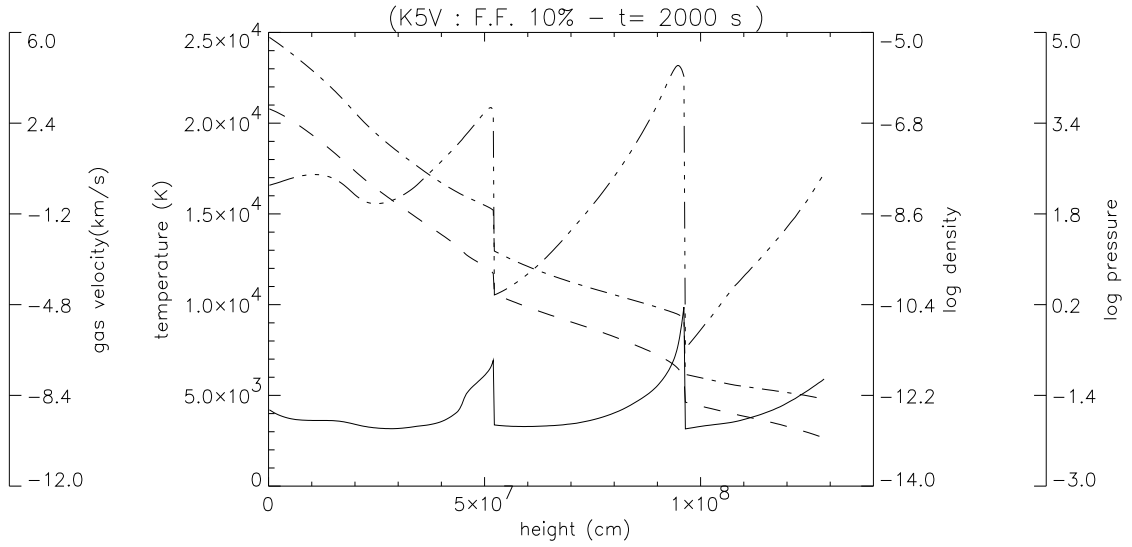

Fig. 5.4 The same as in Fig. 5.3 but for a K5V star.

height of 2400 km, while the gas pressure decreases by more than 6 orders of magnitude for the same height interval. Figure 5.4 shows also a snapshot for the same physical parameters for a K5V star after a time span of 2000 sec, about 37 shocks were developed and dissipated their energy to the outer layers of this star. The temperature jumps at shocks are larger for the F5V star than for the K5V star.

One of the important processes which affects the propagation of waves in stellar atmospheres, is the exchange of the mechanical and radiative energy, and the damping of the waves due to the presence of radiation. The atmosphere of late-type stars can be divided into two main zones of radiation. Figures 5.5 a,b show snapshots of the cooling function $D = dS/dt|_{rad}$ (given by Eq. (3.37)) for the radiation by H^- and lines, respectively as a function of height. It is seen that the emission occurs mainly behind shocks. There are two distinct radiative zones. The first (lower) zone extends from 0 km height up to about 640 km, and is dominated by the radiation of H^-, the second (upper) zone starts at about 520 km height and extends upward till approximately 1100 km height, in which the radiation by lines is dominant, and the cooling by H^- is approximately negligible. These two zones of radiation are found to be common in all late- type stars.

5.4 Mean Chromospheric Models

The time-averaged models show enhancement of the chromospheric temperatures of late-type stars. All late-type stars show an outward increase of the temperature, that is, we obtain 'classical chromospheres'. Figure 5.6 shows the time-averaged temperatures (over 400 sec) at $t = 2000$ sec versus height. With decreasing T_{eff} the temperature rise of the chromosphere is found to be steeper.

Despite of a lower shock formation height for F5V stars as compared to that of M0V stars it is seen that the chromospheric temperature rise occurs at much greater height in

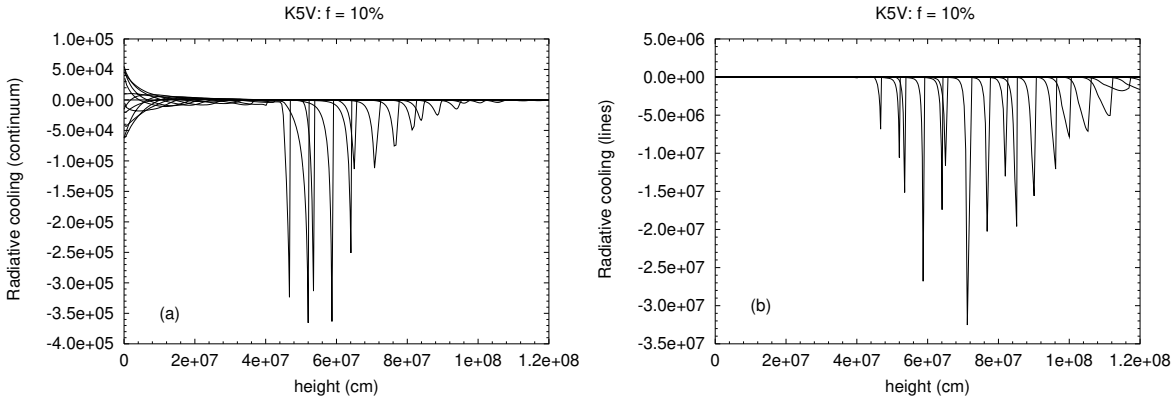

Fig. 5.5 Snapshots of the radiative cooling function **D** (in $erg\ g^{-1}\ K^{-1}\ sec^{-1}$) vs. height (in cm) for a K5V star with 10% magnetic filling factor.
5.5 a (*left*) For the H^- continuum radiation
5.5 b (*right*) For the total radiation of the lines (Mg II + Ca II + Fe II)

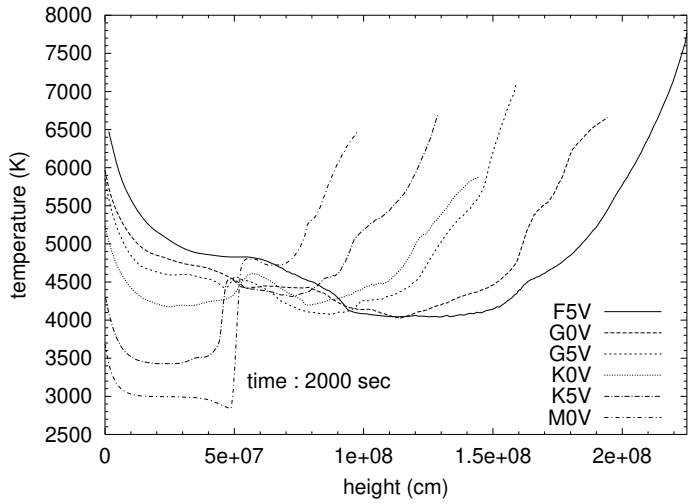

Fig. 5.6 Mean temperatures as function of heights for the sample of main sequence stars of magnetic filling factor 10%

F5V than that in M0V stars. This systematic behavior is a well known property already encountered in calculations (see, Schmitz & Ulmschneider 1981) and is due to the severe radiation damping suffered in F5V stars, which prevents a rapid temperature rise close to the height of shock formation.

Chapter 6

The Rotation - Emission Activity Relation

Summary. In the current chapter we present theoretically computed Mg II & Ca II emission core fluxes from the chromospheres of late-type stars of different magnetic activities. We construct two-component model atmospheres, a magnetic atmosphere which is heated by longitudinal tube waves, surrounded by an external non-magnetic atmosphere heated by purely acoustic waves.

6.1 Introduction

Solar and stellar chromospheric activities can be studied through the emissions of the Ca II H+K and Mg II h+k lines. A linkage between solar Ca II H+K emission and activity was first suggested by Eberhard and Schwarzschild (1913), Howard (1959) and Leighton (1959) found a correlation between Ca II H+K emission and magnetic flux density on the solar surface, concluding that the radiative losses from the outer layers of the Sun depend on the magnetic flux density of the underlying photosphere. The Sun provides us with detailed observations because of the high spatial resolution, while observing stars give us a wide range of basic parameters (i.e., mass, age, rotation rate, and composition) which are important for studying the parameters affecting the stellar activities. Schrijver, Dobson & Radick (1989) classified the Mount Wilson Ca II H+K fluxes of cool dwarf stars into two main components, (1) a basal component which is independent of stellar magnetic fields or rotation, and thought to be of non-magnetic origin, (2) a component which is related to the magnetic activity and rotation. Inactive and slowly rotating stars have basal chromospheres, while active stars have both components. Now, it is widely accepted that basal chromospheres are heated by the dissipation of acoustic waves independent on rotation, and can be best modeled only by the effective temperature and gravity (see, Ulmschneider 1991).

It has been known for a long time that stellar chromospheric activity is correlated with the stellar rotation rate and the convection zone through a dynamo mechanism. The number of the magnetic flux tubes covering the stellar surface is constrained also by these two parameters, the faster the star rotates the more magnetic flux tubes cover its surface

and vice versa. Rapidly rotating stars are active stars, while slow rotators are less active. One of the first remarkable studies by Skumanich (1972) showed that the Ca II emission decays as the inverse square root of the age and the rotation decay curve follow the same law. He concluded that since the Ca II emission is linearly proportional to magnetic field strength at the surface, therefore the surface magnetic fields are proportional to the angular velocity and decay as the inverse square root of the age. From this one can conclude that, the efficiency of generating magnetic fields through a dynamo increases with increasing the rotation rate, which results in larger fractions of the magnetic areas (more flux tubes; higher filling factors), and as a result, more Mg II and Ca II emissions.

6.2 Observational Results

The tight connection between stellar rotation rate and the overall chromospheric activity levels together with the stellar age dates back to the earlier work of Wilson (1963) and Kraft (1967). They found that, the Ca II emission and rotation in main sequence stars decline with age. The rotation rate diminishes as the square root of the age, and the chromospheric Ca II H+K emission is shown to follow the same relation (Skumanich 1972). This suggests that, the chromospheric emission is directly proportional to the rotation period P as $F_{CaII} \sim \frac{1}{P}$. Young stars have faster rotation rates and exhibit high chromospheric activity levels, while stars of intermediate age ($\sim$ 1-2 Gyr for 1 $M_{\odot}$) show moderate activity levels and rotation rates, and old stars as the Sun and older have slower rotation rates and lower activity levels (Baliunas et al. 1995). Analysis of X-ray data by Pallavicini et al. (1981) and Walter (1981; 1982) show that coronal emission is also correlated with rotation.

The magnetic field not only heats, but also penetrates the outer atmospheric layers carrying away angular momentum in a magnetized wind. The interaction of the stellar wind with the magnetic field of the star (magnetic braking) results in a loss of the angular momentum, which slows down the rotation rate with advancing age (Schatzman 1962; Parker 1965).

On the other side, the rotation velocities show a dependence on spectral type in the sense that the rotation velocities of equal-age main sequence stars exhibit a monotonic decrease with advancing spectral type (Gray 1982; Fig. 1).

Areas of concentrated magnetic field on the Sun show more intense Ca II H+K emission than areas with less magnetic field (Skumanich et al. 1975). The Ca II emitted flux show roughly a one-to-one relation with the magnetic flux density (the product of the magnetic field strength and area) (Skumanich et al. 1975; Schrijver et al. 1989). The surface magnetic activity is correlated with the rotation rate as expected from the dynamo theory, which predicts an increase of the magnetic flux with decreasing the rotation period $B \cdot A \sim (\frac{1}{P})^n$. Not only rotation which plays the key role in the magnetic activity, there is also the depth of the convection zone, both parameters determine the efficiency of regenerating magnetic fields through the dynamo mechanism. For a given rotation period, stars with deeper convection zones (later spectral types) exhibit stronger magnetic activity than stars with shallow convection zones (earlier spectral types).

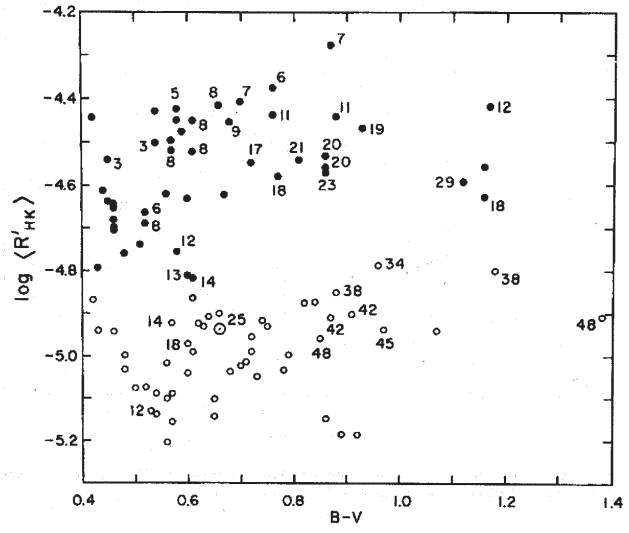

Fig. 6.1 The mean chromospheric Ca II H+K flux ratio $< R'_{HK} >$, as obtained from the mean Wilson (1978) survey data. Labels give observed periods in days of the measured stars, from: Noyes et al. (1984; Fig. 2).

A long term program for monitoring the chromospheric activity variation for main sequence stars through the emission of Ca II H and K lines was initiated by Wilson (1968, 1978) and extended by Baliunas et al. (1995). Baliunas et al. (1995) classified the 25 yr records into two groups shown in the $\log < S >$ (S is a quantity used as an indicator of the chromospheric activity; see Schrijver (1989)) versus $(B - V)$ diagram, the first group is for stars in the upper region of the digram with higher values of $< S >$, rapidly rotating and young stars, and the second group of stars in the lower region (including the Sun) with lower $< S >$ values, old and slowly rotating. Between the two groups there is a "gap" first pointed by Vaughan and Preston (1980) nearly devoid of points (see, Fig. 6.1) separating stars with higher Ca II emission from those of lower Ca II emission. The variation of the chromospheric emission with time shows dependence on the stellar mass and age. F-type stars have very slow secular variations, this is due to the fact that these stars have shallow convective zones. Stars with significant cyclic variability in their chromospheric emission are young and rapid rotators (Baliunas et al. 1995).

Noyes et al. (1983) found that the mean Ca II emission fluxes normalized by the bolometric emission of the star ($R_{HK} = F_{CaIIH+K}/\sigma T_{eff}^4$) can be approximated as the product of the angular rotation rate and an additional function which depends on spectral type. Then, he mentioned that the function of spectral type has the same shape as the convective overturn time calculated from convective zone models. This connection allowed him to suggest that the inverse of the Rossby number $1/R_0$ ($R_0 = P/\tau_c$ is the rotation period divided by the convective overturn time) may be a good parameter for determining the stellar surface magnetic activity.

In a subsequent study by Noyes et al. (1984), the rotation periods have been measured for the long term activity stars (with emission fluctuations occur over long time scales compared to rotation period) observed by Wilson (1978). The mean chromospheric flux ratio after subtracting the flux of non-chromospheric origin $< R'_{HK} >= R_{HK} - R_{phot}$ (R_{phot} is the total flux passed by the H-K photometer outside the K1 and H1 profile minima and R_{HK} is the total observed Ca II flux) versus $B - V$ as shown in Fig. 6.1 (Noyes et al. 1984; Fig. 2) with the observational periods marked on each point, shows

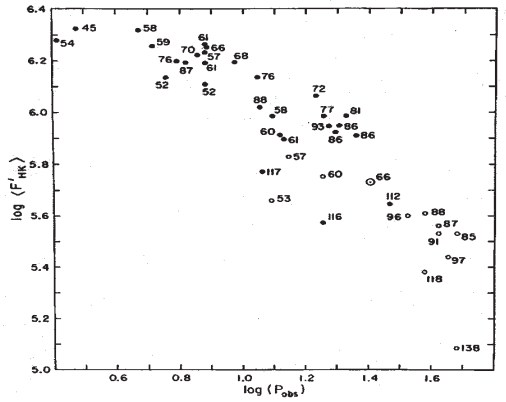

Fig. 6.2 The mean chromospheric Ca II H+K flux ratio $< R^{'}_{HK} >$, as obtained from the mean Wilson (1978) survey data. Labels give observed periods in days of the measured stars, from: Noyes et al. (1984; Fig. 4).

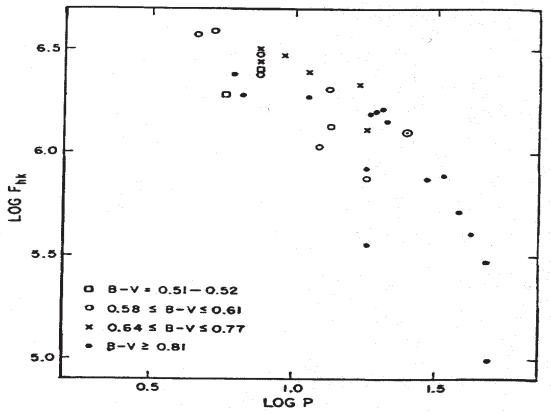

Fig. 6.3 The surface-averaged Mg II h+k fluxes, measured in units $ergs\ cm^{-2}\ s^{-1}$, as a function of rotational period for main sequence stars, from: Hartmann et al. (1984; Fig. 3).

the two concentrations of old and slowly as opposed to young, rapidly rotating stars with lower and higher Ca II H+K emissions respectively, separated by the gap pointed by Vaughan and Preston (1980). Fig. 6.2 (Noyes et al. 1984; Fig. 3) shows the correlation between the flux $F^{'}_{HK} = R^{'}_{HK} \times \sigma T^4_{eff}$ and the logarithm of the observed rotational period, log P_{obs}, the emitted flux $F^{'}_{HK}$ decreases with increasing rotational period. He also noted that the scatter in the plot is smaller when using the Rossby number instead of the rotation period and when using $\alpha = 2$ (the ratio of the mixing length to scale height) for computing the convective overturn time. To summarize, Noyes et al. (1984) suggested that the chromospheric emission ratio $R^{'}_{HK}$ is a tight function of the Rossby number ($R_0 = P/\tau_c$, with $\tau_c \approx 2\Delta z/v_{conv}$ being the color dependent overturn time and computed near the base of the convection zone for models with $\alpha = 2$, where Δz is the depth of the convection zone and v_{conv} the convective velocity at the base of convection zone).

The analysis of Mg II fluxes obtained with the IUE satellite for main sequence stars by Hartmann et al. (1984) shows that the average surface flux F_{hk} of the Mg II h+k lines normalized to the bolometric flux $R_{hk} = F_{hk}/\sigma T^4_{eff}$ is correlated with the rotation period P (see, Fig. 6.3). They found that a function of the form

$$log\ R_{hk} = a\ P + b \tag{6.1}$$

represents well the data, while the fitting parameters a and b depend on $B - V$. This exponential dependence of Mg II emission on rotational period was also suggested by Blanco et al. (1982).

Rutten (1986) analyzed a sample of 55 main sequence stars of spectral types between F3 to M4 and found a color dependent linear relation between the Ca II H+K line core flux density F_{CaII} and the logarithm of the rotation rate of the form

$$F_{CaII} = a\ logP + b \tag{6.2}$$

while the coefficients of the linear fits (a and b) depend on $B - V$ (see, Fig. 1.4).

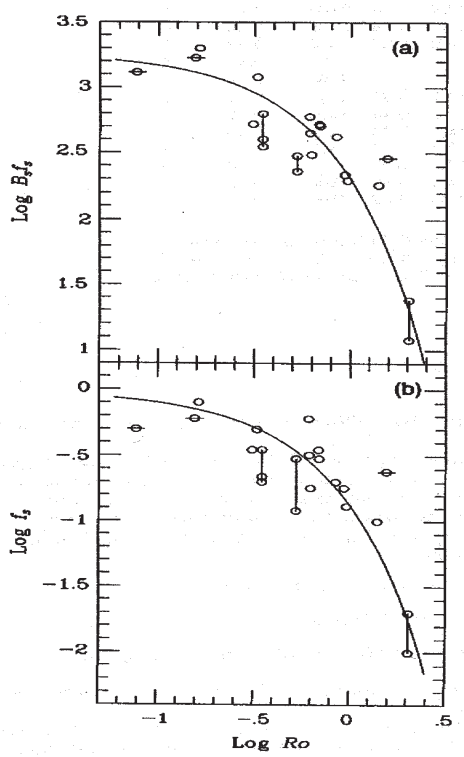

Fig. 6.4 The observed (a) $\log B_s f_s$ and (b) $\log f_s$ plotted against Rossby number $\log R_0$ for G and K dwarf stars. The lines shown are the best fits to the data. The points crossed by a horizontal line are stars not included in the correlations. Vertical lines connect different measurements for the same star, from: Montesinos & Jordan (1993).

In an attempt to correlate empirically the magnetic flux density $B_s f_s$ (B_s is the magnetic field strength, and $f_s = A_{mag}/A_{tot}$ is the ratio between the surface area covered by magnetic field to the total surface area) measured at the star's surface with the rotation period or Rossby number, Montesinos and Jordan (1993) found for a sample of late-type dwarf stars of spectral types F, G, and K, that the surface magnetic flux $\log B_s f_s$ is best fitted with a linear dependence on R_0 (see, Fig. 6.4 a) of the form

$$log\ B_s f_s = 3.27(\pm 0.08) - 0.97(\pm 0.08) R_0 \tag{6.3}$$

with the Rossby number being the ratio of the rotation period P to the convective overturn time τ_c which is a function of $B-V$ as given by Noyes et al. (1984). The observed surface filling factors are found to be linearly correlated with R_0 (see, Fig. 6.4 b) for the same sample of stars as

$$log\ f_s = -0.01(\pm 0.07) - 0.86(\pm 0.07) R_0 \tag{6.4}$$

The different representations of the data by different authors resulted in different relations between the emitted chromospheric flux and rotation period or Rossby number, while the use of the normalized activity units and Rossby number generally improves the correlation between activity and rotation.

The chromospheric Ca II emission flux has shown a close correlation with the underlying photospheric magnetic flux density Bf in an analysis by Marcy and Basri (1989) for K-dwarfs. Stars with short rotation periods and large magnetic flux have strong chromospheric emissions.

6.3 Previous Theoretical Simulations

Montesinos et al. (1987) established theoretically for a sample of main sequence stars of spectral types G and K a connection between the dynamo mechanism (represented by the magnetic filling factor, f) which operates at the base of the convection zone and the observed chromospheric activity as seen through the emission of Mg II and Ca II lines. Their model is based on a time-dependent dynamo model by Robinson & Durney (1982). The main results of this work can be drawn as follow: For a fixed spectral type, the magnetic field strength increases with decreasing the rotation period, and larger for stars with deeper convection zones. The relationships between log f versus $B-V$ and log f versus Rossby number, show that stars with larger rotation periods occupy the regions of lower values of f, and f follows the same trend against Rossby number the same way as the chromospheric emission fluxes (Mg II & Ca II). This suggests that the chromospheric emission is proportional to the area covered by magnetic fields (f). Stars with shallow convection zones show lower B and f values.

Cuntz et al. (1999) constructed time dependent two-component models for the chromospheres of K2V stars with different magnetic activities by using an observed relation connecting $B_s f_s$ with P of the form

$$B_s f_s = 238 - 5.51P \tag{6.5}$$

for P in the range 10 days $\leq \ P \ \leq$ 50 days. The flux tubes are assumed to be distributed uniformly and in a network structure over the star's surface, and the integrated Ca II emission is computed based on multiray 1.5-dimensional radiative transfer with the assumption of partial redistribution (PRD). It has been found that the heating in the magnetic component is larger than the heating in the non-magnetic component. Also, magnetic heating is found to be stronger in flux tubes which spread least with height (larger values of f), this is expected to be found on rapidly rotating stars. The emitted Ca II flux is larger for stars with shorter rotational periods. Their usage of longitudinal tube waves for heating the chromospheres of K2V stars produced Ca II H+K fluxes which are in agreement with observations, which means that waves are sufficient to heat the chromospheres of these stars. A good agreement with observations is obtained for the case where the flux tubes are uniformly distributed over stellar surface.

Brandenburg et al. (1998) combined the measured values of $< R^{'}_{HK} >$ (Baliunas et al. (1995); Rutten (1987)) and recent measurements of magnetic field strengths for K and G dwarfs (Saar 1996) with results from a mean field dynamo model and found

$$\langle R^{'}_{HK} \rangle \ \propto \ (\langle B \rangle / B_{eq})^k, \qquad \text{with k} = 0.47 \tag{6.6}$$

where B_{eq} is the equipartition field strength, which results when assuming an equipartition between the thermal and magnetic energy densities.
He also found a positive correlation between the α-parameter in mean field dynamo theory which has a direct proportionality with the magnetic field strength and the mean normalized Ca II H+K emission flux $\langle R_{HK} \rangle$.

6.4 Current Work

The magnetic filling factor is the most suitable parameter to connect theory with observations, as the stellar values of B are almost constant, f alone may be used to represent the stellar magnetic activity. In the current models of main sequence stars, B is constant for a fixed spectral type and f changes with values depending on the magnetic activity levels.

The magnetic filling factor f is tied to the rotation rate as mentioned above, so it is an indirect measure of the rotation rate. A possible way to construct theoretical models for stars of different magnetic activities (different rotation rates) is to assume a wide range of f covering different levels of activities, this is because of the lack of observed and theoretical relations between f and P. Slowly rotating stars are covered with a small number of flux tubes which are not crowded and have the chance to spread and expand exponentially with height, filling factors of 1% and 5% are used for modeling such stars (filling factor of 1% is the lowest activity value in our models). Increasing the rotation rate gradually results in increasing the magnetic filling factors. The most rapidly rotating star in our models which has a 50% filling factor. Figure 6.5 shows a side view for magnetic flux tubes of a slowly and rapidly rotating stars.

Three different quantities were chosen to describe the chromospheric emission, the chromospheric luminosity L_{hk}, the average surface flux F_{hk}, and the ratio $R_{hk} = F_{hk}/(\sigma T_{eff}^4)$. The analysis by Hartmann et al. (1984) showed that the relation between the Mg II emission and rotation is unaffected by the choice of exact parameter form of emission and rotation, i.e., R_{hk}, F_{hk}, L_{hk} are roughly equivalent, also the choice of the rotational velocity or the rotation period is also equivalent, as the rotational velocity is directly related to the rotation period. Therefore we have chosen for the current analysis the average surface flux F_{hk} as a parameter for measuring the Mg II and Ca II emission.

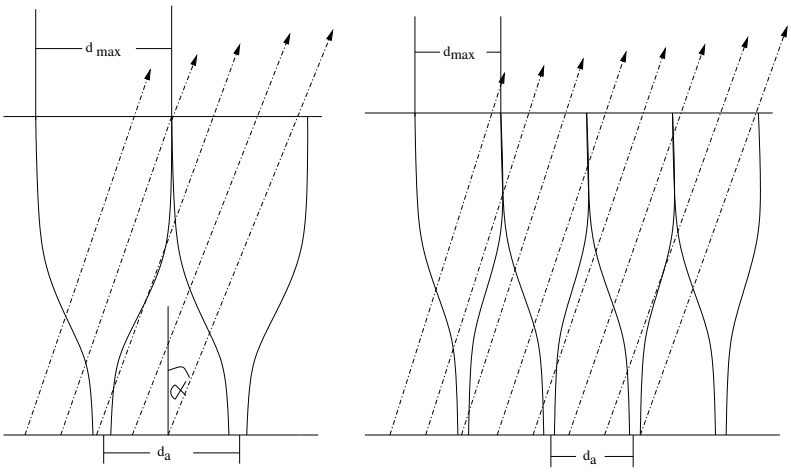

Fig. 6.5 A side view of rows of flux tubes for two stars of different rotational rate; slowly rotating star (left) and rapidly rotating star (right), dashed arrows show the ray paths.

6.5 Magnetic and Acoustic Heating

The importance of the magnetic and acoustic heating vary from star to star and from one position to another on the stellar surface. Some areas on stellar surfaces are dominated by

strong fields while others are either field-free or contain weak fields. Because of the lack of spatial resolution, observations do not show these regions separately, so it is not easy to distinguish both mechanisms. The observed flux-color diagrams of the chromospheric Mg II h+k and Ca II H+K surface flux densities (e.g. Rutten, 1991; Vilhu, 1987) show clear lower limits in F_{MgII} *and* F_{CaII}, and scatter of data with more emission above this boundary. The lower limit is determined by the least active stars. Magnetic braking through the magnetized stellar wind decelerates the stellar rotation, which results in a steady loss of the angular momentum throughout the stellar age. Old stars are slowly rotators while young stars are rapidly rotators. As the efficiency of the generation of magnetic field increases with stellar rotation rate and the depth of the convection zone (dynamo mechanism), we expect that the lower limits of Mg II and Ca II emission fluxes are determined by old, slowly rotating stars. In our models, the basal chromospheres (the voids between flux tubes) are heated by the dissipation of acoustic waves, and magnetic regions are heated by the dissipation of longitudinal tube waves. The two atmospheres are combined together in one model to compute the emitted Mg II and Ca II fluxes.

6.6 Method

6.6.1 Stellar Parameters

a. The Flux Tube Geometry

Magnetic flux tubes might have different distributions on stellar surfaces, they may be distributed uniformly or arranged in a network structure. The geometry of the tubes is subjected to the region which contains them. In a crowded region, with high filling factor, (e.g. supergranulation cell boundaries) they show less expansion with height, and they merge at lower heights forming canopies. While in a region with lower filling factor (quiet regions), the tubes are less crowded and have the chance to expand, merging together at greater heights (see, Fig. 6.5). In the case of uniformly distributed flux tubes, the chromospheric magnetic filling factor f_c at the merging height is $f_c = 1$, while for flux tubes arranged in a network structure, there exists a non-magnetic component of chromosphere, which means that the chromospheric magnetic filling factor is always $f_c < 1$.

In the current study, stellar magnetic flux tubes are assumed to be uniformly distributed over the stellar surface. For the construction of stellar flux tube models, several parameters should be specified. The expansion rate and the top radii of the tubes are determined by the photospheric magnetic filling factors together with the bottom radii (see, Chapter 3). Because of the lack of spatial resolution, stellar magnetic flux tubes cannot be resolved, therefore the bottom radii are assumed to be equal to half the local pressure scale height similar as on the Sun.

Different levels of magnetic activities (e.g. different rotational periods) can be studied by assuming different photospheric (at height $z = 0$ km) magnetic filling factors, f_0. Since we do not have an observed relation between the rotation periods and the magnetic filling factors for each spectral type of the late-type stars, we assume different values of f_0 (f_0 = 1%, 5%, 10%, ..., 50%) to cover the range from the least active stars (with

$f_0 = 1\%$) to the most active star in our sample (with $f_0 = 50\%$).

The flux tubes expand with height reaching a maximum diameter d_{max} at which the magnetic field fills completely the entire space. The value of d_{max} in the case of uniformly distributed flux tubes can be computed as follows: the magnetic photospheric area, F_0, is given by $F_0 = f_0 F_T = \pi r_0^2$, where F_T is the total surface area and r_0 is the photospheric tube radius. The chromospheric magnetic area, F_1, is given by $F_1 = 4r_{max}^2$, with r_{max} being the maximum tube top radius, this is because the magnetic chromosphere consists of squares with inscribed circular flux tubes. Assuming that above the merging height, the chromosphere is completely filled with flux tubes, which implies that $f_1 = F_1/F_T = 1$ and results in a value of $d_{max} = 2r_{max}$ given by, $d_{max} = r_0\sqrt{\pi/f_0}$. As shown in Fig. 6.5, rapidly rotating stars have higher coverage of magnetic flux tubes with larger magnetic filling factors than slow rotators (e.g., for a G5V star, $d_{max} = 334$ km for $f_0 = 10\%$ and $r_0 = 60$ km, while for $f_0 = 50\%$, $d_{max} = 136$ km).

b. The Surface Magnetic Field Strength

It is more difficult to measure magnetic fields for stars other than the Sun, therefore we calculate the magnetic field strength inside the flux tube at the photospheric level where $\tau_{5000} = 1$ assuming equipartition between the external gas pressure and magnetic pressure inside the tube (Solanki 1996), similar to the Sun, the gas pressure outside the tube, p_e, and the gas pressure inside, p_i, can be related by $p_i : p_e = 1 : 4$, we assume that this ratio holds for late-type stars. The computed magnetic field strength is constant for a fixed spectral type, while the magnetic filling factors vary with the stellar rotation.

c. The Input Mechanical Energy

The input mechanical energy fluxes carried by magnetic waves are calculated following the procedure described in Chapter 2, the input monochromatic wave periods are the periods correspond to the maximum of the velocity power spectrum of these waves (see, Fig. 2.23). The input acoustic wave energy fluxes were computed following the same procedure described by Ulmschneider et al. (1996), also the input monochromatic wave periods are those correspond to the maximum velocity power spectrum of these waves. Table 6.1 summarizes the input parameters used for constructing the model chromospheres of late-type stars.

6.6.2 Two-component Chromosphere Models

By two-component models we mean a combination of magnetic and non-magnetic atmospheres. The non-magnetic atmosphere exists in the voids between the tubes, for the computation of the emitted Mg II and Ca II line radiation flux, both atmospheres are integrated together. The non-magnetic atmosphere is heated by the dissipation of acoustic waves, while the magnetic atmosphere is heated by the dissipation of longitudinal tube waves. Other types of tube waves are also generated in the convection zones; e.g., transverse and torsional waves, which may be an additional source of energy. One important mechanism for dissipating the transverse tube waves is that they couple to the longitudinal tube waves by a non-linear mode coupling mechanism (Ulmschneider et al. 1991).

Star	$T_{\rm eff}$(K)	$\log g$	$B-V$	$B(G)$	$F_{\rm A}$	$P_{\rm A}$	$F_{\rm M}$	$P_{\rm M}$
F5V	6440	4.34	0.44	1407	$6.67 \cdot 10^8$	55	$5.70 \cdot 10^8$	85
G0V	6030	4.39	0.58	1574	$3.22 \cdot 10^8$	46	$4.40 \cdot 10^8$	75
G5V	5770	4.49	0.68	1741	$1.70 \cdot 10^8$	42	$2.80 \cdot 10^8$	63
K0V	5250	4.49	0.81	1846	$5.24 \cdot 10^7$	38	$1.90 \cdot 10^8$	58
K5V	4350	4.54	1.15	2370	$3.83 \cdot 10^6$	34	$5.50 \cdot 10^7$	54
M0V	3850	4.59	1.40	3258	$3.55 \cdot 10^5$	31	$5.00 \cdot 10^6$	50

Table 6.1 The parameters used for constructing the magnetic and non-magnetic chromosphere models, B is the magnetic field strength, F_A, P_A, F_M and P_M are the acoustic flux ($erg\ cm^{-2}s^{-1}$), the monochromatic period (sec) corresponds to the maximum acoustic flux, the magnetic wave flux ($erg\ cm^{-2}s^{-1}$), and the monochromatic period (sec) corresponds to the maximum magnetic flux respectively.

Then the energy carried by the transverse tube waves can be dissipated after conversion to longitudinal tube waves (Nakariakov et al. 1996). The height at which this mode coupling takes place and the percentage of the transformed waves still need more theoretical work. Huang et al. (1995) shows that the efficiency of generating transverse waves is one order of magnitude higher than generating longitudinal waves.

For the Sun, the generated transverse tube wave energy flux is roughly 30 times larger than the longitudinal tube waves energy flux (Ulmschneider & Musielak, 1998). A high fraction of the energy carried by transverse waves suffer leakages from the tube boundaries to the surrounding as found by Ziegler & Ulmschneider (1997 a&b), a fraction of the energy may couple with the longitudinal waves to add more energy for heating the outer layers, also the leaked fraction might add additional energy to the acoustic waves outside flux tubes. As will be shown later heating the chromospheres with energies carried only by longitudinal tube waves are not sufficient to account for the observed emission losses.

Also, the acoustic wave adds longitudinal wave energy when the magnetic canopy is intercepted. We have disregarded this effect which primarily affects models with low filling factors. Currently, no computation exist to tell how much energy flux carried by transverse waves or external acoustic waves may be transformed to longitudinal wave mode. In a work by Cuntz et al. (1999), only 10% of the transverse wave energy flux is assumed to be transformed to the longitudinal mode. In the current computations, we start heating the magnetic flux tubes of different filling factors by purely longitudinal tube wave fluxes, then we assume different multiplication factors M of the energies carried by the longitudinal mode ($M = 2,\ 5,\ 10$) to account for the energies added by the transverse and acoustic modes.

6.6.3 Multiray Radiative Transfer

After constructing the initial magnetic and non-magnetic atmospheres for late-type stars with different magnetic activities, radiatively damped longitudinal tube waves and acoustic waves are introduced at photospheric level $\tau_{5000} = 1$, then they are followed till they dissipate their energy in form of shocks and the chromospheric emission lines are computed by means of a time-dependent MHD wave code (see, Chapter 3). To avoid switch-on effects, the initial wave energy fluxes are gradually introduced into the atmosphere over

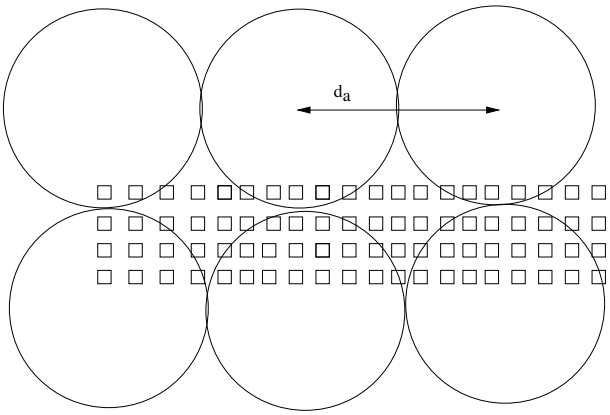

Fig. 6.6 A top view of rows of flux tubes, small squares mark the ray paths.

a time span of 3 wave periods. In the acoustic and MHD codes only one atmosphere is simulated, while for the computation of the total chromospheric emission fluxes, we have to take into account many parameters, namely, the total number of flux tubes, the voids between the tubes, the distribution of the tubes, and the radiative transfer effects.

The atmosphere takes time to reach dynamical equilibrium between the locally dissipated wave energy and the local radiative losses, which is important to have stable time-dependent models. For this purpose we monitored the variation of the emitted flux with time, Fig. 6.7 shows a G5V star, with $f_0 = 10\%$, the resulting emitted Mg II h+k fluxes are computed after the passage of certain number of shocks (marked on the plot). As seen starting after the passage of 40 shocks the emitted flux is stable and dynamical equilibrium is reached. After this state is reached 4 snapshots of the atmosphere separated in time by one quarter of a wave period are computed for different wave phases.

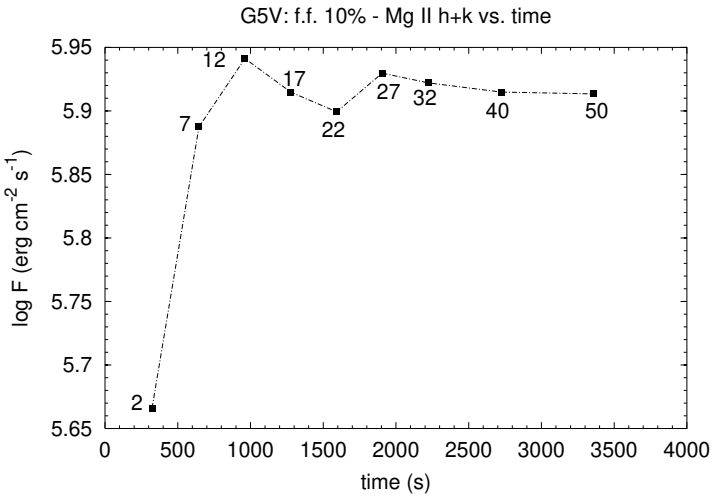

Fig. 6.7 The variation of the emitted Mg II h+k flux with time, for a G5V star of surface magnetic filling factor $f_0 = 10\%$. Numbers mark the number of passed shocks through the atmosphere.

In our treatment, we follow the procedure described by Cuntz et al. (1999) using a method developed by Rammacher & Ulmschneider (2001), the flux tubes are arranged in rows, each row consists of a strip of expanding tubes with identical geometries at all heights as shown in Fig. 6.5. The forest of flux tubes is intercepted by a two-dimensional array

of ray paths which emanate from equidistantly spaced surface grid points indicated by small squares in Fig. 6.6. To ensure that the line fluxes and profiles represent the different wave phases existing in stars, the atmospheres inside the tubes are filled randomly with different wave phases (selected from the total of four). The total number of flux tubes N intercepted by the ray path in one row depends on the angle α between the surface normal and the line of sight; for large angles, more tubes are intersected by the ray path, and N also increases with the photospheric filling factor. The value of N is given by

$$N = H \ \tan\alpha \sqrt{f_0/(\pi r_0^2)} + 5 \tag{6.7}$$

where H is the total height of the atmosphere, r_0 and f_0 are the bottom tube radius and the photospheric filling factor, respectively.

For the choice of the external atmosphere (the voids between tubes), the non-magnetic atmosphere is heated separately by acoustic waves and the resulting Mg II and Ca II fluxes are computed for different wave phases. Here one selects a phase which is close to the average of all phases to be the external atmosphere in our simulation.

The stellar atmospheres are sampled equidistantly for a total of 600 spatial grid points. For the computation of the surface integrated fluxes we use five angles for our computations ($\cos\alpha = \mu = 0.9, 0.7, 0.5, 0.3$, and 0.1), the radiative transfer is calculated along all the different rays for a given angle, this ensure that all surface areas equally contribute to the integrated flux.

The radiative transfer for the Mg II k and Ca II K lines are computed with the assumption of partial redistribution (PRD) along rays passing through the tube rows and by using a two-level atom description. The operator splitting method described by Ulmschneider (1994) is used for the computation of the PRD source functions of the Mg II and Ca II lines. We use 47 frequency points, distributed within $\pm$ 10 Å of line center. Since the K_1 minima in the models are always located within $\pm$ 0.3 Å, the frequency points are more concentrated in this range. The $\pm$ 0.3 Å frequency interval is also used to calculate the emitted flux. Examples of such line profiles are seen in Figs. 6.17 to 6.19.

A comparison with observations requires the computation of the total Ca II H+K and Mg II h+k fluxes. Because our treatment of the line transfer is based on two-level atom model, we compute single Ca II K and Mg II k lines and multiply the obtained fluxes by a factor of two to account for the emission of the HK and hk doublets and to be compared with the observed fluxes. This is a valid approximation for low-activity stars, while the Ca II H flux is reduced relative to the Ca II K flux in more active stars (Vaughan et al. 1978). Cuntz et al. (1999) computed a scaling factor to account for this reduction which depends on the stellar activity expressed in terms of the rotational periods, he found for their models that this factor ranges from 1.87 to 1.95 for the most active star and the least active one, respectively. Because of the usage of the factor two, our computed fluxes should be considered as an upper limit.

6.7 Results

6.7.1 The Basal Flux

In a two-component chromosphere (magnetic & non-magnetic), one heating mechanism may be more dominant than the other, but both mechanisms work together even for least active stars which might still have a remaining magnetic activity from a residual dynamo effect or from a background, non-variable turbulent dynamo (e.g., Saar 1998; Schrijver et al. 1998). If we assume that the magnetic heating mechanism does not contribute to the heating of the outer layers of low-activity slowly rotating stars or stars at the minimum activity cycle, one can construct chromospheric models based on a purely acoustic heating mechanism. Theoretical chromospheric models based only on acoustic heating, have been constructed by Buchholz et al. (1998) for main-sequence stars between spectral type F0V and M0V and two giants of spectral type K0III and K5III. These computations were based on monochromatic acoustic waves. A comparison of the computed Mg II h+k and Ca II H+K fluxes with the lower limit of the flux-color diagram presented by Rutten (1991) (see, Fig. 1.2) showed a good agreement over nearly 2 orders of magnitude. Theurer (1998) used acoustic wave spectra instead of monochromatic waves and found that heating the outer layers of late-type stars with wave spectra results in a small number of shocks with very large strengths and therefore larger emission fluxes relative to the monochromatic waves. The computed time averaged fluxes of Mg II and Ca II lines by Theurer are larger than the observed basal flux line of Rutten (1991), this is explained by the higher jumps of a shock with the higher postshock temperatures and the lack of treating the non-instantaneous ionization.

In this section we compute the Mg II h+k and Ca II H+K flux losses from one-component acoustically heated chromospheres, while in the remaining parts we assume always two-component models, which are more realistic. The computed surface integrated PRD emission fluxes of the Ca II H+K and Mg II h+k lines are compared with the lower limit of the flux-color diagram of Rutten (1991) and with an average observed minimum fluxes of Stepien (2000; private communication) (only for Ca II h+K fluxes) together with the results of Buchholz (1995).

Before the comparison with observations, Fig. 6.8 shows how the computed total emission flux relates to the acoustic input fluxes. The computed total emission flux (Ca II + Mg II) depends on $B-V$ ($B-V = 15.7 - 4 \log T_{\rm eff}$ (Böhm-Vitense 1981)). Hot stars (small $B-V$) show more emission than cool stars (large $B-V$). The fraction of the input acoustic wave energy flux seen as emitted total flux to the input acoustic flux increases towards cool stars ($\approx 0.3\%$ for F5V stars to $\approx 15\%$ for M0V stars). For early type stars till G5V spectral type, the chromospheres show more emission in Ca II H+K lines, while for later types till M0V stars the Mg II h+k emission is larger than that of the Ca II H+K (see, Tab. 6.2 and Fig. 6.8). The energy difference between the input energy flux and the total Mg II + Ca II flux goes into H^- emission and wind losses.

Figures 6.9 shows a comparison between our computations for the Ca II H+K emission fluxes (x-sign) and the previously computed fluxes by Buchholz (1995) (empty squares) as well as with the lower limit of the flux-color diagram of Rutten (1991) (filled circles) and fluxes provided by Stepien (2000; private communication) (filled squares). The two

Star	$T_{\rm eff}$(K)	$\log g$	B-V	log $F_{\rm MgII}$	log $F_{\rm CaII}$	$F_{MgII+CaII}/F_A \times 100(\%)$
F5V	6440	4.34	0.44	5.91	6.08	0.30
G0V	6030	4.39	0.58	5.79	6.06	0.55
G5V	5770	4.49	0.68	5.89	5.98	1.01
K0V	5250	4.49	0.81	5.76	5.69	2.04
K5V	4350	4.54	1.15	5.48	4.79	10.24
M0V	3850	4.59	1.40	4.55	4.29	15.33

Table 6.2 The computed basal fluxes for the Mg II and Ca II lines.

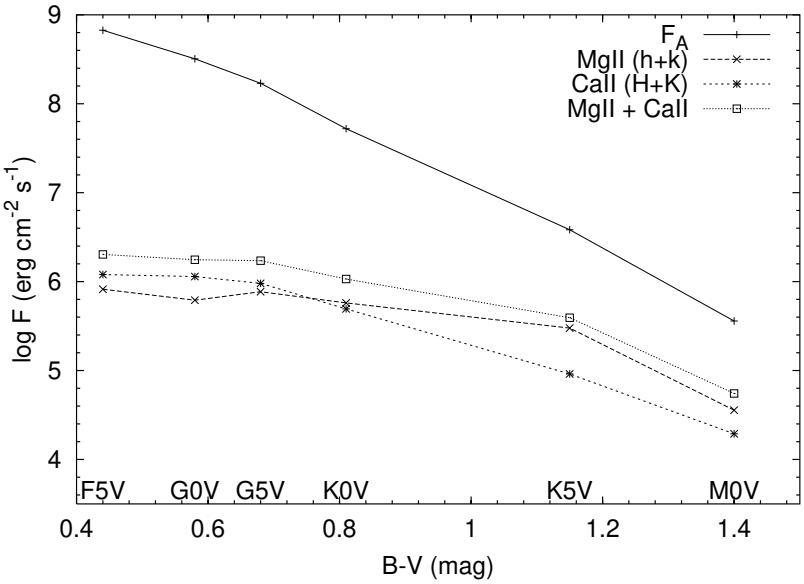

Fig. 6.8 A comparison between the input mechanical fluxes (acoustic fluxes) and the emitted Mg II h+k and Ca II H+K core fluxes.

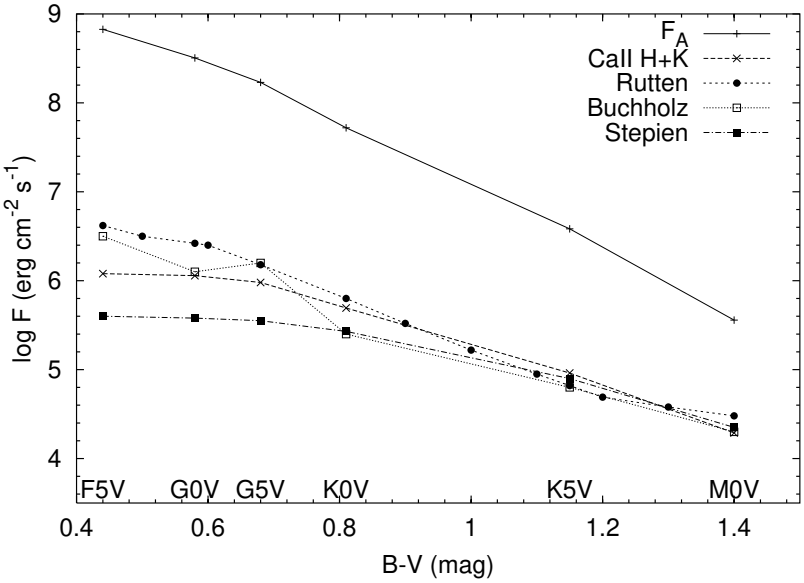

Fig. 6.9 A comparison between the computed emission fluxes (dashed line with x-sign) with the input acoustic fluxes (drawn line with plus sign), the theoretical fluxes obtained by Buchholz (1995), the observed basal flux line by Rutten et al. (1991) (dashed with filled circles), and fluxes collected by Stepien (2000; private communication) (filled squares).

observed lower limits given by Rutten and Stepien agree well for cool stars, while for hot stars they deviate from each other. The computed Ca II H+K fluxes drops by a factor of 62 from the hottest star in our sample (F5V) to the coolest one (M0V). Starting from K0V spectral type and later-types, the computed fluxes are getting closer to the empirical lower limit given by Rutten as $R_1 = F_{CaII}(computed) = 0.8 F_{CaII}(Rutten)$ for K0V stars, when comparing with the empirical values given by Stepien, a ratio of

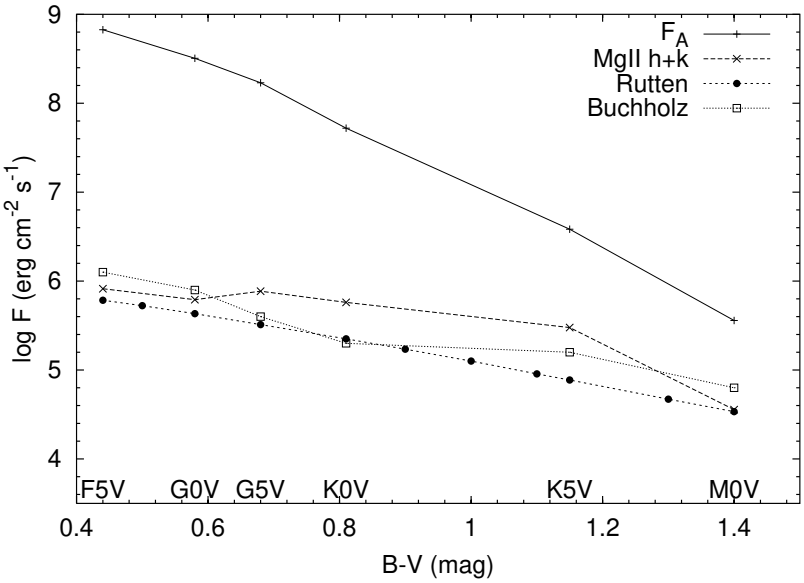

Fig. 6.10 The same as in Fig. 6.9 but for the Mg II h+k lines.

$R_2 = F_{CaII}(computed) = 1.8F_{CaII}(Stepien)$ is obtained. The empirical values given by Rutten and Stepien show a deviation from each other by a factor of 2.3 for the same spectral type. This deviation is attributed to a different handling of the data reduction of the observations. For the coolest star in our sample (M0V), the ratios R_1 and R_2 are 0.6 and 0.9, respectively. The hotter stars in our sample show noticeable deviations from both empirical values of Rutten and Stepien, the values of R_1 and R_2 for F5V spectral type are 0.3 and 3.0, respectively. On the other hand, both empirical values deviate by a factor of 10.5 for the same spectral types. The previous results of Buchholz (1995) show better agreement for hot stars (of spectral types F5V & G5V) with the empirical values of Rutten ($R_1 = 0.8$ for F5V spectral type), while Rammacher (2000; private communication) trying to recover the results of Buchholz, found that a factor of $2\pi\mu$ has been forgotten in Buchholz's flux integrations for G5V (for Mg II core fluxes) and K5V stars (for both the Ca II and Mg II core fluxes). The deviations of our computed fluxes from the observed fluxes might result from our assumptions, to use monochromatic waves instead of the realistic wave spectra, and our limited treatment of the convection zone models especially for hot stars, also the two-level atom approach results in less Ca II K flux in comparison with the five-atom approach as found by Solanki et al. (1991). Finally our method suffers from the assumption that we neglected a full time-dependent treatment of Hydrogen ionization. As mentioned above when discussing Theurer's results, however, the influence of that approximation is minimized by using monochromatic waves.

The computed Mg II fluxes are shown in Fig. 6.10 together with the empirical values of Rutten and the computations of Buchholz. The computed Mg II fluxes for F5V, G0V and M0V spectral types show better agreement with the empirical values of Rutten, while a noticeable deviation exists for other spectral types.

6.7.2 Effects of the Wave Energy and Periods

The turbulent motions of the convection zone generate different modes of acoustic and magnetic waves. Some of these modes may be coupled together for supplying the upper atmospheric layers with more mechanical energy fluxes (e.g., longitudinal and transverse

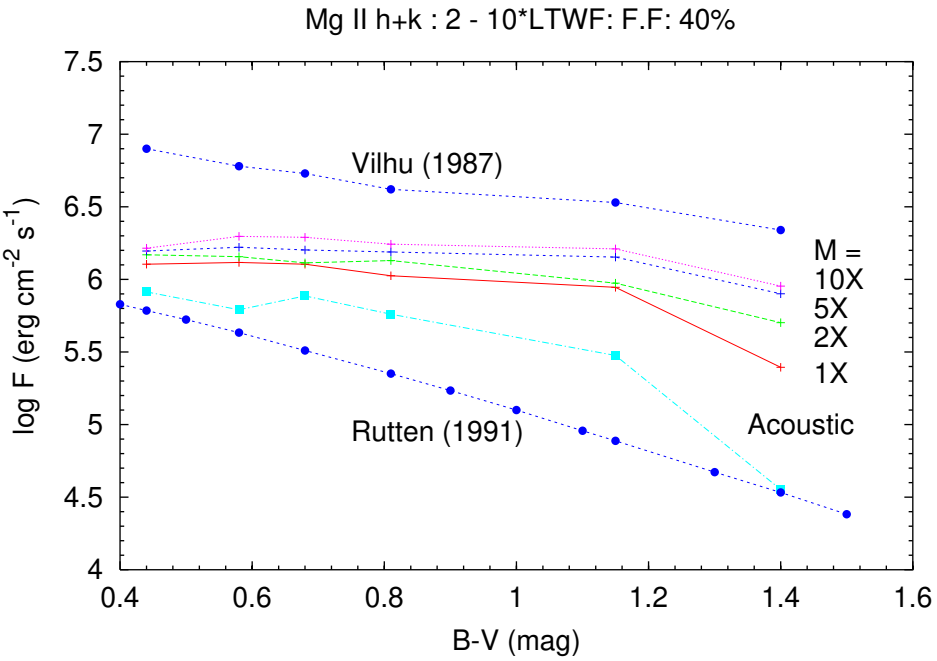

Fig. 6.11 The logarithm of Mg II h+k emission fluxes vs. $B-V$ for different input mechanical energy fluxes ($F_{tot} = M \cdot F_{LTW}$ with M = 1, 2, 5, 10), marked by 1X, 2X, 5X, 10X, respectively, showing the effect of the input longitudinal energy flux on the emitted radiative flux from two-component model atmospheres, with a 40% magnetic filling factor.

tube waves). The longitudinal waves can easily dissipate energy by forming shocks, while the transverse waves are difficult to dissipate energy (Narain & Ulmschneider 1996). A fraction of the energy carried by the transverse waves can be transformed into the longitudinal mode by a mechanism called the non-linear mode coupling. Here one needs to know the height at which the mode coupling occurs and the transformed fraction in order to compute the total longitudinal energy fluxes introduced into the atmosphere.

Preliminary computations of the longitudinal and transverse mode coupling and the formation of a joint shock from both modes have been carried out by Zhugzhda et al. (1995). However as the systematic study of the transverse wave generation for late-type stars is presently missing, we cannot be certain what amount of transverse energy couples to longitudinal energy. Recent results by Ulmschneider & Musielak (1998) show that, the transverse wave energy generated in the solar convection zone is about 30 times larger than the generated longitudinal wave flux. Yet it is clear that only a fraction of the transverse energy will be transformed to the longitudinal mode. Also, the loss of energy by leakage in non-magnetic regions will increase the acoustic heating. Cuntz et al. (1999) assumed a fraction of 10% of the generated transverse waves (for the Sun) to be mode coupled with the longitudinal waves, and used the total energy flux as an input mechanical energy to their models.

For the current computations therefore we multiply the input longitudinal energy fluxes by an arbitrary multiplication factor M to account for the contributions of other sources of wave energy mentioned above. Also, we approximate the generated wave spectra by monochromatic waves of periods which correspond to the maximum energy fluxes carried by the longitudinal waves. The choice of the wave periods is significant for the

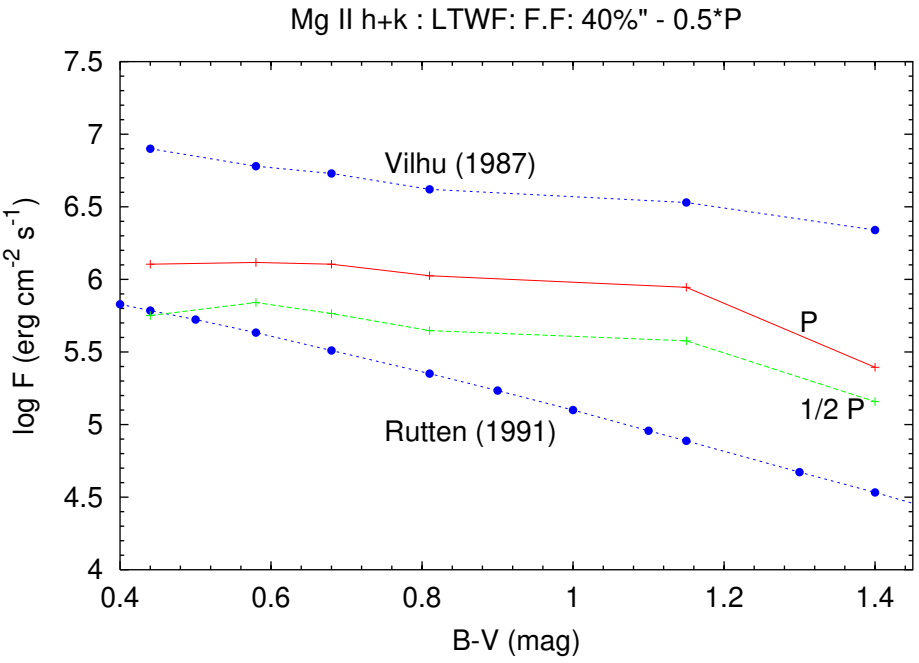

Fig. 6.12 The logarithm of the computed Mg II h+k fluxes vs. $B-V$ using half the periods used before (marked with 1/2 P - dashed line with plus sign) together with the results using the full periods (marked P - solid line with plus sign), shown also the basal flux line given by Rutten (1991) and the upper limit of individual stars given by Vilhu (1987).

wave propagation and the shock formation and dissipation. Waves with shorter periods can form shocks faster and can merge easier than with longer periods, while the shock strength is small for shorter periods. This means that the energy dissipated in form of shocks for short period waves is smaller than that of longer periods, which results in less radiative emissions (see, Fawzy et al. 1998; Fig. 2)

Figure. 6.11 shows the computed PRD fluxes for the Mg II h+k lines for late-type stars, in which the emitted fluxes are integrated over the magnetic and non-magnetic atmospheres. The presented case is for a forest of flux tubes with 40% magnetic filling factor at the surface, the flux tubes are filled randomly with different atmospheres representing different wave phases (total of 4). The results are for different values of the input total energy fluxes carried by magnetic waves $F_{tot} = M \cdot F_{LTW}$, with $M = 1,\ 2,\ 5,\ 10$ (marked by 1X, 2X, 5X, and 10X, respectively) and F_{LTW} being the energy flux carried by purely longitudinal tube waves. The lower empirical limits of Rutten (1991) together with the upper saturated limits observed for the most active stars (Vilhu 1987) are also shown in dashed lines with filled circles, the Mg II fluxes computed from one-component acoustic models are also shown as dashed lines with filled squares.

Increasing the longitudinal energy flux directly generated in the convection zone F_{LTW} results in increasing the emitted radiative fluxes, while this increasing of the radiative fluxes shows a dependence on $B-V$. For the hottest star in our sample (F5V), the emitted Mg II total flux increase only by a factor of 1.3, when F_{tot} increases by a factor of 10, while a jump by a factor of 3.6 is seen for the coolest star (M0V). The ratio of the emitted Mg II fluxes between F5V and M0V stars decreases from 5.1 to 1.8 for $M = 1$ & 10, respectively. This shows that the emitted radiative flux saturates or show

very little variations after the input mechanical energy fluxes reach a certain limit, this is can be seen in Fig. 6.11 when the value of F_{tot} increased from $5F_{LTW}$ to $10F_{LTW}$. Figure 6.27 shows the results for the Ca II fluxes.

It is clearly seen that the presence of the magnetic field enhances the heating of the outer layers of late-type stars. This is because of the low density inside the flux tubes, wave amplitudes can grow more rapidly and shocks can form easier. When we compare the emitted flux seen in the Mg II lines (see, Fig. 6.11) for the one-component model (purely acoustic heating) and two-component model (marked as 1X) we find an increase by a factor of 1.6 for the F5V star, and a factor of 7.0 for the M0V star. This small jump for the F5V star is due to the fact that in early type stars more acoustic energy is generated than generating magnetic waves because of the high turbulent velocities (Ulmschneider et al. 1996), while it is reversed for cool stars, in which the generation of magnetic waves is more efficient than generating acoustic waves.

The computations were repeated for the same cases but with half the wave periods used before. As seen in Fig. 6.12 the emitted radiative flux in the Mg II h+k lines decreases with decreasing the wave period by factors of 2.3 and 1.7 for F5V and M0V stars, respectively. This is can be explained by the decreasing shock strengths when using half periods, and the fact that the main contribution of the Mg II and Ca II emission arises from the hot part of the shock region.

6.7.3 Mg II and Ca II Emissions vs. Magnetic Filling Factor

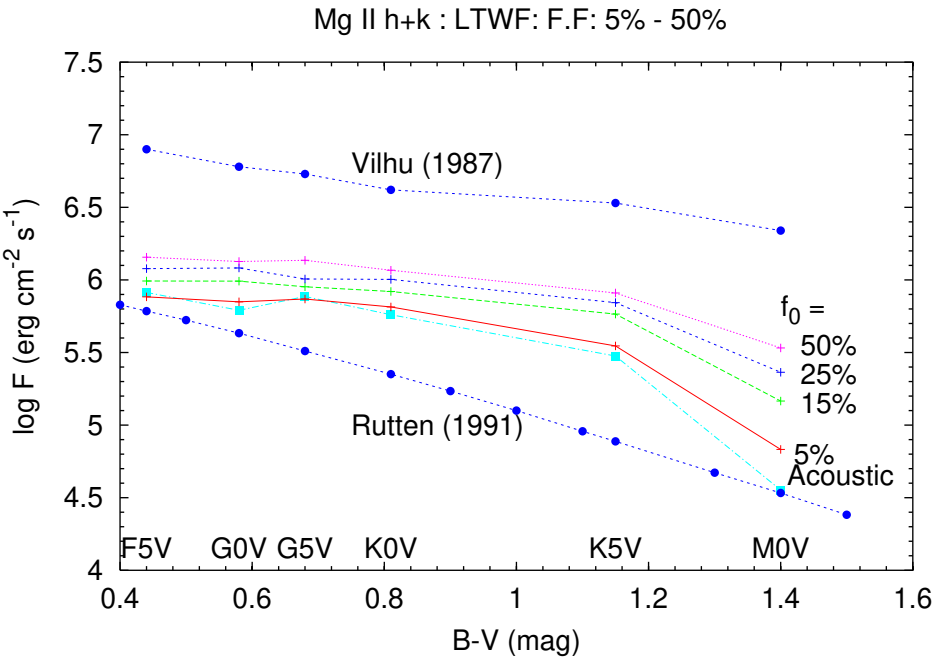

Fig. 6.13 The surface averaged Mg II h+k fluxes from late-type stars of different magnetic activities in form of different filling factors ($f_0 = 5\%,\ 15\%,\ 25\%$ and 50%). The input mechanical energy fluxes are the purely generated longitudinal tube waves energy fluxes ($M = 1$).

The presented results clearly show that the magnetic filling factor strongly affects the level of Mg II h+k and Ca II H+K emission. Figure 6.13 shows the dependence of the surface averaged Mg II h+k flux on the magnetic filling factor for different ranges of $B-V$, Fig. 6.14 shows the same dependence for the Ca II H+K flux. The emission levels increase with increasing magnetic filling factor, and decrease for a given filling factor with increasing $B-V$. The results shown in both figures are the computed surface averaged fluxes for filling factors $f_0 = 5\%,\ 15\%,\ 25\%,$ and 50% (marked with plus signs), also the computed basal fluxes (filled squares) are shown together with the lower and upper (filled circles) observed limits by Rutten (1991) and Vilhu (1987), respectively. It is clearly seen that the spread of the excess emitted flux with increasing f_0 increases with increasing $B-V$. While, solar type stars (F5V, G0V, G5V) show in general less spreading in Ca II emission (a factor of 1.4 for F5V star, when f_0 changes from 5% to 50%) in comparison with the spreading seen in Mg II emission (1.9 for the same ratio of f_0). The coolest star in our sample (M0V) shows larger spreading in Ca II emission (a factor of 5.6 when f_0 changes from 5% to 50%) than that observed in Mg II emission (a factor of 5.0 for the same ratio of f_0).

Star	$T_{\rm eff}$(K)	$\log g$	B-V	$f_0 = 5\%$	$f_0 = 15\%$	$f_0 = 25\%$	$f_0 = 50\%$
F5V	6440	4.34	0.44	$3.82 \cdot 10^5$	$4.91 \cdot 10^5$	$5.98 \cdot 10^5$	$7.17 \cdot 10^5$
G0V	6030	4.39	0.58	$3.53 \cdot 10^5$	$4.90 \cdot 10^5$	$6.05 \cdot 10^5$	$6.70 \cdot 10^5$
G5V	5770	4.49	0.68	$3.70 \cdot 10^5$	$4.49 \cdot 10^5$	$5.07 \cdot 10^5$	$6.82 \cdot 10^5$
K0V	5250	4.49	0.81	$3.26 \cdot 10^5$	$4.16 \cdot 10^5$	$5.04 \cdot 10^5$	$5.83 \cdot 10^5$
K5V	4350	4.54	1.15	$1.75 \cdot 10^5$	$2.91 \cdot 10^5$	$3.49 \cdot 10^5$	$4.07 \cdot 10^5$
M0V	3850	4.59	1.40	$3.40 \cdot 10^4$	$7.32 \cdot 10^4$	$1.16 \cdot 10^5$	$1.70 \cdot 10^5$

Table 6.3 The computed Mg II k emission fluxes for stars of different spectral types and different magnetic filling factors f_0 and $M = 1$.

Star	$T_{\rm eff}$	$\log g$	B-V	$f_0 = 5\%$	$f_0 = 15\%$	$f_0 = 25\%$	$f_0 = 50\%$
F5V	6440	4.34	0.44	$6.04 \cdot 10^5$	$6.65 \cdot 10^5$	$7.11 \cdot 10^5$	$8.68 \cdot 10^5$
G0V	6030	4.39	0.58	$5.32 \cdot 10^5$	$5.76 \cdot 10^5$	$6.57 \cdot 10^5$	$7.48 \cdot 10^5$
G5V	5770	4.49	0.68	$4.48 \cdot 10^5$	$4.89 \cdot 10^5$	$5.69 \cdot 10^5$	$7.00 \cdot 10^5$
K0V	5250	4.49	0.81	$2.59 \cdot 10^5$	$3.40 \cdot 10^5$	$4.03 \cdot 10^5$	$4.96 \cdot 10^5$
K5V	4350	4.54	1.15	$6.16 \cdot 10^4$	$1.32 \cdot 10^5$	$2.08 \cdot 10^5$	$2.32 \cdot 10^5$
M0V	3850	4.59	1.40	$8.00 \cdot 10^3$	$1.91 \cdot 10^4$	$2.41 \cdot 10^4$	$4.51 \cdot 10^4$

Table 6.4 The computed Ca II K emission fluxes for stars of different spectral types and different magnetic filling factors f_0 and $M = 1$.

The numerical results are also given in Tab. 6.3 and 6.4. Different representations have been tried to connect F_{MgII} with f_0 for each spectral type, the best representation which gives less scattering is a linear relation between $\log F_{MgIIh+k}$ and $\log f_0$. The lines shown in Fig. 6.15 represent least square linear fits with a function of the form

$$log\ F_{MgII} = a\ log\ f_0 + b \tag{6.8}$$

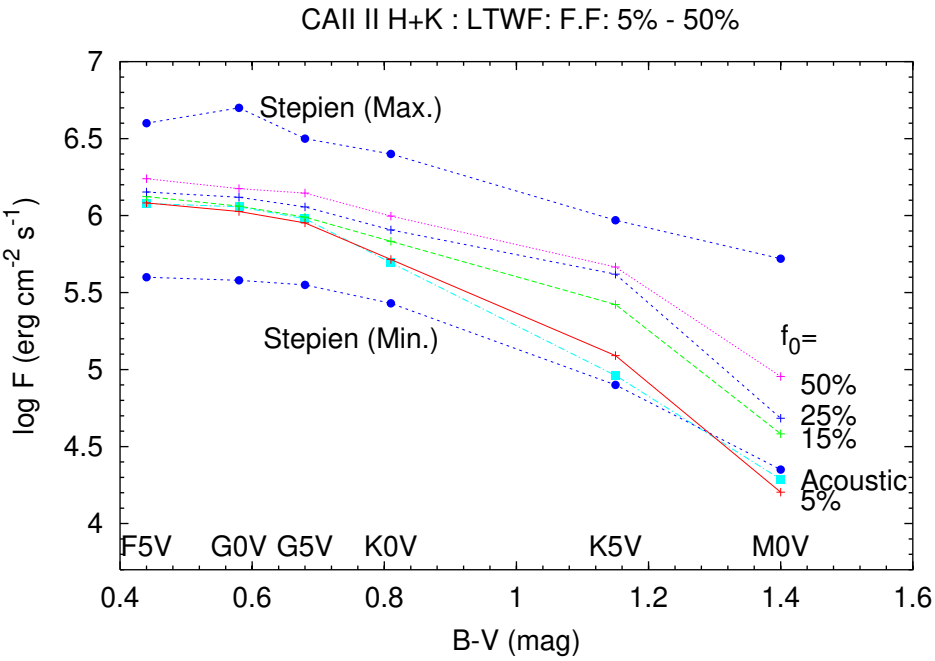

Fig. 6.14 The same as in Fig. 6.13 but for the Ca II H+K emission fluxes.

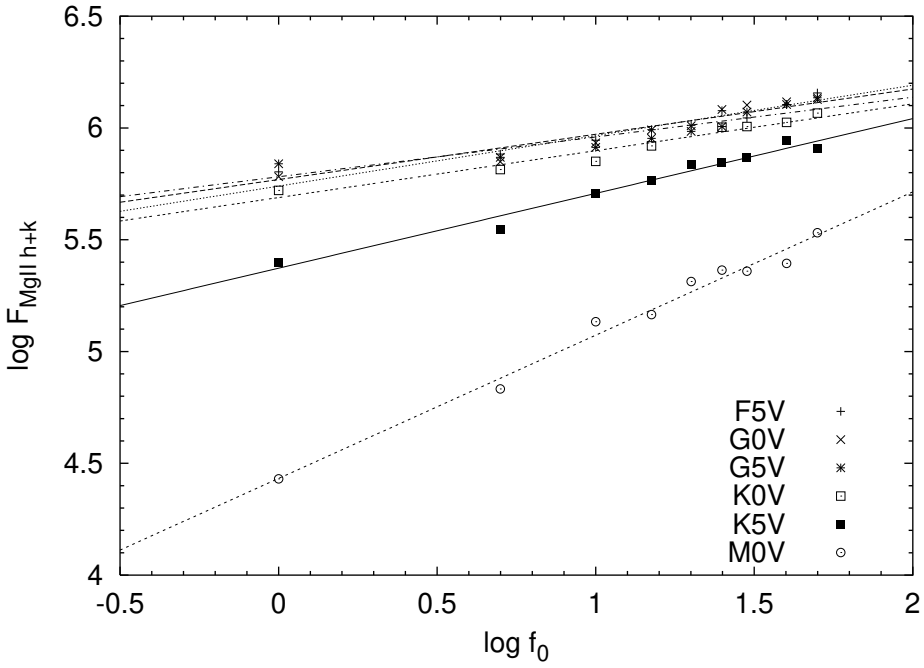

Fig. 6.15 The least square fit of the log $F_{MgIIh+k}$ emitted flux vs. log f_0 for late-type stars for $M = 1$.

Table 6.5 lists for each spectral type the coefficients a and b including the values of the standard errors. The slope, a, decreases slowly for early type stars with increasing $B-V$ and then decreases rapidly for cooler stars, the same behavior is found in the analysis of Rutten (1986) and explained as an indication for a diminishing response in Mg II emission to rotation rate (filling factor). As shown in Fig. 6.15, the dependence of Mg II emission

Star	$T_{\rm eff}$(K)	$\log g$	B-V	a	b
F5V	6440	4.34	0.44	5.769 ± 0.026	0.203 ± 0.020
G0V	6030	4.39	0.58	5.740 ± 0.028	0.226 ± 0.022
G5V	5770	4.49	0.68	5.782 ± 0.038	0.178 ± 0.030
K0V	5250	4.49	0.81	5.689 ± 0.024	0.210 ± 0.019
K5V	4350	4.54	1.15	5.373 ± 0.028	0.335 ± 0.022
M0V	3850	4.59	1.40	4.432 ± 0.038	0.641 ± 0.030

Table 6.5 Coefficients of the linear fits $\log F_{MgIIh+k} = a\ log\ f_0 + b$, for late-type stars, for $M = 1$.

on magnetic filling factor in the early spectral types (F5V, G0V, G5V) is different from that of cooler stars (K5V, M0V). This may be explained with the depth of convection zones, which play an important role in establishing the level of chromospheric emission.

6.7.4 Estimating the Rotation Periods

Based on the computed Mg II h+k fluxes for stars of different magnetic activities and an observed empirical relation between the emitted flux and rotation period, we can estimate the rotation periods which correspond to the computed fluxes. The choice of Mg II h+k fluxes for estimating the rotation periods is better than choosing the Ca II H+K fluxes, as for the observed Ca II flux the photospheric emission must be subtracted to obtain the net chromospheric flux which is not the case for Mg II, where the photospheric background emission is much smaller and can be neglected, this results in more accurate empirical relation between the Mg II flux and rotation period.

The analysis of the Mg II emission fluxes for stars with well determined rotation periods by Hartmann et al. (1984) show a power-law relation between the average surface flux normalized by the bolometric emission ($R_{hk} = F_{hk}/(\sigma T_{eff}^4)$) and the rotation period P as

$$log\ R_{hk} = a\ P + b \tag{6.9}$$

and the coefficients of the least square fit have different values depending on $B - V$ as shown in Tab. 6.6 (Hartmann et al. 1984; Tab. 4).

$B - V$ Range	a	b
$0.64 \leq B - V \leq 0.77$	-0.022 ± 0.004	-4.097 ± 0.052
$0.58 \leq B - V \leq 0.60$	-0.051 ± 0.009	-4.006 ± 0.095
$B - V \geq 0.64$	-0.013 ± 0.002	-4.177 ± 0.042

Table 6.6 The coefficients of the least square fits to observed chromospheric emission, from: Hartmann et al. (1984); Tab. 4.

Using the above empirical relation of Hartmann et al., we estimated the values of the rotation periods for G & K stars from our computed Mg II h+k fluxes representing different magnetic activities and for $M = 1$, the results are shown in Tab. 6.7

Star	$P(f_0 = 5\%)$	$P(f_0 = 15\%)$	$P(f_0 = 25\%)$	$P(f_0 = 50\%)$
G0V	19.9	17.1	15.3	14.5
G5V	38.2	34.3	31.9	26.0
K0V	49.6	41.7	35.5	30.9
K5V	44.4	27.7	21.7	16.7

Table 6.7 The estimated rotational periods P (in days) based on the empirical relation by Hartmann et al. (1984) for G & K spectral types and $M = 1$.

Star	$P(M = 1)$	$P(M = 2)$	$P(M = 5)$	$P(M = 10)$
G0V	14.7	13.9	12.6	11.2
G5V	27.4	27.0	22.9	18.9
K0V	33.9	26.2	21.8	17.8
K5V	14.0	11.9	-	-

Table 6.8 The estimated rotational periods P (in days) based on the empirical relation by Hartmann et al. (1984) for G & K spectral types of magnetic filling factors $f_0 = 40\%$ and different values of M (M = 1, 2, 5, and 10).

We examined the variation of the rotation periods for different values of M (M = 1, 2, 5, and 10) and $f_0 = 40\%$. As shown in Tab. 6.8, the rotation periods decrease with increasing M as a result of increasing the emitted Mg II h+k flux with M. The estimated rotation periods for stars which possess the highest magnetic activity in our sample ($F_{tot} = 10 \cdot F_{LTW}$ and $f_0 = 40\%$) are shown in the last column of Tab. 6.8. The rotation period is shorter by a factor of 0.77 for G0V type than that which corresponds to $F_{tot} = F_{LTW}$ and $f_0 = 50\%$, and a factor of 0.73 for G5V type, while K0V type has a shorter period by a factor of 0.53. The computed Mg II h+k fluxes for the cases of $M = 5$ & 10 for K5V stars in our sample are out of the range of the observed fluxes, and not covered by the empirical formula given by Hartmann et al. (1984).

6.7.5 The Relationship between Mg II and Ca II fluxes

The radiative emission fluxes originating from the different outer atmospheric layers are found to be highly correlated for the majority of cool stars as shown by many studies (e.g., Oranje 1985; Schrijver 1987; Cappelli et al. 1989). It has been found that most the flux-flux relations between two diagnostics A_i and A_j formed at two different layers of the atmosphere follow a power law relation of the form (Schrijver & Zwaan 2000)

$$A_j = c_{ij}(A_i)^{e_{ij}} \tag{6.10}$$

This relation is very sensitive to units in which it is expressed, for example Schijver et al. (1992) found a linear relationship ($e_{ij} = 1$) between the nearly simultaneous measurements of the IUE Mg II h+k excess fluxes (with subtracted basal fluxes) and Mount Wilson Ca II H+K excess fluxes for a sample of F5-K3 main sequence stars. The value of e_{ij} exceeds unity as the difference in formation temperatures of the diagnostics used increases

(Schijver & Zwaan 2000), this is clearly seen in the relation between the soft X-ray flux density measured by the EINSTEIN/IPC and the Mt. Wilson Ca II H+K flux density ($e_{XCa} = 1.67$).

The relationships between the computed Mg II and Ca II emission fluxes for main sequence stars are displayed in Fig. 6.16 for different magnetic activities (i.e., different filling factors f_0). Straight lines are the least-squares best fits to the data of the form:

$$log\ F_{CaII} = a\ log\ F_{MgII} + b \tag{6.11}$$

where the coefficients a & b depend on the filling factor as shown in Tab. 6.9. This shows that Mg II is directly proportional with Ca II and they are well correlated. At the minimum Ca II H+K flux, the Mg II h+k core emission still shows higher fluxes.

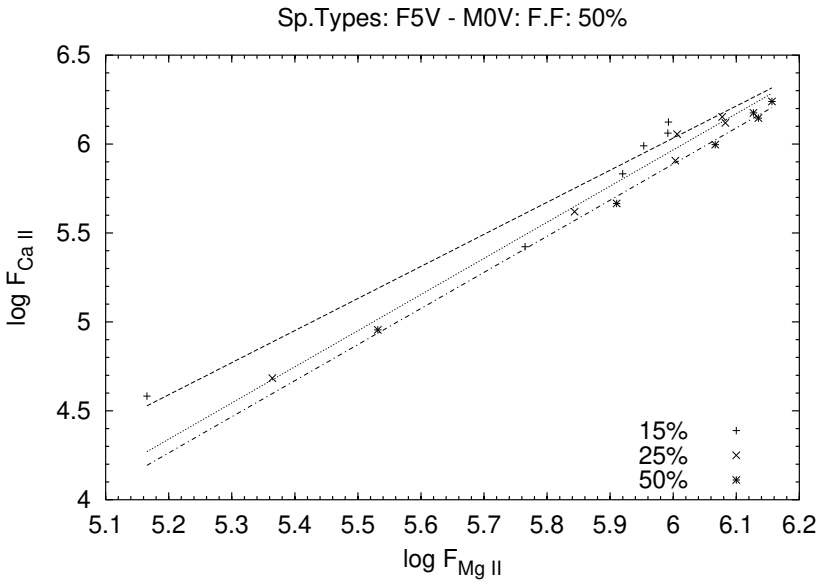

Fig. 6.16 The least square fit of log Ca II H+K emission fluxes vs. log Mg II h+k fluxes for late-type stars of different magnetic activities (i.e., $f_0 = 15\%$, 25%, and 50 %) for $M = 1$.

$f(\%)$	a	b
5	1.748 ± 0.065	-4.333 ± 0.387
15	1.804 ± 0.164	-4.789 ± 0.953
25	2.033 ± 0.090	-6.231 ± 0.534
50	2.030 ± 0.065	-6.293 ± 0.387

Table 6.9 The coefficients of the linear fits log $F_{CaII} = a\ logF_{MgII} + b$, for late-type stars and $M = 1$.

The slope a of the fitted lines shows a small variation with f_0, it increases with increasing f_0, and the scatter around the best fitted line is smaller for larger values of f_0. This suggests that the correlation is higher for larger values of f_0. It also suggests that the degree of the magnetic activity determines the nature of the flux-flux relationships, or in other words the rotation rate which controls the magnetic activity is the main key for determining such relationships. Fig. 6.16 shows the best fit of the data for late-type

stars which posses different magnetic activities expressed here in terms of the magnetic filling factor as $f_0 = 15\%,\ 25\%$, and 50 %, with the input total wave energy fluxes being the energy carried by purely longitudinal waves without including additional sources of energy ($M = 1$).

Zwaan (1983) argued that, the flux-flux relationships suggest that one activity parameter controls the structure of the outer atmosphere. This parameter varies along the flux-flux relationships and can be determined by the stellar rotation rate which is the primary key determining the dynamo mechanism. Schijver & Zwaan (2000) also suggest the existence of an activity parameter Υ, and they expected that the excess flux density ΔF_i depends on Υ through a power law relationship of the form

$$\Delta F_i = a_i \Upsilon^{b_i(T_f)} \tag{6.12}$$

where $b_i(T_f)$ is a function of the formation temperature T_f of the diagnostic i. The activity parameter Υ is a function of at least stellar the rotation rate and stellar structure.

6.7.6 The Computed Mg II k and Ca II K Profiles

The intensity profiles of the Mg II k line vary strongly for different angles, so in our treatment of the radiative transfer we use five angles ($\cos\alpha = \mu = 0.9$, 0.7, 0.5, 0.3, and 0.1) to compute average profiles. This also ensures that all parts of the stellar surface contribute to the integrated profiles. Figure. 6.17 shows the computed Mg II k line profiles from a two-component chromospheric structure for different angles, and for a G5V star with magnetic filling factor $f_0 = 20\%$. The line intensity increases with decreasing μ. Observing the flux tubes at large angles results in stronger emission lines, this can be explained as for large angles, the rays intersect a larger number of flux tubes, which results in higher contributions from magnetically heated regions to the total flux.

The intensity of the emitted Mg I k lines increases with decreasing $B - V$. As shown in Fig. 6.18, the coolest star in our sample (M0V) shows very weak emission lines, this emission becomes stronger when the magnetic filling factor increases, and can be seen in Figs. 6.18 & 6.19. Varying the magnetic filling factor from 10% to 40% results in stronger emission lines by a factor of about 2 for the coolest star M0V and a factor of 1.5 for the hottest one. The stronger emission for larger filling factors owing to the relatively small voids between the tubes (Cuntz et al. 1999).

Figures 6.20, 6.21, and 6.22 show the computed Mg II k emission lines for stars of spectral types F5V, K0V, and M0V, respectively as a function of the magnetic filling factor ($f_0 =$ 5%, 15%, 30%, *and* 50%). For all spectral types, the emitted lines become stronger with increasing f_0. The computed Ca II K line profiles for spectral types F5V, K0V and M0V, with different values of f_0 ($f_0 = 5\%,\ ,15\%,\ 25\%$, and 50%) are shown in Figs. 6.23, 6.24, and 6.25, respectively. The intensity of Ca II K lines is higher than that of the Mg II k lines for F5V stars and K0V, while for M0V it is getting weaker.

6.7.7 Upper Limits of Mg II and Ca II Emission Fluxes

In addition to the previously mentioned lower limit of the observed chromospheric line emission, an observed upper limit is clearly seen in the flux vs. color diagrams. Single

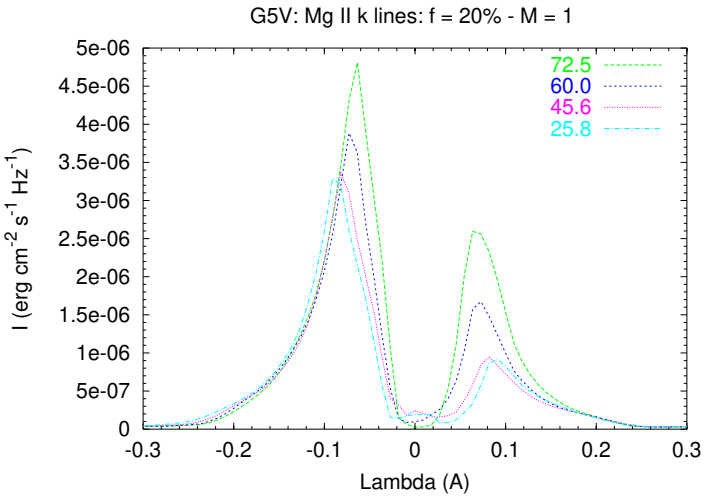

Fig. 6.17 Mg II k line profiles for different angles α for a star of spectral type G5V and magnetic filling factor $f_0 = 20\%$ and $M = 1$.

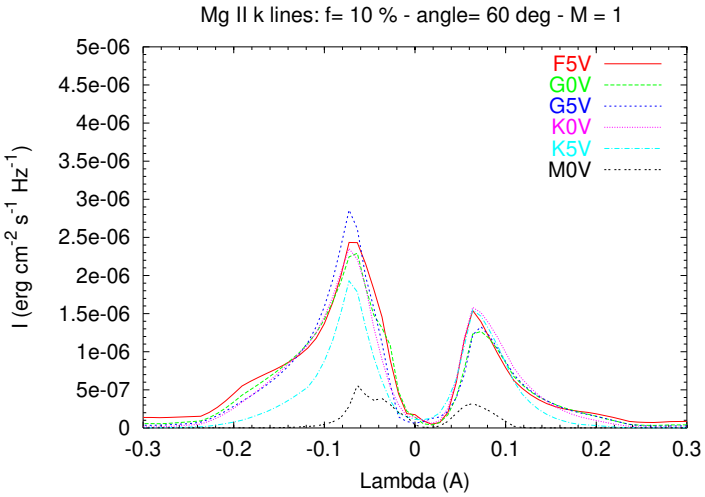

Fig. 6.18 Mg II k line profiles for stars of different spectral types, and the same magnetic filling factor $f_0 = 10\%$, for an angle of 60^0 and $M = 1$.

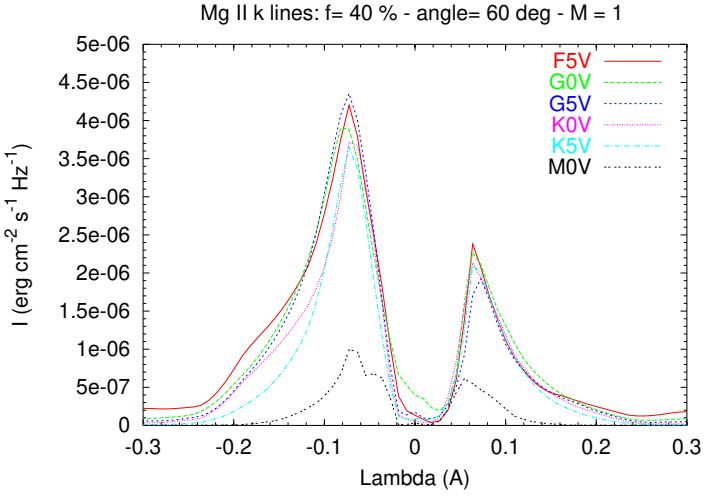

Fig. 6.19 The same as in Fig. 6.18 but for magnetic filling factor $f_0 = 40\%$ and $M = 1$.

and binary stars of spectral types F-M and luminosity classes V-III were surveyed by Vilhu (1987) looking for the stars with strongest chromospheric and coronal emission. The sample includes also contact binaries and T Tauri stars. The chromospheric Mg II emission fluxes, the transition region C IV emission fluxes as well as the coronal X-ray

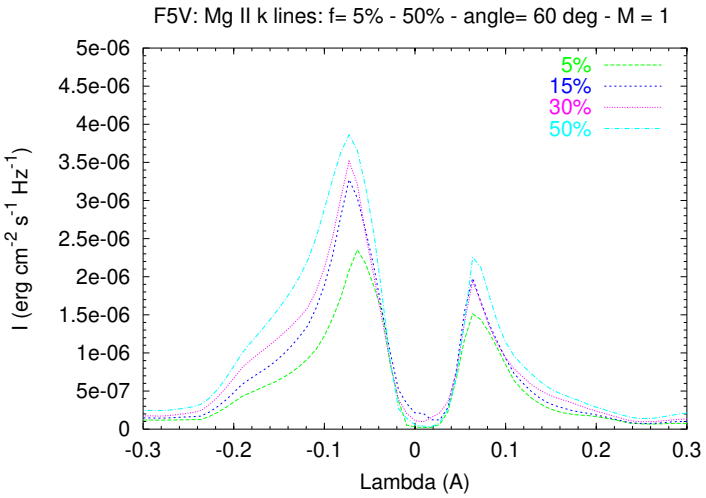

Fig. 6.20 The variation of the Mg II k emission line intensity I ($erg\ cm^{-2}\ s^{-1}\ Hz^{-1}$) with the level of magnetic activity. Stars of spectral type F5V and different filling factors are shown (i.e. $f_0 = 5\%,\ 15\%,\ 30\%$ and 50%), for $\alpha = 60^0$ and $M = 1$.

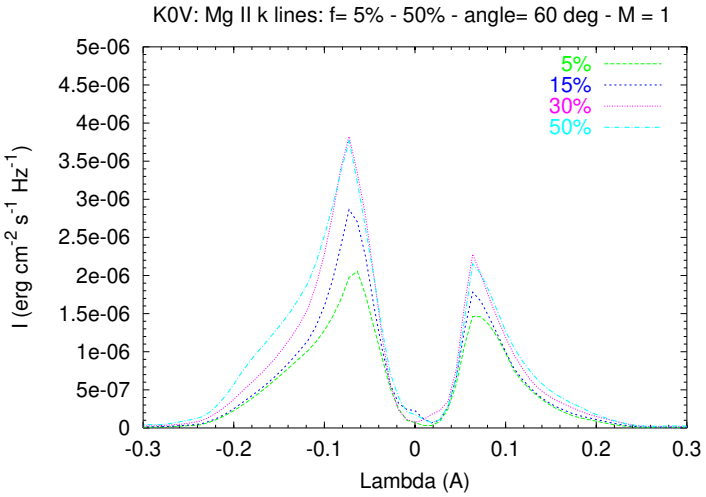

Fig. 6.21 The same as in Fig. 6.20 but for spectral type K0V.

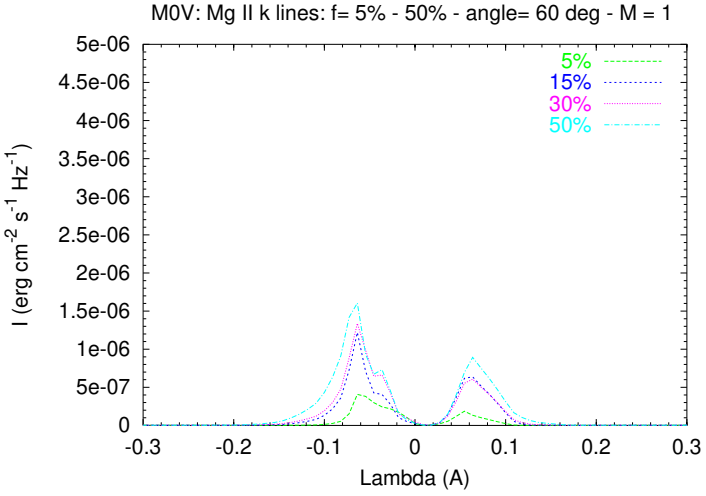

Fig. 6.22 The same as in Fig. 6.20 but for spectral type M0V.

fluxes show clear upper boundaries (Fig. 1.3). T Tauri stars lie far above the observed upper limit of the single and binary stars, because their activities have a different origin (accretion). The upper boundary is occupied by the fastest rotators, mainly by contact binary stars which have additional source of emission because their rotation rate (spin)

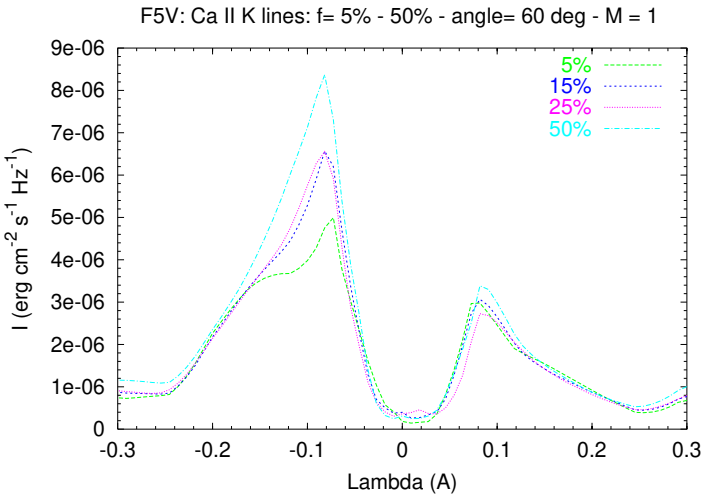

Fig. 6.23 The variation of the Ca II K emission line intensity I ($erg\ cm^{-2}\ s^{-1}\ Hz^{-1}$) with the level of magnetic activity. Stars of spectral type F5V and different filling factors are shown (i.e. $f_0 = 5\%,\ 15\%,\ 25\%$ and 50%), for $\alpha = 60^0$ and $M = 1$.

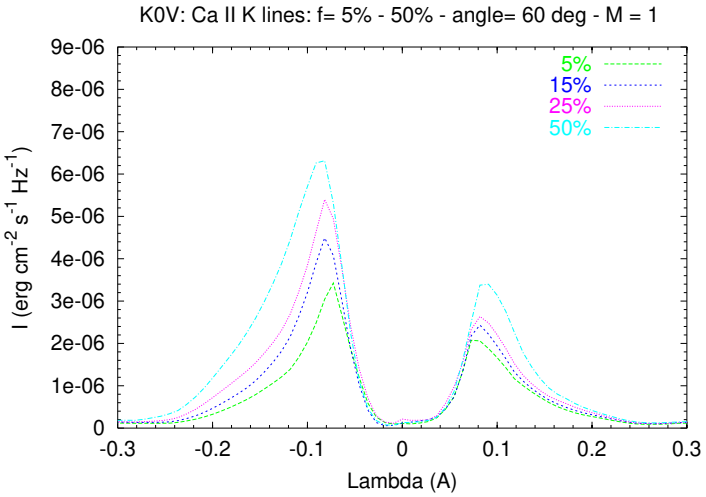

Fig. 6.24 The same as in Fig. 6.23 but for spectral type K0V.

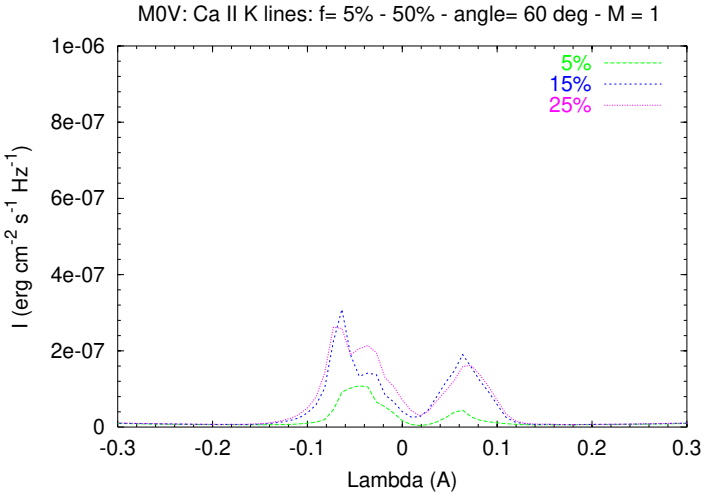

Fig. 6.25 The same as in Fig. 6.23 but for spectral type M0V.

is increased due to the spin - orbit interaction in the binary system.

In an analysis by Doyle (1987) for the Mg II flux of main sequence stars, a saturation limit is observed to occur at a rotation period of ≈ 4 days for main sequence stars (see, Doyle (1987); Fig. 1). This saturation is explained to be a saturation of the dynamo

mechanism or, the star's surface is completely covered with magnetic structures (f tends to be close to 1).

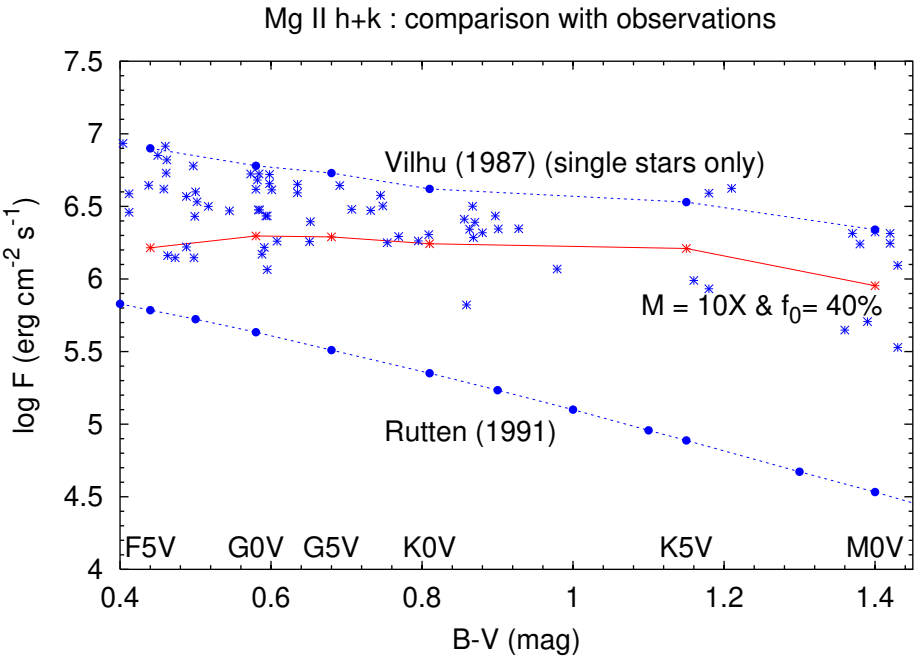

Fig. 6.26 The theoretical upper limit of Mg II h+k emission fluxes reached by our models in comparison with observed upper limit by Vilhu (1987) and lower limit by Rutten (1991). The observed single stars by Vilhu are marked with * -sign.

As our computations are only carried out for single stars, for a comparison with the observed upper limit of Mg II by Vilhu (1987), we have to exclude the contact and detached binary stars from the sample and redraw the upper limit for single main sequence stars. The results are shown in Fig. 6.26 for the highest activity levels reached by our model ($F_{tot} = 10 \cdot F_{LTW}$ and $f_0 = 40\%$) together with the observed upper limit of Vilhu and the observed lower limit of Rutten (1991).

We also compare our computed Ca II H+K fluxes with observations collected by Stepien (2000; private communication) for the most and least active main sequence stars. Such a comparison is shown in Fig. 6.27 for different input mechanical energy fluxes ($F_{tot} = M \cdot F_{LTW}$, with $M = 1,\ 2,\ 5,\ 10$; marked by 1X, 2X, 5X, and 10X), for stars with $f_0 = 40\%$. Figure 6.28 shows the computed lower and upper limits reached by our models together with the full set of observations collected by Stepien.

A noticeable gap between our computed upper limits and the observed limits is seen, especially for hot stars, this gap is smaller for the Ca II lines (≈ 0.25 in log-scale for F5V stars) and larger for Mg II lines (≈ 0.70 in log-scale for same stars). For cool stars (K5V & M0V) we are able to recover the observed upper limit for Ca II lines with input mechanical energy flux $F_{tot} = 10 \cdot F_{LTW}$, while for hotter stars, still noticeable differences exist which in general less than those differences found for Mg II lines.

These differences may be due to the following reasons : (1) As mentioned by Vilhu (1987), the saturated stars which occupy the upper limit of the emitted flux, seem to be filled with magnetic field of strength equal to the equipartition field strength and the

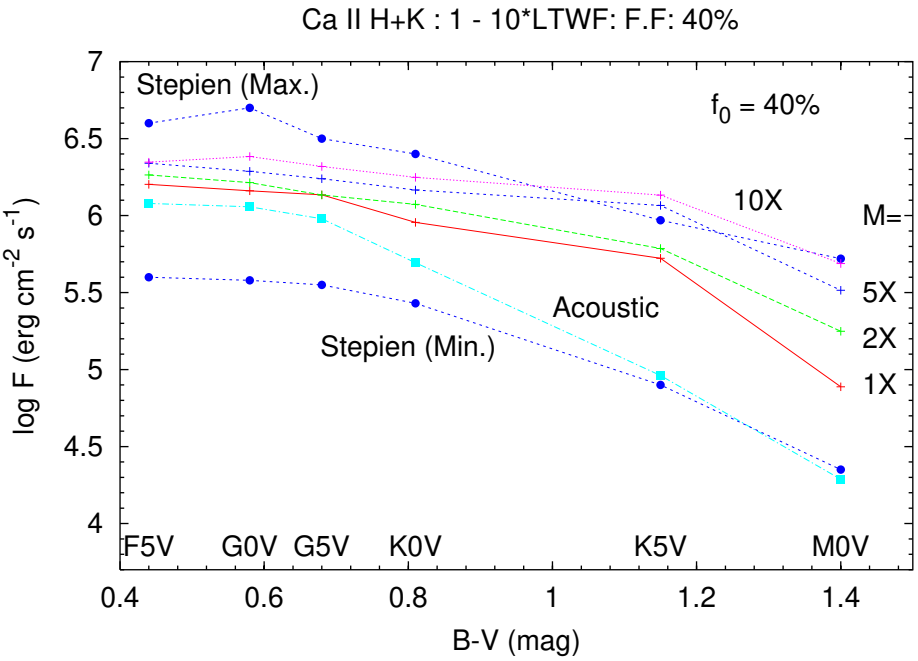

Fig. 6.27 The variation of the computed upper limit of Ca II H+K emission fluxes with the input mechanical energy, together with the upper and lower limits of the observed Ca II fluxes by Stepien (2000; private communication), the computed lower limit is also shown (dashed line with filled squares).

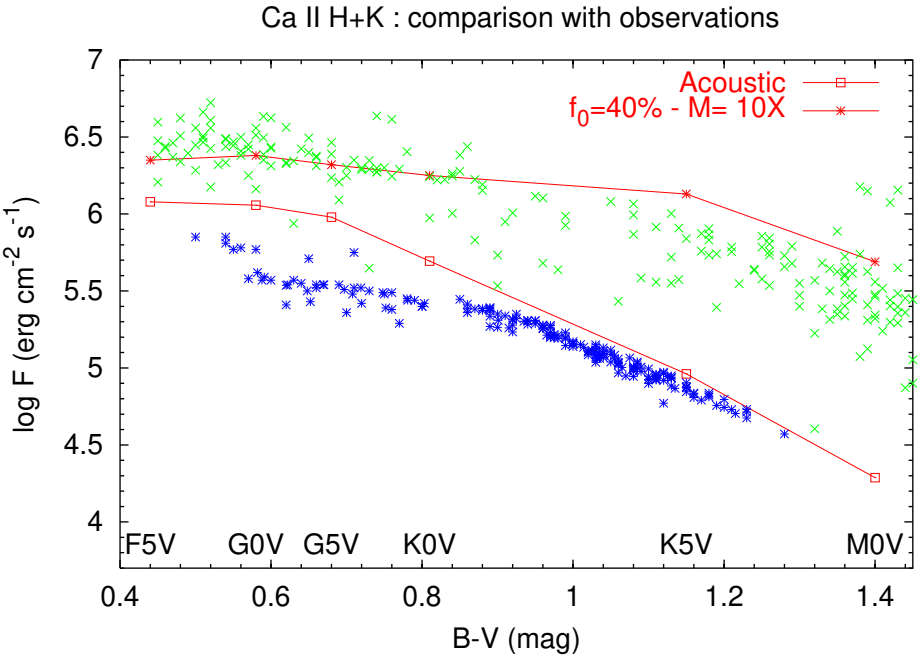

Fig. 6.28 The theoretical upper and lower limits of Ca II emission fluxes in comparison with observations collected by Stepien (2000; private communication).

whole surface is used to heat the outer layers. In our models, the magnetic field strength is assumed to be 0.85% of the equipartition field strength similar to the Sun, which may not be the case for stars with higher levels of activities.

(2) The Mg II lines form at greater heights in the atmosphere compared to the Ca II lines which form at lower layers (lower temperatures), because the ionization potential of Mg II (15.04 eV) is larger than that of Ca II (11.87 eV). As the wave energy flux decreases with height, the efficiency to heat the upper layers by only waves might not be sufficient, so other heating mechanisms existing at great heights will take over. At the heights of Mg II formation, the magnetic reconnections might start to be an important heating mechanism especially for active stars.

(3) Our monochromatic computations may be inadequate. However it is presently a good approximation because it avoids the mishandling of the large shock strengths obtained in the treatment of Theurer (1998) when time-dependent ionization is not treated.

(4) The upper limit of the magnetic filling factor used in our models is 40%, while for the very active stars; which occupy the observed saturation limit; the magnetic filling factors may be even closer to unity, filling factors up to 80% were observed by Saar (1987) for some very active stars.

(5) All the computations are done for non-magnetic convection, while the inclusion of the magnetic field for rapidly rotators might be important.

(6) In our NLTE treatment, we assume a two-level representation for the Ca II and Mg II emission lines. On the other hand a comparison between a five-level treatment for the Ca II K_2 emission and the two-level one (Solanki et al. 1991) shows that emission is stronger in the the five-level treatment, so we expect that our computed fluxes could be closer to observations when using a more sophisticated multi-level treatment.

We can also suppose that waves alone may account for the observed chromospheric emission Mg II and Ca II fluxes for stars of moderate activity levels. while for higher activity levels additional heating mechanisms might work together with waves to account for the large chromospheric losses. Therefore, up to the Ca II formation height, the most reasonable explanation is that waves alone are the important heating mechanism, while in the upper layers additional non-wave heating mechanisms come into play. Observations of the turbulent events in the Sun (Innes et al. 1997) as well as the observations of stellar C IV lines by Wood et al. (1997) show that at the height of the upper chromosphere and transition layer other heating mechanisms take role.

6.8 Other Possible Heating Mechanisms

The whole zoo of possible additional heating mechanisms are described by Narain & Ulmschneider (1990 & 1996). Among these magnetic reconnection appears most likely. For rapidly rotating (highly active) stars, the heating of the stellar chromospheres by longitudinal tube waves alone might not be sufficient. One of the most important mechanisms which might be responsible for heating the outer layers of highly active stars is the energy released from magnetic reconnections. Random flows in the photosphere bring together the footpoints of two magnetic flux tubes, if these footpoints have opposite polarities, reconnection is possible (Roald et al. 2000) and the magnetic energy then converts into plasma kinetic energy. It has been found that the energy released in reconnection in the chromosphere and photosphere is sufficient enough to contribute to the heating of outer

layers (Sturrock 1996).

The analysis of the spectra obtained by the Naval Research Laboratory's High Resolution Telescope and Spectrograph (HRTS) of solar active regions by Brueckner (1981) shows the existence of what is called "explosive events" seen in the C IV spectrum over a plage, with observed velocities of about 200 km s^{-1}. These explosive events cover only a small fraction (less than 1%) of the solar surface. He also mentioned that the explosive events might be caused by MHD instabilities rather than shock waves, and they could be a source for ejecting plasma outward. Recent observations by SUMMER onboard SOHO (Innes et al. 1997) shows that magnetic reconnection might be responsible for the observed plasma jets in explosive events in the solar chromosphere and transition region.

A recent study by Litvinenko (1999) shows that for the quiet Sun, magnetic reconnection takes place in a slab of 100 km thickness and is more efficient around the temperature minimum region at height $z \approx 600$ km above the photosphere. He also show that reconnection is inhibited below the temperature minimum region because of the high plasma density and also above this region because of the high electric conductivity.

Wang & Shi (1993) show that slow reconnection takes place continuously in the solar photosphere, while bursts of rapid reconnection occur in the transition region or in the lower corona. Fast reconnection models for flare energy release in the corona have been confirmed by Yohkoh observations (e.g., Tsuneta 1996).

A two-dimensional MHD simulation of a solar flare by Yokoyama & Shibata (1998) shows that the flare energy is released by the magnetic reconnection mechanism and part of the released energy is transported into the chromosphere by heat conduction.

Similar phenomenae like that observed on the Sun (e.g. explosive events) have been observed for late-type stars. Wood et al. (1997) found in the spectra of late-type stars that the Si IV and C IV lines formed around 10^5 K can be decomposed into two components, a broad component and a narrow one. The large widths of the broad component suggests the presence of supersonic velocities, which they explained as being due to jets of plasma expelled from magnetic reconnections. The widths of these components show variation with the magnetic activity, which suggests that the heating mechanism is tight to magnetic activity.

From the above, one can conclude that photospheric reconnection may contribute significantly to the heating of the chromosphere and also part of the energy released at the height of the corona might be transformed back to the chromosphere by heat conduction and contribute to the heating of the chromosphere. These speculations might be also valid for late-type stars as similar phenomenae like the Sun were observed.

Chapter 7

Conclusions

In the current work, we have studied the generation and propagation of longitudinal tube waves in late-type stellar atmospheres, as well as the rotation-emission activity relation. A completely theoretical and self- consistent study is performed which starts from the first stages of the wave generation in the convection zone, going through the stage of their propagation along field lines, till the last stage of computing the observed emission line fluxes as a result of shock formation. Each stage works as a boundary condition for the next one. In addition, we studied the relation between the surface magnetic filling factor and the emitted Ca II and Mg II lines. We also predict rotational periods of G- and K-type stars based on our computed fluxes. The relation between the rotation period and the emitted fluxes from outer layers has been known from observations of late-type stars for quiet a long time and was in need to be proved from theoretical simulations.

7.1 The Generation of Longitudinal Tube Waves

The interaction between magnetic flux tubes and the turbulent medium of the convection zone is identified as a source of the generation of longitudinal tube waves. Based on the approach developed by Ulmschneider and Musielak (1998), we computed the energy fluxes carried by longitudinal tube waves for stars of gravities $logg = 3,\ 4,\ 5$ and temperature range from $T_{eff} = 3500$ K to $T_{eff} = 7000$ K.

The conclusions of calculations of the longitudinal wave energy generation for late-type stars are as follows:

- The generated wave energy fluxes are higher for hot stars because of the higher turbulent velocities in comparison with cool stars. The sharp increase of the magnetic field strength and the decrease of the turbulent velocities for cool stars results in a decreasing of the generated energy fluxes.

- Stars with low surface gravity have larger wave fluxes than stars with higher gravity, this is because of a larger convective velocities which results in larger turbulent velocities.

- The increase of magnetic field strength results in a stiffer flux tube as a result of decreasing gas density inside the tube, therefore the tube is harder to squeeze, and the generated fluxes decrease.

7.2 The Heating of Magnetic Flux Tubes

The generated wave energy fluxes are used as input mechanical energy fluxes for constructing model chromosphere. In Chapter 3, we studied the propagation of the adiabatic and radiatively damped longitudinal waves along flux tubes and the heating of the solar chromosphere. The main results of this study can be drawn as follows:

- The chromospheric line losses were computed assuming a pseudo-PRD procedure in which the line wings are cut artificially. The scaled Mg II , Ca II and Fe II lines losses are assumed to be representative for the total chromospheric line losses. A comparison with the empirical models of Anderson & Athay (1989) shows that Mg II h+k line losses are represented well by 2 times the Mg II k line losses, 5 times the Ca II K line losses represent well the 5 lines of Ca II (H, K, and 3 IRT), also it has been found that 5 times the Ca II K line losses represents the total Fe II losses.

7.2.1 Adiabatic and Radiatively Damped Longitudinal Tube Waves

Different flux tube models (of constant cross-section, of filling factor $\approx$ 2.8%, and an exponentially spreading flux tube) representing different regions of the solar active regions were constructed and heated by various wave energy fluxes and different monochromatic wave periods. A new treatment of radiation is implemented in our computations, which takes into account the PRD effects and is much less time consuming. The main results are as follows:

- The geometry of the magnetic flux tubes plays an important role in the heating of outer stellar layers. The *constant cross-section* tube has the maximum efficiency for heating upper layers, the *exponential* tube does not show any heating, while the *wine-glass* tube of filling factor $\approx$ 2.8% shows less efficiency than that of the constant-cross section and remarkable heating compared to that of the exponential tube.

- Increasing the wave period results in an increasingly steeper chromospheric temperature rise, while the increase of the wave energy leads to shock formation at lower heights.

- The decrease of the magnetic field strength results in an increase of the shock formation height, the reason for that is lowering the field strength results in increasing the gas density inside the tube, which which in turn leads to lower wave amplitudes and then to a delay in the shock formation.

- The emission of Mg II and Ca II increases with increasing filling factor, the line cooling rates increase by a factor of about 7.4 from a magnetic filling factor 1% to a 20% filling factor.

7.3 Chromospheric Resonance Oscillations

The response of the magnetic and non-magnetic chromospheres of the Sun and two stars of spectral types F5V and M0V to the excitation by small and large amplitude monochromatic and wave spectra is studied and the following results are found

7.3.1 Small Amplitude Waves

- The excitation by small amplitude waves (frequency $\nu = 1$ mHz) results in resonance oscillations around the acoustic and Defouw cut-off frequencies of these atmospheres, for acoustic and longitudinal tube waves, respectively.

- Over a short period of time, one gets an exciting component and a resonance component. The exciting waves decay faster with height in the magnetic atmosphere than in the non-magnetic atmosphere. After long time (depends on the temperature gradient of the atmosphere), the resonance oscillation decays with time t as $t^{-3/2}$ for the solar case, and only the exciting component is seen in the velocity power spectrum.

- The excitation of the non-magnetic atmospheres by wave spectra (with velocity amplitudes following Gaussian distribution which is cut at low frequencies) show oscillations with frequencies in the range of 4.5 - 5.5 mHz for F5V stars, around 7.5 mHz for the Sun, and with frequencies in the range of 8.5 - 10.0 mHz for M0V stars.

- The excitation of the magnetic atmospheres show oscillations with longer period, which is in the range of 5.5 - 6.0 mHz for the Sun.

7.3.2 Large Amplitude Waves

The excitation by large amplitude waves shows the existence of a critical period which determines the behavior of the resonance oscillations. The excitation by waves with periods greater than this critical period results in an atmospheric resonance which decays rapidly with time, while a persistent resonance is found when the exciting waves have periods smaller than the critical period.

- The non-magnetic atmosphere of the Sun shows resonance oscillations around 6.5 mHz, while the chromosphere of F5V stars show oscillations around 5.0 mHz and 11.0 mHz for M0V stars. The magnetic atmospheres show oscillations with lower frequencies, which are 6.0, 4.5, and 10.0 mHz for the Sun, F5V, and M0V stars, respectively.

7.4 Stellar Chromospheric Models

The time-dependent models of magnetically heated chromospheres of late-type stars are constructed and shows the following features.

- The emission of the continuum and lines radiation show two zones with respect to height. At low heights the H^- radiation is dominant. At greater heights where the temperature increases, radiation by ionized atoms (Mg II, Ca II, and Fe II) is dominant.

- All late-type stars show a monotonically increasing time-averaged temperature rise with height. A steeper rise is seen for cool stars.

7.5 The Rotation - Emission Activity Relation

Two-component model atmospheres (magnetic & non-magnetic) are constructed and the integrated Mg II and Ca II fluxes emitted from a forest of magnetic flux tubes are computed for late-type stars of different magnetic activities. From this study, we can conclude the following points.

- A new basal flux line for the Mg II fluxes is computed and shows a good agreement with the empirical values of Rutten (1991) for F5V, G0V, and M0V stars, while a deviation still exists for other spectral types.

- Increasing the longitudinal energy flux by different factors results in increasing the emitted radiative fluxes for each $B-V$. The Mg II flux increase by a factor of 1.3 for F5V stars when the input flux increases by a factor of 10, and by a factor of 3.6 for M0V stars for the same ratio of the input flux. The ratio of the emitted Mg II fluxes between F5V and M0V stars decreases from 5.1 to 1.8 when the input energy increases by a factor of 10, this means that the emitted flux saturates or show very little variations after the input energy reaches a certain limit.

- The presence of the magnetic field enhances the heating of the outer layers, it has been found that the computed Mg II flux increases by a factor of 7.0 for M0V when two-component model atmospheres are used instead of one-component acoustic models. This factor decreases to 1.6 for F5V stars, because of the increasing efficiency of acoustic wave generation with increasing the effective temperature.

- The least square fits between the emitted Mg II fluxes F_{MgII} and the surface magnetic filling factor f_0 is found to be of the form $log\ F_{MgII} = a\ log\ f_0 + b$, with color dependent coeffcients a and b.

- The rotation periods of G- and K- type stars are estimated from our computed Mg II fluxes and show a decreasing in the rotation period with increasing the surface magnetic filling factor and input mechanical wave energy fluxes.

- The relationship between the emitted Mg II and Ca II is found to be linear, which indicate that the source of activity of both lines is the same.

- The computed Mg II and Ca II profiles are presented for the stars of different spectral types and different magnetic activities.

- Comparing the observed upper limit of chromospheric emission in Ca II (Stepien 2000; private communication) with the theoretical Ca II fluxes from a 'maximum wave case', that is a case where we have a filling factor of 40% and where the longitudinal wave flux has been enhanced by a factor of 10 due to mode-coupling from transverse waves, we are able to reproduce the observations. This shows that MHD wave heating is able to explain the chromospheric Ca II emission in rapidly rotating stars.

- Comparing the observed upper limit of chromospheric emission in Mg II (Vilhu 1987) with our theoretical simulations for the 'maximum wave case' we however found a gap. That is MHD wave heating appears to be insufficient to reproduce the maximum of the chromospheric Mg II emission observed in the most active stars.

- Since the Mg II emission originates in a higher layer than the Ca II emission, this suggests that with greater height additional non-wave heating mechanisms come into play.

- This is in good agreement with solar observations of turbulent events seen in the transition region C IV line by Brueckner (1981). Also this picture is supported by Wood et al. (1997) who found from the analysis of stellar C IV and Si IV emission line profiles that two heating processes appear to work, MHD wave heating and micro-flare type reconnection.

- It appears now that the chromospheric emission of stars can be explained by an ordered sequence of different heating processes which systematically vary as a function of height in the star and with the speed of its rotation:

  1. The *lowest chromospheric layers* of all late-type stars independent of rotation (and thus magnetic field coverage) are heated by pure acoustic shock waves.

  2. With increasing rotation the star is covered by increasing amounts of magnetic flux. In these flux tubes heating by longitudinal and transverse MHD waves through shocks occurs. This magnetic wave heating augments and strongly enhances the chromospheric emission in the *middle and upper chromosphere*. The most rapidly rotating stars produce the largest amount of MHD wave heating.

  3. Near the *top of the chromosphere* and near the foot of the *layer* where the *transition to the corona* occurs other non-wave heating mechanisms come into play. There are indications that these mechanisms are very likely micro-flares produced by magnetic field reconnection.

7.6 Deficiencies and Proposals for Further Work

Further improvements of our codes like the inclusion of the time-dependent ionization of the Hydrogen will improve more our treatment and our results will be more realistic and closer to the observations. This also allows us to use wave spectra instead of monochromatic waves which is more realistic, and the computations will be more self-consistent as the generated wave spectra in the convection zone will be the same which will propagate and heat the upper layers. Extending the two-level atom approach to larger number of levels will allow us to compute the other lines.

Appendix A

The Characteristic Equations

In this appendix we present in details the transformation of the magnetohydrodynamic equations (3.1 - 3.4) into characteristic form and the integration of the combined equations with time. In our treatment we use a co-moving frame (Lagrangian frame) which has the benefit of simplifying the MHD equations and allows tracing the expansion of the gas elements inside the flux tubes. We define the Lagrangian height coordinate $a = z(t = 0)$ as the position of the gas element at time $t = 0$. The Eulerian height coordinate z, the position of a gas element at time t, is a function of a and t as $z = z(a, t)$. The time derivative of the co-moving frame with $u = \left(\frac{\partial z}{\partial t}\right)_a$ is defined as

$$\left(\frac{\partial}{\partial t}\right)_a = \left(\frac{\partial}{\partial t}\right)_z + u\left(\frac{\partial}{\partial z}\right)_t \tag{A.1}$$

The conservation of mass inside the tube implies that $\rho(a,t)A(a,t)\mathrm{d}z = \rho_0(a)A_0(a)\mathrm{d}a$ with ρ and A being the density and tube cross section and ρ_0 and A_0 are their values at time t_0.

With ρ, T, u, p being the density, temperature, velocity and pressure of the gas inside the flux tube, respectively, the continuity, momentum, and energy equations in Lagrangian form can be rewritten as

$$A\left(\frac{\partial \rho}{\partial t}\right)_a + \rho\left(\frac{\partial A}{\partial t}\right)_a + \frac{\rho^2 A^2}{\rho_0 A_0}\left(\frac{\partial u}{\partial a}\right)_t = 0 \tag{A.2}$$

$$\left(\frac{\partial u}{\partial t}\right)_a + \frac{A}{\rho_0 A_0}\left(\frac{\partial p}{\partial a}\right)_t + g = 0 \tag{A.3}$$

$$\left(\frac{\partial S}{\partial t}\right)_a = \left.\frac{\mathrm{d}S}{\mathrm{d}t}\right|_{\mathrm{rad}} \tag{A.4}$$

since we have

$$\frac{1}{A}\left(\frac{\partial A}{\partial t}\right)_a = \frac{1}{A}\left(\frac{\partial A}{\partial t}\right)_z + \frac{u}{A}\left(\frac{\partial A}{\partial z}\right)_t \tag{A.5}$$

From the conservation of the magnetic flux together with the pressure balance equation one can eliminate the magnetic field strength B in favor of A as

$$B.A = \phi \quad , \tag{A.6}$$

$$p + \frac{B^2}{8\pi} = P_e(z) \quad , \tag{A.7}$$

$$A = \frac{\phi}{\sqrt{8\pi}} \frac{1}{\sqrt{P_e - p}} \tag{A.8}$$

where $P_e(z)$ is the gas pressure outside the flux tube, therefore the following derivatives of A can be derived

$$\frac{1}{A}\left(\frac{\partial A}{\partial t}\right)_z = \frac{1}{2}\frac{\left(\frac{\partial p}{\partial t}\right)}{(P_e - p)} \tag{A.9}$$

$$\frac{1}{A}\left(\frac{\partial A}{\partial z}\right)_t = \frac{1}{2}\frac{\left(\frac{\partial p}{\partial z}\right) - \left(\frac{\partial P_e}{\partial z}\right)}{(P_e - p)} \tag{A.10}$$

from Eqs. (A.9) and (A.10) into Eq. (A.5) yields,

$$\frac{1}{A}\left(\frac{\partial A}{\partial t}\right)_a = \frac{1}{2}\frac{1}{(P_e - p)}\left[\left(\frac{\partial p}{\partial t}\right)_a - u\frac{\mathrm{d}P_e}{\mathrm{d}z}\right] \tag{A.11}$$

Eq. (A.2) can then be rewritten as

$$\frac{1}{\rho}\left(\frac{\partial \rho}{\partial t}\right)_a + \frac{1}{2(P_e - p)}\left(\frac{\partial p}{\partial t}\right)_a - \frac{u}{2(P_e - p)}\frac{\mathrm{d}P_e}{\mathrm{d}z} + \frac{\rho A}{\rho_0 A_0}\left(\frac{\partial u}{\partial a}\right)_t = 0 \tag{A.12}$$

with the usage of the Alfvén speed, $c_A^2 = \frac{B^2}{8\pi\rho}$ and the pressure balance equation, $\frac{1}{2(P_e - p)} = \frac{4\pi}{B^2}$, Eq. (A.12) can be rewritten as

$$\frac{1}{\rho}\left(\frac{\partial \rho}{\partial t}\right)_a + \frac{1}{\rho c_A^2}\left(\frac{\partial p}{\partial t}\right)_a - \frac{u}{\rho c_A^2}\frac{\mathrm{d}P_e}{\mathrm{d}z} + \frac{\rho A}{\rho_0 A_0}\left(\frac{\partial u}{\partial a}\right)_t = 0 \tag{A.13}$$

From the following thermodynamic relations, one can eliminate p and ρ in favor of c and S as

$$\mathrm{d}p = \frac{2c}{\gamma - 1}\rho\,\mathrm{d}c - \frac{\mu c^2}{\gamma \Re}\rho\,\mathrm{d}S \tag{A.14}$$

$$\mathrm{d}\rho = \frac{2}{\gamma - 1}\frac{\rho}{c}\,\mathrm{d}c - \frac{\mu\rho}{\Re}\,\mathrm{d}S \tag{A.15}$$

substituting from Eqs. (A.14) and (A.15) into Eq. (A.13) results in,

$$\frac{2}{\gamma - 1}\left(1 + \frac{c^2}{c_A^2}\right)\left(\frac{\partial c}{\partial t}\right)_a - \frac{\mu c}{\gamma \Re}\left(\gamma + \frac{c^2}{c_A^2}\right)\left(\frac{\partial S}{\partial t}\right)_a - \frac{uc}{\rho c_A^2}\frac{\mathrm{d}P_e}{\mathrm{d}z} + c\frac{\rho A}{\rho_0 A_0}\left(\frac{\partial u}{\partial a}\right)_t = 0 \tag{A.16}$$

Also Eq. (A.3) will take the form,

$$\left(\frac{\partial u}{\partial t}\right)_a + \frac{A}{\rho_0 A_0}\frac{2c}{\gamma-1}\rho\left(\frac{\partial c}{\partial a}\right)_t - \frac{A}{\rho_0 A_0}\frac{\mu c^2}{\gamma\Re}\rho\left(\frac{\partial S}{\partial a}\right)_t + g = 0 \tag{A.17}$$

Now, Eqs. (A.4), (A.16), and (A.17) form a quasi-linear system of hyperbolic partial differential equations with u, c, S are the independent variables. Adding Eq. (A.16) and (A.17) results in ,

$$\begin{aligned}&\left[\left(\frac{\partial u}{\partial t}\right)_a + c_{\mathtt{T}}\frac{\rho A}{\rho_0 A_0}\left(\frac{\partial u}{\partial a}\right)_t\right] + \frac{2}{\gamma-1}\frac{c}{c_{\mathtt{T}}}\left[\left(\frac{\partial c}{\partial t}\right)_a + c_{\mathtt{T}}\frac{\rho A}{\rho_0 A_0}\left(\frac{\partial c}{\partial a}\right)_t\right]\\ &-\frac{\mu c^2}{\gamma\Re c_{\mathtt{T}}}\left[\left(\frac{\partial S}{\partial t}\right)_a + c_{\mathtt{T}}\frac{\rho A}{\rho_0 A_0}\left(\frac{\partial S}{\partial a}\right)_t + (\gamma-1)\frac{c_{\mathtt{T}}^2}{c^2}\left.\frac{\mathrm{d}S}{\mathrm{d}t}\right|_{\mathrm{rad}}\right] - \frac{c_{\mathtt{T}}u}{\rho c_{\mathtt{A}}^2}\frac{\mathrm{d}P_e}{\mathrm{d}z} + g = 0\end{aligned} \tag{A.18}$$

where $c_{\mathtt{T}}^2 = \frac{c^2 c_{\mathtt{A}}^2}{c^2+c_{\mathtt{A}}^2}$ is the gas velocity inside the tube.

which results in the following equation in the characteristic form along C_+– characteristic

$$\begin{aligned}&\mathrm{d}u + \frac{2}{\gamma-1}\frac{c}{c_{\mathtt{T}}}\,\mathrm{d}c - \frac{\mu c^2}{\gamma\Re c_{\mathtt{T}}}\left[\mathrm{d}S + (\gamma-1)\frac{c_{\mathtt{T}}^2}{c^2}\left.\frac{\mathrm{d}S}{\mathrm{d}t}\right|_{\mathrm{rad}}\mathrm{d}t\right] - \frac{c_{\mathtt{T}}u}{\rho c_{\mathtt{A}}^2}\frac{\mathrm{d}P_e}{\mathrm{d}z}\,\mathrm{d}t + g(r)\,\mathrm{d}t = 0\ ,\\ &\text{along}\quad \frac{\mathrm{d}a}{\mathrm{d}t} = c_{\mathtt{T}}\frac{\rho A}{\rho_0 A_0}\ :\quad \text{slope of } C^+\text{–characteristic.}\end{aligned} \tag{A.19}$$

Subtracting Eq. (A.16) and (A.17) results in the following characteristic form along C^-– characteristic,

$$\begin{aligned}&\mathrm{d}u - \frac{2}{\gamma-1}\frac{c}{c_{\mathtt{T}}}\,\mathrm{d}c + \frac{\mu c^2}{\gamma\Re c_{\mathtt{T}}}\left[\mathrm{d}S + (\gamma-1)\frac{c_{\mathtt{T}}^2}{c^2}\left.\frac{\mathrm{d}S}{\mathrm{d}t}\right|_{\mathrm{rad}}\mathrm{d}t\right] + \frac{c_{\mathtt{T}}u}{\rho c_{\mathtt{A}}^2}\frac{\mathrm{d}P_e}{\mathrm{d}z}\,\mathrm{d}t + g(r)\,\mathrm{d}t = 0\ ,\\ &\text{along}\quad \frac{\mathrm{d}a}{\mathrm{d}t} = -c_{\mathtt{T}}\frac{\rho A}{\rho_0 A_0}\ :\quad \text{slope of } C^-\text{–characteristic.}\end{aligned} \tag{A.20}$$

with a new time step, physical variables of any interior grid point P can be computed with solutions along the three characteristics with three foot points at R for the C^+, C for the C_0 and S for the C^-–characteristic, respectively; as shown in Fig. 3.1 The time integration between values given at old time step labeled R and those given at new time step labeled P in the case of C^+–characteristic, is given by

$$\begin{aligned}u_{\mathtt{P}} &- u_{\mathtt{R}} + \underbrace{\frac{1}{\gamma-1}\left(\left.\frac{c}{c_{\mathtt{T}}}\right|_{\mathtt{R}} + \left.\frac{c}{c_{\mathtt{T}}}\right|_{\mathtt{P}}\right)}_{\mathrm{F_1}}(c_{\mathtt{P}} - c_{\mathtt{R}}) - \underbrace{\frac{\mu}{2\gamma\Re}\left(\left.\frac{c^2}{c_{\mathtt{T}}}\right|_{\mathtt{R}} + \left.\frac{c^2}{c_{\mathtt{T}}}\right|_{\mathtt{P}}\right)(S_{\mathtt{P}} - S_{\mathtt{R}})}_{\mathrm{F_2}}\\ &- \underbrace{\frac{\mu(\gamma-1)}{2\gamma\Re}\left(c_{\mathtt{T}}D|_{\mathtt{R}} - c_{\mathtt{T}}D|_{\mathtt{P}}\right)\Delta t}_{\mathrm{F_3}} - \underbrace{\left(\left.\frac{uc_{\mathtt{T}}}{\rho c_{\mathtt{A}}^2}\frac{\mathrm{d}P_e}{\mathrm{d}z}\right|_{\mathtt{R}} + \left.\frac{uc_{\mathtt{T}}}{\rho c_{\mathtt{A}}^2}\frac{\mathrm{d}P_e}{\mathrm{d}z}\right|_{\mathtt{P}}\right)\frac{\Delta t}{2}}_{\mathrm{F_4}}\\ &+ g\Delta t = 0\end{aligned} \tag{A.21}$$

while the corresponding equation along C^-–characteristic between grid point S in old time step and P in the time step is given by

$$\begin{aligned} u_{\mathtt{P}} \;-\; & u_{\mathtt{S}} - \underbrace{\frac{1}{\gamma-1}\left(\left.\frac{c}{c_{\mathtt{T}}}\right|_{\mathtt{S}} + \left.\frac{c}{c_{\mathtt{T}}}\right|_{\mathtt{P}}\right)}_{\mathrm{S}_1}(c_{\mathtt{P}} - c_{\mathtt{S}}) + \underbrace{\frac{\mu}{2\gamma\Re}\left(\left.\frac{c^2}{c_{\mathtt{T}}}\right|_{\mathtt{S}} + \left.\frac{c^2}{c_{\mathtt{T}}}\right|_{\mathtt{P}}\right)(S_{\mathtt{P}} - S_{\mathtt{S}})}_{\mathrm{S}_2} \\ + \; & \underbrace{\frac{\mu(\gamma-1)}{2\gamma\Re}\left(c_{\mathtt{T}}D|_{\mathtt{S}} + c_{\mathtt{T}}D|_{\mathtt{P}}\right)\Delta t}_{\mathrm{S}_3} + \underbrace{\left(\left.\frac{uc_{\mathtt{T}}}{\rho c_{\mathtt{A}}^2}\frac{\mathrm{d}P_e}{\mathrm{d}z}\right|_{\mathtt{S}} + \left.\frac{uc_{\mathtt{T}}}{\rho c_{\mathtt{A}}^2}\frac{\mathrm{d}P_e}{\mathrm{d}z}\right|_{\mathtt{P}}\right)\frac{\Delta t}{2}}_{\mathrm{S}_4} \\ + \; & g\Delta t = 0 \end{aligned} \tag{A.22}$$

Multiplying Eq. (A.21) by S_1 and Eq. (A.22) by F_1 and adding the resulting equations, results in a solution for the gas velocity at new time step:

$$u_{\mathtt{P}} = \frac{F_1\left[u_{\mathtt{S}} - S_2 - S_3 - S_4 - g\Delta t\right] + S_1\left[u_{\mathtt{R}} - F_2 - F_3 - F_4 - g\Delta t\right]}{F_1 + S_1} \tag{A.23}$$

Subtracting Eq. (A.21) from Eq. (A.22) yields a solution for the speed of sound at the new time step:

$$c_{\mathtt{P}} = \frac{u_{\mathtt{R}} - u_{\mathtt{S}} + F_1 c_{\mathtt{R}} + S_1 c_{\mathtt{S}} + F_2 + F_3 + S_2 + S_3 + F_4 + S_4}{F_1 + S_1} \tag{A.24}$$

The physical variables at the footpoints of the characteristics R, C and S are computed by interpolation from gridpoints A, C and B (see, Fig. 3.1), solutions given by Eq. (A.23) and Eq. (A.24) are for points lie inside the computational domain. The treatment of upper most gridpoint and the lowest gridpoint need boundary conditions. An iterative procedure starts with a fixed value of the radiative damping function D, and iteratively compute the physical variables p, T, and u till convergence. Then, the new physical variables at the new time step are used in the radiative transfer routines to compute a new value of D for every grid point, this sequence is repeated again till convergence is achieved for D.

Bibliography

[1] Anderson L.S., Athay R.G., 1989, ApJ 346, 1010

[2] Ayres T.R., Linsky J.L., Vaiana G.S., Golub L., Rosner R., 1981, ApJ 250, 293

[3] Baliunas S.L. et al., 1995, ApJ 438, 269

[4] Basri G.S., Linsky J.L., 1979, ApJ 234, 1023

[5] Beckers J.M., Schulz R.B., 1972, Solar Physics 27, 61

[6] Biermann L., 1946, Naturwissenschaften 33, 118

[7] Blanco C., Bruca L., Catalano S., Marilli E., 1982, Astr. Ap. 115, 280

[8] Böhm-Vitense E., Dettman T., 1980, ApJ 236, 560

[9] Brandenburg A., Schmitt D., 1998, A&A 338, L55

[10] Brandenburg A., Saar S.H., Turpin C.R., 1998, ApJ 498, L51

[11] Brueckner G.E., 1981, In: Solar Active Regions - A monograph from Skylab Solar Workshop III, Frank Q. Orrall (ed.), Colorado Associated University Press

[12] Buchholz B., 1995, Ph.D. thesis, University of Heidelberg

[13] Buchholz B., Ulmschneider P., 1994. In: Cool Strs, Stellar Systems, and the Sun XIII, Caillault J.-P. (eds.), ASP Conf. Series 64, p. 363

[14] Buchholz B., Hausschildt P., Rammacher W., Ulmschneider P., 1994, A&A 285, 987

[15] Buchholz B., Ulmschneider P., Cuntz M., 1998, ApJ 494, 700

[16] Cappelli A., Cerruti-Sola M., Cheng C.C., Pallavicini R., 1989, A&A 213, 226

[17] Carlsson M., Stein R.F., 1995, ApJ 440, L29

[18] Choudhuri A.R., Auffret H., Priest E.R., 1993 a, Solar Physics 143, 49

[19] Choudhuri A.R., Dikpati M., Banerjee D., 1993 b, ApJ 413, 811

[20] Cooly J.W., Tukey J.W., 1965, Math. Comput. 19, 297

[21] Cuntz M., Rammacher W., Ulmschneider P., 1994, ApJ 432, 690

[22] Cuntz M., Rammacher W., Ulmschneider P., Musielak Z.E., Saar S.H., 1999, ApJ 522, 1053

[23] Defouw R.J., 1976, ApJ 209, 266

[24] Deubner F.-L., Waldschik T., Steffens S., 1996, A&A 307, 936

[25] Deubner F.-L., 1998, In: New Eyes to See Inside the Sun and Stars, Deubner F.-L, Christian-Dalsgaard J., and Kurtz D. (eds.), IAU Symposium no. 185, p. 427

[26] Doyle J.G., 1987, Mon. Not. R. astr. Soc. 224, Short Communication, 1

[27] D'Silva S., Choudhuri A.R., 1993, A&A 272, 621

[28] Eberhard G., Schwarzschild K., 1913, ApJ 38, 292

[29] Edwin P.M., Roberts B., 1983, Solar Physics 88, 179

[30] Fan Y., Fisher G.H., DeLuca E.E., 1993, ApJ 405, 390

[31] Fawzy D.E., Ulmschneider P., Cuntz M., 1998, A&A 336, 1029

[32] Fawzy D.E., Musielak Z.E., Ulmschneider P., 1999 Rom.Astron.J. Supplement 9, 149, Bucharest

[33] Frazier E.N., Stenflo J.O., 1972, Solar Physics 27, 330

[34] Giovanelli R.G., Harvey J.W., Livingston W.C., 1978, Solar Physics 59, 40

[35] Gray D.F., 1982, ApJ 261, 259

[36] Grossmann-Doerth U., Schüssler M., Steiner O., 1998, A&A 337, 928

[37] Hale G.E., 1908, ApJ 28(4), 315

[38] Hale G.E., Ellerman F., Nicholson S.B., Joy A.H., 1919, ApJ 49, 153

[39] Hartree D.R., 1952, Los Alamos Report LA-HU-1

[40] Hartmann L., Baliunas, S.L., Duncan D.K., Noyes R.W., 1984, ApJ 279, 778

[41] Harvey K.L., 1993, PhD thesis, Univ. of Utrecht

[42] Harvey K.L., Zwaan C., 1993, Solar Physics 148, 85

[43] Hasan S.S., 1985, A&A 143, 39

[44] Hasan S.S., 1986, MNRAS 219, 357

[45] Hasan S.S., Kalkofen W., 1999, ApJ 519, 899

[46] Herbold G., Ulmschneider P., Spruit H.C., Rosner R., 1985, A&A 145, 157

[47] Howard R., 1959, ApJ 130, 193

[48] Howard R., Stenflo J.O., 1972, Solar Physics 22, 402

[49] Huang P., Musielak Z.E., Ulmschneider P., 1995, A&A 279, 579

[50] Hünerth G., Ulmschneider P., 1995, A&A 293, 166

[51] Hünsch M., Schröder K.-P., 1997, A&A 309, L51

[52] Innes D.E., Inhester B., Axford W.I., Wilheim K., 1997, Nature 386, 811

[53] Judge P.G., Tarbell T.D., Wilhelm K., 2000, ApJ (in press)

[54] Kalkofen W., 1997, ApJ 486, L145

[55] Kalkofen W., Ulmschneider P., 1984, In: Methods in radiative transfer, Cambridge University Press, p. 131

[56] Kalkofen W., Ulmschneider P., Schmitz F., 1984, ApJ 287, 952

[57] Kalkofen W., Rossi P., Bodo G., Massaglia S., 1994, A&A 284, 976

[58] Kalkofen W., Ulmschneider P., Avrett E.H., 1999, ApJ 521, L141

[59] Kraft R.P., 1967, ApJ 150, 551

[60] Krause F., Rädler K.-H., 1980, In: Mean-Field Magnetohydrodynamics and Dynamo Theory, Pergamon Press, Oxford

[61] Kulsrud R.M., 1955, ApJ 121, 461

[62] Kurucz R., 1970, Smithsonian Astrophys. Obs. Spec. Rept. 309

[63] Leighton R.B., 1959, ApJ 130, 366

[64] Leighton R., Noyes R., Simon G.W., 1962, ApJ 135, 474

[65] Lighthill M.J., 1952, Proc. Roy. Soc. London A211, 564

[66] Lister M., 1960. The numerical solution of hyperbolic partial differential equations by the method of characteristics, In: Ralston A., Wilt H.S. (eds.) Mathematical Methods for Digital Computers I. Wiley, New York

[67] Litvinenko Y.E., 1999, ApJ 515, 435

[68] Maltby P., Avrett E.H., Carlsson M., Kjeldseth-Moe O., Kurucz R., Loeser R., 1986, ApJ 306, 284

[69] Marcy G.W., Basri G., 1989, ApJ 345, 480

[70] Moffatt H.K., 1978, In: Magnetic Field Generation in Electrically Conducting Fluids, Cambridge University Press, Cambridge

[71] Montesinos B., Fernández-Figueroa M.J., de Castro E., 1987, Mon. Not. R. Astron. Soc. 229, 627

[72] Montesinos B., Jordan C., 1993, Mon. Not. R. Astron. Soc. 264, 900

[73] Moore R.L., Rabin D., 1985, ARA&A 23, 239

[74] Moreno-Insertis F., 1992, In: Sunspots, Theory and Observations, J.H. Thomas and N.O. Weiss (eds), Kluwer, Dordrecht, 385

[75] Muller R., 1989, In: Solar and Stellar Granulation, R.J. Rutten & G. Severino (eds.), Kluwer Academic Publ., Dordrecht, p. 101

[76] Muller R., Roudier Th., Vigneau J., Auffret H., 1994, A&A 283, 232

[77] Musielak Z.E., Rosner R., Ulmschneider P., 1989, ApJ 337, 470

[78] Musielak Z.E., Rosner R., Stein R.F., Ulmschneider P., 1994, ApJ 423, 474

[79] Musielak Z.E., Rosner R., Gail H.P., Ulmschneider P., 1995, ApJ 448, 865

[80] Musielak Z.E., Rosner R., Ulmschneider P., 2000, ApJ 541, 410

[81] Nakariakov V.M., Zhugzhda Y.D., Ulmschneider P., 1996, A&A 312, 691

[82] Narain U., Ulmschneider P., 1990, Space Sci. Rev. 54, 377

[83] Narain U., Ulmschneider P., 1996, Space Sci. Rev. 75, 453

[84] Nesis A., Hanslmeier A., Hammer R., Komm R., Mattig W., 1990, In: The Dynamic Sun, Proceeding of the 6^{th} European Meeting on Solar Physics, L. Dezso (ed.)

[85] Nordlund A., Spruit H.C., Ludwig H.-G., Trampedach R., 1997, A&A 328, 229

[86] Noyes R.W., 1983, In: IAU Symposium 102, Solar and Stellar Magnetic Fields: Origins and Coronal Effects, J.O. Stenflo (ed.), p. 133

[87] Noyes R.W., Hartmann L.W., Baliunas S.L., Duncan D.K., Vaughan A.H., 1984, ApJ 279, 763

[88] Oranje B.J., 1985, A&A 154, 185

[89] Osterbrock D.E., 1961, ApJ 134, 347

[90] Pallavicini, R., Golub L., Rosner R., Vaiana G., Ayres T., Linsky J., 1981, ApJ 248, 279

[91] Parker E.N., 1955 a, ApJ 121, 491

[92] Parker E.N., 1955 b, ApJ 122, 293

[93] Parker E.N., 1963, ApJ 138, 552

[94] Parker E.N., 1965, Space Sci. Rev. 4, 666

[95] Parker E.N., 1978, ApJ 221, 368

[96] Parker E.N., 1994, ApJ 433, 867

[97] Priest E., 1984, In: Solar Magnetohydrodynamics, Reidel Publishing House, England

[98] Rammacher W., 2000, private communication

[99] Rammacher W., Cuntz M., 1991, A&A 250, 212

[100] Rammacher W., Ulmschneider P., 2001, in preparation

[101] Roald C.B., Sturrock P.A., Wolfson R., 2000, ApJ 538, 960

[102] Roberts B., Webb A.R., 1979, Solar Physics 64, 77

[103] Robinson R.D., Durney B.R., 1982, A&A 108, 322

[105] Rutten R.G.M., 1986, A&A 159, 291

[105] Rutten R.G.M., 1987, A&A 177, 131

[106] Rutten R.G.M., Schrijver C.J., Lemmens A.F.P., Zwaan C., 1991, A&A 252, 203

[107] Rüedi I., Solanki S.K., Mathys G., Saar, S.H., 1997, A&A 318, 429

[115] Saar S.H., 1987, PhD Thesis, Univ. of Colorado

[140] Saar S.H., 1996, IAU Symp. 176, 237

[110] Saar S.H., 1998, In: ASP Conf. Ser. 154, Cool Stars, Stellar Systems, and the Sun X, Donahue R.A., Bookbinder J.A. (eds.), san Francisco: ASP, 211

[111] Schatzman E., 1962, Ann. d'Astrophys. 25, 18

[112] Schmitz F., Ulmschnieder P., 1981, A&A 93, 178

[113] Schmitz F., Ulmschnieder P., Kalkofen W., 1985, A&A 148, 217

[114] Schröder K.-P., Eggleton P.P., 1996, Rev. Mod. Astr. 9, 221

[115] Schrijver C.J., 1987, A&A 172, 111

[134] Schrijver C.J., 1992, A&A 258, 507

[117] Schrijver C.J., Cotè J., Zwaan C., Saar S.H., 1989, ApJ 337, 964

[118] Schrijver C.J., Dobson A.K., Radick R.R., 1989, ApJ 341, 1035

[119] Schrijver C.J., Harvey K.L., 1994, Solar Physics 150, 1

[136] Schrijver C.J., 1995, Astron. Astrophys. Rev. 6, 181

[121] Schijver C.J., Zwaan C., 2000, In: Solar and Stellar Magnetic Activity, Cambridge Astrophysics Series 34.

[122] Schrijver C.J., Title A.M., Harvey K.L., Sheeley N.R., Jr., Wang Y-M., van den Oord G.H.J., Shine R.A., Tarbell T.D., Hurlburt N.E., 1998, Nature 394, 152

[123] Schüssler M., Caligari P., Ferriz-Mas A., Moreno-Insertis F., 1994, A&A 281, L69

[124] Schwarzschild M., 1948, ApJ 107, 1

[125] Simon T., Landsman W., 1991, ApJ 380, 200

[126] Skumanich A., 1972, ApJ 171, 565

[127] Skumanich A., Smythe C., Frazier E.N., 1975, ApJ 200, 747

[140] Solanki S. K., 1996, IAU Symp. 176, 201

[129] Solanki S. K., Steiner O., Uitenbroeck H., 1991, A&A 250, 220

[130] Spruit H.C., 1979, Solar Physics 61, 363

[131] Spruit H.C., Zweibel E.G., 1979, Solar Physics 62, 15

[132] Spruit H.C., 1982, Solar Physics 75, 3

[133] Spruit H.C., Nordlund $\dot{A}$, Title A.M., 1990, ARAA 28, 263

[134] Steffen M., 1992, Habilitation thesis, University of Kiel

[135] Stein R.F., 1967, Solar Physics 2, 385

[136] Steiner O., 1995, In: Solar and Galactic Magnetic fields, D. Schmitt (ed.), Nachr. der Akad. der Wiss. in Göttingen, Göttingen

[140] Steiner O., 1996, In: Nachr. Akad. Wiss. Göttingen 4, Solar and Galactic Magnetic fields, D. Schmitt & H.-H. Voigt (eds.) (Göttingen: Vandenhoeck & Ruprecht), 15

[138] Stenflo J.O., 1994, Solar Magnetic Fields, Kluwer Academic Publishers

[139] Stepien K., 2000, private communication

[140] Sturrock P.A., 1996, In: ASP Conf. Ser. 111, Magnetic Reconnection in the Solar Atmosphere, Bentley R.D. & Mariska J.T. (eds.) (San Francisco: ASP), 105

[141] Sutmann G., Ulmschneider P., 1995 a, A&A 294, 232

[142] Sutmann G., Ulmschneider P., 1995 b, A&A 294, 241

[143] Sutmann G., Musielak Z.E., Ulmschneider P., 1998, A&A 340, 556

[144] Theurer J., 1993, Diplom Thesis, Univ. Heidelberg, Germany

[145] Theurer J., 1998, PhD Thesis, Univ. Heidelberg, Germany

[146] Theurer J., Ulmschneider P., Kalkofen W., 1997, A&A 324, 717

[147] Trampedach R., Christensen-Dalsgaard, J., Nordlund A., Stein R.F., 1996, In: Solar Convection and Oscillations and their Relationship., Astrophysics and Space Science Library Vol. 225, p. 73, Kluwer Academic Publishers

[148] Tsuneta S., 1996, ApJ 456, 840

[152] Uitenbroek H., 1989, A&A, 213, 360

[150] Ulmschneider P., 1970, Solar Phys. 12, 403

[156] Ulmschneider P., Kalkofen W., Nowak T., Bohn U., 1977, A&A 54, 61

[152] Ulmschneider P., 1989, A&A 222, 171

[153] Ulmschneider P., 1991, Acoustic Heating. In: Mechanisms of Chromospheric and Coronal Heating, Ulmschneider P., Priest E.R., Rosner R. (eds.), Springer, Berlin, p. 328

[154] Ulmschneider P., 1994, A&A 288, 1021

[155] Ulmschneider P., Musielak Z.E., 1998, A&A 338, 311

[156] Ulmschneider P., Kalkofen W., Nowak, T., Bohn, H.U., 1977, A&A 54, 61

[157] Ulmschneider P., Muchmore D., Kalkofen W., 1987, A&A 177, 292

[158] Ulmschneider P., Zähringer K., Musielak Z.E., 1991, A&A 241, 625

[159] Ulmschneider P., Zähringer K., Musielak Z.E., 1996, A&A 315, 212

[160] Ulmschneider P., Theurer J., Musielak Z.E., 1996, A&A 315, 212

[161] Ulmschneider P., Theurer J., Musielak Z.E., Kurucz R., 1999, A&A 347, 243

[162] Unno W., Ando H., 1979, Geophys. Astrophys. Fluid Dyn. 12, 107

[163] Vaiana G.S., Cassinelli J.P., Fabbiano G., Giacconi R., Golub L., Gorenstein P., Haisch B.M., Harnden Jr. F.R., Johnson H.M., Linsky J.L., Maxson C.W., Mewe R., Rosner R., Seward F., Topka K., Zwaan C., 1981, ApJ 245, 163

[164] Vaughan A.H., Preston G.W., 1980, Pub. A.S.P. 92, 385

[165] Vaughan A.H., Preston G.W., Wilson O.C., 1978, Pub. A.S.P. 90, 267

[166] Vernazza J.E., Avrett E.H., Loeser R., 1981, ApJ Suppl. 45, 635

[167] Vilhu O., 1987, Cool Stars, Stellar Systems, and the Sun proceedings, Linsky J., & Stencel R.E. (eds.), Boulder, Colorado.

[168] Walter F.M., 1981, ApJ 245, 677

[169] Walter F.M., 1982, ApJ 253, 745

[170] Wang H., Shi Z., 1993, Solar Physics 143, 119

[171] Webb A.R., Roberts B., 1978, Solar Physics 59, 249

[172] Wilson O.C., 1963, ApJ 138, 832

[173] Wilson O.C., 1968, ApJ 153, 221

[174] Wilson O.C., 1978, ApJ 226, 379

[175] Wood, B.E., Linsky J.L., Ayres T.R., 1997, ApJ 478, 745

[176] Yokoyama T., Shibata K., 1998, ApJ 494, L113

[177] Zhugzhda Y.D., Bromm V., Ulmschneider P., 1995, A&A 300, 302

[178] Ziegler U., Ulmschneider P., 1997 a, A&A 324, 417

[179] Ziegler U., Ulmschneider P., 1997 b, A&A 327, 854

[180] Zwaan C., 1983, In: Solar and Stellar Magnetic Fields, J.O. Stenflo (ed.), IAU Symp. 102, Reidel, Dordrecht, p. 85

[181] Zwaan C., 1987, In: Elements and patterns in the solar magnetic field, ARAA, Vol. no. 25, p. 83-111

Acknowledgements

Words can not express about my deep thanks to Prof. Dr. P. Ulmschneider for giving me the chance to be one of his students, and for his continuous efforts with me. I am very grateful to him for the interesting discussions, comments, and advises during my Ph.D. study.

I would like to thank Dr. Hans Martin Schmid for accepting to be the second referee of my thesis.

I am very grateful to Prof. Dr. Z. Musielak of Texas University for the interesting discussions and comments.

Special thanks are due to my family, my wife Nilay and my son Ahmed, for their patience and efforts with me.

It is of great pleasure to thank my colleagues at the Institute of Theoretical Astrophysics for the friendly atmosphere, special thanks for the computer system manager of the institute Mr. Rainer Kürschner for the interesting discussions.

Finally, I would like to acknowledge the financial support of the Deutsche Forschungsgemeinschaft (DFG).